Jan Dlugosz University

in Częstochowa

Ph.D. Thesis

Discipline: Physics

The influence of environment on the electronic and optical properties of thin-film composite materials

Lucia Nechalova

Scientific Supervisor: prof. dr. hab. Małgorzata Makowska-Janusik

Assistant Supervisor: dr hab. Anna Migalska-Zalas

Czestochowa 2022

I dedicate the Thesis to my husband and daughter.

Acknowledgment

First and foremost I want to thank my supervisor **Prof. Malgorzata Makowska-Janusik**, the person without whom this thesis would never come to life. She drew mi into the theoretical computing world, introduced me to all computing techniques, always knew how to advise me, and had a lot of patience with me. She has been my support throughout my studies and has guided me successfully until its completion. I am very grateful to her for everything.

I also want to thank my second supervisor **dr hab. Anna Migalska-Zalas** for help with the experimental part of the work, she had good advice for me, which has always helped.

Many thanks also to **Prof. Bouchta Sahraoui** for accepting my person in his laboratory in Moltech Anjue and offering his valuable experience in SHG and THG measurements.

I would like to express my gratitude to **Prof. Barbara Morzyk-Ociepa** for her help during my PhD studies at Jan Dlugosz University.

I would like to thank all the employees of the university and our department for their support and help, especially when Poland was a new place for me and Polish was a foreign language to me.

I am also grateful to my friends for their support, in particular **Karolina Ordor**, **Tatiana Babuka** and **Karolina Dysz**.

And I would like to thank my husband **Dominik Nechala** and my daughter **Zara** for their support and patience. They always gave me as much time as I needed to create this dissertation.

Contents

List of publications

1. Makowska-Janusik, M.; Kajzar, F.; Miniewicz, A.; **Mydlova, L.;** Rau, I. *First principle calculations of the electronic and vibrational properties of the 3-(1,1-dicyanoethenyl)—phenyl-4,5-dihydro-1H-pyrazole molecule,* J. Phys. Chem. A. 119, 1347-1358, 2015.

2. Ayadi, A.; **Mydlova, L.;** Zouari, N.; Makowska-Janusik, M.; Sahraoui, B.; El-Ghayoury, A. *Electronic and optical properties of New synthesized TTF-based Azie derivatives - Experimental and theoretical study*, Opt. Mat., 56, 27-35, 2016.

3. Yenupuri, T. V.; **Mydlova, L.;** Agarwal, D. S.; Sharma, R.; Sakhuja, R.; Makowska-Janusik, M.; Pant, D. D. *Experimental and Quantum Chemical Calculations of Imidazolium Appended Naphthalene Hybrid in Different Biomimicking Aqueous Interfaces,* J. Phys. Chem. A., 120, 6563-6574, 2016.

4. **Mydlova, L.;** Ayadi, A.; El-Ghayoury, A.; Sahraoui, B.; Makowska-Janusik, M. *Analyses of electronic and optical properties of TTF-based azine derivatives,* Proceedings Vol. 10603, Photonics, Devices, and Systems VII, 2017.

5. **Mydlova, L.;** Taboukhat, S.; Ayadi, A.; Migalska-Zalas, A.; El-Ghayoury, A.; Zawadska, A.; Makowska-Janusik, M.; Sahraoui, B. *Theoretical and experimental investigation of multifunctional highly conjugated organic push-pull ligands for NLO applications,* Opt. Mat. 86, 304-310, 2018.

6. **Mydlova, L.;** Kluza, K.; Halama, M.; Makowska-Janusik, M. *Anti-corrosive surface effect of ascorbic acid caused on the ZnO nanoparticles – Experiment and theoretical investigations,* Applied Surface Science, 483, 562-571, 2019.

7. **Mydlova, L.;** Taboukhat, S.; Waszkowska, K.; Ibrahim, N.; Migalska-Zalas, A.; Sahraoui, B.; Frere, P.; Makowska-Janusik, M. *Selected molecules based on (-1-cyanovinyl)benzonitrile as new materials for NLO applications – experimental and computational studies*, Journal of Molecular Liquids, 314,113622-113632, 2020.

8. **Mydlova, L.;** Sahraoui, B.; Waszkowska, K.; Karout, H. E.; Makowska-Janusik, M.; Migalska-Zalas, A. *Computational and experimental study of*

nonlinear optical susceptibilities of composite materials based on PVK polymer matrix and benzonitrile derivatives, Materials, 15, 2073-2100, 2022.

Prize and Awards

The first place in the contest of posters at the conference: Corrosion and surface treatment in the industry, the title of poster: *Effect of environment on the electronic properties of nanoparticles*, Liptovsky Mikulas, Slovakia, 30.09 - 02.10.2015.

Grants

PI of the PRELUDIUM No. 2017/25/N/ST2/02587 grant funded by the National Center of Sciences, Poland, Title of grant: *Multipole discrete local field model in modeling of NLO properties of the thin composite films*

Participation in the conferences

Oral communications:

1. **Mydlova, L.;** Halama, M.; Makowska-Janusik, M. *Effect of vitamin C on the electronic properties of ZnO nanoclusters*, International Students and Young Scientists Conference in Theoretical and experimental Physics HEUREKA-2015, Lviv, Ukraine, 13-15.05.2015.
2. **Mydlova, L.;** Halama, M.; Makowska-Janusik, M. *The Antioxidantive effect of vitamine C on the electronic properties of ZnO nanoclusters,* The XXTH International seminar on physics and chemistry of solids (ISPCS `15), Lviv, Ukraine, 13-16.09.2015.

3. **<u>Mydlova, L.;</u>** Ayadi, A.; El-Ghayoury, A.; Sahraoui, B.; Makowska-Janusik, M. *The theoretical and experimental study of new TTF-based azine derivatives,* Fifth International Workshop on Advanced, Nano- and Biomaterials and Their Applications, Constanta, Romania, 20 - 25.09.2016.

4. **<u>Mydlova, L.;</u>** Ayadi, A.; El-Ghayoury, A.; Sahraoui, B.; Makowska-Janusik, M. *Teoretyczne I eksperymentalne badania azynowych pochodnych TTF,* II Częstochowskie Forum Młodych, XII Forum Młodych Nauki, Częstochowa, 13.06.2017.

5. **<u>Mydlova, L.;</u>** Ayadi, A.; El-Ghayoury, A.; Sahraoui, B.; Makowska-Janusik, M. *Analyses of electronic and optical properties of new TTF-based azine derivatives,* Photonics Prague 2017, Praga, Czech Republic, 28-30.08.2017.

6. **<u>Mydlova, L.;</u>** Ayadi, A.; El-Ghayoury, A.; Sahraoui, B.; Makowska-Janusik, M. *Analiza własności elektronowych oraz optycznych nowo syntezowanych ligandów do zastosowania w optice nieliniowej,* VI Ogólnopolska konferencja dla młodych naukowców, Pomiedzy Naukami, Chorzów, Poland, 15.09.2017.

7. **<u>Mydlova, L.;</u>** Ayadi, A.; El-Ghayoury, A.; Sahraoui, B.; Migalska-Zalas, A.; Makowska-Janusik, M. *Structural and optical properties of composite materials based on TTF-azine organic chromophores,* The 5th International conference on the physics of optical materials and devices, Igalo, Montenegro, 27-31.08.2018.

Posters:

1. **<u>Mydlova, L.;</u>** Halama, M.; Makowska-Janusik, M. *Effect of environment on the electronic properties of nanoparticles,* Corrosion and surface treatment in industry, Liptovsky Mikulas, Slovakia, 30.09. - 2.10.2015.

2. **<u>Mydlova, L.;</u>** Ayadi, A.; El-Ghayoury, A.; Sahraoui, B.; Makowska-Janusik, M. *Elektronowe i optyczne własności azynowych pochodnych tetratiafulwalenów do zastosowań nieliniowooptycznych,* 44. Zjazd fizyków polskich, Wrocław, Poland, 10-15.09.2017.

Scientific internships abroad

- University of Angers, France, from 1st June to 31st July 2015.
- University of Angers, France, from 15st May to 15st July 2016.
- National Hellenic Research Foundation in Athens, Greece 1st Novenber 2018 to 30 January 2019

Abstract

Organic nonlinear optical (NLO) materials play a crucial role in modern optoelectronic elements. Most of them are chromophores based upon aromatic π-electron systems unsymmetrically end-capped with electron-donating and accepting groups to influence the electronic bias. These chromophores are embedded in polymer matrixes forming guest-host composite materials in thin-film forms. However, to talk about the practical use of these materials, it is necessary to study the properties of composites and to describe the mechanisms of physical phenomena occurring in separated molecules as well as in composites as a whole. In this case, computer simulations are helpful.

This thesis aimed to develop a theoretical computational model and methodology for proceeding to predict the macroscopic optical properties of composite materials in thin-film forms. In this case, the molecular dynamics technique was used to model the structures of composites and quantum chemical calculations were employed to predict the optical properties of chromophores in a polymer environment. The optical properties were calculated by implementing a discrete local field model hierarchically. The computationally obtained data were compared with experimental results taken from SHG and THG responses of the material.

Poly (methyl methacrylate) (PMMA) and poly(vinyl carbazole) (PVK) based composites were chosen as model guest-host materials. Two groups of NLO chromophores were embedded into these polymers. One group of chromophores is four different tetrathiafulvalene (TTF)-attended azine derivatives and the other group is based on three benzonitrile derivatives. The results of molecular dynamics simulation of chromophore/PMMA and chromophore/PVK composite materials as well as structural, electronic, and optical properties of chromophores in a vacuum and a polymer matrix are discussed. The obtained computational data were compared with the experimental results testing the correctness of the implemented computational local field model. The influence of polymer matrices on the enhancement of the NLO properties of benzonitrile derivatives in the PVK matrix and the neutrality of the PMMA matrix concerning the tested chromophores was explained. The optical properties of the investigated composites were discussed based on the spatial distribution of chromophores in the polymer matrix.

Abstrakt

Organiczne materiały nieliniowooptyczne (NLO) odgrywają kluczową rolę we współczesnych elementach optoelektronicznych. Większość z nich to chromofory oparte na aromatycznych układach π-elektronowych niesymetrycznie zakończonych donorowymi i akceptorowymi grupami elektronowymi mającymi wpływ na polaryzację materiału. NLO aktywne chromofory są zazwyczaj umieszczone w matrycach polimerowych, tworząc cienkowarstwowe materiały kompozytowe typu gość-gospodarz. Aby mówić o praktycznym zastosowaniu tych materiałów, konieczne jest zbadanie właściwości kompozytów oraz opisanie mechanizmów zjawisk fizycznych zachodzących zarówno w poszczególnych komponentach, jak i w kompozycie jako całości. W tym przypadku pomocne są symulacje komputerowe.

Celem niniejszej pracy było opracowanie teoretycznego modelu obliczeniowego oraz metodyki postępowania w zakresie przewidywania makroskopowych właściwości optycznych cienkowarstwowych materiałów kompozytowych. Do modelowania struktur kompozytów wykorzystano technikę dynamiki molekularnej, a obliczenia kwantowo-chemiczne posłużyły do przewidywania właściwości optycznych chromoforów w środowisku polimerowym. Właściwości optyczne obliczono stosując model dyskretnego pola lokalnego w podejściu hierarchicznym. Dane uzyskane z obliczeń porównano z wynikami eksperymentalnymi zaczerpniętymi z badań sygnałów SHG i THG.

Jako modelowe materiały typu gość-gospodarz wybrano kompozyty na bazie poli(metakrylanu metylu) (PMMA) i poli(winylo karbazolu) (PVK). W matrycach polimerowych osadzono dwie grupy chromoforów NLO. Jedną grupę stanowiły cztery różne pochodne tetratiafulwalenu (TTF) z przyłączonymi azynami, a drugą grupę - trzy pochodne benzonitrylu. Omówiono wyniki symulacji dynamiki molekularnej materiałów kompozytowych chromofor/PMMA oraz chromofor/PVK, a także właściwości strukturalne, elektroniczne i optyczne chromoforów w próżni i w matrycy polimerowej. Uzyskane dane obliczeniowe porównano z wynikami eksperymentalnymi, co stanowiło test poprawności wdrożonego modelu obliczeniowego. Wyjaśniono wpływ matryc polimerowych na wzmocnienie właściwości NLO pochodnych benzonitrylu w matrycy PVK oraz neutralność matrycy PMMA w stosunku do badanych chromoforów. Właściwości

optyczne badanych kompozytów wyjaśniono na podstawie przestrzennego rozkładu chromoforów w matrycy polimerowej.

Abbreviations and symbols

NLO – nonlinear optical

EO – electro-optical

OPO – optical parametric oscillator

SHG – second-harmonic generation

THG – third-harmonic generation

KTP – potassium titanyl phosphate

LBO – lithium triborate

PMMA – poly(methyl methacrylate)

PVK – poly(vinyl carbazole)

TTF – Tetrathiafulvalene

DMF – Dimethylformamide

DMSO – Dimethyl sulfoxide

D – donor

A – acceptor

α – polarizability

β – second-order hyperpolarizability

γ – third-order hyperpolarizabilities

$\chi^{(2)}$ – second-order susceptibility

$\chi^{(3)}$ – third-order susceptibility

$\widehat{H}$ – Hamilton operator

$\widehat{H}^{(0)}$ – unperturbed Hamiltonian

$\hat{h}(i)$ – one-electron Hamiltonian

$\Psi(r,R)$ – wave function

PCM – polarizable continuum model

MD – molecular dynamics

HF – Hartree-Fock

DFT – density functional theory

TD-DFT – Time-dependent density functional theory

ρ – charge density

F – local electric field intensity

E – electric field intensity

D – electric induction

H – magnetic field intensity

B – magnetic induction

P – Polarization

σ – current density

q – electric charge

e – charge of electron

m_e – mass of electron

ε_0 – dielectric permittivity of vacuum

μ_0 – magnetic permeability of vacuum

ε – dielectric constant of the medium

μ – electric dipole moment

ω – frequency

n – refractive index

T_g – glass transition temperature

$(< cos^2\theta >$ – order parameter

$I(\omega)$ – intensity of the incident beam

d – thickness of the material

RDF – radial distribution function

COM – center of mass

PME – two-dimensional particle-mesh Ewald method

NVT – Number, volume, temperature constant

NVE – Number, volume, energy constant

NPT – Number, pressure, temperature

B3LYP – Becke, three-parameter Lee-
Yang-Parr functional

VWN – Vosko, Wilk, and Nusair
functional

CAM-B3LYP – Coulomb-attenuating
B3LYP method

LC-BLYP – Long-Correlated Becke
Lee-Yang-Parr functional

PLD – Pulsed laser deposition
technique

ICT – Intramolecular charge transfer

Constant

SA – simulated annealing process

HOMO – highest occupied molecular
orbital

LUMO – lowest unoccupied
molecular orbital

CVFF – All-atom consistent valence
force field

PVD – physical vapor deposition
process

CVD – chemical vapor deposition
process

List of figures

of the molecule B and different subunits of PVK mer (c,d) and cyanovinyl CN2 at the back of the molecule B and different subunits of PVK mer (e,f).

List of tables

Chapter 1

Introduction

The rapid development of modern optics is mainly due to simultaneous progress in laser technology. Only lasers can provide sufficiently strong and coherent radiation that can be efficiently used as the input signal of nonlinear optical (NLO) and electro-optical (EO) effects. After the discovery of the NLO effects, scientists recognized that their practical applications depend on the development of new, NLO-active materials [1].

Both organic and inorganic NLO materials are known. Their advantages and disadvantages are presented in Fig. 1.1. The first inorganic materials employed as the optical parametric oscillators (OPO) and second harmonic generators (SHG) were $LiNbO_3$[2], $LiTaO_3$[3], and KTP (potassium titanyl phosphate) [4]. They played an important role in the establishment of NLO as a major area of laser science and such techniques as harmonic generations, frequency mixing, and parametric generation of light as methods of generation of coherent radiation in new regions of the optical spectrum. Currently, their main application areas are optical data storage and laser printing. The $LiNbO_3$ crystal is used as a waveguide electro-optic modulator for

optical communication applications [5-7]. However, the mentioned crystal suffers from photorefractive damage that, probably is due to the creation of defects in the crystal lattice [8]. Materials such as KTP [9] and $LiNbO_3$ have been investigated for waveguide QPM-SHG device application. The BaB_2O_4 is an inorganic NLO crystal with many attractive features, including a relatively high optical damage threshold, large nonlinear coefficients, and wide acceptance bandwidths. The AlGaAs and GaAs materials have been specially designed for frequency-doubling in laser diodes exhibiting an output at around 800-850 nm [10]. Lithium triborate (LBO) is one of the most versatile nonlinear crystals discovered to date, with a wide range of applications throughout the ultraviolet, visible, and near-infrared [11]. Many of the mentioned materials have been successfully used in mixers, frequency-doublers, and parametric generators to manage coherent laser radiation at high efficiency in new regions of the spectrum inaccessible by the traditional materials and conventional laser sources [12]. Several thousand nonlinear crystals and their closely related isomorphs have been developed and still, new materials are searched for. However, the synthesis of high-quality crystals is a time-consuming process.

	Organic materials	Inorganic materials
Advantages	Chemical and structural versatility Low cost, better processability ultra-fast response Higher EO activity	Highest bulk susceptibility Compatible physical properties
Disadvatages	Susceptibility relies on non symmetric crystal packinig Thermal degradation due to laser radiation Back orientation after corona poling	Absorption in the visible region Poor response time Degradative photorefractive effects

Figure 1.1. Determination of advantages and disadvantages of organic and inorganic materials.

Semiconductors are also extensively employed in electronic and optoelectronic applications. They are composed of elements from groups II to VI of the periodic table combined as II-VI, III-V, and IV [13]. Other materials used in optical applications are nonlinear glasses. They are attractive NLO materials because of their obvious compatibility with existing fiber networks. Additionally,

glasses possess a sub-picosecond response time. Telecommunication systems based on optical fiber are limited by the rate at which information can be encoded and decoded at each end of the link [14]. Semiconductor-doped glasses (SDGs) have received attention as possible NLO materials [15]. They exhibit relatively large optical nonlinearities with the 10-ps timescale response time. In addition, they are compatible with waveguide fabrication techniques and have been drawn into optical fibers. The SDGs contain small semiconductor crystallites, typically based on the mixed CdS_xSe_{1-x} system [15]. It has been shown that thermal effects pose severe limitations to the utility of the SDGs in all-optical switching applications. Glass system for the observation of NLO interactions and switching requires a high nonlinearity, low propagation losses, sub-picosecond response time, and a high optical damage threshold [16].

One useful group of nonlinear glasses are those doped with transition metal ions composed of highly polarizable *d*-electrons. The satisfactory nonlinearities predicted for such doped glasses depend on the particular ion species and follow: Ti^{4+}, V^{5+}, Cr^{6+}, Mo^{6+}, W^{6+}, Nb^{5+}, Ta^{5+} in decreasing order of influence. Glasses based on the Ti^{4+}, Nb^{5+} doped systems are considered with most experimental attention and may indeed be optimum [17]. Other studies suggest that the nonlinear index is much more sensitive to the identity of the Ti and Nb cations [18]. The results show that larger values of cation concentration (> 30 %) caused a problem with the homogeneity of the resulting glass. The best results have been achieved by mixing Nb and Ti-doped systems [19]. An alternative type of doping was the heavy metal ions such as Pb, Ga, and Bi. The experimental results showed insignificant nonlinear absorption in that glass at 1.06 μm [20]. Second-order effects require a non-centrosymmetric material, and since glass is isotropic, such phenomena would not be expected.

Organic materials form an interesting part of NLO structures. They possess low dielectric constants, inherent synthetic flexibility, high optical damage thresholds, and large NLO response over a broad frequency range comparable to those of inorganic materials. In organic molecules, the valence electrons of some atoms are not completely paired in their localized bonds. The π-electrons of delocalized molecular orbitals in the organic system are more mobile than those in the σ-framework and are therefore more easily polarizable causing NLO effects in atom structure [21, 22]. Most organic chromophores are aromatic compounds with

extended ranges of π-conjugation which is the main reason leading to the occurrence of large hyperpolarizabilities [23 - 25]. The π-electron system has a highly polarizable nature and the possibility of obtaining near-resonant behavior at frequencies doubled or tripled from the incident light. For example, hydrogen atoms do not contribute to the π-electron system but nitrogen possessing five valence electrons gives three of them into the σ-bonds, and two electrons are involved in the π-system. Each oxygen atom of the nitro group (the important group in NLO molecules) contributes one electron to the σ-bond to the nitrogen and four more are located as lone pairs in the two on-bonded sp^2 hybrids.

The NLO organic compounds often are composed of two groups: electron donor (D) and electron acceptor (A). Between them, the main charge transfer enhancing the nonlinearities of the molecule occurs. Investigations of the electronic properties of molecules show that the hyperpolarizability can be enhanced by either increasing the electron asymmetry by using more potent donating and accepting groups or increasing the conjugation length between the D and A moiety [26]. It is known that the NLO properties of the molecules can be improved by the modification of the donor bridge and acceptor portions of the chromophores. It can be done by synthesis of the *gradient bridge* chromophores where a weak donor (e.g., thiophene) is located near the strong amine donor and a weak acceptor (thiazole) is located near the strong acceptor (the tricyanofuranvinylene TCF and the tricyanopyrrolinevinylene TCP) [27]. In addition, the static electric dipole moment and the polarizabilities are usually greater where D and A groups are connected via a delocalized π-electron system creating the D-π-A molecule. Generally, the D-π-A chromophores represent a suitable structure for second-order NLO responses.

Traditional D-π-A chromophores used for the NLO applications are p-nitroaniline (PNA) and dimethylaminotrostilbene (DANS). Many chromophores with conjugated bridges fall into the category of substituted biphenyls, benzenes, stilbenes, azostilbenes, and tolanes. The amine structures are usually the donor moieties. Electron acceptor moieties of NLO materials contain cyano, nitro, alkoxy, isoxazole, tricyanovinyl, 1,3-bis(dicyanomethylidene)indane, and diarlythiobarbituric acid groups [28]. Typical nonlinear organic crystals are 4-nitroaniline, 3-nitroaniline, 2-methyl-4-nitroaniline, 3-methyl-4-nitropyridine 1-oxide, 2-α-methylbenzylamino-5-nitropyridine, 4-N,N-dimethylamino-3-

acetamidonitrobenzene, 4-nitro-4'-methylobenzyleneaniline, N-4-nitrophenyl-L-prolinol [29,30].

As described above, many organic NLO materials are known, but new ones are constantly being developed that have stable optical properties over time as well as under the influence of external factors. However, organic materials have some intrinsic weaknesses: for example, low mechanical strength and poor physicochemical stability. Jiang and Fang [31] in their study have tried to enhance the physicochemical stability of the molecular crystals by increasing their intermolecular interactions. They discovered that four conjugated sulfur atoms in the molecule play a role in enhancing its stability by S•••S intermolecular interactions. Their study confirms that a combination of inorganic and organic materials provides a potentially useful approach to more efficient and more stable NLO materials. Metal-organic coordination complexes can provide the following advantages: 1) an enhancement of the physicochemical stability, 2) the breaking up of the centrosymmetry of the ligands in the crystal, and 3) an increase in NLO intensity via the metal-ligand bridging interactions [32].

Many organic molecules have high hyperpolarizability β, but the susceptibility $\chi^{(2)}$ of a material as an assembly of molecules can be relatively small. The reason for this is the fact that a high β-value is usually accompanied by a large molecular electric dipole moment. The large dipole moment encourages the molecules to create pairs aligned in an antiparallel fashion, which usually prefer centrosymmetric forms, thereby ruling out the possibility of SHG-activity [33]. If highly polarizable organic molecules, with large second-order molecular hyperpolarizability, could be prevented from forming unfavorable agglomerates, their full potential could then be utilized. In this case, the organic NLO molecules are embedded into the polymer matrix, creating *guest-host* composite materials. Composite materials are defined as a material made from two or more constituent materials with significantly different physical or chemical properties that, when combined, produce a material with characteristics different from the individual components. Composite materials are prepared by dissolving chromophores in a non-NLO active polymer host such as polymethylmethacrylate (PMMA), polycarbonate (PC), polyvinyl carbazole (PVK), or polyquinoline (PQ).

Translation of molecular nonlinearity into macroscopic nonlinearity has shown a serious problem. The NLO properties of composite materials largely

depend on their structure and arrangement of the chromophores. For a generation of second-order NLO phenomena, materials without a center of symmetry are required. Additionally, chromophores should be isolated from each other in dipole order. They can be aligned by the action of the static external electric field on their permanent dipole moment. The noncentrosymmetric order of chromophores can be achieved by the corona poling process. In this process, the *guest-host* system is heated up to a temperature little bit below transition temperature (T_g) to easily reorient the chromophores. The rate of loss of poling-induced order is related to the difference between the material glass transition temperature (T_g) and the measurement temperature (temperature of operating equipment) [34].

Host and chromophore-guest can influence dipolar interactions and the poling fields will affect both of them. The poling field can reduce the effective lattice dimensionality and the intermolecular electrostatic interactions between them can further amplify the effect leading to enhancing the poling efficiency. In addition, the shapes of guests and hosts can play an important role in performing the detailed assembly of composite materials [35]. The control of intermolecular electrostatic interactions between guest and host is a difficult task in composite materials. Lattice dimensionality and molecular organization should be defined by measurement of the order parameter ($< cos^2\theta >$). The arrangement of the system can be measured by the ratio χ_{zzz}/χ_{xxz} described by the equation:

$$\frac{\chi_{zzz}}{\chi_{xxz}} = \frac{\langle cos^3\theta \rangle + b\frac{3}{2}\langle sin^2\theta cos\theta \rangle}{\frac{1}{2}\left\{\langle sin^2\theta cos \rangle + b\left\{\langle cos\theta \rangle - \frac{3}{2}\langle sin^2\theta cos\theta \rangle\right\}\right\}} \cdot$$

$$\cdot \frac{\langle sin^2\theta cos\theta \rangle}{\langle cos^3\theta \rangle} = \frac{\langle cos\theta \rangle}{\langle cos^3\theta \rangle} - 1 \qquad (1.1)$$

For the most simple complex, the anisotropy of β can be approximately defined by a parameter $b = \{\beta_{ZXX} + \beta_{ZYY}\}/\beta_{ZZZ}$ [36]. Computationally molecular dynamics simulations can predict the order parameters using various techniques to analyze the obtained data.

To improve the NLO parameters of the *guest-host* materials engineering composite materials structure became an important action. However, sometimes it is very difficult to find appropriate polymer materials to prevent the loss of the NLO properties of chromophores. The solution to this problem is computer simulations,

which, without the need for expensive syntheses, will allow the selection of polymers that do not quench chromophore hyperpolarization.

Computer simulations play an important role in the engineering of molecular materials. However, the complexity of organic *guest-host* materials is a challenge to the use of computational methods. The usefulness of the calculation of linear and nonlinear optical properties of materials, including their dependence on optical frequency [37] and dielectric permittivity [38] by time-dependent density functional theory (TD-DFT) [39] has been proved. Improvement of quantum chemical calculations has been based on careful correlation of theoretical and experimental studies and also on the development of hybrid functionals. Molecular dynamics (MD) and Monte Carlo (MC) methods are also useful for composite material structural properties simulations. However, computational resources are very demanding and time-consuming [40, 41]. Cooperation between quantum chemical methods and molecular mechanics develops reliable structure/electron function relationships that can be used in the prediction of NLO properties of composite materials. This issue will be elaborated on in this paper.

Through numerous experimental studies and computer simulations, it has been suggested that materials intended for practical use in NLO devices must meet certain requirements. The basic condition for the materials to be useful in the generation of NLO phenomena is their transparency for light and its harmonics. A wide transmission range of material extends the useful frequency range of the device and it is often desirable for NLO materials. In addition, the materials should exhibit low optical losses at the working frequencies and high optical damage tolerance. Irreversible damage is the most predominant type of optical damage, it can be caused by thermal heating, induced absorption, self-focusing, stimulated Brillouin scattering, dielectric breakdown, or several other mechanisms. The optical quality of nonlinear devices is extremely important for NLO operations [42]. In addition, the material must be free from optical inhomogeneity, inclusions, and other imperfections and impurities. The presence of inclusions or impurities in the particular thin film or crystal sample can strongly affect the material damage threshold. Accurate determination of the damage threshold for a given material is often difficult, as it depends on the wavelength of the radiation, the quality of using sample, and the exact experimental condition under which the measurements are performed as well. The great importance to the design and successful operation of

nonlinear devices is dedicated to the subject of material damage and has been intensively studied and reported. The identification of the mechanisms responsible for optical damage in different materials remains a difficult task [43].

Optical loss is important, and three components of loss must be considered: 1) material absorption loss, 2) material scattering loss, and 3) device insertion loss (loss associated with impedance matching of passive and active (electro-optic) waveguide structures). Absorption loss, at telecommunication wavelengths, is controlled by overtone absorptions related to hydrogen, thus, reduction of material loss to required values of 1 dB/cm or less desired minimizes hydrogen density including by means such as fluorination. Material loss values as low as 0.1-0.2 dB/cm have been obtained with heavily fluorinated chromophore-containing dendrimer materials [44]. Scattering loss can mainly be associated with some aspect of material processing and involves either material heterogeneity (emerging during electric field poling, deposition of cladding layers, and waveguide fabrication by reactive ion etching or photolithographic methods) [45 - 48]. In addition, the scattering loss can be kept to very low values and electro-optic waveguide loss of 1dB/cm or less can be obtained with attention to the details of processing. Insertion loss is the combination of absorption, scattering, and optical mode impedance matching losses. The mode size mismatch arising from passive (typically silica) to active (organic electro-optic) waveguide is the greatest source of loss in organic electro-optic waveguides. This is because low loss silica waveguides are spherical with active core diameters on the order of 10 μm while organic electro-optic waveguides are typically ellipsoidal with cross-sectional dimensions on the order of 2x6 μm. The mode size mismatch problem is mainly solved by performed of some type of mode transformation structure [49, 50]. These structures can be readily created by reactive ion etching using special mask structures and optical loss values as low as 0.2 dB per transition have been obtained (the exact values depend on the length of the transition structure). When great care is taken, total insertion loss for a 2-cm organic electro-optic modulator device can be obtained on the order of 3 dB although total insertion loss values of 5-10 dB are more common. One should be noted, that the optical loss is an important problem demanding detailed attention through all stages of material development and processing, contributions to final total insertion loss appear to be well understood and controllable within acceptable limits.

Stability is the next requirement of organic NLO materials including under conditions of elevated temperature, high optical power, and space radiation. Thermal stability is usually connected with thermally induced loss of electric-field-poling-induced noncentrosymmetric order [51, 52]. Temperature stability of composite materials can be associated with the glass transition of the final polymer matrix, i.e., arrangement caused by poling is lost at an increasingly rapid rate as the difference between device operating temperatures and the glass transition temperature of the organic electro-optic material is decreased. Improved thermal stability has been performed by lattice hardening, i.e., chemical crosslinking after electric field poling. Chemical additives are embedded in chromophores that allow chemical cross-linking of chromophores to a three-dimensional supermolecular matrix while the electric field is on. Two different crosslinking reactions have been investigated: 1) Thermally induced crosslinking and 2) photoinduced crosslinking. The temperature dependence of the crosslinking reaction must be compatible with temperatures used in electric field poling, which is related to thermally induced crosslinking reactions. Otherwise, a significant reduction in the effectiveness of polling results. Thermally-induced crosslinking chemistries utilized in the 1990s often involved condensation reactions and the elimination of water. Crosslinking may be sensitive to atmospheric moisture and it is difficult to maintain the desired reaction stoichiometry. Crosslinking reactions that avoid this problem have been introduced [53]. With a photoinduced crosslinking reaction, care must be taken to avoid competitive absorption of light by the electro-optic chromophore and the proto-initiator. The advantage of photocrosslinking is that it can be de-coupled from the temperature-dependent poling process. Photochemical stability appears to be a more serious problem, especially in the presence of oxygen atoms. It's possible to improve stability by several things, including lattice hardening (it slows down the diffusion of singlet oxygen and reactive species), the use of physical and chemical singlet oxygen quenchers, and the exclusion of oxygen. Photochemical stability may also be significantly improved by eliminating or sterically protecting chromophore sites subject to singlet oxygen attack [54]. Materials appropriate for applications involving telecommunication optical power levels can be produced.

One can see that the synthesis of the efficient NLO organic *guest-host* material is no easy task. In the presented work I would like to show the methodology which can predict the NLO properties of composite materials using computer

simulation methods. The molecular mechanic methods combined with quantum chemical calculations using the hierarchical model can be used as a tool before performing experiments to find an appropriate polymer matrix for chromophores to not lose their NLO activities. The methodology of calculations presented in this work can predict the NLO properties of composite materials without their synthesis.

References

[1]   Chen Ch-T., Liu G-Z., Ann. Rev. Mater. Sci. 16, 203-43, (1986).

[2]   Li H. P., Tang D. Y., Ng S. P., Kong J., J. Opt. Las. Tec. 38, 192-195 (2006).

[3]   Cho K-H., Rhee B. K., Proc. SPIE 6875, Nonlinear Frequency Generation and Conversion: Materials, Devices, and Applications VII, 68751A (2008).

[4]   Cheung E., Palese S., Injeyan H., Hoefer C., Ho J., Hilyard R., Komine H., Berg J., Boseberg W., Opt. Soc. of Am. 26 (1999).

[5]   Glavas E., Cabrera J. M., Townsend P. D., J. Phys. D: Appl. Phys. 22, 611 (1989).

[6]   Laurell F., Roelofs M. G., Hsiung H., Appl. Phys. Lett. 60, 301 (1992).

[7]   Castaldini D., Bassi P., Aschieri P., Tascu S., Micheli M. D., Baldi P., Opt. Express. 17, 17868-17873 (2009).

[8]   Solntsev A. S., Kumar P., Pertsch T., Sukhorukov A. A., Setzpfandt F., APL Photonics. 3, 021301 (2018).

[9]   Arie A., Rosenman G., Mahal V., Skliar A., Oron M., Katz M., Eger D., Opt.Comm. 142, 265-268 (1997).

[10]   Tran T. T., Yu, H., Rondinelli J. M., Poeppelmeier K. R., Halasyamani P. S., ACS publications, Chem. Mater. 28, 5238-5258 (2016).

[11]   Sastry B. S. R., Hummel F. A. J., Amer. Ceram. Soc. 41, 7 (1958).

[12]   Bordui P. F., Fejer M. M., Annu. Rev. Mater. Sci. 23, 321-379 (1993).

[13]   Yu P. Y., Cardona M., Fundamentals of semiconductors, Physics and Material Properties, (4 ed.) Springer-Verlag Berlin Heidelberg. P.2., ISBN 978-3-642-00710-1.

[14] Grundmann M., The Physics of Semiconductors, Springer International Publishing Switzerland 2016, ISBN 978-3-319-23880-7.

[15] Elisa M., Vasiliu C., Striber J., Radu D., Trodahl J. H., Dalley M., Journal of optoelectronics and advanced materials. 8, 2, 811-814 (2006).

[16] Remitz K. E., Neuroth N., Speit B., Mat. Scie. And Engi. B9, 413-416 (1991).

[17] Lines M. E., J. Appl. Phys. 69, 6876-6884 (1990).

[18] Vogel E. M., Kosinski S. G., Krol D. M., Jackel J. L., Friebeg S. R., Oliver M. K., Powers J. D., J. Non. Cryst. Solids. 107, 244, (1989).

[19] Jackel J. L., Vogel E. M., Aitchison J. S., Appl. Opt. 29, 3126-3130 (1990).

[20] Hall D. W., Borrelli N. F., Dumbaugh W. H., Newhouse M. A., Weidman D. L., Appl. Phys. Lett. 54, 1293 (1989).

[21] Sun Y-H., Zhao K., Wang Ch-K., Luo Y., Ren Y., Tao X-T., Jiang M-H., J. of Molec. Struc. 682 185-189 (2004).

[22] Wheeler S. E., Houk K. N., J. Am. Chem. Soc. 130, 10854-10855 (2008).

[23] Davydov B. L., Derkacheva L. D., Dunina V. V., Zhabotinskii M. E., Zolin V. F., Koreneva L. G., Samokhina M. Opt. Soektrosc. 30, 503, (1971).

[24] Davydov B. L., Derkacheva L. D., Dunina V. V., Zhabotinskii M. E., Zolin V. F., Koreneva L. G., Samokhina M. A., JETP Lett. 1970, (English translation), Opt. Spectrosc. 30, 274-276 (1971).

[25] Zyss J., Chemla D. S., Nonlinear Optical Properties of Organic Molecules and Crystals, Elsevier, ISBN:9780323157766, 1, 23-192 (1987).

[26] Nicoud J. F., Twieg R. J., Nonlinear Optical Properties of Organic Molecules and Crystals, Elsevier, ISBN:9780323157766, 1987, 227-229 (1987).

[27] Molla M. R., Das A., Ghosh S., Chem. Eur. J. 16 10084-10093 (2010).

[28] Lee S. K., Cho M. J., Kim G. W., Jun W. G., Jin J-I., Dalton L. R., Choi D. H., Opt. Mat. 29 451-456 (2007).

[29] Verbiest T., Houbrechts S., Kauranen M., Clays K., Persoons A., J. Mater. Chem., 7(11), 2175-2189 (1997).

[30] Teng C. C., Garito A. F., Phys. Rev. Lett. 50, 350352 (1983).

[31] Teng C. C., Garito A. F., Phys. Rev. B, 28, 6766-6773 (1983).

[32]   Jiang M.-H., Fang Q., Adv. Mater. 11, 13 (1990).

[33]   Wang S.-J., Wang Y.-F., Cai CH., J. Phys. Chem. C, 119, 16256-16262, (2015).

[34]   Zang H., Tian Y., Bo S., Xiao, L., Ao Y., Zhang J., Li M., J. Mater. Chem. C 8 1380-1390 (2020).

[35]   Cho M. J., Choi D. H., Sullivan P. A., Akelaitis A. J. P., Dalton L. R., Prog. Polym. Sci. 33 1013-1058 (2008).

[36]   Neilsen R., Rommel H., Robindon B., J. Phys. Chem. 108, 8659-8667 (2004).

[37]   Dalton L., Benight S., Polymers. 3, 1325-1351 (2011).

[38]   Takimoto Y., Vila F. D., Rehr J. J., J. Chem. Phys. 127, 154114-10 (2007).

[39]   Johnson L. E., Barnes R., Draxler T. W., Eichinger B. E., RobinsonB. H., J. Phys. Chem. B 114, 8431-8440 (2010).

[40]   TakimotoY., Isborn C. M., Eichinger B. E., Rehr J. J., Robinson B. H., J. Phys. Chem. C 112, 8016-8221 (2008).

[41]   Kim W.-K., Hayden L. M., J. Chem. Phys. 111 5212-5222 (1999).

[42]   Leahy-Hoppa M. R., Cunningham P. D., French J. A., Hayden L. M., J. Phys. Chem. A. 110, 5792-5797 (2006)

[43]   Mahadeva S. K., Berring J., Walus K., Stoeber B., J. Phys. D: Appl. Phys. 46 285305, (2013).

[44]   Senthil K., Kalainathan S., Kumar A. R., Aravindan P. G., RSC Adv. 4 56112-56127 (2014).

[45]   Dalton L.R., J. Phys. Condens. Matter 15, R897, (2003).

[46]   Dalton L. R., Harper A., Ren A., Wang F., Todorova G., Chen J., Zhang C., Lee M., Ind. Eng. Chem. Res. 38, 8 (1990).

[47]   Mao S. S. H., Ra Y., Guo L., Zhang C., Dalton L. R., Chem A., Garner S., Steier W. H., Chem. Matter. 10, 146, (1998).

[48]   Wise D. L., Wnek G., Trantolo D. J., Cooper T. M., Gresser J. D., Electrical and Optical Polymer Systems, Marcel Dekker, New York 1998.

[49]   Dalton L. R., Adv. Polym. Sci. 158, 1, (2002).

[50]   Garner S. M., Lee S. S., Chuyanov V., Chen A., Yacoubian A., Steier W. H., Dalton L. R., IEEE J. Quantum Electron. 35, 1146, (1990).

[51]   Chen A., Chuyanov V., Marti-Carrera F. I., Garner S. M., Steier W. H., Chen J., Sun S. S., Dalton L. R., Opt. Eng. 39, 1507, (2000).

[52]   Burland D. M., Miller R. D., Walsh C. A., Chem. Rev. 94, 31, (1994).

[53]   Dalton L. R., Harper A. W., Wu B., Ghosn R., Laquindanum J., Liang Z., Hubbel A., Xu C. Adv. Mater. 7, 519, (1995).

[54]   Luo J., Liu S., Haller M., Li H., Kim T. D., Kim K. S., Tang H. Z., Kang S.H., Jang S. H., Ma H., Dalton L. R., Jen A. K. Y., Proc. SPIE 4991, 520, (2003).

[55]   Galvan-Gonzalez A., Belfield K. D., Stegeman G. I., Canva M., Marder S. R., Staub K., Levina G., Twieg R. J., J. Appl. Phys. 94, 756, (2003).

Chapter 2

Optical properties of dielectric materials

2.1. Polarization of dielectric materials

Nonlinear optics is based on material phenomena occurring as a result of modifying the optical properties of a material system by the presence of light. A Maxwell equation of electromagnetics is the principal law of optics applied to all materials. However, in each case, the solution of the equations depends on the mutual relations characteristic of the materials. They relate the current density to the electric field through the conductivity, and the electric displacement to the electric field through the permittivity describing materials features as follows:

$$\nabla \boldsymbol{D} = \rho \, , \tag{2.1}$$

$$\nabla \boldsymbol{B} = 0 \, , \tag{2.2}$$

$$\nabla \times \boldsymbol{E} = -\frac{\partial \boldsymbol{B}}{\partial t} \, , \tag{2.3}$$

$$\nabla \times \boldsymbol{H} = \frac{\partial \boldsymbol{D}}{\partial t} + \sigma \, \boldsymbol{E} \,. \tag{2.4}$$

The **E, D, H, B**, are vectors of the electric field intensity, electric induction (displacement field), magnetic field intensity, and magnetic induction. ρ is the charge density (electric field per unit of volume at any point in space and time), and σ is the current density. *D* and *B* characterized the magnetic and electric fields with small intensities and describe the properties of matter. Electric displacement *D* is related to the electric field *E* according to:

$$D = \varepsilon \varepsilon_0 \, E \,, \tag{2.5}$$

$$B = \mu \mu_0 H \,, \tag{2.6}$$

where ε_0 and μ_0 are electric permittivity and magnetic permeability of vacuum, respectively, ε is the dielectric constant of the medium, and μ is the permeability of the media.

The electric field can move charge *q* (electron cloud shift with respect to the placement of the nuclei) inducing dipole moment in the dielectric material $p^{(ind)} = qr$. The amount of dipole moments *N* per volume unit is defined by the polarization vector $P = Nqr$. For electric fields with their intensity not exceeding 1000 V/cm, generated by classic light sources, it can be assumed, that the polarization vector is proportional to the field intensity [1].

$$\boldsymbol{P} = \varepsilon_0 \chi \boldsymbol{E} \,, \tag{2.7}$$

where χ is the electric susceptibility tensor of dielectric media dependent on the microscopic structure of the material. The material for each polarization is proportional to the electric field intensity is called linear. When, several light waves (**E₁, E₂, E₃, …**) pass through the material, they spread independently of each other, without any interaction. Optical phenomena subject to the principle of superposition are named linear optical phenomena.

Polarization can be defined by considering, that the charge shift in the dielectric determines the electric displacement:

$$D = \varepsilon_0 E + P \,. \tag{2.8}$$

By comparing expressions (2.7) and (2.8) to the equation (2.5), one can get:

$$\chi = \varepsilon - 1 \,. \tag{2.9}$$

Electric susceptibility of the anisotropic materials is a tensor containing nine components, whereas for isotropic material there is a dependency $\lfloor \chi_{ij} \rfloor = \chi \lfloor \delta_{ij} \rfloor$.

The interactions of electromagnetic waves with dielectric media can be described by the classic harmonic oscillator model, the main assumption of the Lorentz electron theory [2,3]. The external electric field causes the separation of positive and negative charges to a certain distance r creating an induced dipole moment. The movement of negative charge within of molecule is caused by acting of the electric field force $qE(t)$, the quasi-elastic force - $m\omega_0^2 r(t)$ and oscillator vibration damping force - $m\gamma \frac{dr(t)}{dt}$, what can be described by the equation [4]:

$$m\frac{d^2 r(t)}{dt^2} = -m\gamma \frac{dr(t)}{dt} - m\omega_0^2 r(t) + qE(r,t),\qquad (2.10)$$

where ω_0 is the eigenfrequency of the oscillation of electron cloud and γ is the damping factor. Solution of equation (2.10) takes the form:

$$r(t) = r_0 \exp(-i\omega t)\,.\qquad (2.11)$$

After substituting the obtained expression into equation (2.10), the amplitude of the deflection of the charge q from the equilibrium position is equal to:

$$r_0 = \frac{qE_0}{m(\omega_0^2 - \omega^2 - i\gamma\omega)}\,,\qquad (2.12)$$

and the induced dipole moment is written as:

$$p(t) = qr(t) = \frac{q^2 E_0}{m(\omega_0^2 - \omega^2 - i\gamma\omega)}\exp(-i\omega t).\qquad (2.13)$$

One can see from the above equation that in the theory of the harmonic oscillator the dipole moment is proportional to the electric field strength. When one assumes that a particle has j oscillators vibrating with frequencies ω_j, and there are N particles in the volume unit, the polarization of the medium is expressed by the formula:

$$P(t) = \frac{Nq^2}{m}\left(\sum_j \frac{f_j}{\omega_j^2 - \omega^2 - i\gamma_j\omega}\right) E(t)\,,\qquad (2.14)$$

where f_j is a quantum-chemical quantity called the oscillator strength determining the intensity of the spectral absorption or emission line. Using the expression (2.7), the electric susceptibility of a dielectric medium can be written as:

$$\chi(\omega) = \frac{Nq^2}{m\varepsilon_0}\left(\sum_j \frac{f_j}{\omega_j^2 - \omega^2 - i\gamma_j\omega}\right).\qquad (2.15)$$

Substituting the above expression into dependence (2.9) one can get:

$$\varepsilon(\omega) = 1 + \frac{Nq^2}{m\varepsilon_0}\left(\sum_j \frac{f_j}{\omega_j^2 - \omega^2 - i\gamma_j\omega}\right) = n^2(\omega). \qquad (2.16)$$

The refractive index n is a complex quality, with its real part is equal to:

$$n'^2(\omega) = 1 + \frac{Nq^2}{m\varepsilon_0}\sum_j \frac{f_j}{\omega_j^2 - \omega^2}. \qquad (2.17)$$

The presented model of the harmonic oscillator is only the approximation of the description of the discussed phenomena; however, it gives good results [5]. The interaction of the electromagnetic wave with a medium is fully explained by quantum mechanics.

Lasers discovered in the early sixties of the last century are light sources with high coherence and power density reaching 10^{14} W/m^2. This corresponds to field intensity equal to 10^8 V/m. This value is comparable to the field intensity existing in the matter. So intensive electric field can change the optical properties of the material. It leads to a significant shift of electric charges within the molecule that causes polarization of the medium, which is not a linear function of the intensity of the electromagnetic wave. The nonlinear polarization vector depends on the order and the type of nonlinearity. The nonlinearity may be of microscopic and macroscopic origin. The induced polarization in the macroscopic medium is given by the series [6]:

$$P = \varepsilon_o\left(\chi^{(1)} \cdot E + \chi^{(2)} : E^2 + \chi^{(3)} \vdots E^3 + \ldots\right), \qquad (2.18)$$

where $\chi^{(2)}$ and $\chi^{(3)}$ are the coefficients representing the second and third-order susceptibilities of the medium, respectively [7].

Substitution of the electric field in equation (2.18) by its form $E(r,t) = E_0 \exp[i(k \cdot r - \omega t)]$ gives the formula:

$$P(r,t) = \varepsilon_0\chi^{(1)}E_0 \cos(k \cdot r - \omega t) + \varepsilon_0\chi^{(2)}E_0^2 \cos^2(k \cdot r - \omega t)$$
$$+ \varepsilon_0\chi^{(3)}E_0^3 \cos^3(k \cdot r - \omega t) + \ldots \qquad (2.19)$$

Using trigonometric transformations one can write:

$$P(r,t) = \varepsilon_0\chi^{(1)}E_0 \cos(k \cdot r - \omega t) + \frac{1}{2}\varepsilon_0\chi^{(2)}E_0^2[1 + \cos 2(k \cdot r - \omega t)]$$
$$+ \varepsilon_0\chi^{(3)}E_0^3\left[\frac{3}{4}\cos(k \cdot r - \omega t) + \frac{1}{4}\cos 3(k \cdot r - \omega t)\right] \quad (2.20)$$

The second-order polarization one can divide into two components:

$$P_i^{(2)}(r,t) = \frac{1}{2}\varepsilon_0\chi_{ijk}^{(2)}(0)E_j^0 E_k^0 +$$

$$+ \frac{1}{2} \varepsilon_0 \chi_{ijk}^{(2)} (2\omega, 2k) E_j^0 E_k^0 \cos 2(k \cdot r - \omega t). \qquad (2.21)$$

The first part of equation (2.21) corresponds to permanent polarization independent of the time, while the second part describes the polarization changes varying in the time with *2ω* frequency. Equation (2.20) shows that components of the electromagnetic field can generate polarization with double, triple, or arbitrarily multiplied frequencies.

2.2. Dielectric molecules in the electric field

The Hamilton of the molecule affected by a local electric field with intensity F is the sum of two Hamiltonians: the Hamiltonian of an unperturbed system without the action of the field ($\hat{H}^{(0)}$) and the perturbed Hamiltonian ($\hat{H}^{(1)}$):

$$\hat{H} = \hat{H}^{(0)} + \hat{H}^{(1)} . \qquad (2.22)$$

The perturbed Hamiltonian has a form:

$$\hat{H}^{(1)} = - \sum_{i=x,y,z} \hat{p}_i F_i - \frac{1}{3} \sum_{i,i'=x,y,z} \hat{\Theta}_{ii'} \frac{\partial F_i}{\partial i'} ..., \qquad (2.23)$$

where spatial derivatives of the field components are calculated at a defined point of the molecule. $\hat{p}_i$ and $\hat{\Theta}$ are operators of cartesian multipolar moments of the molecule. In the case when the electric field is homogeneous, the Hamiltonian of the system takes the form:

$$\hat{H} = \hat{H}^{(0)} - \sum_{i=x,y,z} \hat{p}_i F_i . \qquad (2.24)$$

Derivative of the Hamiltonian with the respect to the strength of the electric field gives the expression $\partial \hat{H} / \partial F = -\hat{p}_i$. The Hellman-Feynman theorem shows that the rate of change of energy $\mathcal{E}$ depending on the parameter K is described by the formula $\frac{\partial \mathcal{E}}{\partial K} = \langle \psi \left| \frac{\partial \hat{H}}{\partial K} \right| \psi \rangle$. Taking as the parameter K the electric field intensity the above relationship can be written as:

$$\langle \psi \left| \frac{\partial \hat{H}}{\partial F_i} \right| \rangle = \frac{\partial \mathcal{E}}{\partial F_i} . \qquad (2.25)$$

considering that $\qquad \langle \psi \left| \frac{\partial \hat{H}}{\partial F_i} \right| \psi \rangle = -\langle \psi | \hat{p}_i | \psi \rangle = -p_i , \qquad (2.26)$

one can get dependency $\qquad\qquad \frac{\partial \mathcal{E}}{\partial F_i} = -p_i . \qquad (2.27)$

For electric fields with low intensity, the energy of the atom system can be expanded into the Taylor series:

$$\mathcal{E}(F) = \mathcal{E}^{(0)} + \sum_{i=x,y,z} \left(\frac{\partial \mathcal{E}}{\partial F_i}\right)_{F=0} F_i + \frac{1}{2!} \sum_{i,j=x,y,z,} \left(\frac{\partial^2 \mathcal{E}}{\partial F_i \partial F_j}\right)_{F=0} F_i F_j +$$

$$+ \frac{1}{3!} \sum_{i,j,k=x,y,z} \left(\frac{\partial^3 \mathcal{E}}{\partial F_i \partial F_j \partial F_k}\right)_{F=0} F_i F_j F_k + \cdots \tag{2.28}$$

By derivative of the expression (2.28) over the local electric field intensity F_i, one can get:

$$\frac{\partial \mathcal{E}}{\partial F_i} = \left(\frac{\partial \mathcal{E}}{\partial F_i}\right)_{F=0} + \sum_{j=x,y,z} \left(\frac{\partial^2 \mathcal{E}}{\partial F_i \partial F_j}\right)_{F=0} F_j + \frac{1}{2} \sum_{j,k=x,y,z} \left(\frac{\partial^3 \mathcal{E}}{\partial F_i \partial F_j \partial F_k}\right)_{F=0} F_j F_k +$$

$$+ \cdots = -p_i \tag{2.29}$$

The formula (2.39) can be presented as:

$$p_i = p_{0,i} + \sum_{j=x,y,z} \alpha_{ij} F_j + \frac{1}{2} \sum_{j,k=x,y,z} \beta_{ijk} F_j F_k + \cdots \tag{2.30}$$

The total dipole moment of the molecule is the sum of the permanent static dipole moment p_0 and induced dipole moments – linearly dependent on the local electric field and nonlinear terms. Polarizability tensor characterizing the linear dependence of the induced dipole moment versus the field $\alpha_{ij} = \sum_{j=x,y,z} \left(\frac{\partial^2}{\partial F_i \partial F_j}\right)_{F=0}$ is symmetrical, i.e. $\alpha_{ij} = \alpha_{ji}$. From the symmetry conditions of the tensors follows that the tensor of the third rank β_{ijk} takes the value zero for media with the center of symmetry. The quantities α, β, γ are called polarizability, second-order, and third-order hyperpolarizabilities of molecules, respectively.

2.3. The relationship between the optical properties of a material and the polarizability of molecules

The polarization of the medium depends not only on the properties of individual molecules but also on their special arrangement. The relationship between the parameters of the molecule at the microscopic level and their macroscopic counterparts in the non-centrosymmetric crystal has been described by Oudar and Zyss [8]. Then, their theory was extended to the thin film of the ordered polymer [9]. Oudar and Zyss based on the oriented gas model determined the relationship between the susceptibility of the medium and the polarizability and hyperpolarizability of molecules. The mentioned relation can be defined as [10,11]:

$$\chi^{(2)}_{IJK} = N f_I(\omega_1 \pm \omega_2) f_J(\omega_1) f_K(\omega_2) b_{IJK} \; , \qquad (2.31)$$

where

$$b_{IJK} = \frac{1}{N_g} \sum_{ijk} \left(\sum_{s=1}^{N_g} \cos \theta^{(s)}_{Ii} \cos \theta^{(s)}_{Jj} \cos \theta^{(s)}_{Kki} \right) \beta_{ijk} , \qquad (2.32)$$

N is the number of molecules in a volume unit (V) of the crystal. $N = N_g/V$, where for disordered or partially ordered materials $N_g = 1$. b_{IJK} is the equivalent of β_{ijk} in the laboratory coordinates. The angle $\theta^{(s)}_{Kk}$ is contained between the K axis of the laboratory coordinate system and the k axis of the system related to the molecule located in the s unit cell of the studied system (see Fig. 2.1). Tensor b_{IJK} determines the contribution of the hyperpolarizability of individual molecules of the system to the NLO susceptibility of the tested material. In our consideration, the vector of the dipole moment of the molecule is along the k axes.
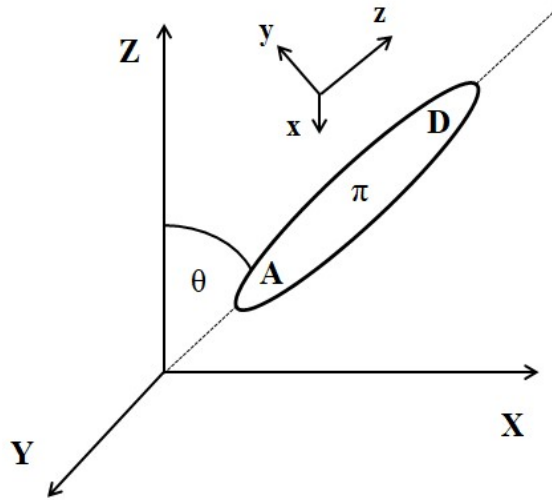
Figure 2.1. Relationship between laboratory and molecular coordinate systems.

The probability of finding a molecule for which the angle between the vector of its dipole moment and the selected direction in the laboratory coordinate system is θ, taking into account the Boltzmann distribution, is described by the formula:

$$\mathcal{P}(\theta) = exp\left(-\frac{\mathcal{E}}{kT}\right) = exp\left(\frac{pEcos\theta}{kT}\right), \qquad (2.33)$$

E is the intensity of the electric field acting on the molecule. The average value of the cosine of the directional angle $\langle \cos \theta \rangle$ is represented by the relationship:

$$\langle \cos \theta \rangle = \frac{\int_0^\pi \mathcal{P} \cos \theta \sin \theta d\theta}{\int_0^\pi \mathcal{P}(\theta) \sin \theta d\theta} \; . \tag{2.34}$$

By calculating the integrals from equation (2.34) one can obtain the expression:

$$\langle \cos \theta \rangle = ctgh\left(\frac{pE}{kT}\right) - \left(\frac{pE}{kT}\right)^{-1} = L_1\left(\frac{pE}{kT}\right), \tag{2.35}$$

where $L_1(pE/kT)$ is a first-order Lengevin order function. When the molecules of the tested system are arranged along the Z-axis of the laboratory system and the system has cylindrical symmetry, one can obtain the relation:

$$\langle b_{ZZZ} \rangle = \langle \cos^3 \theta \rangle \beta_z \; . \tag{2.36}$$

The $\beta_z = \beta_{zxx} + \beta_{zyy} + \beta_{zzz}$. According to the Boltzmann distribution law, the average value of the order parameter is determined from the expression:

$$\langle \cos^3 \theta \rangle = \frac{\int_0^\pi exp(pE \cos \theta / kT) \cos^3 \theta \sin \theta d\theta}{\int_0^\pi exp(pE \cos \theta / kT) \sin \theta d\theta} =$$

$$= \left(1 + 6\left(\frac{pE}{kT}\right)^{-2}\right) L_1\left(\frac{pE}{kT}\right) - 2\left(\frac{pE}{kT}\right)^{-1} = L_3\left(\frac{pE}{kT}\right) \tag{2.37}$$

In this case, the component of the susceptibility tensor corresponding to the SHG generation can be expressed as [12]:

$$\chi_{ZZZ}^{(2)} = N f_Z^2(\omega) f_Z(2\omega) \beta_z L_3(p) \; . \tag{2.38}$$

Molecules having a permanent dipole moment, exposed to an external electric field, tend to align along the force field lines, gradually reaching the state of thermodynamic equilibrium. The orientation polarization of molecules is opposed by their thermal motion. Langevin [13] was the first to formulate a method for calculating the magnetic susceptibility of paramagnetic materials and on its basis Debye [14] built an analog for polar dielectric materials. In the adopted model, the ordering effect of electric dipoles depends mainly on the intensity of the acting electric field and the temperature of the entire system.

2.4. The nonlinear optical phenomena

The nonlinear optical phenomena are created by the interaction between matter and light. Generally, all media are nonlinear however, their optical nonlinearity can be weak and the observation of the nonlinear optical processes is possible only with involving of lasers as a source of strong coherent optical

radiation. The nonlinear optical (NLO) phenomena belonging to the second-order susceptibility are the difference-frequency generation, sum-frequency generation, and second-harmonic generation (SHG). Another set of nonlinear optical phenomena related to the third-order susceptibility is self-focusing, self-phase modulation (SPM), four-wave mixing (FWM), and third-harmonic generation (THG). The methods used in the presented work are described in more detail[15].

2.4.1. The second-harmonic generation

Second-harmonic generation (SHG) is a nonlinear optical process in which two photons with the same frequency interact with a nonlinear material. They generate a new photon with twice the energy of the initial photons that conserves the coherence of the excitation. The SHG, like other even-order nonlinear optical phenomena, is not allowed in media with inversion symmetry. The nonlinear polarization formed in that medium corresponding to the SHG generation is given by the second part of the equation (2.18):

$$\tilde{P}^{(2)}(t) = \epsilon_0 \chi^{(2)} \mathcal{E}^3 cos2\omega t, \tag{2.39}$$

where ε_0 is the dielectric permittivity of vacuum, $\chi^{(2)}$ is the second-order NLO susceptibility of the nonlinear material, associated with the SHG process, and $\mathcal{E}$ is the electric field of the fundamental laser beam[16].
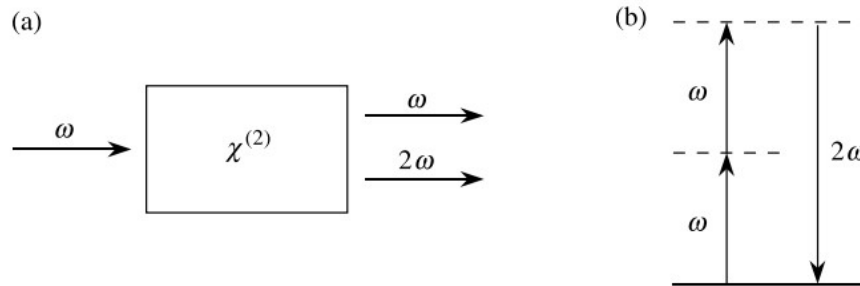
Figure 2.2. The geometry of second-harmonic generation (a), and energy-level diagram describing second-harmonic generation (b).

The schema of the SHG process is presented in Fig. 2.2 (a), where two photons with the same frequency (ω) interact with a nonlinear material. These photons generate a new photon with twice the frequency (2ω) and twice the energy of initial photons. Figure 2.2 (b) described the energy-level diagram where the solid

line represents the atomic ground state and the dashed lines present virtual energy levels.

2.4.2. Third-harmonic generation

The third harmonic generation (THG) is an NLO process in which a third-order nonlinear polarization $P^{(3)}$ is induced in a material by a fundamental harmonic laser beam with the frequency ω. The polarizability is described by the third part of the equation (2.18)[16]:

$$\tilde{P}^{(3)}(t) = \frac{1}{4}\epsilon_0\chi^{(3)}\mathcal{E}^3cos3\omega t \qquad (2.40)$$

here ε_0 is the dielectric permittivity of vacuum, $\chi^{(3)}$ is the third-order NLO susceptibility of the nonlinear material, associated with the THG process, and $\mathcal{E}$ is the electric field of the fundamental laser beam. The schema of the THG generation is presented in Fig. 2.3.
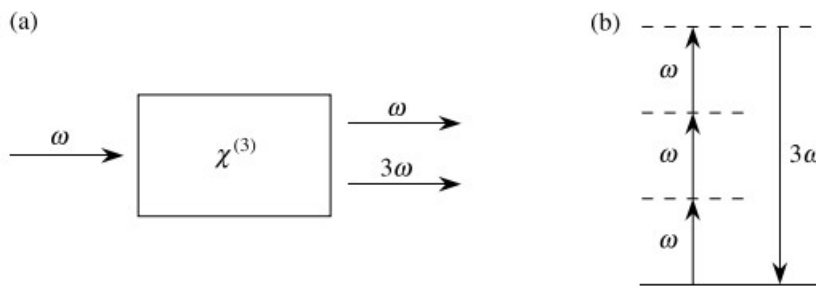
Figure 2.3. The geometry of the interaction of the third-harmonic generation (a) and the energy-level description (b).

References

[1]   Chełkowski A., Fizyka dielektryków, PWN, Warszawa 1979.

[2]   Lorentz H. A. , Theory of electrons, Teubner, Leipzig 1909.

[3]   Born M., Optic, Springer, Berlin 1965.

[4]   Chmela P., Wprowadzenie do optyki nieliniowej, PWN, Warszawa 1987.

[5]   Feynman R. P., Leighton R. B., Sands M., Feynmana wykłady z fizyki, PWN, Warszawa 2001.

[6]   Nalwa H. S., Miyata S, Nonlinear optics of organic molecules and polymers, CRC Press, New York 1997.

[7]   Eaton D. F., Nonlinear optical materials, Science, 253, (1991).

[8]   Oudar J. L., Zyss J., Phys. Rev. A 26, 2016 (1982).

[9]   Meredith G. R., Van Dusen J. G., Williams D. J., Macromolecules, 15,(1982) 1385. Chen D., Wu L., Chen Q., Yu X., Polymer Bulletin 39, 157-163 (1997).

[10]   Singer K. D., Kuzyk M. G., Sohn J. E., J. Opt. Soc. Am. B 4 6 (1987).

[11]   Horiuchi N., Lefaucheux F., Ibanez A., Josse D., Zyss J., , J. Opt. Soc. Am. B 19 8 (2002).

[12]   Prasad P. N., Williams D. J., Introduction to nonlinear optical effects in molecules and polymers, Wiley New York 1991.

[13]   Langevin P., J. Phys. 4 (1905) 678.

[14]   Debye P., Polar Molecules, Dover, New York 1945.

[15]   Boyd R. W., The Nonlinear optics (fourth edition) Science Direct, 1-64 (2020).

[16]   Lembrikov B. I., Introductory Chapter: Nonlinear Optical Phenomena, Nonlinear Optics, IntechOpen, London, ISBN: 978-1-78985-164-9, 1-154 (2019).

Chapter 3

Local field models

Quantum-chemical calculations of NLO properties of molecules are often carried out for isolated particles in a vacuum, while measurements of physical quantities are performed for materials in liquid or solid-state. The environment in which the molecule is located, through intermolecular interactions of various origins, modifies its physical properties, as well as changes its electron polarizability and hyperpolarizability. Due to the interaction between the molecules of the system, their geometrical structure also changes. A molecule surrounded by other molecules, especially those in a solid-state, is exposed to an electric field generated by the components of the system. To calculate the magnitude of the electric field acting on a molecule, the so-called local field F, the contributions from all forms of intermolecular interactions, and the value of the external field must be taken into account. The local field is different from an external electric field applied to a macroscopic system. There is no general way to define the relationship between an external field and a local field. However, several theoretical models exist that make it possible to find the relationship between these values [1].

Local field models can be divided into two groups – continuous models and discrete models. The idea of the continuous model is to separate the molecular system into two parts, microscopic – close to the molecule under consideration, where atoms are explicitly taken into account, and the other macroscopic, where the properties of the system are described in an averaged manner as continuous atom system. Known continuous models differ in the way of describing the reaction between a molecule and its surroundings and in the shape of the cavity that limits the molecule of interest. The space into which the molecule is "inscribed" may have a spherical [2] or ellipsoidal shape [3] or assume the shape of the molecule being studied [4]. Thus, the magnitude of the local field intensity F is influenced by: the external field E, the field coming from a part of the macroscopically described system (continuously) $E^{(macr)}$ and from the part described in a discrete manner $E^{(disc)}$:

$$F = E + E^{(macr)} + E^{(disc)}. \tag{3.1}$$

The nature and method of describing $E^{(macr)}$ and $E^{(disc)}$ fields depend on the choice of the theoretical model characterizing the corresponding structural areas. For an amorphous or regular system, composed of identical molecules, the discrete local field is equal to zero. Discretely treating the entire molecular system is very complicated due to the number of atoms required to be included. The known discrete models of local fields use different approximations to reduce procedural difficulties.

3.1. Polarizable Continuum Model (PCM)

The polarizable continuum model assumes the existence of a molecule in a cavity taking the shape of a molecule. It is an extension of the SCRF method [5]. Still, the dielectric surrounding the active molecule is treated as a homogeneous medium with electric permittivity ε, while the polarizability of the molecule is calculated by quantum-chemical methods. To describe the electrostatic interaction between the solvent and the molecule, the PCM model assumes the existence of an induced charge on the surface of the cavity. The molecule polarizes the surrounding environment, which in turn also disturbs the distribution of its charge. Achieving such an effect is carried out by the self-consistent procedure.

The PCM model is widely used to estimate the influence of the environment on the linear and nonlinear optical properties of molecules in a solvent [6 – 8]. It also attempts to describe the problem of the local field by estimating the effective response of the molecule to the influence of the environment under the action of electromagnetic radiation [9,10].

When a time-dependent electric field is applied to the system under consideration, a perturbative time-dependent disturbance component describing the interaction of the molecule with the electromagnetic wave $\hat{V}(\Psi)$ is added to the undisturbed Hamiltonian $\hat{H}^0$. The component responsible for the interaction of the molecule with the surrounding medium $\hat{V}'(t)$ is also added to the Hamiltonian giving the equation:

$$\hat{H} = \hat{H}^0 + \hat{V}(\Psi) + \hat{V}'(t), \qquad (3.2)$$

where

$$\hat{V}'(t) = -(\hat{p}_0 + \hat{p}_{ind})E(t). \qquad (3.3)$$

The $\hat{p}_0$ is the operator of the dipole moment of the molecule, and $\hat{p}_{ind}$ is a molecule's dipole moment induced by the environment. The PCM method is based on the assumption of the ACS theory, in which the charge induced by the molecule of interest arises on the surface of the cavity. The surface of the cavity, on the other hand, is divided into areas with a constant surface charge and induces charge redistribution on the molecule.

Based on the PCM model, popular COSMO (Conductor Like Screening Model) [11] and C-PCM [12] procedures were created. In the COSMO model, the solvent is treated as a conductor for which $\varepsilon = 0$, while the charge is rescaled to keep the medium as a dielectric. The rescaling factor is equal to $(\varepsilon - 1)/(\varepsilon + k)$, where k takes values from 0 to 2, depending on the shape of the cavity and the distribution of the charge on its surface. The C-PCM model is similar to the COSMO except for k=0.

Another two methods describing the charge distribution on the cavity surface are characterized by the "frozen" charge density distribution (called the isodensity PCM model (IPCM) [13]) or by dynamically changing the density of the electron cloud called the self-consistent isodensity PCM model (SCIPCM) [14].

3.2 Discrete local field model

The discrete local field model does not take into account the presence of the molecule's surroundings as an isotropic medium with constant electric permittivity. The model considers each atom of the studied molecular system as a separate entity that builds a molecule of interest and environment.

In the case of macromolecular systems, when it is necessary to take into account the effects of the environment, a hybrid QM/MM [15 – 19] method is used. The mentioned method combines molecular mechanics (MM) and quantum chemistry (QM) methods. It allows the treating of individual fragments of the system in a varied way. The electronic properties of the interesting molecule and several of its neighbors from the immediate vicinity are calculated using quantum-chemical methods, while the further environment is considered taking into account the formalism of molecular mechanics. This procedure is justified in the case of a solvent composed of relatively small molecules. The main problem with the applicability of this method is the accuracy of the division of the tested system. For best results, when partitioning a system, the molecules should not break apart, which is not always possible.

In the case of large molecular systems of several thousand atoms, the discrete and continuous approach is most often combined to estimate the influence of the environment on the electronic properties of molecules. In the first stage of calculations, the structure of the studied system is modeled discretely, most often with molecular dynamics methods. Then the geometry of the molecular system is used to calculate the intensity of the local electric field acting on the molecule, which should take into account the intermolecular interactions. The local field is considered as the Hamiltonian disorder during calculations of electronic properties of the studied molecule by quantum chemical methods.

In the discrete model, the molecules of interest can be described in two ways. They can be thought of as point dipoles or can be divided into a series of sub-dipoles. The molecule division scheme depends on the number and spatial distribution of functional groups that build the analyzed chemical structure. The sub-molecular model, created by Luty [20], allows determining the contribution of particular parts of the molecule to electron polarizability and hyperpolarizability. Local fields and susceptibility are calculated for each part of the molecule and then

averaged over the whole molecule. Point dipole approximation, i.e. embedding the dipole moment in the center of the molecule's mass, does not take into account its shape and size, which can cause inaccuracies in the calculation of the local field values and imprecise estimates of its effect. Within the presented model, the local field coefficient takes the tensor form:

$$f_{N,ij}(\omega) = \sum_N \left[\underline{I} - \frac{\underline{L} \cdot \underline{A}(\omega)}{\varepsilon_0 V} \right]^{-1}_{Ni,N'j} , \qquad (3.4)$$

$\underline{I}, \underline{L}, \underline{A}$ are matrices of the 3N order, where $I_{Ni,N'j} = \delta_{ij}\delta_{NN'}$, while $\underline{A}(\omega) = \alpha_{N,ij}(\omega)\delta_{NN'} \cdot \underline{L}_{NN'}$ is the Lorents [21] factor tensor calculated by the Ewald summation technique, describing the electric field acting on the N molecule resulting from the dipole interaction of all N' molecules surrounding it.

References

[1] Leach, A. R., Molecular modelling principles and applications, Pearson Education Limited, ISBN 0-582-38210-6 (2001).

[2] Mikkelsen K. V., Lou Y., Agren M., Joirgensen P., J. Chem. Phys. 100, 8240 (1994).

[3] Willetts A., Rice J. E., J. Chem. Phys., 99, 426 (1993).

[4] Cammi R., Tomasi T., J. Comput. Chem. 16, 1449 (1995).

[5] Mennucci B., WIREs Comput Mol Sci, 2, 386-404 (2012).

[6] Mennucci B., Tomasi J., Cammi, R., Cheeseman J. R., Frisch M. J., Devlin F. J., Gabriel S., Stephens P. J., J. Phys. Chem. A. 106, 6102-6113 (2020).

[7] Amovilli C., Barone V., Cammi R., Cances E., Cossi M., Mennuci B., Pomelli Ch. S., Tomasi J., Advances in quantum chemistry, 32, 227-261 (1998).

[8] Vreven T., J. Chem. Phys. 115, 62, (2001).

[9] Norman P., Luo Y., Agren H., J. Chem. Phys., 107, 9535 (1997).

[10] Pipolo S., Corni S., Cammi R., J. Chem. Phys. 140, 164114 (2014).

[11]   Klamt A., J. Phys. Chem. 99,7,2224-2235 (1995).

[12]   Cossi M., Rega N., Scalmani G., Barone V., J Comput. Chem. 24, 669-681, (2003).

[13]   Pliego J. R., Riveros J. M., J. Phys. Chem. A. 105, 7241-7247 (2001).

[14]   Stefanovich E. V., Truong T. N., Chem. Phys. Lett. 244, 65-74 (1995).

[15]   Lin H., Truhlar D. G., Theor. Chem. Acc. 117, 185-199 (2007).

[16]   Senn H. M., Thiel W., QM/MM methods for biological systems. In: Reiher M. (eds) Atomistic approaches in modern biology. Topics in Current Chemistry, 268, Springer, Berlin, Heidelberg (2007).

[17]   Cardenuto M. H., Champagne B., J. Chem. Phys. 141, 234104 (2014).

[18]   Frate G. D., Bellina F., Mancini G., Marianetti G., Minei P., Pucci A., Barone V., Phys. Chem. Chem. Phys. 18, 9724-9733,(2016).

[19]   Difley S., Wang L-P., Yeganeh S., Yost S. R., Voorhis T. V., Acc. Chem. Res. 43, 7, 995-1004, (2010).

[20]   Luty M. A., Phys. Lett. B 414, 71-76 (1997).

[21]   Wang Z., Holm Ch., J. Chem. Phys. 115, 6351 (2001).

Chapter 4
Methodology

4.1. Experimental methods

The experimental techniques used in the investigation of the nonlinear optical (NLO) response and the model used for the determination of the nonlinear optical parameters will be presented. As well as the methodology of the thin films preparation and the corona poling technique, to orientate the chromophores at the thin layer surface, to obtain the second harmonic signal will also be presented.

4.1.1. Thin films preparation

To measure linear and nonlinear optical properties the samples were prepared in the form of a compound embedded in the matrix known as a *guest-host* system. The conjugated polymers are commonly used as an active matrix-host in optoelectronic applications. Poly (methyl methacrylate) (PMMA) is considered one of the potential and useful conducting polymers for various optoelectronic applications, such as sensors, and organic light-emitting diodes (OLED) because of its environmental stability and conductivity [1]. The PMMA (Sigma-Aldrich, Mw=350 000 g/mol) was dissolved in 50g/L 1,1,2-trichloroethane to prepare a host

system for chromophores. The concentration of the PMMA in the solvent was equal to 2 wt %. The crucial issue in the preparation of the solutions was the solubility of the components. Due to the difficulty in dissolving the compounds, the different solvents were used: (DMF (dimethylformamide), DMSO (dimethyl sulfoxide), 1,1,2-TCA (1,1,2-trichloroethane), and the best solubility were obtained for 1,1,2-1,1,2-TCA solvent. The solution of the polymeric matrix and the components were stored in an ultrasonic bath for the next two hours, to achieve a well-dissolved compound. Prepared solutions were deposited on the glass substrates.

All deposition techniques can be broadly divided into two categories, namely physical vapor deposition processes (PVD) and chemical vapor deposition processes (CVD) [2]. Two different methods were used to make the thin layers: the spin coating method [3] and the PVD process – Pulsed Laser Deposition (PLD) technique [4]. Spin coating is a commonly used and relatively simple method to deposit thin film onto a flat substrate. Very important is the correct preparation of substrates and solution, it has the greatest impact on the quality of the deposited layer in the spin coating method [5]. First, the substrate is coated evenly across the surface in the ink containing the molecules dissolved in a solvent. Then the substrate is rotated at high speed and the excess of ink is spread off from the surface. The angular speed used for preparing the thin films was equal to 1000 rpm. The glass plates before coating were washed in distilled water using an ultrasonic bath, cleaned with acetone and ethanol, and then dried. For two days the *guest-host* polymer films were kept at room temperature to remove any remaining solvent. Then the airflow dries the solvent from the thin film and leaves a plasticized film. During a speed time, the solvent evaporates to leave the desired material on the substrate in an even covering [6]. The procedure of the spin coating is presented in Fig. 4.1. The advantage of the spin coating is the ability to have high spin speeds the high airflow leads to fast drying times, which in turn results in high consistency at both macroscopic and nano length scales [7]. The thickness of a film depends upon the material concentration and solvent evaporation rate (which also depends upon the solvent viscosity, temperature, vapor pressure, and local humidity) [6,8].
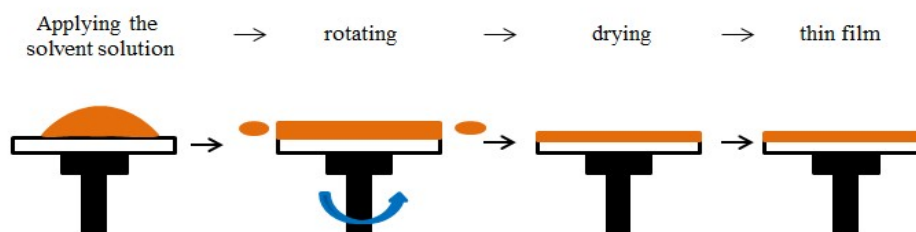
Figure 4.1. Schema of the major spin-coating processes.

To investigate the NLO properties such as second harmonic signal, the investigated material should have noncentrosymmetric structures. This system can be achieved by the technique named "corona poling" (see Fig. 4.2). The dipole moment of polar chromophores has been aligned by the application of an external electric field to achieve the required second-order NLO characteristics of the materials [9]. First of all the samples were heated up to 100 °C on a hot plate of the poling machine. The temperature should be a little lower than the glass transition temperature T_g of polymer because over this temperature the polymer will be lost its properties and degraded the thin film [10]. The tungsten needle is fixed at 1cm above the thin-film surface and applies the external electric field with 5kV. During the sample heating and the temperature holding, the dipole moments of the chromophores reorient in one direction. Then the heater was switched off with remaining of the electric field and the samples were cooled down up to room temperature. The electric field was turned off at the last step. The whole poling process has taken about 2.5 h including heating and cooling down the temperature.

The Pulsed Laser Deposition (PLD) technique also is used to prepare the *guest-host* thin films. This technique was first proposed by Smith and Turner in 1965 to prepare semiconductors and dielectric thin films [11]. Subsequently, in 1987, the work of Dijkkamp and coworkers introduced the main principle of PLD techniques. They reported, the first successful deposition of superconductor thin film using pulsed excimer laser evaporation from bulk target [12]. This versatile deposition technique has been frequently used for all kinds of oxides, nitrides carbides, and also for preparing metallic systems [4]. PLD set-up is schematically shown in Fig. 4.3. The target is struck at an angle of 45° by a pulsed and focused laser beam and the atoms and ions ablated from the targets' are deposited on

substrates. The substrates are placed with the surface parallel to the target surface at a distance of typically 2-10 cm, the whole process is closed in a vacuum chamber.
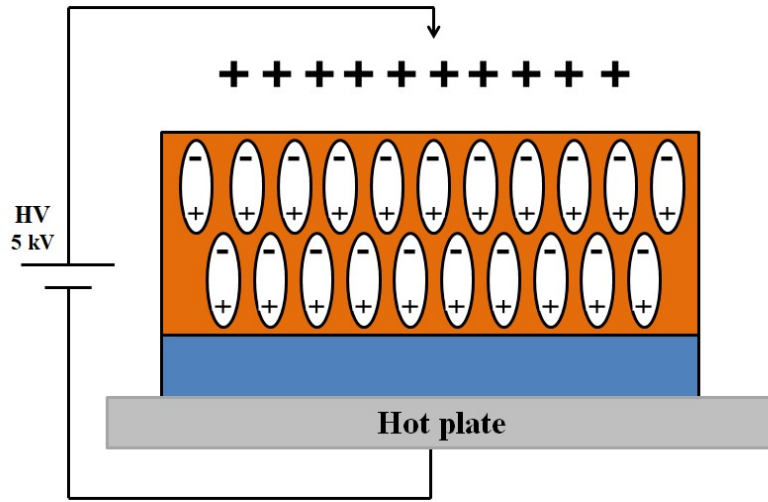
Figure 4.2. The scheme of preparation of the poled thin film.
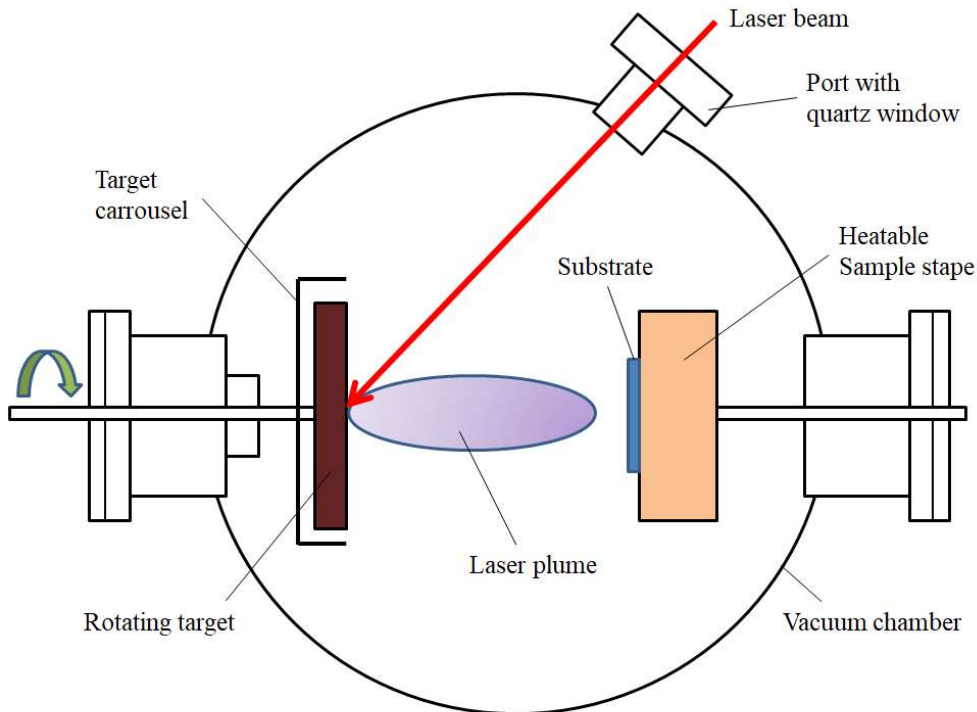
Figure 4.1. The configuration of a PLD deposition chamber.

The thin films were deposited on a fused silica glass substrate and the deposition process was carried out at a pressure equal to $2x10^{-5}$ Torr. Multilayers with desired single-layer thicknesses can be created by adjusting the number of laser pulses in each target. The compounds were thermally evaporated from a quartz crucible heated by a tungsten resistance coil and the temperature of the evaporation source has been manually controlled. Temperatures of the source for investigated materials are presented in Table 4.1. The film thickness depends on the evaporation's time and the distance between source and substrate. The deposition rate was in the range of 0.1-0.2 nm/s and it depended on the source materials and temperature. The PLD is a versatile technique because many experimental parameters can be changed, however, they have a strong influence on film properties. The laser parameters can be changed (laser fluence, wavelength, pulse duration, and repetition rate) and the preparation conditions (target-to-substrate distance, background gas, pressure, substrate temperature) may be varied. Last but not least is the small target size, the spot size of the focused laser beam is small and, therefore, the target area may be less than 1 cm^2. Hansen and Robitaille in 1988 present the preparation of thin-film from a single bulk polymer target, the chemical structure and chain length strongly depend on the applied laser wavelength and fluence, in the case of polymers [13].

Table 4.1. Parameters used during PLD deposition process.

Sample	Temperature of sublimation's beginning [°C]	Temperature of deposition process [°C]	Time of deposition process [minute]	Pressure of deposition process [Torr]
L1	108	120-125	20	$2*10^{-5}$
L2	103	115-120	20	$2*10^{-5}$
L3	95	100-105	20	$2*10^{-5}$
L4	167	210-220	20	$2*10^{-5}$

4.1.2. Measurements of the second (SHG) and third harmonic generation (THG) by Maker fringe technique

The first demonstration of optical harmonic generation was revealed by Franken et al. in 1961 [14]. They have observed the second harmonic produced upon the projection of an intense beam of light through crystalline quartz. Maker et al. in 1962 [15] introduced a good comparative measurement technique to measure

the nonlinearity of a material. This technique was named after him as the Maker fringe method. He used radiation of the ruby laser with a wavelength of 694,3 nm for the irradiation of quartz plates and excited the non-linear polarization. On the photographic plate were registries of the radiation of the ruby laser and in addition the radiation of the second harmonic with a wavelength of 347,1 nm. Later, the Maker fridge technique was detailed described by Jerphagnon and Kurtz [16].

The Second Harmonic Generation (SHG) is a nonlinear optical effect, which was historically the first experimentally observed second-order optical phenomenon. It is the optical interaction of two photons of energy $h\nu$ interacting with the nonlinear material combined to form a new photon of energy $2h\nu$. A pump wave with a frequency of ω propagates through a medium with quadratic nonlinearity and generates a signal at the frequency 2ω (see Fig. 2.2). The incidence angle of a laser beam is varying on a plane parallel sample of NLO material. The intensity of the SHG generated and transmitted is found to oscillate periodically. The transmitted second harmonic vanishes for highly absorbing materials. All even-order nonlinear susceptibilities $\chi^{(n)}$ vanish in centrosymmetric media. In this case, the SHG can occur only in media with no inversion symmetry. From the spacing between the minima (or maxima) of the Maker fringes can be concluded the coherence length between the bound and free harmonic waves, while the NLO coefficient is correlated with the peak amplitudes of the oscillations.

The SHG Maker fringes method is a frequently used optical characterization technique for measuring second-order NLO effects. This method has a few advantages; it does not require precise absolute measurements of the fundamental and second harmonic powers. And, the effects of multiple modes are the same in the sample and the reference material, and it follows that it does not require knowledge of the longitudinal mode structure of the pump laser. However, the preparation of a proper sample for Maker fringe measurements is difficult and it creates the main issue of this method [17]. The purpose of this method is to measure the second harmonic power generated by a slab of material as a function of the angle of incidence θ of the fundamental beam, and the results are compared to the standard well-characterized material to obtain the $\chi^{(2)}_{eff}$ of the sample. The changes in the second harmonic light intensity versus the incident angle are measured during the experiments. When the incident angle is changed, the length of the optical

pathway within the sample is varied as well. The *p*-polarized beam was passed through the sample as it was being rotated in the plane of incidence (Z plane) from -70° to 70° and the second harmonic light was generated in the sample. A photomultiplier tube collected this light after passing a bandpass filter. The generated second harmonic signal is described as a series of the maxima and minima called "Maker fringes" and the plot of the second harmonic signal is presented in Fig. 4.4.
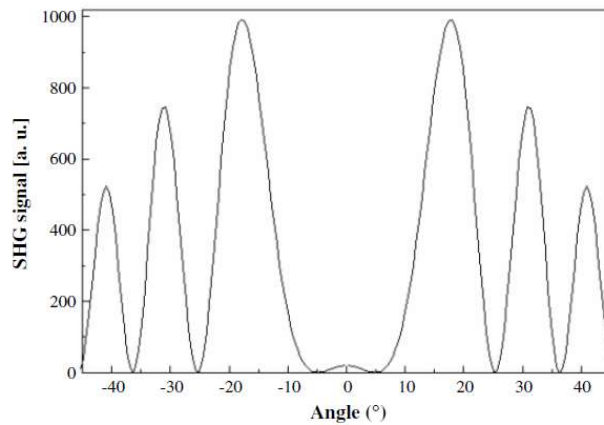
Figure 4.4. An example of the second harmonic signal as a function of the incidence angle of the laser beam [18].

These Maker fringes were theoretically described by Jerphagnon and Kurtz in 1970 [16]. According to them, the intensity of the second harmonic is induced by the propagation of the fundamental wave through a nonlinear material in the emerging phase and it is given by the relation:

$$I_{2\omega} = I_M(\theta)sin^2\Psi, \tag{4.1}$$

where

$$\Psi = \frac{2\pi}{\lambda_\omega}(n_\omega \cos\theta_\omega - n_{2\omega}\cos\theta_{2\omega})L \approx \frac{\pi}{2}\frac{L}{L_c(\theta)}. \tag{4.2}$$

The Ψ is the interference factor between the constraint and free waves and $L_c(\theta)$ is the coherence length, depending on the angles θ_ω and $\theta_{2\omega}$.

The principle of the SHG technique is presented in Fig. 4.5. Maker fringes are characterized by the change in the interaction length of a sample placed at the rotational stage.
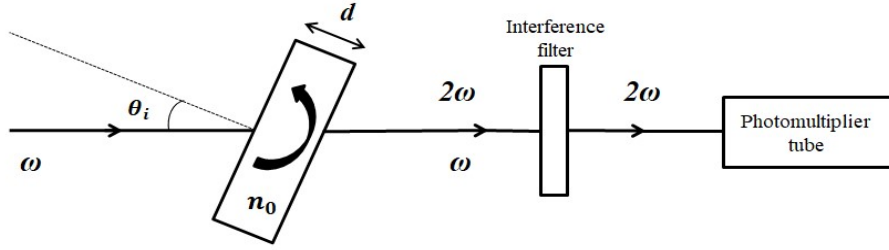
Figure 4.5. The principle of the SHG technique.

The interaction length is defined as:

$$L = \frac{d}{\cos \theta_t},\tag{4.3}$$

where the angle $\theta_t = \arcsin\left[\frac{\sin_i}{n_0}\right]$, θ_i is the incident angle, n_0 is the refractive index of the material and d denotes the thickness of the material. Theoretical description of the intensity overlapping Maker Fringes $I_M (\theta)$, is given by the equation:

$$I_M (\theta) = \left(\frac{1}{n_{2\omega}^2 - n_\omega^2}\right)^2 \left(d_{eff}(\theta)\right)^2 I_\omega^2 \, [t_\omega (\theta)]^4 \, T_{2\omega} (\theta),\tag{4.4}$$

where, $d_{eff}(\theta)$ is the projection of the effective nonlinear coefficient on the electric field of the fundamental wave and $t_\omega(\theta)$ and $T_{2\omega}(\theta)$ are related to the transmission coefficients (Fresnel coefficients) at the frequencies ω and 2ω, respectively. $I(\omega)$ is the intensity of the incident beam and n_ω and $n_{2\omega}$ are the refractive indices of the fundamental beam and second harmonic wave.

To determine the $\chi^{(2)}$ of the thin film, the simplified comparative model (also known as the Lee model) is frequently used. This model is based on the direct comparison of the macroscopic NLO properties of the sample under study to those of 0.5 mm thick Y-cut quartz. Taking into account the film thickness d, and the coherence length of quartz $l_{c,q}$:

$$\frac{\chi^{(2)}}{\chi_q^{(2)}} = \frac{2}{\pi} \frac{l_{c,q}}{d} \sqrt{\frac{I^{2\omega}}{I_q^{2\omega}}},\tag{4.5}$$

where

$$l_{c,q} = \frac{\lambda_\omega}{4(n_{q(2\omega)} - n_{q(\omega)})}.\tag{4.6}$$

where, $\chi^{(2)}$ and $\chi_q^{(2)}$ indicate the second-order nonlinear susceptibilities of the studied material and quartz, respectively. The second harmonic intensities of the

studied material and quartz are $I^{2\omega}$ and $I_q^{2\omega}$. The wavelength of the fundamental beam is λ_ω and $n_{q(\omega)}$ and $n_{q(2\omega)}$ are the refractive indices of quartz at the wavelength of the fundamental and the second harmonic beam.

The Third Harmonic Generation (THG) technique is a coherent four-photon process, in which three photons with angular frequency ω create the one-photon with triple frequency 3ω, through a material medium polarization (see Fig. 2.3). It is a frequently used technique to measure third-order susceptibility $\chi^{(3)}(-3\omega;\ \omega, \omega, \omega)$ of randomly oriented molecules in the polymeric matrix. The technique can be applied to powders, liquids, and thin solid films. The refractive index of the material at the frequency of the incident beam (ω) and the third harmonic signal (3ω) should be known in measurement to obtain reasonable accuracy.

The model proposed by Kubodera and Kobayashi is applied for the calculation of third-order susceptibility; it compares directly the maximum amplitudes of third harmonic light intensity, for the studied nonlinear material, to those of a 1 mm fused silica, used as a reference. It proposed two different approaches. The first approach is for materials with negligible absorbance and the equation used to determine the order of magnitude $\chi^{(3)}$ is:

$$\frac{\chi^{(3)}}{\chi_S^{(3)}} = \frac{2}{\pi} \frac{L_{c,S}}{l} \sqrt{\frac{I^{3\omega}}{I_S^{3\omega}}}\ , \qquad (4.7)$$

where $\chi_S^{(3)} = 2 \cdot 10^{-22} m^2 \cdot V^{-2}$ is the third-order susceptibility of the reference material (fused silica), l is the thickness of the investigated material, $L_{c,S} = 6{,}7\mu m$ is the coherent length of silica and $I^{3\omega}, I_S^{3\omega}$ are the maximum intensities of the envelope of the third harmonic signal of the studied material and the reference. In the case of significant absorption (T < 0.9), the equation is following:

$$\frac{\chi^{(3)}}{\chi_S^{(3)}} = \frac{2}{\pi} \frac{L_{c,S}}{l} \frac{\frac{\alpha d}{2}}{1 - e^{-\left(\frac{\alpha d}{2}\right)}} \sqrt{\frac{I^{3\omega}}{I_S^{3\omega}}}\ , \qquad (4.8)$$

where: d denotes the sample thickness, α the linear absorption coefficient of material at the fundamental wavelength.

4.2. Computational methods

Computational methods and computer simulations complement the experimental methods in the study of the structural, electronic, and optical properties of isolated molecules, liquids, and solids. These methods allow for a better interpretation of the physicochemical properties of composite materials. The current development of materials science requires a quantitative analysis of physical phenomena with high accuracy of the results obtained. It is impossible to analyze quantitative properties with simple computational methods. Large-scale numerical calculations based on approximate model physicochemical theories are essential. Computational methods turn out to be an invaluable tool in the stage of designing atomic structures, developing manufacturing technology, and predicting their properties. Theoretical calculations allow predicting the electronic properties of various materials before their production. A wide range of computer modeling methods is known and they are successfully used in the physic and chemistry field.

Since the birth of quantum mechanics, one of the basic tasks of theoretical chemistry is the determination of the electron structures of molecules. Unfortunately, the complexity of even the simplest chemical systems excludes the use of quantum mechanics in its axiomatic form. It is necessary to introduce additional approximations and schemes, which together with axioms of quantum chemistry create a scientific discipline called quantum chemistry. The basic differential equation for quantum chemistry is the Schrodinger equation. For the first time in 1920, the equation has been formulated by the Austrian physicist Erwin Schrodinger. The Schrodinger equation has two forms, one in which time explicitly appears, and it describes how the wave function of a particle will evolve in time. The equation behaves as a wave and it is named the time-dependent Schrodinger wave equation. The other is the equation known as the time-independent Schrodinger equation which is found to describe the allowed energies of the particle.

The source of information about the system of electrons and nuclei, which create atoms and molecules, is the wave function ψ. The one option how to find the wave function is to solve the time-dependent Schrodinger equation:

$$\hat{H}\Psi(r, R, t) = i\hbar \frac{\partial \Psi(r,R,t)}{\partial t} , \qquad (4.9)$$

where $\widehat{H}$ is Hamilton operator corresponding to the total energy of the system, Ψ is a wave function describing the quantum state of the system. In case of, when Hamilton operator is not changed in the time, we get the time-independent Schrodinger equation:

$$\widehat{H}\Psi_s(r,R) = E_s\Psi_s(r,R), \tag{4.10}$$

$\Psi_s(r,R)$ are eigenfunctions of stationary states with energy E_s. The index s denotes successive solutions to the Schrodinger equation. Hamilton operator has the form:

$$\widehat{H} = -\frac{\hbar^2}{2m_e}\sum_i \nabla_i^2 - \sum_k \frac{\hbar^2}{2M_k}\nabla_k^2 + \sum_{j>i=1}\frac{1}{4\pi\varepsilon_0}\frac{e^2}{|r_i - r_j|}$$
$$- \sum_{i,k}\frac{1}{4\pi\varepsilon_0}\frac{Z_k e^2}{|r_i - R_k|} + \sum_{l>k=1}\frac{1}{4\pi\varepsilon_0}\frac{Z_k Z_l e^2}{|R_k - R_l|}, \tag{4.11}$$

In equation (4.11), the part $-\frac{\hbar^2}{2m_3}\sum_i \nabla_i^2$ and $\sum_k \frac{\hbar^2}{2M_k}\nabla_k^2$ represent the kinetic energy operator of electrons and nuclei, respectively, and the three potential energy operators: the electrostatic electron-electron interactions $\sum_{j>i=1}\frac{1}{4\pi\varepsilon_0}\frac{e^2}{|r_i - r_j|}$, electron-nuclei interactions $\sum_{i,k}\frac{1}{4\pi\varepsilon_0}\frac{Z_k e^2}{|r_i - R_k|}$ and nuclei-nuclei interactions $\sum_{l>k=1}\frac{1}{4\pi\varepsilon_0}\frac{Z_k Z_l e^2}{|R_k - R_l|}$. R_k, R_l are vectors of the nuclei positions, and r_i, r_j describe the location of electrons. M_k means mass on nuclei; m_e mass of an electron, ∇_i^2 and ∇_k^2 are Laplace operators. It is a differential operator of each electron and nuclei coordinate, and is defined as: $\nabla_i^2 = \frac{\partial^2}{\partial x_i^2} + \frac{\partial^2}{\partial y_i^2} + \frac{\partial^2}{\partial z_i^2}$ and $\nabla_k^2 = \frac{\partial^2}{\partial x_k^2} + \frac{\partial^2}{\partial y_k^2} + \frac{\partial^2}{\partial z_k^2}$.

Schrodinger's equation could be solved only for a simple system, for example, a harmonic oscillator, a particle in a potential box, a rigid rotor, and the hydrogen atom. In more complicated cases, it is necessary to use approximate methods. One of the most important approximations of quantum chemistry is the adiabatic approximation and the resulting Born-Oppenheimer approximation. The coupling of instantaneous positions of electrons and nuclei is completely ignored and treated as separate elements. The adiabatic approximation is defined as:

$$\Psi(r,R) \approx \psi_p(r;R)f_p(R), \tag{4.12}$$

where the electron part of the wave function $\psi_p(r;R)$ is depending on coordinates of the electrons and parametrized on nucleus position. Whereas the nucleus part of

the wave function $f_p(R)$ is dependent only on the coordinates of the electrons. Therefore, the Schrodinger equation is separated into two parts;

1. the electron part:

$$\widehat{H^e}(r;R)\psi_p(r;R) = E_p^e(R)\psi_p(r;R), \tag{4.13}$$

with the electron Hamiltonian:

$$\widehat{H^e}(r,R) = -\frac{\hbar^2}{2m_e}\sum_i \nabla_i^2 + \sum_{j>i=1}\frac{1}{4\pi\varepsilon_0}\frac{e^2}{|r_i - r_j|} - \sum_{i,k}\frac{1}{4\pi\varepsilon_0}\frac{Z_k e^2}{|r_i - R_k|}, \tag{4.14}$$

2. the nuclear part:

$$\widehat{H^N}(R)f_p(R) = E_p^{tot}f_p(R), \tag{4.15}$$

with the nuclear Hamiltonian:

$$\widehat{H^N}(R) = -\sum_k \frac{\hbar^2}{2M_k}\nabla_k^2 + E^e(R) + E_{ad}(R). \tag{4.16}$$

The Hamiltonian of the nuclear part is supplemented by the nuclei position-dependent energy of the electron system $E^e(R)$ derived from equation (4.13), defined for a specific "frozen" configuration of atoms and constituting effective potential energy of their motion. The energy $E_{ad}(R) = \int \psi^* \widehat{T_N} \psi \, d\tau_e$ is an average kinetic energy operator of the motion of nuclei. Because its value is very small compared to the $E^e(R)$ electron energy, it can be omitted. The presented approach characterize the Born-Oppenheimer approximation.

4.2.1. Hartree-Fock methodology

The Hartree-Fock method serves to solve the electron Schrodinger equation by applying the Born-Oppenheimer approximation. The nuclei move much slower than an electron and this approach allows the separation of the motion of these two types of particles. In this case, it is possible to determine the electron structure at the given positions of all nuclei.

The next approximation concerns the form of wave functions describing the fermion system. These functions must fulfill Pauli's rule, i.e. be anti-symmetric due to the exchange of any two electrons. It means that to everyone electron is assigned a wave function ϕ_i called the spin-orbital. It describes the state of a single electron using the orbital function φ_j dependent on the spatial coordinates of the electron and spin function σ_{m_s} characterized by spin coordinate ($\sigma = 1/2$ or $-1/2$):

$$\phi_i = \varphi_j \, \sigma_{m_s} \, . \tag{4.17}$$

The total wave function of the *N*-electron system can be written as a spin-orbital combination. It can be represented by the Slater determinant, building from the ϕ_i functions of single electrons:

$$\psi = \frac{1}{\sqrt{N!}} \begin{vmatrix} \varphi_1(1) & \varphi_1(2) & \dots & \varphi_1(N) \\ \varphi_2(1) & \varphi_2(2) & \dots & \varphi_2(N) \\ \vdots & \vdots & \ddots & \vdots \\ \varphi_N(1) & \varphi_N(2) & \dots & \varphi_N(N) \end{vmatrix} . \tag{4.18}$$

The presented wave function of the electron system is constructed as a determinant with rows corresponding to different electrons located at different orbitals (location of columns). The multi-electron Slater determinant is a good approximation for the closed-shell system. In this system, each orbital is occupied by electrons with different spin functions, which means that each orbital φ_i are assigned two spin-orbitals ϕ_i .

The Hartree-Fock method is an iterative minimization of the energy of the system calculated by the changing of the form of the spin-orbital. This procedure is based on the solution of the Hertee-Fock equation similar in the character to the time-independent Schrodinger equation:

$$\hat{F}(i)\varphi_{HF\,\mu}(i) = \varepsilon_\mu \varphi_{HF\,\mu}(i) \, , \tag{4.19}$$

where ε_μ is an eigenenergy corresponding to the orbital φ_μ. The $\hat{F}$ is called the Fock operator and it has a form:

$$\hat{F}(i) = \hat{h}(i) + \sum_{\mu=1}^{N/2} \left(2\,\widehat{J_\mu(\iota)} - \widehat{K_\mu(\iota)} \right) , \tag{4.20}$$

where the $\hat{h}(i)$ is one-electron Hamiltonian. The Fock operator is the differential-integral operator with a solution not easy to be found because it needs the numerical methods to be used. The problem is also caused by finding a Hamiltonian describing the interaction of an electron with an averaged field derived from other electrons. In this case, it is necessary to know all orbitals which can be designated to solve the Hartree-Fock equation. In consequence, the Hartree-Fock equation can be solved using the self-consistent field (SCF) method.

The one-electron Hamiltonian is the sum of the kinetic and potential energy of electrons in the field of frozen nuclei and characterizes the state of a single electron. It can be defined as:

$$\hat{h}(i) = -\frac{\hbar^2}{2m_i}\nabla_i^2 - \frac{e^2}{4\pi\varepsilon_0}\sum_{a=1}^{M}\frac{Z_a}{r_i - R_a}, \qquad (4.21)$$

The M means the number of atomic nuclei. Based on the Slater determinant ψ, the average energy value obtained for Hamiltonian defined by (4.20) and (4.21) can be described as:

$$\langle E \rangle = 2\sum_{\mu=1}^{N/2} I_{\mu\mu} + \sum_{\mu>\nu=1}^{N/2}\left(2J_{\mu\nu} - K_{\mu\nu}\right), \qquad (4.22)$$

here:

$$I_{\mu\mu} = \int \varphi_\mu^*(i)\hat{h}(i)\varphi_\mu(i)dv_i. \qquad (4.23)$$

Is the expected value of a one-electron Hamiltonian i in quantum state μ. The μ and ν index orbitals. The one-electron integral over dv_i means integral of spatial coordination of i electron.

The first two-electron integral from (4.20) is called coulomb integral:

$$J_{\mu\nu} = \frac{e^2}{4\pi\varepsilon_0}\iint \varphi_\mu^*(i)\varphi_\nu^*(j)\frac{1}{r_i - r_j}\varphi_\mu(i)\varphi_\nu(j)dv_idv_j. \qquad (4.24)$$

The coulomb integral characterizes the repulsion of the electron i being in a quantum state μ with an electron j, which is located in a quantum state ν. The second integral from (4.20) is an exchange integral:

$$K_{\mu\nu} = \frac{e^2}{4\pi\varepsilon_0}\iint \varphi_\mu^*(i)\varphi_\nu^*(j)\frac{1}{r_i - r_j}\varphi_\mu(j)\varphi_\nu(j)dv_idv_j. \qquad (4.25)$$

The coulomb integral denotes any electron (i and j) of investigated system, whereas the exchange integral described the exchange interaction occurring only between electrons with the same spin.

4.2.2. Density function theory (DFT)

The very effective and commonly used method to analyze electronic properties of atom systems is a procedure based on density function theory (DFT). The main purpose of the DFT method is to compute the electron density and energy without using any concept of a wave function or orbitals. The method allows significantly reduces the difficulty of solving the Schrödinger equation for multi-electron systems. It can be accomplished by describing the electrons as identical

molecules in the external electric potential V_{ext}. This is an alternative method to the *ab initio* approach. In 1964 Hohenberg and Kohn proved that the ground-state electron density ρ_0 (r) and the ground-state electron wave function ψ_0 can be used alternatively. The electron density is defined as follows:

$$\rho(r) = N \sum |\psi(r_1, r_2, \dots, r_N,)|^2 \, dr_2 dr_3 \dots dr_N, \qquad (4.26)$$

where N is the number of electrons. The average electron energy of the ground state, called the density functional, is expressed by the formula:

$$E[\rho] = F[\rho] + \int V_{ext}(r)\rho(r)dr. \qquad (4.27)$$

The functional $F[\rho] = \langle \psi | \hat{T} + \hat{W} | \psi \rangle$ is characterized by kinetic energy $\hat{T}$ of electrons and Coulomb interaction energy occurring between electrons $\hat{W}$. The second part of the equation (4.27) describes electron interactions with external potentials. The functional $F[\rho]$ does not depend on external potential and it is not exactly defined. With help to find $F[\rho]$ comes the Kohn-Sham theorem based on the projection of the real electron system into an auxiliary system. It is the hypothetical system of non-interacting electrons which moves in an effective potential describing the electrostatic interactions of nuclei and other electrons and the correlation-exchange potential. Functional $F[\rho]$ is described as follows:

$$F[\rho] = T_0[\rho] + W_0[\rho] + E_{XC}[\rho], \qquad (4.28)$$

where $E_{XC}[\rho]$ denotes the exchange-correlation energy (XC) raised as an effect of the disorder of electron density distribution caused by interactions of external or electron fields. It contains a correlation correction to the electron kinetic energy and is non-classical.

The analog of the Hartree-Fock equation in the density functional theory is the Kohn-Sham (KS) equation:

$$\left(-\frac{\hbar^2}{2m} \frac{\partial^2}{\partial r^2} + V_{KS}(r) \right) \psi_n(r) \equiv \widehat{H_{KS}} \psi_n(r) = \varepsilon_0 \psi_n(r). \qquad (4.29)$$

For the non-interacting electrons moving in the effective potential the KS potential can be written as follow:

$$V_{KS}(r) = V_{ext}(r) + e^2 \int \frac{\rho(r_2)}{|r_1 - r_2|} \, dr_2 + v_{XC}(r). \qquad (4.30)$$

The correlation-exchange potential v_{XC} can be defined as the derivative of the correlation-exchange energy:

$$v_{XC}(r) = \frac{\delta E_{XC}(\rho)}{\delta \rho(r)}. \tag{4.31}$$

Solution of the equation (4.29) by using the SCF method leads to the expression of the total energy of the tested system:

$$E[\rho] = 2\sum_{N=1}^{N/2} \varepsilon_N - \frac{e^2}{2}\int \frac{\rho(r_1)\rho(r_2)}{|r_1 - r_2|}\, dr_1\, dr_2 +$$

$$+ E_{XC}[\rho] - \int \rho(r)v_{XC}(r)dr. \tag{4.32}$$

To calculate the energy of the electron system the correlation-exchange potential v_{XC} is necessary to be known and it is the biggest problem of DFT theory. For example, Becke proposed the potential called "hybrid". It is a combination based on Hartree-Fock exchange and correlation-exchange DFT calculations, defined as:

$$E_{hybry}^{XC} = c_{HF}\, E_{HF}^X + c_{DFT}\, E_{DFT}^{XC}. \tag{4.33}$$

where c_{HF} and c_{DFT} are constant values.

4.2.2.1. The B3LYP hybrid functional

The B3LYP functional belongs to the hybrid (mixing) functional. It is based on GGA calculating exchange energy according to Beck functional (B3) and correlation energy according to Lee, Yang, and Parra (LYP) functional. The B3LYP functional is presented as:

$$E_{XC}^{B3LYP} = (1 - a_0)E_X^{LSDA} + a_0 E_{HF}^{HF} + a_x E_x^{B8} +$$

$$+ a_c E_C^{LYP\,88} + (1 - a_c)E_C^{VWN\,80}. \tag{4.34}$$

The E_x^{B88} is Becke's gradient correction to the exchange functional. The suggested coefficients present in (4.34) are equal to $a_0 = 0.2, a_x = 0.72, a_c = 0.81$. The VWN local correlation expression has been used to provide the different coefficients of local and gradient corrected correlation functionals. This hybrid functional works well in calculating vibrational frequencies, spectra as well as thermochemical properties [20]. The B3LYP functional is commonly used because it connected a good compromise between computational cost and accuracy of results [20]. Developed methodology applying the hybrid functionals enhanced the broad use of DFT for electronic structure calculations of isolated molecules; it is now significant in a wide range of applications.

4.2.2.2. The long-range corrected functional (LC-BLYP)

DFT methods have a problem with examined of Rydberg excitation energies, oscillator strengths, and charge-transfer excitation mainly in organic molecules. Especially, for this reason, the functionals named long-correlated (LC) were developed. The calculations of charge-transfer excitation energies of ethylene-tetrafluoroethylene by employing LB94 or B3LYP functionals show that they are significantly underestimated with increasing intermolecular distance [21,22]. It suggested that exchange-correlation functionals should be created concerning the charge-transfer problem. While charge transfer is based on single excitation that is taken into consideration in the HF wave function, it is assumed that this failure may come from the insufficient long-range exchange effect in the exchange functionals [23]. The LC scheme integrates the long-range orbital-orbital interaction part in the exchange functional combined with the HF exchange integral. Tsuneda and co-workers [24] present this deficiency through the Ewald split of r_{12}^{-1}

$$\frac{1}{r_{12}} = \frac{1 - \mathrm{erf}(\mu r_{12})}{r_{12}} + \frac{\mathrm{erf}(\mu r_{12})}{r_{12}} , \tag{4.35}$$

where the first term presents the short-range interaction and the second accounts for the long-range interaction. The $r_{12} = |r_1 - r_2|$ is a coordinate vector of electrons distribution and μ is a parameter that defines the separation of these short and long parts. The short-range part of the exchange interaction is implemented by modification of the usual exchange functional form $E_x = -(1/2) \sum_\sigma \int \rho_\sigma^{4/3} K_\sigma d^3 r$, into:

$$E_x^{sr} = -\frac{1}{2} \sum_\sigma \int \rho_\sigma^{4/3} K_\sigma \left\{ \begin{array}{c} 1 - \frac{8}{3} a_\sigma \cdot \\ \cdot \left[\sqrt{\pi} \, erf\left(\frac{1}{2a_\sigma}\right) + 2a_\sigma(b_\sigma - c_\sigma) \right] \end{array} \right\} d^3 r , \tag{4.36.}$$

where a_σ, b_σ and c_σ are:

$$a_\sigma = \frac{\mu K_\sigma^{1/2}}{6\sqrt{\pi}\rho_\sigma^{1/3}} , \tag{4.37}$$

$$b_\sigma = \exp\left(-\frac{1}{4a_\sigma^2}\right) - 1 , \tag{4.38}$$

$$c_\sigma = 2a_\sigma^2 b_\sigma + \frac{1}{2} . \tag{4.39}$$

The part *erf(μr₁₂)* has been multiplied by the square of the one-particle density matrix for the uniform electron gas and then integrated. The K_σ allows the

incorporation of generalized gradient approximation functionals. The long-range part of the exchange interaction is presented by the HF exchange integral

$$E_x^{lr} = -\frac{1}{2} \sum_{\sigma} \sum_{i}^{occ} \sum_{j}^{occ} \int \int \psi_{i\sigma}^*(r_1)\psi_{j\sigma}^*(r_1) \cdot$$

$$\cdot \frac{\text{erf}(\mu r_{12})}{r_{12}} \psi_{i\sigma}(r_2)\psi_{j\sigma}(r_2)d^3r_1 d^3r_2 \qquad (4.40)$$

where $\psi_{i\sigma}$ is the ith σ-spin molecular orbital.

When μ is equal to zero, the LC-DFT calculation responds to the pure DFT calculation, and when $\mu = \infty$ the calculations correspond to the standard HF calculation. Tsuneda has shown that the LC method with μ = 0.33 provides well results for most of the investigated phenomena [23]. Performed calculations show that the LC functional gives more accurate Rydberg excitation energies, and also gives accurate valence excitation energies. The LC functional gives accurate excitation energies compared to results obtained by the B3LYP functional. It can be confirmed that the accurate LC results may be due to the long-range correction rather than the hybridization of the HF exchange integral [24]. Another important advantage of the LC-DFT is the accurate description of orbital energies [25].

4.2.2.3. Long-range corrected modification of B3LYP functional (CAM-B3LYP)

A relatively new exchange-correlation functional named CAM-BLYP (*Coulomb-attenuating method*) combines the hybrid qualities of B3LYP and the long-range correction presented by Tawada et al. [24]. Hybrid functional B3LYP provides a great contribution to density functional theory. However, it is unsuccessful in important applications such as the polarizability of long chains, charge-transfer excitations, and excitations using time-dependent DFT theory. That issue is connected with long-range exchange potential behaving as $-0.2r^{-1}$, instead of the exact value $- r^{-1}$. In CAM functional the equation (4.35) is generalized by using two extra parameters α and β as follows:

$$\frac{1}{r_{12}} = \frac{1 - [\alpha + \beta \cdot \text{erf}(\mu r_{12})]}{r_{12}} + \frac{\alpha + \beta \cdot \text{erf}(\mu r_{12})}{r_{12}}, \qquad (4.41)$$

Where the relation $0 \leqslant \alpha + \beta \leqslant 1$, $0 \leqslant \alpha \leqslant 1$, and $0 \leqslant \beta \leqslant 1$ should be satisfied. The parameter α describes the HF exchange contribution over the whole range by a factor of α, and the parameter β allows to implement of the DFT counterpart over

the whole range by a factor of 1 – (α + β). Hybrid B3LYP functional takes CAM potential with α = 0.2 and β = 0.0. Also the LC functional corresponds to the CAM with α = 0.0 and β = 1.0. Fig. 4.6(a-c) presents the contributions to exchange from r_{12}^{-1}, apportioned into DFT and HF, for B3LYP, LC, and CAM methodologies. Way of recording a CAM functional presents be the parameters α and β taking into account how important the HF exchange contribution is for the short-range region and the DFT counterpart in the long-range region.
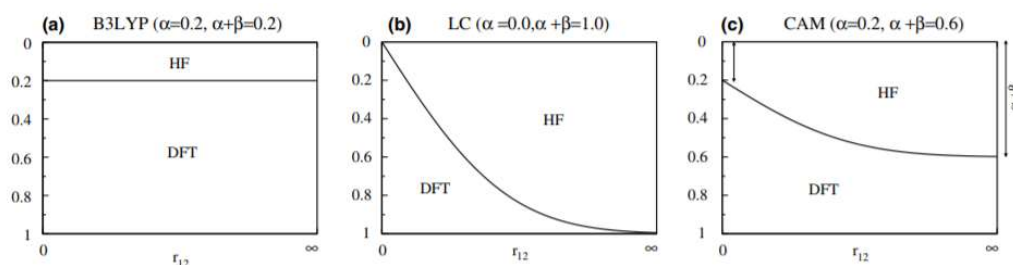
Figure 4.6. Plots of the contributions to exchange functional from r_{12}^{-1}, apportioned into DFT and HF, for a) B3LYP, b) LC and c) CAM [26].

4.2.3. Molecular dynamics (MD)

Molecular dynamics (MD) was created to investigate the influence of a real temperature of tested media on its physicochemical properties. The study of the dynamic behavior of molecules requires taking into account the actual temperature of investigated complexes [27]. The basic task is to find changes in atoms' positions over time, it means - their trajectory. Classic molecular dynamics consists in solving Newton's equations of motion [28].

Assuming that a set of molecules subjected to MD simulation contains N atoms the second principle of Newton's dynamics for any *i*-th atom can be written as:

$$m_i a_i = F_i \, , \tag{4.42}$$

where m_i is the mass of the atom *i*, while a_i means its acceleration. F_i is the force acting at the *i*-th atom. The acceleration of the atom is the second derivation of the change in its position over time *t*:

$$a_i = \frac{d^2 r_i}{dt^2} \, . \tag{4.43}$$

The Newton motion equation is a second-order differential equation:

$$m_i \frac{d^2 r_i}{dt^2} = F_i. \tag{4.44}$$

Assuming that for time $t=0$ the position and velocity of the atom are respectively equal to $r=r_0$ and $v=v_0$, then after the time t one can get a new atom position and a new velocity:

$$r_i = r_{i0} + v_{i0}t + \frac{F_i t^2}{2m_i}, \tag{4.45}$$

$$v_i = v_{i0} + \frac{F_i t}{m_i}. \tag{4.46}$$

In the case when the potential energy $V(r)$ of the molecule system is known as a function of the position of individual atoms, the force acting on them can be calculated from the expression:

$$F_i = -\nabla_i V_i \quad \text{or} \quad m_i = \frac{d^2 r_i}{dt^2} = -\nabla_i V_i. \tag{4.47}$$

Newton's differential equation is numerically solved by using minor intervals (femtosecond temporal step). In this case, the instantaneous position of the atom can be expressed into time-dependent Taylor series:

- for the next step:

$$r(t + \Delta t) = r(t) + \frac{dr}{dt}\Delta t + \frac{1}{2}\frac{d^2 r}{dt^2}(\Delta t)^2 = r(t) + v\Delta t + \frac{1}{2}a(\Delta t)^2, \tag{4.48}$$

- for the previous step:

$$r(t - \Delta t) = r(t) - v\Delta t + \frac{1}{2}a(\Delta t)^2, \tag{4.49}$$

Adding equations (4.48.) and (4.49.) one can get the expression:

$$r(t + \Delta t) + r(t - \Delta t) = 2r(t) + a(\Delta t)^2, \tag{4.50}$$

that can be transformed into the form:

$$r(t + \Delta t) = 2r(t) - r(t - \Delta t) + a(\Delta t)^2, \tag{4.51}$$

giving an equation describing the new location of the atom after the time Δt. The equation (4.51) gives the possibility to find the trajectory of atoms included in the studied system and it can be solved numerically.

The method that gives good effects on numerical integration is the Verlet algorithm [29]. This algorithm assumes that the coordinates of atoms in the next step can be calculated by knowing the current location of the atom and their previous position. The acceleration occurring in the equation (4.51) is calculated using equations (4.42) and (4.47).

The velocity of atoms is necessary to calculate the temperature of the tested system. To calculate the velocity of an atom at time t its position at time $t+\Delta t$ must be known according to the equation:

$$v(t) = \frac{r(t + \Delta t) - r(t - \Delta t)}{2\Delta t}.$$

(4.52)

One variation of the Verlet algorithm says that, if the position of the atom r(t) and its acceleration a(t) at time t is known, as well as the velocity v(t – Δt/2) at time t – Δt/2, it is possible to calculate velocity v(t + Δt/2), position r(t + Δt) and acceleration a(t + Δt) using the following forms:

$$v\left(t + \frac{1}{2}\Delta t\right) = v\left(t - \frac{1}{2}\Delta t\right) + \Delta t \cdot a(t),$$

(4.53)

$$r(t + \Delta t) = r(t) + \Delta t \cdot v\left(t + \frac{1}{2}\Delta t\right),$$

(4.54)

$$a(t + \Delta t) = \frac{F(t + \Delta t)}{m}.$$

(4.55)

The mentioned modification of the Verlet algorithm is called the leap frog algorithm [30]. The calculated velocity is delayed by Δt/2 from the position, so the value v(t) is calculated as the arithmetic average of the expressions v(t + Δt/2) and v(t – Δt/2).

Another method based on the assumptions of the modified Verlet algorithm is the Beeman method [31]. Its advantage is a more accurate reproduction of the trajectory of the system in comparison with the procedure consistent with the leap frog algorithm. The next-step velocities and atomic positions are calculated taking into account the expressions:

$$v(t + \Delta t) = v(t) + \left[\frac{1}{3}a(t + \Delta t) + \frac{5}{6}a(t) - \frac{1}{6}a(t - \Delta t)\right]\Delta t,$$ (4.56)

and

$$r(t + \Delta t) = r(t) + v(t)\Delta t + \left[\frac{2}{3}a(t) - \frac{1}{6}a(t - \Delta t)\right]\Delta t^2.$$

(4.57)

The disadvantage of this method is the long integration time of motion equations for large molecular systems. This drawback often disqualifies the Beeman method, because the main criterion for choosing the MD algorithm is its stability over time and speed of calculation.

One of the starting parameters of MD is the velocities of atoms. They should positively satisfy the Maxwell-Boltzmann velocity distribution. Monitoring the system parameters should start after finding its equilibrium state. This particularly

applies to heterogeneous systems. Changes in the total energy of the system depend on the selected calculation time step, which should be comparable to the frequency of the fastest movements occurring in the molecule. The molecules characterized by flexible bonds should be modeled with the time step equal to 1 fs.
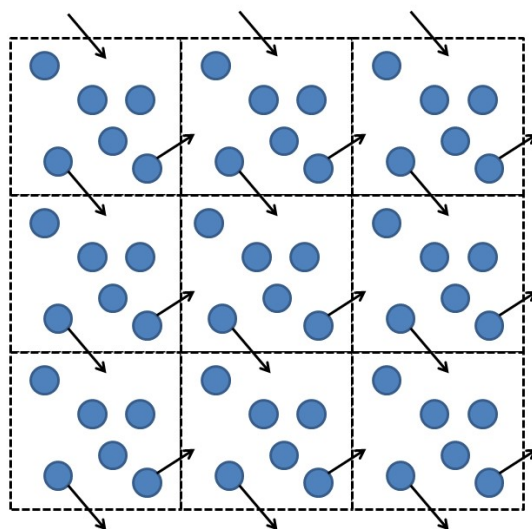
Figure 4.7. Periodic boundary conditions model and importance of unit cell in a molecular system.

The MD method can model the conformational effects of the simulation box which contains hundreds and even thousands of molecules. Undesirable surface effects of bulk materials are prevented by introducing the periodic boundary condition approach. This is particularly important during simulations of solid states. It is assumed that the system is built of an infinite number of unit cells repeated in all directions (see Fig. 4.7). It means that all operations during MD simulation are performed only for one unit cell. When any atom in the central cell moves into the neighbor cell it is replaced by the same atom from the side cell. The replica of atoms' behavior in the unit cell is prevented. The presented way of atoms moving guarantees the fixed number of atoms in a unit cell (N=const).

The MD process can be kept in constant conditions of the number of atoms, the unit cell volume, or/and the total energy of the system. This approach is named a microcanonical (NVE). The canonical ensemble (NVT) is simulated with a constant number of atoms, the unit cell volume, and the temperature of the structure. The system simulated in constant conditions of the number of atoms, pressure, and temperature of structure is an isobaric-isothermic set (NPT). Using the above-

mentioned assemblies, it can model the molecular systems in the bulk form as well as in the thin layers.

The classic MC is based on the force field methodology. The force field (FF) is a set of parameters describing the potential energy of a system of atoms depending on their position. The mentioned potential is used in equation (4.47). The type of the force field and its parameters are empirical and matched to the specific type of atoms and bonds contained in the compounds under study. Accordingly, the choice of the force field depends on the type of structure being tested and is an extremely important element of the simulation.

The total potential energy of the examined system E_p described using appropriate approximations, is expressed as a superposition of interactions bonding E_b and non-bonding E_{nb}. The bonding interactions consist of the energy of interatomic bonds E_{bond}, angles E_{ang}, torsion angles E_{tor}. The non-bonding interactions consist of the van der Waals energy E_{vdW} and the electrostatic energy E_C as follows:

$$E_p = E_b + E_{ang} + E_{tor} + E_{vd} + E_C \qquad (4.58)$$

Determination of the non-bonded interaction potential energy is the most time-consuming part of MD processes. The quantity of calculations is proportional to $\sim N^2$, therefore the cut-off limited zone of potential acting is introduced. Outside the cut-off zone, where the $r > r_{cut-o}$ the acting potential is equal to zero $V(r) = 0$. The cut-off radius $r_{cut-off}$ should be less than half of the shortest length of the cell. The limitation of electrostatic interaction by introducing a cut-off of potential acting is very important during the simulation of the Raman spectrum [32 – 34]. It does not affect the structure of modeled system [35]. The advantage of this effect is the reduction of calculation time.

References

[1]   Mohajerani E., Farajollahi F., Mahzoon R., Baghery S., J. Opt. Adv. Mat. 9, 12, 3901-3906 (2007).

[2]   George J., Preparation of thin films, Cochin University of Science and Technology Cohin, Kerala, India, ISBN 0-8247-8196-1, Marcel Dekker, INC. New York, (1992).

[3]   Norrman K., Ghanbari-Siahkali A., Larsen N. B., Annu. Rep. Prog. Chem., Sect. C. 101, 174-201 (2005).

[4]   Krebs H.-U., Weisheit M., Faupel J., Suske E., Scharf T., Fuhse Ch., Stormer M., Sturm K., Seibt M., Kijewski H., Nelke D., Panchenko E., Buback M., Advances in Solid State Physics, 43, 101-107 (2003).

[5]   Hall D. B., Underhill P., Torkelson J. M., Polymer Engineering and Science, 38, 2039-2045 (1998).

[6]   Tyona M. D., Advances in Material research, 2, 181-193 (2013).

[7]   Makhlouf A. S. H., Woodhead Publishing Series in Metals and Surface Engineering, 3-23 (2011).

[8]   Weszka J., Szindler M. M., Szczęsna M., Szindler M., Journal of Achievements in Materials and Manufacturing Engineering, 61, 302-307 (2013).

[9]   Hill R. A., Knosen A., Mortazavi M. A., Appl. Phys. Lett. 65, 1733-1735 (1994).

[10]   Ahmadi N., Kheradmand R., Kavaz E., J. Nonlinear Optic. Phys. Mat. 27, 2, 1850024-1850032 (2018).

[11]   Smith H. M., Turner A. F., Appl. Opt. 4, 147-146 (1965).

[12]   Dijkkamp D., Venkatesan T., Wu X. D., Shaheen S. A., Jisrawi N., Min-Lee Y. H., McLean W. L., M. Croft M., Appl. Phys. Lett. 51, 8, 619-621 (1987).

[13]   Hansen S. G., Robitaille T. E., Appl. Phys. Lett. 52, 1, 88-83(1988).

[14]   Franken P. A., Hill A. E., Peters C. W., Weinreich G., Phys. Rev. Lett. 7, 4, 118-119(1961).

[15]   Maker P. D., Terhune R. W., Nisenoff M., Savage C. M., Phys. Rev. Lett. 8, 1, 21-22(1962).

[16]   Jerphagnon J., Kurtz S. K., J. Appl. Phys. 41, 1667-1681 (1970).

[17]   Kato M., Kiguchi M., J. Appl. Phys. 81, 2, 550-553 (1997).

[18]   Sahraoui B., Luc J., Czaplicki R., Fillaut J.-L., Migalska-Zalas A., J. Opt. A: Pure Appl. Opt. 11, 1-26 (2009).

[19]   Stephens P. J., Devlin F. J., Chabalowski C. F., Frisch M. J., J. Phys. Chem. 98, 45, 11623-11627 (1994).

[20]   Tirado-Rives J., Jorgensen W. L., J. Chem. Theory Comput. 2008, 4, 297-306 (2008).

[21]   Dreuw A., Weisman J. L., Head-Gordon M., J. Chem. Phys. 119, 6, 2943-2946 (2003).

[22]   Bokareva O. S., Shibl M. F., Al-Marri M. J., Pullerits T., Kuhn O., J. Chem. Theory Comput. 13, 1, 110-116 (2007).

[23]   Iikura H., Tsuneda T., Yanai T., Hirao K., J. Chem. Phys. 115, 8, 3540-3544 (2001).

[24]   Tawada Y., Tsuneda T., Yanagisawa S., J. Chem. Phys. 120, 18, 8425-8433 (2004).

[25]   Tsuneda T., Song J.-W., Suzuki S., Hirao K., J. Chem. Phys. 133, 174101-17410 (2010).

[26]   Yanai T., Tew D. P., Handy N. C., Chem. Phys. Lett. 393, 51-57 (2004).

[27]   Rapaport D. C., The art of molecular dynamics simulation, Cambridge University Press, Cambridge 2004.

[28]   Pang T., An introduction to computational physics, Cambridge University Press, Cambridge 2006.

[29]   Verlet L., Phys. Rev. 159, 98 (1967).

[30]   Hockney R. W., Meth. Compu. Phys. 20, 135 (1970).

[31]   Beeman D., J. Comput. Phys. 20, 130 (1976).

[32]   Ladd A. J. C., Litovitz T. A., Clarke J. H. R., Woodcock L. C., J. Chem. Phys. 72, 1759 (1980).

[33]   Clarke J. H. R., Woodcock L. V., Chem. Phys. Lett. 78, 121 (1981).

[34]   Teboul V., Chaussedent S., Comp. Phys. Commun. 105, 151 (1997).

[35]   Beck D. A. C., Armebt S. R., Daggett V., Biochemistry, 44, 609 (2005).

Chapter 5

Thesis of work and hypotheses

Nonlinear optics attracts attention because of its versatile applications in many areas of life. The materials used for non-linear optical (NLO) purposes are still changing over time and the researchers constantly are looking for new materials. At a present time, the most studied are organic chromophores embedded into host polymer thin films creating *guest-host* composites. However, preparing a *guest-host* composite material is not so easy. The preparation of this kind of material induces several problems, such as the concentration of chromophores in the matrix as well as the degree of their order, which is especially important for second-order NLO phenomena. To resolve the technological problems of synthesis the appropriate type of matrix should be chosen, whose structural properties, thermodynamic and electric parameters are beneficial for the used chromophores.

To create composite NLO materials important is knowledge of the nature of intermolecular interactions occurring between components of the system and in particular their structural stability. The NLO properties of composites depend

primarily on the optical properties of components, and their spatial distribution in the polymeric matrix.

Synthesis of the thin-film composite materials is time-consuming and it is a method based on trial and error in selecting components. The computer simulations can help to find appropriate polymer matrices for the chosen chromophores but the methodology of the quantitative calculations should be implemented. In the present work, the theoretical study of composites with the physical explanation of their optical properties and optical phenomena occurring in the polymer host materials and organic guest NLO active molecules are presented. The obtained results will be compared with experimentally obtained data

Therefore, the thesis of the work was proposed as follows:

The environmental impacts on the organic chromophores embedded in a polymeric matrix forming thin-film composites change their electron and optical features.

Performed work aimed to develop a universal model and methodology of proceedings to predict the macroscopic optical properties of *guest-host* composites materials in thin-film forms.

To verify the correctness of the proposed methodology the following hypothesis were required to be verified:

1. *The polymer matrix changes the electronic parameters of the chromophores affecting the optical properties of the composite material.*

2. *The polymeric matrix affects the electron properties of polar chromophores more efficiently than molecules with a small electric dipole moment.*

3. *The optical properties of composites depend on the structural arrangement of chromophores and polymer chains.*

4. *Discrete local field model can be used to describe the linear and nonlinear optical properties of thin-film composite materials.*

Chapter 6

Investigated materials

The presented work concerns experimental and computational investigations of optical properties of composite materials based on polymer matrix and nonlinear optical (NLO) active chromophores. The samples are synthesized as thin-film systems.

6.1. Organic dyes

There are two types of colorants: dyes, and pigments. A dye is an organic substance that can react with the medium in which it is located. The pigment is an opaque coloring substance, most often mineral and insoluble but dyes are usually soluble in water. The color of a dye is dependent upon the ability of the substance to absorb light within the visible region of the electromagnetic spectra (400-700 mn). This theory is based on an electronic structure stating that the color in dyes is due to the excitation of valence π-electrons by visible light. Dyes are divided into two groups: natural and synthetic dyes. The first synthetic dye, called Mauveine

after its mauve color, was discovered in 1856 by Willian Henry Perkin. 1856 was the start of synthetic dyes and organic chemistry in general. Thousands of dyes were synthesized within a few decades.

In physical chemistry, the term chromophore is often used in addition to the term dye. A chromophore is an atom, ion, molecule, or other chemical entity within which or in which electronic transitions corresponding to the spectral band take place. In summarizing one can say that chromophore is the part of a molecule responsible for its color. The atoms of the chromophore system contribute to the absorption of visible and ultraviolet light. Famous organic chromophores are azobenzenes and their derivatives due to their special properties, such as good stability, low flammability, bright colors, and rapid, reversible photoisomerization. Azobenzene can exist in both the trans and cis conformation [1]. The nitro group (-NO2) is commonly designed as an electron acceptor in a push-pull system. It has been widely considered like a strong electron-acceptor group and could be used as a precursor for azo dyes. These nitro-containing dyes can be characterized by spectroscopic aspects such as strong emission solvatochromism due to the gigantic change of the dipole moment between ground and excited states. Many chromophores incorporate NO_2 moiety as such imidazole, diimidazole, benzimidazole, nitroaniline, diaminomaleonitrile (DAMN), and triarylimidazoles [2]. The structure of chromophore groups can be defined as a) azobenzenes containing –N=N– group, b) stilbenes with >C=C< bond, and c) azomethines containing –CH=N– group. Azobenzene derivatives containing –N=N– (azo) chromophore group undergo a reversible trans-cis-trans photoisomerization cycle. The UV-vis absorption characteristic is near $\lambda_{max} \sim 440$ nm assigned to the n→π* transition or S1 excited state and at $\lambda_{max} \sim 340$ nm connected to the π→π* transition or S2 excited state. It is well known that most azobenzenes isomerize and exhibit the photo-orientation effect and the azobenzene molecules mainly absorb light polarized along the long axis of the molecule.

In nonlinear optics, a chromophore is often called a molecule that is NLO active. The typical design of second-order NLO chromophores also called linear push-pull design, is based on a conjugated π-electron system asymmetrically substituted by an electron-donor (D) and electron acceptor (A) group. Organic push-pull materials have been subject to intensive research due to their potential in various optoelectronic applications. In such a molecular system, efficient

intramolecular charge transfer (ICT) occurs from the donor to the acceptor leading to the polarization of the molecule (see Fig. 6.1). The ICT can easily be illustrated by two limiting resonance forms (neutral and zwitterionic form). The NLO response is maximum when the contribution of the two forms is optimized. In push-pull molecules, ICT can easily be tuned by changing various parameters: the nature of the donor/acceptor couple and the π-conjugated spacer. Another way to increase the ICT is the incorporation of pro-aromatic moieties capable of gaining aromaticity. Commonly used acceptors are the following functional groups: nitro ($-NO_2$), nitrile ($-CN$), as well as sulfonic ($-SO_3H$), aldehyde ($-CHO$), phosphonate ($-POR_1R_2$), and triflyl (CF_3SO_2) groups. Examples of common donor groups are hydroxyl ($-OH$), amino ($-NH_2$), and dimethylamino ($-N(CH_3)_2$).
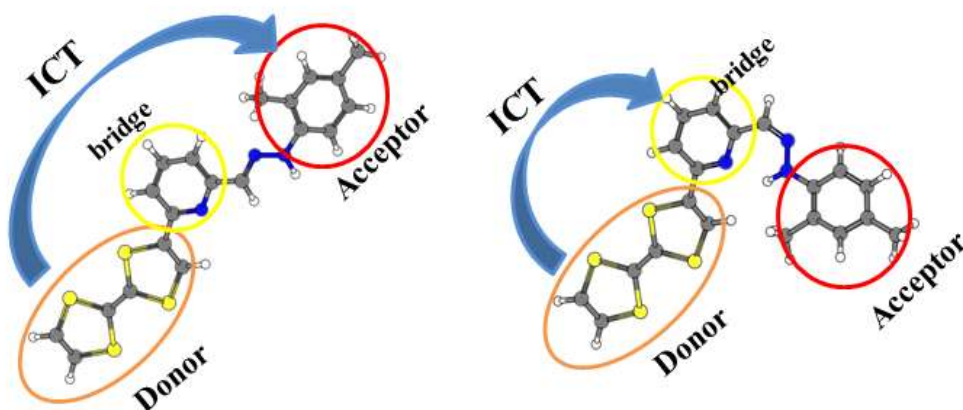
Figure 6.1. Intramolecular charge transfer process between donor and acceptor groups connected by a π-conjugated bridge.

The group of Leu W. C. W. described the synthesis and characterization of "push-pull macrocycles": electron-rich and electron-poor moieties linked by a pair of (matched) conjugated bridges [3]. Another study [4] reported three conjugated chromophores in which the π-conjugated bridge between identical donor and acceptor functionalities is systematically elongated with the sequential introduction of p-phenylenevinylene units. They investigated the effect of an increasing conjugation between the two donor and acceptor ends of the chromophores. They confirm the dependence that the molecular dipole moment gradually increases according to the increasing extension of the π-conjugated bridge. Their study explained how unexpectedly small structural changes in a class of tailorable organic

chromophores bring about opposite behavior in terms of emission in the solution/solid-state, and NLO response.

Chromophores characterized by D-π-A design are also typical of second-order NLO molecules displaying frequency-mixing processes, in particular, second harmonic generation (SHG) is used to make green 532 nm lasers from a 1064 nm source, for terahertz wave generation or second/third harmonic microscopy [5]. The NLO response is directly related to the extent of the ICT occurring in the D-π-A molecular structure. The electrons forming the π-type bond are delocalized and have significant kinetic energy, which makes it possible to easily deform the electron cloud of the system. Hence, the bond structure of conjugated molecules provides an electron redistribution pathway between the donor and acceptor. This causes a disturbance in the symmetry of the distribution of the electric charge of the molecule in the ground state, which is manifested by a significant static dipole moment. Properties of dipolar chromophores can easily be tuned by modification of the donor/acceptor couple [6], optimization of the π-conjugated bridge is also a key parameter affecting the ICT [7 – 9].

Organic molecules which exhibit ICT are important building blocks for advanced optical materials. The degree of ICT character of an electronic transition significantly differs between chromophores and is affected by a nearby environment.

6.1.1. Conjugated organic push-pull dyes consisting of TTF-donor moiety

In the presented work we propose investigations of the linear and nonlinear optical properties of four tetrathiafulvalene (TTF)-appended azine derivatives, namely:

a)   2-([2,2'-bi(1,3-dithiolylidene)]-4-yl)-6-((2,4-dimethylphenyl)hydrazono) methyl)pyridine (L1),

b)   5-([2,2' –bi(1,3-dithiolylidene)]-4-yl)-2-((2,4-dimethylphenyl)hydrazono) methyl)pyridine (L2),

c)   5-([2,2'-bi(1,3-dithiolylidene)]-4-yl)-2-((2,4-dinitrophenyl)hydrazono) methyl)pyridine (L3)

d)   2-([2,2'-bi(1,3-dithioltlidene)]-4-yl)-6-((2,4-dinitrophenyl)hyrdazono)
methyl)pyridine (L4).

These molecules are presented in Fig. 6.2. and have been synthesized in Laboratory MOLTECH Anjou (France). The main driving force behind the synthesis of such molecules was discovering multifunctional molecular materials [10]. L1-L4 molecules are composed of the TTF moiety as donor part and dimethylphenylhydrazone or dinitrophenylhydrazone as acceptor separated by azine group. The great importance is the choice of the π-conjugated spacer which plays a crucial role in the efficient electron communication between the donor and the acceptor parts. These molecules have been incorporated into the host polymer thin-film composite material and their second (SHG) and third harmonic generations (THG) have been evaluated.

L1   **L2**

L3   **L4**
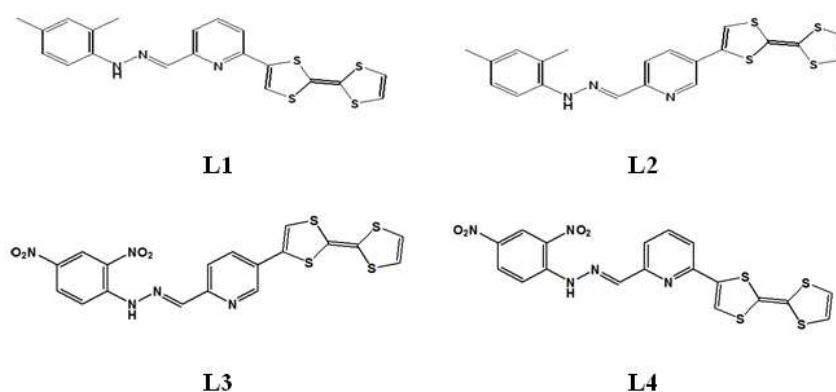
Figure 6.2. The chemical structures of four investigated tetrathiafulvalene-appended azine molecules L1, L2, L3, and L4.

The TTF moiety [11] was discovered by Wudl et al. in the early 1970s [12]. The TTF is composed of two five-membered heterocyclic rings and is characterized by strong π-π interactions as S•••S and C-H•••S interactions. TTF has advantages as follows:

1) TTF can easily be oxidized due to its low oxidation potential, offering two electrons to allow a stable state (TTF$^{+\bullet}$ and further to TTF^{2+}) [13];

2) can be gently modified by chemical tunability and the oxidation potentials may be changed by the insertion of electron donors or electron acceptors [14];

3) S•••S interactions and π-π overlap are widely located at the whole TTF moiety [15].

Charge transfer occurring in the TTF and its derivatives have been widely studied in the search for molecular conductors and superconductors. Wartelle el. all. [16] performed experimental and theoretical studies of the TTF group (see Fig. 6.3). The TTF is an appropriate heterocyclic system for its application in organic field-effect transistors (OFETs) [17]. Many of the TTF derivatives exhibit poor solubility in most organic solvents which allows aggregation of the molecules and limits their applications. Derivatives of the TTF are also used as supramolecular photoswitches [18], sensors [19], storage devices [20], radio frequency identification (RFID) tags [21], displays [22]. The TTF derivatives were developed in various morphologies, such as dendritic [23], sheet-like [24] and flower-like [25], wire-like [26], and rod-like [27] structures.
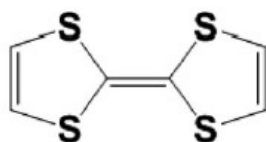
Figure 6.3. Chemical structure of TTF group.

According to the mentioned above the L1-L4 molecules were chosen to assess the effect of the position of the TTF donor part (concerning the pyridyl ring) on the NLO properties of the corresponding molecules. In addition, the presence of the pyridyl-hydrazine fragment can be used for coordinating both metal cations and inorganic anions and which could open new perspectives of optoelectronics applications and could be emerging photonic architectures.

6.1.2. Organic molecules based on benzonitrile entitled A, B, C.

Second group of investigated chromophores are molecules based on benzonitrile moiety, namely:

a) (Z)-4-(1-cyano-2-(5-methylfuran-2-yl)vinyl)benzonitrile (molecule A),

b) (Z)-4-(2-(benzofuran-2-yl)-1-cyanovinyl)benzonitrile (molecule B),

c) (Z)-4-(2-(4-(9H-carbazol-9-yl)phenyl)-1-cyanovinyl)benzonitrile (molecule C).

The structures of these molecules are presented in Figure 6.4. Benzonitrile and its derivatives [28] are widely studied due to their interesting biochemical and physical properties. Benzonitrile is a mono-substituted benzene derivative with a large dipole moment (4.18 D). The benzonitrile and its derivatives can be used in the manufacturing of polymers, anhydrous metallic salts, and intermediates for pharmaceuticals, agrochemicals, pesticides, and other organic chemicals [29]. Benzonitrile contains different binding sites for its interaction with the metal surface, because of an aromatic ring, the π bond of the CN group, and lone pair electrons of the nitrogen atom [30].

Compound **A**

Compound **B**

Compound **C**
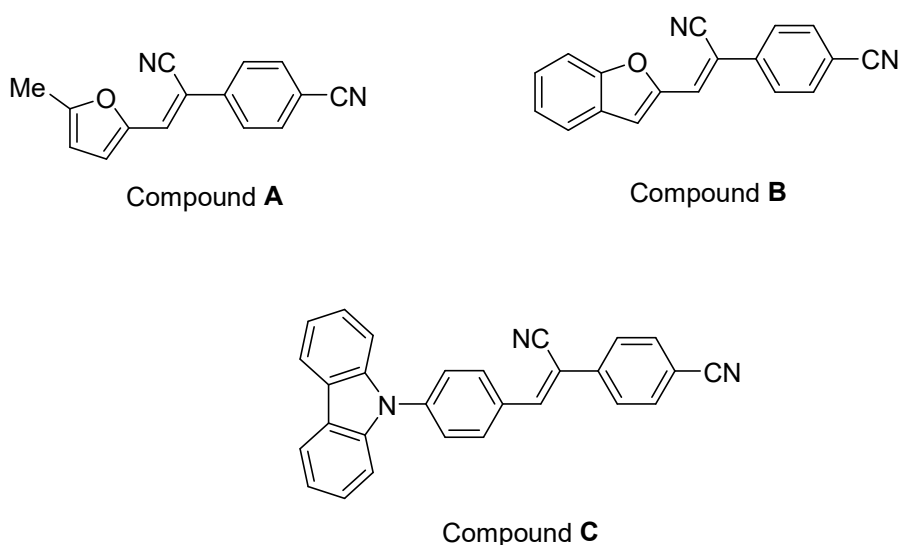
Figure 6. 3. Structures of investigated benzonitrile derivatives named A, B, and C.

Synthesis of NLO materials based on benzonitrile connected through the CN group to the silver atoms shows that they can be used for potential optical applications such as light-emitting diodes and other photonic applications [31]. Other benzonitrile derivatives were applied in OLEDs based on thermally active delayed fluorescence (TADF) [32]. Benzonitrile connected to chlorine in the structure of 3-chlorobenzonitrile or 4-chrolobenzonitrile is used for inhibition of hydrogen absorption [33]. The p-fluronitrobenzenes are commonly used in pharmaceutical products because fluorine can greatly increase the solubility of molecules. It increases the bioavailability of the molecules which is especially important in pharmaceutical products [34]. Last but not least, benzonitrile derivatives have been used as corrosion inhibitors for mild steel. The compound having nitrile group as the substituents are known corrosion inhibitors [35].

In the molecules A, B, and C, investigated in the presented work, the benzonitrile group acts as the acceptor moiety attached to the donor part of molecules through the cyano-vinyl chain. In molecules A and B, the donor is presented by the furan and benzofuran moiety, respectively, and molecule C is composed of the carbazole group. Furan is a heterocyclic organic compound, consisting of a five-membered aromatic ring with four carbons and one oxygen atom. Furan and its derivatives have been extensively studied [36 – 39]. The aromatic properties of the furan ring result from its orbital planar structure. Each carbon provides a single electron in its p orbital while the oxygen atom has electron pairs in p and sp^2 orbitals. The electrons in the p orbital system create delocalized π-electrons giving an aromatic character to the furan ring.

The carbazole is an organic compound with a tricyclic structure that consists of two six-membered benzene rings fused on either five-membered nitrogen-containing ring. Carbazole is famous for its charge transfer functionality and plays an important role in the chromophore [40,41].

6.2.   Composite *guest-host* materials based on polymer matrix

Composites, as materials consisting of two or more components, have physical and chemical properties of the materials that are impossible to achieve for a single ingredient. As materials with wide technological and electronic possibilities, composites have already found wide application in modern technology and their further dynamic development is expected. In the presented work, composites based on polymer matrix in the form of *guest-host* materials were investigated. The host polymers should be characterized by good mechanical strength, thermal stability, high glass transition temperature, and transparency for visible light.

The physical properties of composite materials are dependent on the features of their compounds, especially in the optical domain. The intensity of the SHG signal depends not only on the hyperpolarizability of the chromophores but also on the mobility of the structural groups of the polymer, the efficiency of the molecular ordering process, and the stability of the composite system. In the presented work two polymers were chosen as the matrix of composite systems. The first is poly

(methyl methacrylate) (PMMA), and the second one is polyvinyl carbazole (PVK). Their chemical structures are presented in Fig. 6.5.
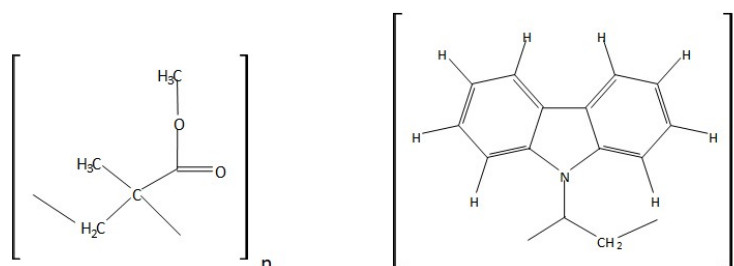
Figure 6.4. Schematic representation of the PVK (left) and PMMA (right) monomer.

The PMMA belongs to the group of typical amorphous, polar polymers. Structural properties and dynamic behavior of PMMA were widely investigated versus pressures and temperatures [42]. The basic characterization of PMMA e.g.: size, shape, and orientation as well as the chain rigidity have been investigated by fully atomistic molecular dynamics [43]. The PMMA polymer is perhaps the most commonly used host material in the preparation of optically active thin films [44]. Its advantages are low cost and the high laser damage threshold. Additionally, PMMA-based thin films can be easily tailored to achieve specific experimental needs [45].

A lot of interest in PVK polymer has been caused by the discovery of photoconductivity in poly(vinyl carbazole) by H. Hoegl [46]. In 1957, was shown that PVK doped with a suitable electron acceptor occurs high photoconductivity that can be useful in practical applications [47]. For the first time in 1970, was used the charge transfer organic photoconductor of PVK with 2,4,7-trinitrofluorenone (TNF) [48]. Additionally, the great interest in carbazole-containing polymers is related to the discovery of organic photorefractive materials and polymeric light-emitting diodes [49]. Compounds based on carbazole are attractive as photoconductors or charge-transporting materials [50]. Conductive polymers are commonly used in optical applications, due to their advantages e.g.: an opportunity to work at room temperature, easiness of manufacturing, and low cost of their synthesis [51,52]. PVK is a thermoplastic material having high dielectric properties and a heat distortion point of up to 150° C [53]. The PVK is frequently used as a

host material with nanocomposites [54, 55], as well as with organic chromophores [56].

Polymer matrices affect the electronic and optical properties of guest molecules. Sometimes they can completely strip the chromophores of their NLO properties. In the presented work the *guest-host* composites were investigated according to their linear and nonlinear optical properties. They were studied experimentally and computationally. The composites were synthesized in the form of thin films. Computationally they were modeled in bulk (volumetric) form and also as thin films.

Studied composite materials consist of mentioned two groups of chromophores and two different polymeric matrixes. The optical properties of the following composite systems were investigated in the presented work:

- ✓ L1/PMMA, L2/PMMA, L3/PMMA, L4/PMMA,
- ✓ A/PMMA, B/PMMA, C/PMMA,
- ✓ A/PVK, B/PVK, C/PVK.

References

[1]   Wei Y., Tang Q., Gong Ch., Lam M. H-W., Anal. Chim. Acta 900, 10-20 (2015).

[2]   Kulhanek J., Bures F., Beilstein J. Org. Chem. 8, 25-49 (2012).

[3]   Leu, W. C. W., Fritz, A. E., Digianantonio, K. M., Hartley, C. S., J. Org. Chem. 77, 5, 2285-2298 (2012).

[4]   Coluccini, C., Sharma, A. K., Caricato, M., Sironi, A., Cariati, E., Righetto, S., Tordin, E., Botta, Ch., Forni, A., Pasini, D., Phys. Chem. Chem. Phys., 15, 1666 (2013).

[5]   Thomas G., Voskuilen J. V., Gerritsen H. C., Sterenborg H. J. C. M., J. Photochem. Photobiol. B Biol., 141, 128 (2014).

[6]   Moreno-Yruela C., Garín J., Orduna S., Quintero E., Navarrete J. T. Lopez, Diosdado B. E., Villacampa B., Casado J., Andreu R., J. Org. Chem. 80, 12115 (2015).

[7]   Bureš F., Schweizer W. B., May J. C., Boudon C., Gisselbrecht J. P., Gross
        M., Biaggio I., Diederich F., Chem. Eur. J., 13, 5378 (2007).

[8]   Forster, V. T., Naturforsch, 4a 321 (1949).

[9]   Tang C. W., VanSlyke S. A., Appl. Phys. Lett. 51, 913-915 (1987).

[10]   Clemente-Leon M., Coronado E., Gomez-Garcia C. J., Matrinez-Ferrero E.,
        Journal of cluster sience 13, 381-407 (2002).

[11]   Mohamud S., Phuoc V. T., Campo L. D., Massa N. E., Pagola S., Synth.
        Met. 214, 71-75 (2016).

[12]   Wudl F., Smith G. M., Hufnagel E. J., J. Chem. Soc. Commun. 1453-1454
        (1970).

[13]   Adeel S., Abdelhamid E., Nafady A., Li Q., Martin L. L., Bond A. M., RSC
        Adv. 5, 18384 (2015).

[14]   Nielsen M. B., Sauer S. P. A., Chem. Phys. Lett. 453, 136-139 (2008).

[15]   Azov V. A., Gomez R., Stelten J., Tetrahedron 64, 1909-1917 (2008).

[16]   Wartelle C., Viruela R., Viruela P. M., Sauvage, F. X., Salle M., Orti E.,
        Levillain E., Le Derf F., Phys. Chem. Chem. Phys. 5 4672-4679 (2003).

[17]   Jiang H., Yang X., Cui Z., Liu Y., Li H., Hu W., Kloc Ch., Cryst. Eng.
        Comm. 16 5968 (2014).

[18]   Feng, Y., Zhang Q., Tan W., Zhang D., Tu Y., Agren H., Tian H., Chem.
        Phys. Lett. 455, 256-260 (2008).

[19]   Garcia-Pineda I., Mayen M., Rodriguez-Mellado J. M., Rodriguez-Amaro
        R., Application as amperometric sensor, Electroanalysis 25 1981-1987
        (2013).

[20]   Xu, J., Li F., Tian Ch., Song Z., An Q., Wang J., Han D., Niu L., Electa.
        Acta. 322, 134683 (2019).

[21]   Xu H., Lin G., Zhao S., Liang Y., Xiao X., Xu W., Zhu D., Synth. Met. 219,
        154-157 (2016).

[22] Mishra S., Yogi P., Saxena S. K., Roy S., Sagdeo P. R., Kumar R., J. Mater. Chem. C, 5, 9504-9512 (2017).

[23] Kimura H., Konishi K., Muraoka S., Shirahata T., Misaki Y., Chem. Lett. 43, 843-845 (2014).

[24] Ueda A., Mori H., Mater. Chem. Front. 2, 566-572 (2018).

[25] Lyskawa J., Canever D., Allain M., Salle M., Tetra. Lett. 51, 5868-5872 (2010).

[26] Sorensen J. K., Vestergaard M., Kadziola A., Kilsa K., Nielsen M. B., Org. Lett. 8, 1173-1176 (2006).

[27] Frenzel S., Baumgarten M., Mullen K., Synth. Met. 118, 97-103 (2001).

[28] Yilmaz E., J. of Mol. Struc. 1166, 407-415 (2018).

[29] Krishnan A. R., Saleem H., Subashchandrabose S., Sundaraganesan N., Sebastain S., Spectrochimica Acta Part A 78, 582-589 (2011).

[30] Fleming G. D., Golsio I., Aracena A., Celis F., Vera L., Koch R., Campos-Vallette M., Spectrochimica Acta Part A 71, 1049-1055 (2008).

[31] John J. S., Sajan D., Narayana Ch., Sundius T., Optics and Laser Technology 107, 454-467 (2018).

[32] Tanaka Y., Takahashi T., Nishide J., Hiraga Y., Nakanotani H., Adachi Ch., Thin Solid Films 619, 120-124 (2016).

[33] Palafox M. A., Rastogi V. K., Mittal L., Int. J. Quant. Chem. 94, 189 (2003).

[34] Udayakumar V., Periandy S., Karabacak M., Ramalingam S., Spectrochimica Acta Part A 83, 575-586 (2011).

[35] Chaouiki A., Lgaz H., Chung I.-M., Ali I. H., Gaonkar S. L., Bhat K. S., Salghi R., Oudda H., Khan M. I., J. of Mol. Liq. 266, 603-616 (2018).

[36] Gandini A., Coelha D., Gomes M., Reis B., Silvestre A., J. Mater. Chem. 19, 8656-8664 (2009).

[37]   Guthrie G. B. Jr., Scott D. W., Hubbard W. N., Katz C., McCullough J. P., Gross M. E., Williamson K. D., Waddington G., J. Am. Chem. Soc. 18, 4662-4669 (1952).

[38]   Brown R. C. D., Angew. Chem. Int. Ed. 44, 850-852 (2005).

[39]   Bak B., Christensen D., Dixon W. B., Hansen-Nygaard L., Andersen J. R., Schottlander M., J. of Mol. Spect. 9, 124-129 (1962).

[40]   Zhang Y., Wada T., Sasabe H., J. Mater. Chem. 8, 809-828 (1998).

[41]   Chen Ch., Chi Z., Chong K. Ch., Batsanov A. S., Yang Z., Mao Z., Yang Z., Liu B., Nat. Mater. 20, 175-180 (2021).

[42]   Shtarkman B. P., Minich I. M., Arzhakov S. A., Averbakh N. Yu., Vysokomol. Soyed. A18, 5, 1047-1052 (1976).

[43]   Frohlich M. G., Zifferer G., Macromol. Theory Simul. 20, 399-410 (2011).

[44]   Essaidi Z., Niziol J., Sahraoui B., Opt. Mat. 33, 1387-1390 (2011).

[45]   Derkowska-Zielinska B., Skowronski L., Biitseva A., Grabowski A., Naparty M. K., Appl. Sur. Scien. 421, 361-366 (2017).

[46]   Hoegl H., J. Phys. Chem. 69,3,755-766 (1965).

[47]   Yamashita K., Suzuki T., Hino T., Jpn. J. Appl. Phys. 21, 1506-1508 (1982).

[48]   Weiser G., J. Appl. Phys. 43, 5028-5033, (1972).

[49]   Burroughes J. H., Bradley D. D. C., Brown A. R., Marks R. N., Mackay K., Friend R. H., Burns P. L., Holmes A. B., Nature 347, 539-541 (1990).

[50]   Kruglenko I. V., Quantum Electronics & Optoelectronics 19, 427-429 (2016).

[51]   Lin C. W., Hwang B. J., Lee C. R., J. Appl. Polym. Sci. 73, 2079-2087 (1999).

[52]   Gallazzi M. C., Tassoni L., Bertarelli C., Pioggia G., Di Francesco F., Montoneri E., Sensors ans Actuators B, 88, 178-189 (2003).

[53]   Buss W. F., Lambert J. M., McKinley C., Davidson H. R., Ind. Eng. Chem. 40, 2271-2275 (1948).

[54]   Tyutnev A. P., Saenko V. S., Pozhidaev E. D., Kolesnikov V. A., J. Phys.: Condens. Matter, 18, 6365-6377 (2006).

[55]   Wang S., Yang S., Yang Ch., Li Z., Wang J., Ge W., J. Phys. Chem. B 104, 11853-11858 (2000).

[56]   Saidi H., Aloui W., Dhifaoui H., Bouazizi A., Boubaker T., J. of Mat. Scien.: Materials in Electronics 30, 10808-10813 (2019).

Chapter 7

Investigations of the physical properties of TTF-based composite materials

The applied nonlinear optical (NLO) active materials based on organic chromophores generally are prepared as thin films. The NLO molecules are embedded into a polymer matrix. Then, by the corona-poling method, the chromophores are aligned applying the external electric field and solidified to obtain dipolar ordered material, useful for second-order NLO applications.

In this chapter, the structural, electron, and optical properties of selected TTF-based chromophores will be presented. They were calculated using quantum chemical methods. Also, the *guest-host* materials based on TTF derivatives and the PMMA polymer were synthesized and their optical properties were investigated experimentally. Because the experimentally obtained data cannot be directly compared to the computational results predicted for the isolated molecule a new

approach to modeling the optical properties of solids was developed. It should be clearly stated that a polymer matrix can change the electronic properties of the chromophores affecting their optical properties. To explain the mechanism of the NLO signal occurrence from the TTF-derivatives/PMMA composites their structures will be modeled using MD techniques. In consequence, the structural properties of the composites are discussed.

Developing the theoretical model based on a discrete multipole local field approach will be shown how the polymer matrix changes the optical properties of the chromophores. The mentioned approach will be used to compare the linear and non-linear optical properties of chromophores in a vacuum and polymer matrix. The presented approach combines two methods, namely the MD of composites and the quantum chemical calculations of electronic properties of chromophores.

7.1. Molecular dynamic simulation of composite *guest-host* materials based on the PMMA polymer and selected TTF-derivatives

The molecular dynamics (MD) method is used in the presented work to determine the structure of the bulk and thin-film composite materials based on tetrathiafulvalene (TTF) derivatives working as guest chromophores and host poly(methyl methacrylate) polymer (PMMA).

7.1.1. Methodology and computational parameters of the MD simulations

Four new-synthesized TTF-attended azine derivatives named L1, L2, L3, and L4 were chosen to be modeled as the component of the *guest-host* composite materials. Their chemical structures are presented in Fig. 7.1. As the host material, the poly(methyl methacrylate) (PMMA) polymer was chosen. The four different composite systems were created, namely: L1/PMMA, L2/PMMA, L3/PMMA, and L4/PMMA. Because the MD is a statistical method, three different starting structures were built for each *guest-host* system using HyperChem software [1].
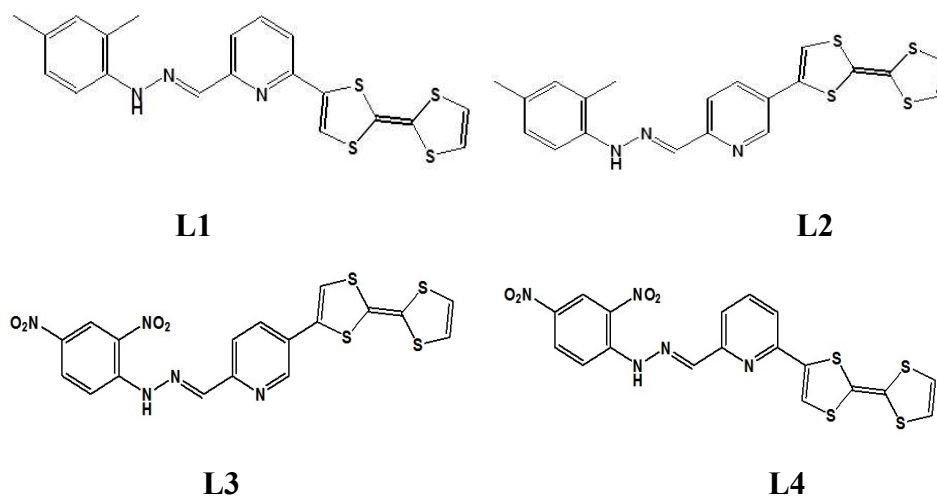
Figure 7.1. The structures of four investigated tetrathiafulvalene-attended azine derivatives named L1, L2, L3, and L4.

The unit cell of each investigated composite system consisted of two chromophore molecules and one chain of the isotactic 90-mer PMMA with a molecular weight of 9012.58 amu. Every investigated unit cell was cubic with an edge length of 24.8 Å and density equal to 1.00 g/cm^3 for all systems. The required density corresponds to the liquid state of the investigated complexes. First of all, each initial structure was optimized by two methods. First, the steepest descent algorithm employing a convergence criterion of 200 kcal mol^{-1} Å^{-1} was used, and then the procedure was continued by the conjugate gradient method with a convergence criterion equal to 50 kcal mol^{-1} Å^{-1}.

The used MD is based on solving the classical equations of motion for the time-dependent positions (and velocities) of the atoms that comprise the system under investigation. The simulations were performed using the GROMACS software [2]. The non-bonded interactions were taken into account with the Lennard-Jones 12-6 potential and a Coulomb potential based on a fixed list of charges. Bonded interactions were computed due to a fixed list of atoms. Bond stretching and bond bending were presented by harmonic potentials, whereas dihedral angle distortions were modeled by a simple cosine function. The all-atom consistent valence force field (CVFF) [3,4] was selected for the MD study.

All MD simulations were employed with the following parameters: simulation time step was 1 fs, and the short-range neighbor list was created employing the grid search method with a cut-off distance equal to 1.10 nm.

Lennard-Jones and Coulomb interactions were computed within the neighbor list employing periodic boundary conditions. The long-range interactions were calculated using the three-dimensional particle-mesh Ewald method (PME) [5,6]. The energies, coordinates, and velocities were recorded every one picosecond. The major part of the simulations was performed in the NVT canonical ensemble employing the Nose-Hoover thermostat. A simulated annealing procedure was modeled in an NPT ensemble using Rahman-Parrinello barostat to control the pressure during simulations.

The composites with optimized geometries were relaxed for 2.0 ns under NVT conditions at a temperature of 500 K. The relaxed structures reached the thermodynamic equilibrium after 1.5 ns of simulations. Then the poling external electric field was applied in the Z-direction of the laboratory coordinate system and the composites were modeled again during 2.0 ns in the NVT ensemble. The applied electric field strength for all complexes in bulk form was equal to 1, 3, 5, 10, and 15 kV/μm and was used for dipolar alignment of the chromophores. Should be noticed that the experimentally commonly-used electric field is equal to 5 kV. However, we want to achieve the equilibrated state of the modeled materials within the time scale of the performed simulations and the intensity of the used external electric field should be accordingly higher.

The composites poled at 500 K, the results of the final configurations of the low-density MD runs, were used in the simulation cooling process from 500 up to 300 K in the presence of the external poling electric field, employing the simulated annealing (SA) process. The SA is conveniently used as an optimization technique mainly well suited to overcome the multiple minima problem. During SA, molecules may cross barriers between conformational energy minima to achieve the lowest minimum. We have used the SA with the MD algorithm in the isobaric-isothermal ensemble with a protocol implemented in GROMACS where the reference temperature is varied linearly. The cooling rate was equal to 1.3×10^{11} K/s. The high-density ordered systems were simulated for 1.5 ns in NVT condition at 300 K keeping the external electric field working. This simulation was performed to obtain thermodynamically equilibrated high-density systems. Then, at the end of the simulations, the stability and back-relaxation of the chromophores in the polymer matrix were investigated. In this case, the composites were modeled during 1.5 ns in the NVT ensemble at 300 K without acting external electric field.

Three equivalent molecular complexes were created for each investigated composite to model thin films. These structures are consistent with two chromophores, respectively L1, L2, L3, or L4, and one isotactic 90-mer PMMA polymer chain in each unit cell. The simulated box of the investigated thin film was equal to 26.25 Å × 26.25 Å × 78.75 Å. Infinite extensions have been applied along the X and Y-axes and finite-length in Z-direction. The geometry of each modeled complex was optimized by energy minimization using the steepest descent algorithm with a convergence criterion of 100 kcal mol^{-1}Å^{-1} and then by conjugate gradient method employing a convergence criterion of 20 kcal mol^{-1}Å^{-1}. The MD simulations were carried out at 500 K and 300 K with a 1 fs size step. All the remaining parameters were the same as employed for the MD of bulk composites. The long-range non-bonded interactions were calculated using the 2D PME method. The values of the external poling electric field were 0.5, 1, 3, and 5 kV/μm. The systems were solidified with a cooling rate of 1.3 x 10^{11} K/s. the final density for all films was 1.173 ± 0.005 g/cm^3, corresponding to the experimental value of the glassy state of PMMA. The methodology of the MD simulations of thin films was exactly like that for bulk materials, presented above.

7.1.2. Structure of composite systems

The spatial distribution of the chromophores embedded into the polymer matrix was examined using the intermolecular radial distribution function (RDF). The RDFs were calculated between the center of mass (COM) of selected groups located at chromophores and polymer, according to the formula:

$$g_{AB}(r) = \frac{\langle \rho_B(r) \rangle}{\langle \rho_B \rangle_{loc}} = \frac{1}{\langle \rho_B \rangle_{loc}} \frac{1}{N_A} \sum_{i \in A}^{N_A} \sum_{j \in B}^{N_B} \frac{\delta(r_{ij} - r)}{4\pi r^2}, \qquad (7.1)$$

where $<\rho_B(r)>$ is the density of group B at distance r around group A, and $<\rho_B>_{loc}$ is the averaged density of elements of group B around group A with the radius of half the unit cell length.

The side groups of chromophores were taken into consideration to calculate the RDFs. They are C_2H_2 atoms located on the (1,3-dithiol-2-one) group of TTF moiety and the methyl group (CH_3) from the (2,4-dimethyl phenyl) moiety of the L1 and L2 chromophores, and the nitro group (NO_2) located on the (2,4-dinitrophenyl) moiety of the L3 and L4 molecules. In PMMA mer four groups were

chosen: the *CH₂, bCH₃* (methyl group bonded to the backbone of an α-carbon atom), *sCH₃* (methyl group at the end of side group), and ***COO*** group. The location of all defined groups is presented in Fig. 7.2. The COMs of the different groups were computed for each snapshot.
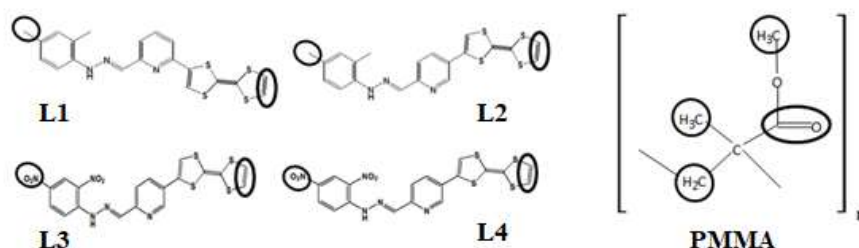
Figure 7.2. Selected groups of atoms considered in the process of RDFs construction located at L1, L2, L3, and L4 chromophores and mer of PMMA.

In Figure 7.3. the RDFs calculated for the L1 chromophore and different groups of PMMA mer are presented. In a liquid state (at 500 K) the L1 chromophores are located close to the sCH₃ and bCH₃ groups of the PMMA. The distance between the TTF group and sCH3 is equal to 0.4 nm and the distance between CH₃ groups of L1 and PMMA is equal to 0.3 nm (see Fig. 7.3 (a) and Fig. 7.3 (c)). In the glassy state (at 300 K) the TTF group of L1 is located close to the sCH₃ side groups of the polymer (see Fig. 7.3 (b)). The CH₃ groups of L1 in the glassy state are located close to the sCH₃ and bCH₃ as it is in the case of the liquid state (see Fig. 7.3 (d)). It means that the solidification of the L1/PMMA composite does not change the special location of the chromophores. The free volume around L1 chromophores has a diameter of 0.4 nm.

The RDFs calculated for the L2/PMMA composites do not have a shape that describes a well-defined position of the molecules in a polymer matrix, except for one arrangement shown in Fig. 7.4 (a). In the liquid state, the L2 molecule is located at 0.4 nm from the PMMA chain. It confirms that the polymer chain is curled with side groups outward. When the L2/PMMA composite is solidified, the CH₃ groups of L2 are the closest located to the sCH₃ groups of the PMMA chain (see Fig. 7.4 (d)).

Figure 7.3. Partial RDFs calculated for distances between the center of mass of different moieties of the L1 molecule and different subunits of PMMA at T = 500K (a,c) and T=300K (b,d) for the bulk L1/PMMA system. Panels a and c present the RDFs for C_2H_2 of L1 molecule and different subunits of PMMA mer. Panels b and d present the RDFs CH_3 of L1 and different subunits of PMMA mer.

The L3 chromophores are located closer to the PMMA chain than the L1 and L2 chromophores. In liquid (see Fig. 7.5 (a)) and in the glassy state (see Fig 7.5 (b)) the L3 molecules are inverted by the TTF group to the bCH_3 group of PMMA. This behavior is significantly visible for the system in the glassy state. There are also some examples that the NO_2 group is located close to the backbone of the polymer chain (see Fig. 7.5 (c)). It means that the L3 chromophores enter into polymer structure in the liquid state locating themselves between the mers. This is also seen in the L3 chromophores being in the glassy polymer (Fig. 7.5 (b)).
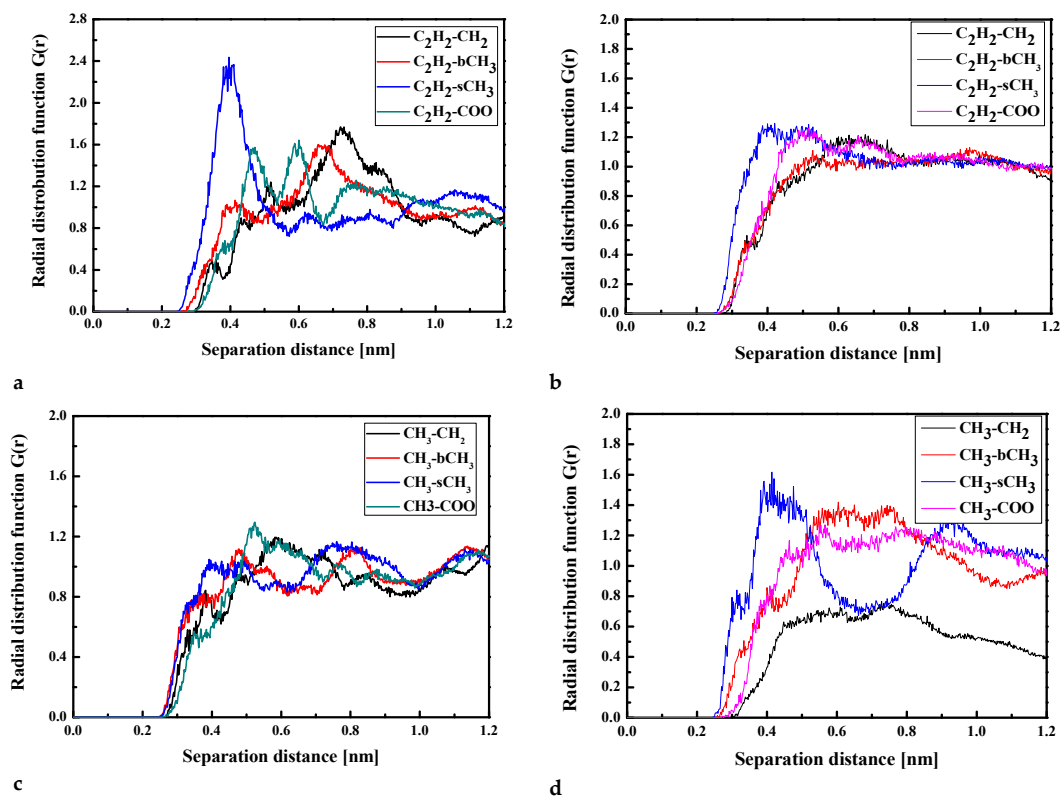
Figure 7.4. Partial RDFs calculated for distances between the center of mass of different moieties of the L2 molecule and different subunits of PMMA at T = 500K (a,c) and T=300K (b,d) for the bulk L2/PMMA system. Panels a and c present the RDFs for C_2H_2 of L2 molecule and different subunits of PMMA mer. Panels b and d present the RDFs CH_3 of L2 and different subunits of PMMA mer.
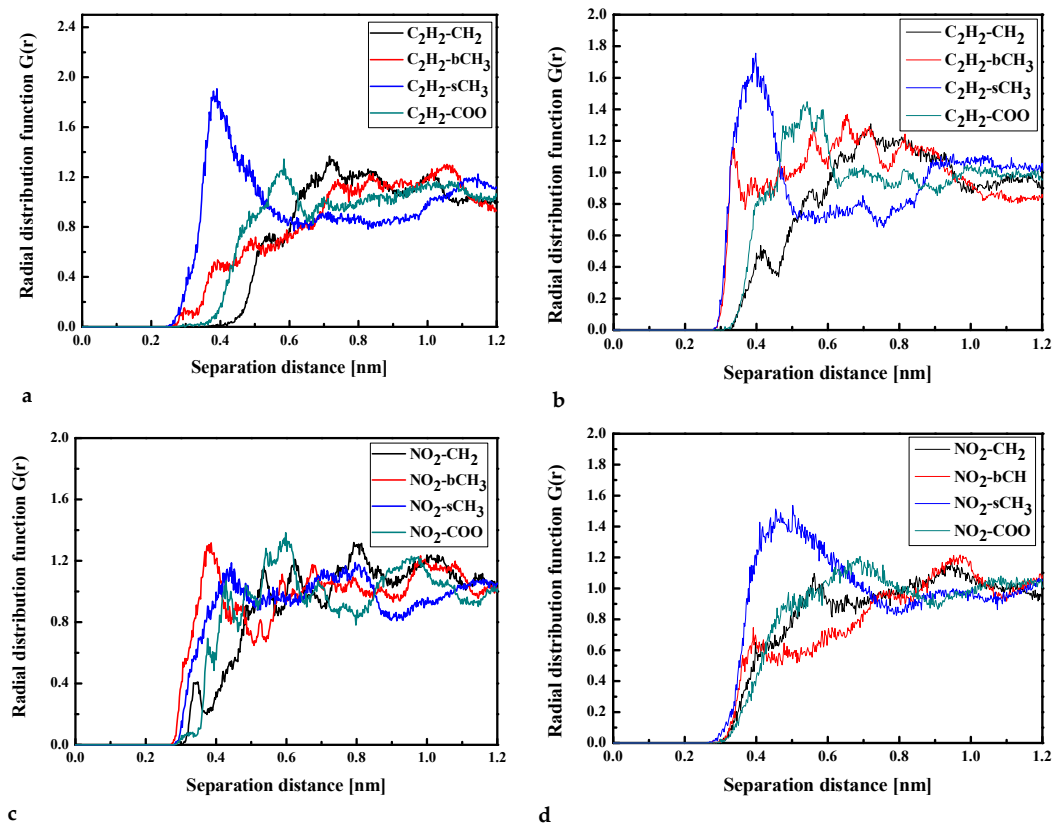
Figure 7.5. Partial RDFs calculated for distances between the center of mass of different moieties of the L3 molecule and different subunits of PMMA at T = 500K (a,c) and T=300K (b,d) for the bulk L3/PMMA system. Panels a and c present the RDFs for C_2H_2 of L3 molecule and different subunits of PMMA mer. Panels b and d present the RDFs NO_2 of L3 and different subunits of PMMA mer.

In the case of L4/PMMA composites, one can see chromophores located at 0.3 nm from the polymer chain. The TTF groups are close to the CH_2 groups of the polymer (Fig. 7.6 (a)). As was observed for the L3/PMMA structure, also here the chromophores enter into the structure of the polymer. In the glassy form of the L4/PMMA composites, their chromophores are at 0.3 nm from polymer. One can conclude that the chromophores possessing the nitro groups tend to be located closer to the PMMA chain than the chromophores with methyl groups. One was confirmed that the para-position of the TTF group on the pyridine tends to the closer location of the chromophores to a polymer chain.
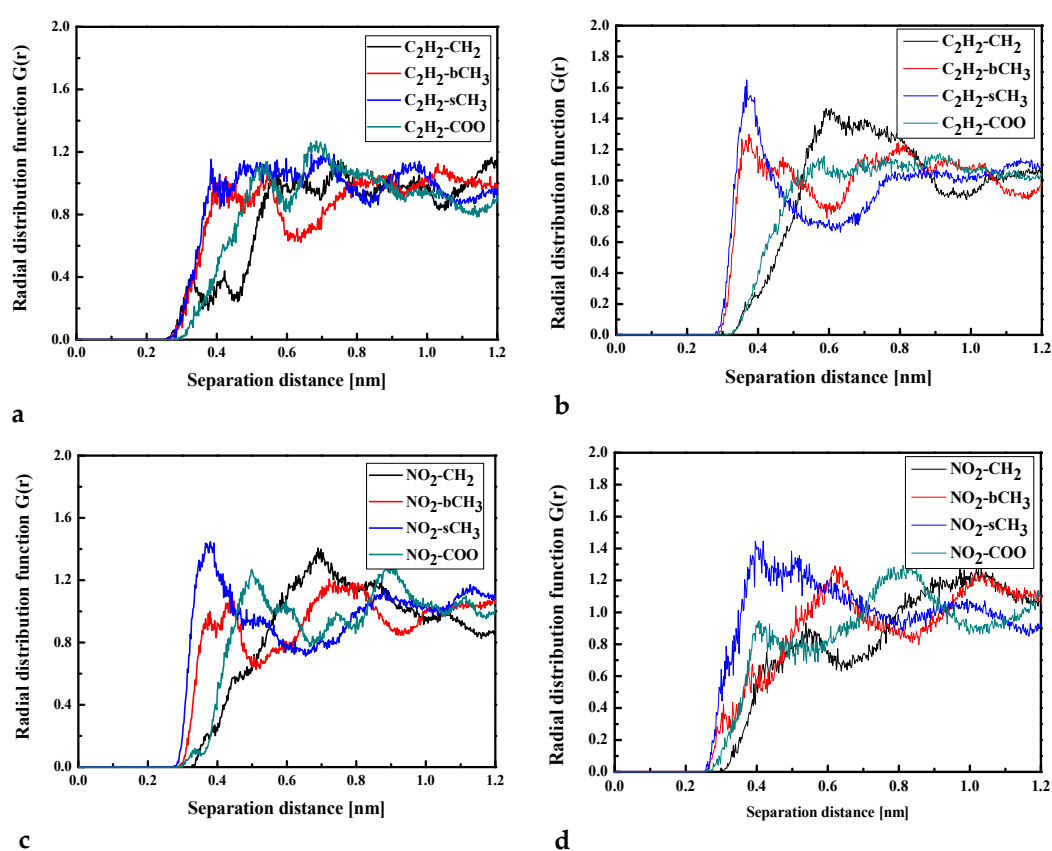
Figure 7.6. Partial RDFs calculated for distances between the center of mass of different moieties of the L4 molecule and different subunits of PMMA at T = 500K (a,c) and T=300K (b,d) for the bulk L4/PMMA system. Panels a and c present the RDFs for C_2H_2 of L4 molecule and different subunits of PMMA mer. Panels b and d present the RDFs NO_2 of L4 and different subunits of PMMA mer.

The RDFs created for the L1/PMMA system in the thin-film form are presented in Fig. 7.7. One may see that the distance between C_2H_2 and bCH_3 groups calculated for the film at 500 K is higher than it was observed for the bulk system (see Fig. 7.3.). In liquid and solid-state, the mentioned distance is equal to 0.4 nm

(see Fig 7.7 (a) and 7.7 (b)). Distances between CH_3 groups of the L1 and the selected groups of PMMA are not well defined (the peaks are broad). It means that the 2,4-dimethyl phenyl groups of the L1 molecules are very mobile when the thin-film system is in a liquid state. When the system is in solid-state both sides of chromophores are at 0.4 nm from the sCH_3 group of PMMA (see Fig. 7.7 (d)).
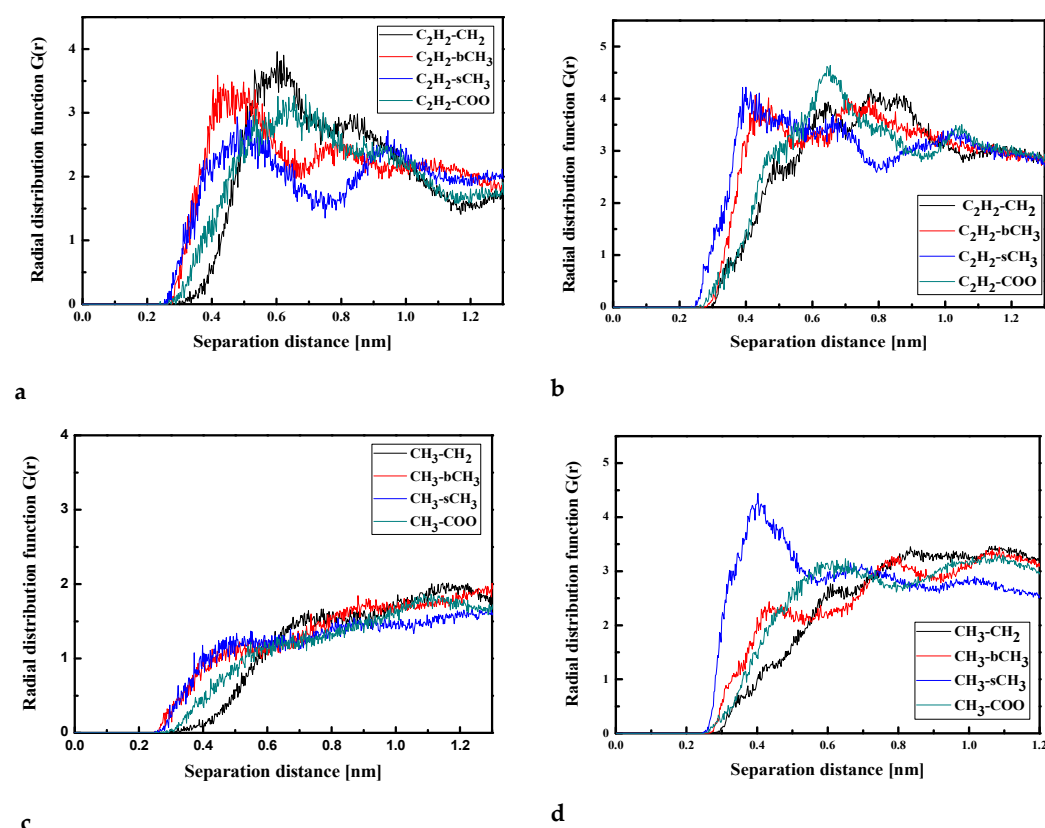
Figure 7.7. Partial RDFs calculated for distances between the center of mass of different moieties of the L1 molecule and different subunits of PMMA at T = 500K (a,c) and T=300K (b,d) for the thin film L1/PMMA system. Panels a and c present the RDFs for C_2H_2 of L1 molecule and different subunits of PMMA mer. Panels b and d present the RDFs CH_3 of L1 and different subunits of PMMA mer.

The L2 molecules in bulk PMMA were close to the chain of the polymer. It is seen by the distance between CH_2 of PMMA and C_2H_2 of the L2 equal to 0.3 nm (see Fig 7.4 (a)). In the thin film, the TTF group of the L2 is the closest (0.4 nm) to the sCH_3 groups of PMMA (see Fig. 7.8 (a)). When the thin film is solidified (Fig. 7.8 (b)) the TTF group of the L2 molecule is entering into a twisted polymer chain. In this case distance between the C_2H_2 of the L2 and all selected groups of PMMA is the same and equal to 0.4 nm. The opposite side of the L2 molecule (the 2,4-

dimethyl phenyl group) is also located the closest to the sCH$_3$ group (at 0.4 nm). It means that the L2 molecule is turned by the TTF group into the polymer chain.
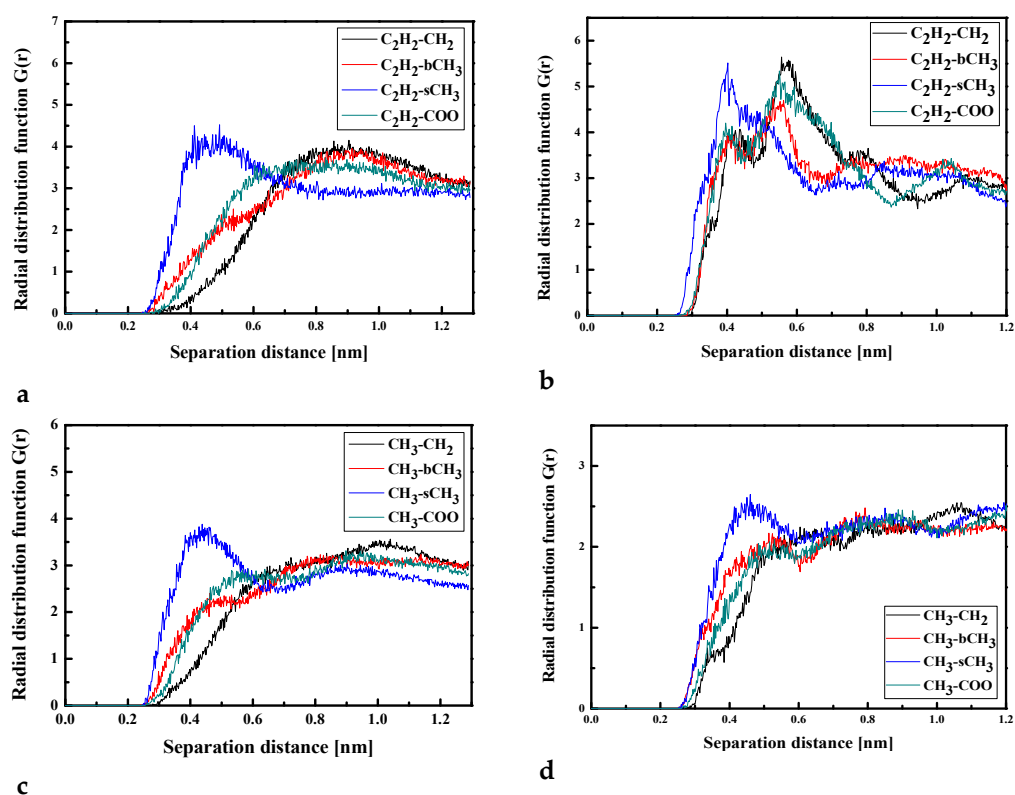
Figure 7.8. Partial RDFs calculated for distances between the center of mass of different moieties of the L2 molecule and different subunits of PMMA at T = 500K (a,c) and T=300K (b,d) for the thin film L2/PMMA system. Panels a and c present the RDFs for C$_2$H$_2$ of L2 molecule and different subunits of PMMA mer. Panels b and d present the RDFs CH$_3$ of L2 and different subunits of PMMA mer.

The RDFs of the L3/PMMA system are presented in Fig. 7.9. The TTF group is at the distance of 0.4 nm from the sCH$_3$ and bCH$_3$ of PMMA in a liquid state. The solidification does not change this behavior for the NO$_2$ group but the TTF group is the closest to the sCH$_3$ group of PMMA (see Fig. 7.9 (b) and 7.9 (d)). Distances between all mentioned groups of the L3 and polymer are equal to 0.4 nm. It means that the polymer chain is not significantly twisted at the surface of the L3/PMMA thin-film system.
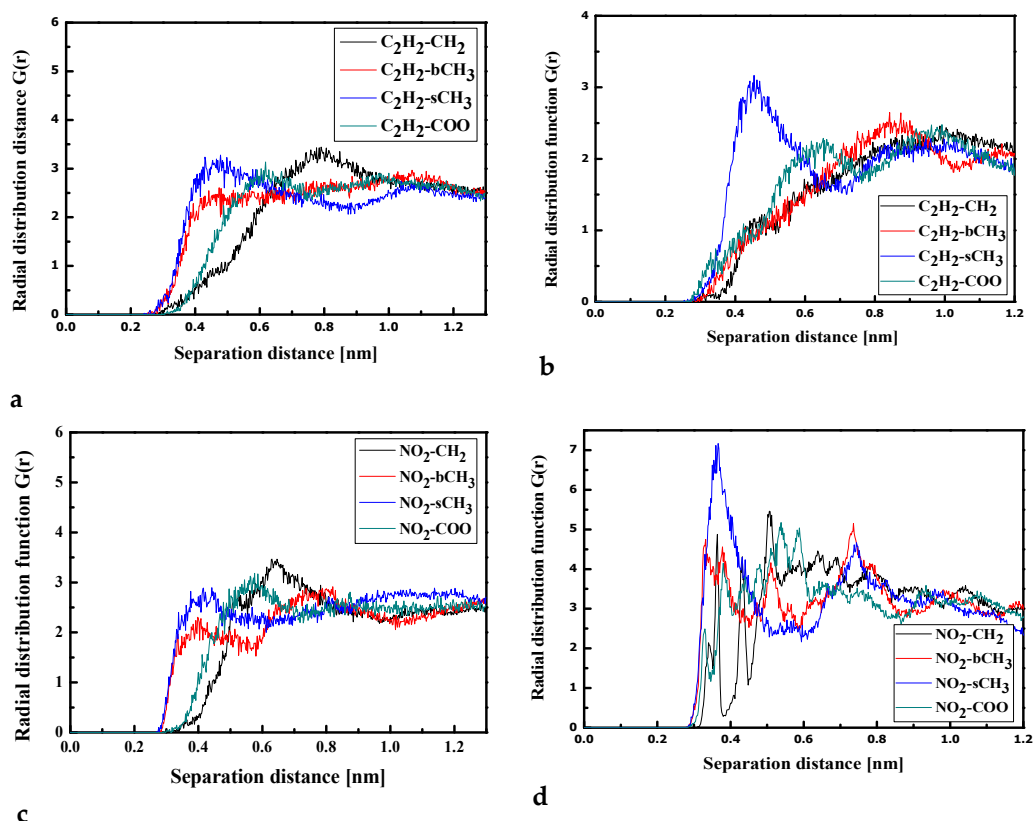
Figure 7.9 Partial RDFs calculated for distances between the center of mass of different moieties of the L3 molecule and different subunits of PMMA at T = 500K (a,c) and T=300K (b,d) for the thin film L3/PMMA system. Panels a and c present the RDFs for C_2H_2 of L3 molecule and different subunits of PMMA mer. Panels b and d present the RDFs CH_3 of L3 and different subunits of PMMA mer.

The L4 chromophore is located close to the sCH3 group of the polymer (see Fig. 7.10). It is true for the liquid and solid state of the thin film of the L4/PMMA composite. For the liquid and glassy state of the L4/PMMA a small peak appears for the distance between bCH_3 and NO_2 groups (see Fig. 7.10 (c) and 7.10 (d)).

Analyzing the data presented in this paragraph one may conclude that around chromophores embedded into the PMMA matrix the free volume is created. Generally, the distance between PMMA and the L1, L2, L3, and L4 chromophores is equal to 0.4 nm but in some cases, the distance can be equal to 0.3 nm. Mostly in investigated bulk *guest-host* systems, the distance between chromophores and the sCH3 group of PMMA is equal to 0.3 nm. Additionally, the L3 and L4 molecules locate themselves close to the bCH_3 groups of PMMA. It means that the chromophores enter into the structure of the polymer chain.

The investigated composites are less dense at the surface than it is observed in the bulk material. The investigated distances are equal to 0.4 nm for almost all

discussed cases. It will influence the reorientation of chromophores in the polymer matrix caused by the external electric field that is described in the next paragraph.
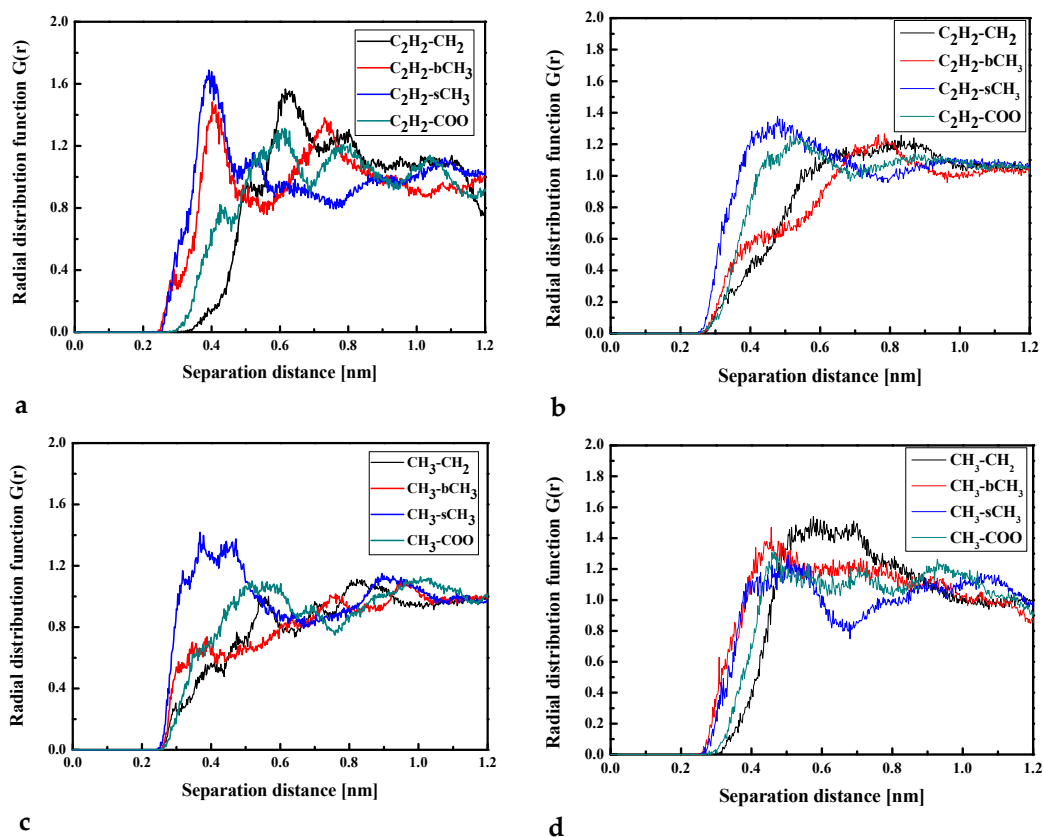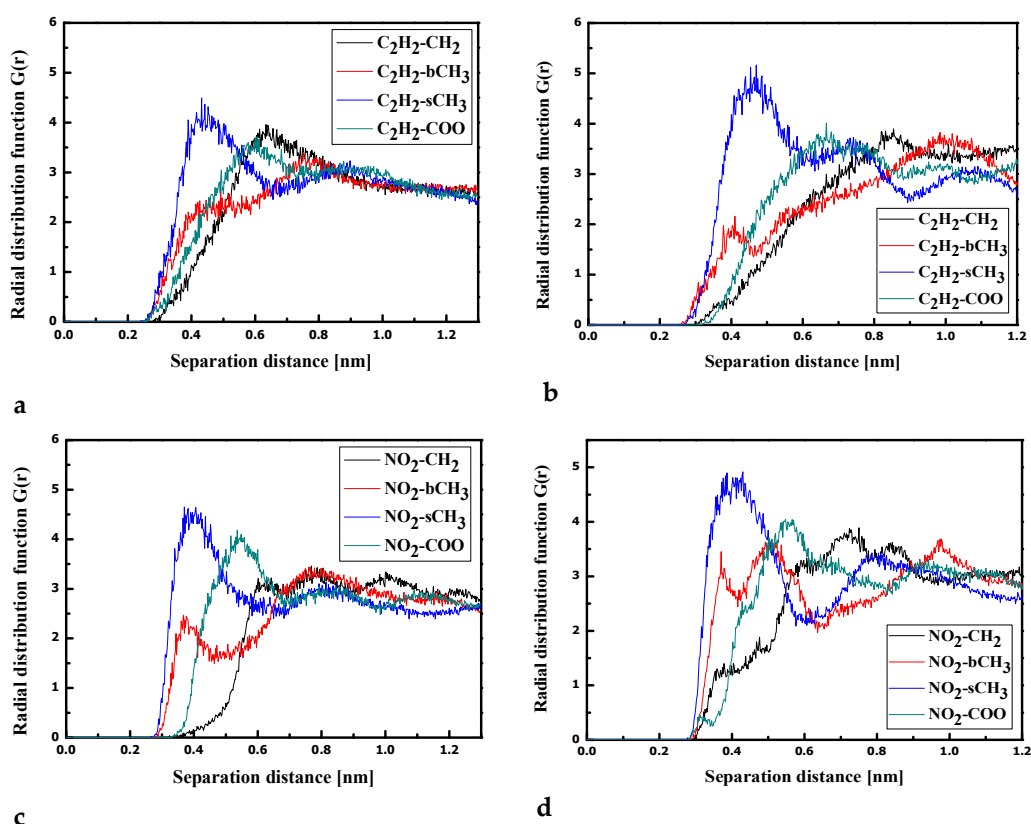

Figure 7.10. Partial RDFs calculated for distances between the center of mass of different moieties of the L4 molecule and different subunits of PMMA at T = 500K (a,c) and T=300K (b,d) for the thin film L4/PMMA system. Panels a and c present the RDFs for C_2H_2 of L4 molecule and different subunits of PMMA mer. Panels b and d present the RDFs CH_3 of L4 and different subunits of PMMA mer.

7.1.3. Reorientation of chromophores

The external electric field-induced reorientation of the chromophores was investigated by computing the *<cos θ(t)>* based on the time-dependent angle between the dipole moment of the chromophore and the vector of the external electric field. The degree of alignment depends on the electric field strength and the spatial extension of the dipolar molecules. The idea of the *cos θ(t)* angle is presented in Fig. 2.1. Values of *<cos θ(t)>* have been computed by averaging over three equivalent structures calculated for each of the L1-L4/PMMA composites and each of two chromophores.

The L1/PMMA composite in bulk form exhibits the complete alignment by applying an external electric field equal to 15 kV/μm. Using the field 10 kV/μm the

system is aligned at 80 %, but using the electric field equal to 1, 3, or 5 kV/mm the chromophores are aligned at 60 % (see Fig. 7.11 (a)). The full alignment of the L2 molecules in the PMMA polymer can be obtained at 10 kV/μm (see Fig. 7.11 (c)). The field 5 kV/μm aligns L2 molecules in 80 %. It means that the alignment of the chromophores L2 is easier than the alignment of the L1 molecules. However, the electric field with an intensity of 1 kV/μm is too small to align the L2 chromophores. The molecules L3 and L4 are significantly more difficult to be aligned than the L1 and L2 chromophores. In the case of L3 electric field with intensities of 10 and 15 kV/μm aligns the molecules at 80 %. The alignment of 50 % is possible using the electric field equal to 3 and 5 kV/μm (see Fig. 7.11 (e)). The chromophore L4 embedded into PMMA bulk polymer can be aligned by the electric field equal to 15 kV/μm and in consequence by the electric field equal to 10 kV/μm (see Fig. 7.11 (g)). However, the lower electric field almost does not align the L4 molecules.

The molecules L3 and L4 possess much higher electric dipole moment than the L1 and L2 chromophores (it will be discussed in the next paragraph) and their interaction with the external electric field is much higher. The difficult alignment of the molecules L3 and L4 should be caused by the close distance between chromophores and the PMMA. The L3 and L4 molecules enter deeper into the polymer structure taking localization in polymer cages and their rotation is more difficult.

It should be noted that the poling electric field was acting on the chromophores during the solidification process and realizing the *guest-host* systems. Then the external electric field was switched off and the composites were modeled under an NVT ensemble to investigate their back relaxation. The order parameter $<cos\ \theta(t)>$ versus the time modeled for the bulk L1/PMMA, L2/PMMA, L3/PMMA, and L4/PMMA in the glassy state is presented in Fig. 7.11 (b, d, f, h). Analyzing the data presented in mentioned Figures one can see that the L4 chromophores are relatively difficult to be aligned but also their back relaxation is prevented. The modeled L4/PMMA composites after 1.5 ns of MD without acting of the external electric field are still aligned at 80 %. At the same time, the alignment of the L3 molecules in PMMA decreases up to 50 – 60 %. In addition, the back relaxation of the L1 and L2 molecules is almost at the same level.
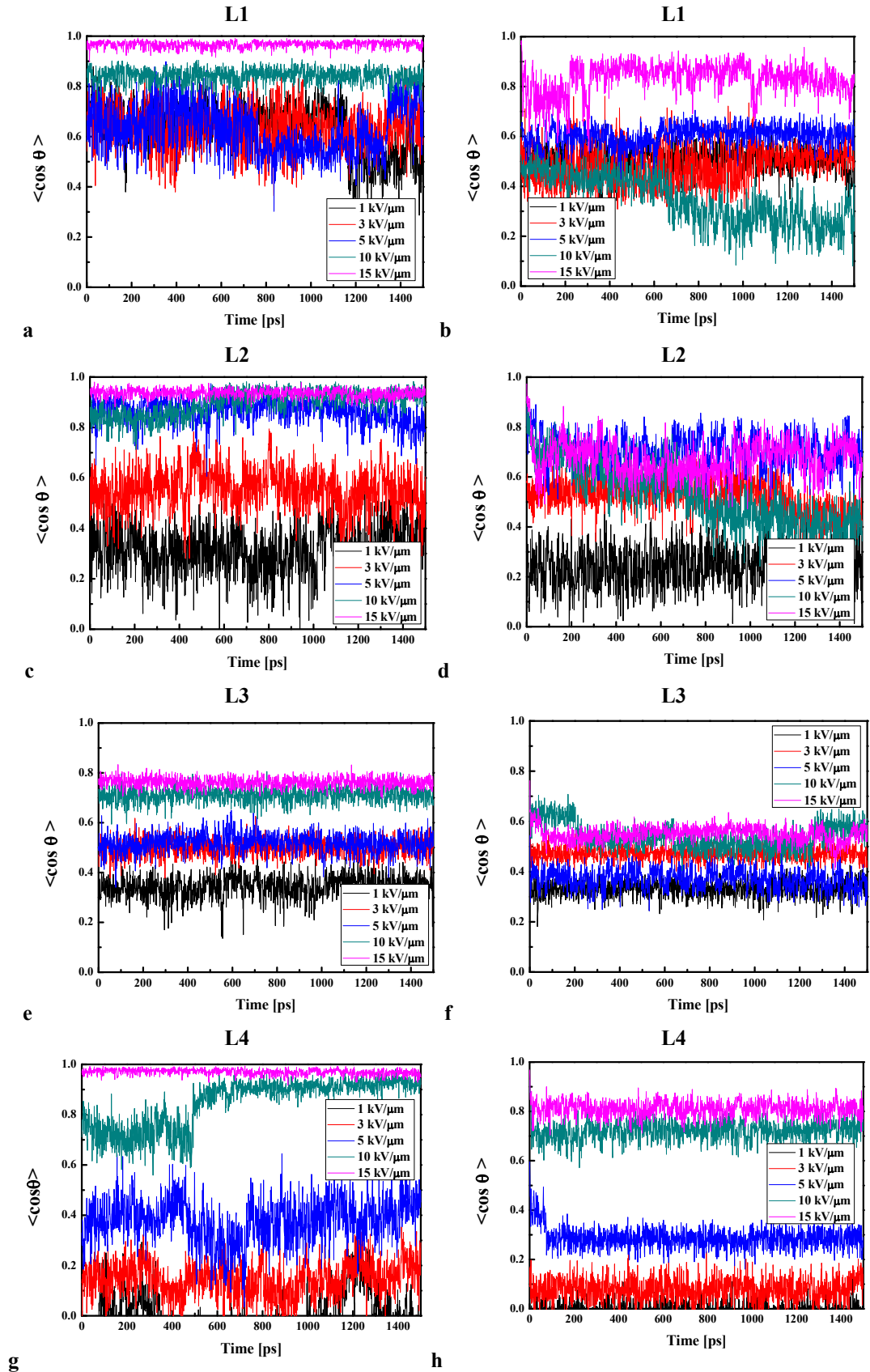
Figure 7.11. Changes in the value of the order parameter $<cos\theta(t)>$ versus the time of simulation and applied external electric field calculated by MD technique for the L1/PMMA (a,b), L2/PMMA (c,d), L3/PMMA (e,f), and L4/PMMA (g,h) composites in the volumetric form at the temperature of 500 K (a,c,e,g) and 300 K after the simulated annealing (b,d,f,h).

Only for the systems poled with an electric field equal to 15 kV/mm the alignment is still at the level of 80% but in real systems the alignment of chromophores equal to 100% is practically impossible. In consequence, the systems L1/PMMA and L2/PMMA will be disordered by back relaxation up to 40%.

Because the experimental alignment of the chromophores in a polymer matrix is at the level of 60 – 80 %, the lower external electric field was decided to be taken modeling composites in thin-film form. In the case of thin-film, the 0.5 – 5.0 kV/μm intensity of the external electric field was taken into consideration. Modeling the bulk L1/PMMA structure was found that the electric field equal to 5 kV/mm aligns chromophores at 60 %. Lower electric fields align chromophores L1 at a lower degree. It allows us to conclude that it easier is to align chromophores L1 in liquid bulk PMMA polymer than in the same system in thin-film form (see Fig. 7.12 (a)). It is not the case for the L2/PMMA system in thin-film form. The surface limitation does not have any influence on the alignment of the L2 molecules in PMMA (see Fig. 7.12 (c)). Is much easier to align the L3 chromophores in the liquid thin film of the PMMA than it was done for the bulk materials. In this case, the electric field equal to 5 kV/μm and 3 kV/μm align the L3 chromophores at the level of 90 and 60 %, respectively (see Fig. 7.12e). The same situation is noticed for the L4/PMMA thin-film system (see Fig. 7.12g).

Analyzing the back relaxation one can conclude that the L1/PMMA system is completely disordered after the back relaxation process. Relatively rigid is the L3/PMMA system. Also for the system, L2/PMMA and L4/PMMA are not distorted after MD without an external electric field acting.

7.2. Structural, electronic, and optical properties of TTF derivatives

Electron and optical properties of the L1, L2, L3, and L4 chromophores were investigated computationally by applying quantum chemical methods. First of all their geometries were optimized upon to the energy minimization procedure applying the *ab initio* formalism within the GAMESS program package [7]. The initial structures of the investigated molecules have been created out in the ACD/ChemSketch program package. The minimum of the potential energy surface
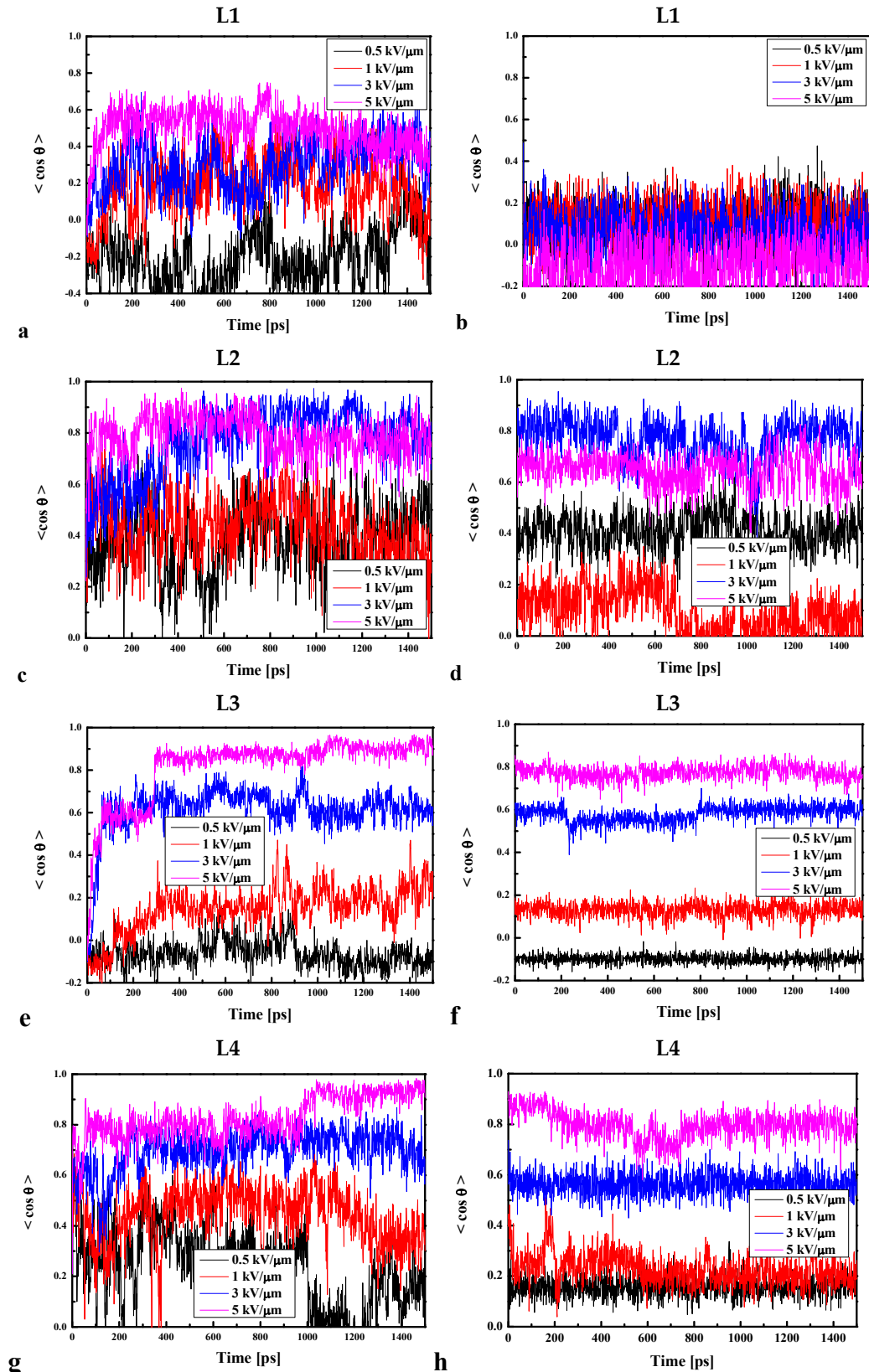
Figure 7.12. Changes in the value of the order parameter *<cosθ(t)>* versus the time of simulation and applied external electric field calculated by MD technique for the L1/PMMA (a,b), L2/PMMA (c,d), L3/PMMA (e,f), and L4/PMMA (g,h) composites in the thin film form at the temperature of 500 K (a,c,e,g) and glassy state (300 K) after the simulated annealing (b,d,f,h).

was calculated at the restricted Hartree-Fock (RHF) level with the 6-311G basis set in C1 symmetry. The quadratic approximation (QA) optimization algorithm based on augmented Hessian techniques achieved the geometry of the studied molecules with the minimum of the total energy. The gradient convergence tolerance was equal to 10^{-6} Hartree/Bohr. After that, the optimized structures were used to calculate their electron and optical properties. The structures of the molecules L1, L2, L3, and L4 are presented in Fig. 7.1.

The electron properties of the molecules L1, L2, L3, and L4 were calculated applying the DFT methodology implemented in Gamess program package. The calculations were performed with the 6-311++G** basis set for the isolated molecules placed in a vacuum and dichloromethane (CH_2Cl_2). The DFT calculations were performed by implementing B3LYP and LC-BLYP functionals. The RHF SCF energy convergence criterion was chosen to be 10^{-12} Hartree. The separation parameter μ was equal to 0.33. The Polarizable Continuum Model (PCM) [8] was used to investigate the solvent effect on the electron properties of the chromophores. The oscillator strength values for the electron excited states of the molecules were calculated using the iterative Davidson method [9] with an accuracy of 10^{-12} Hartree.
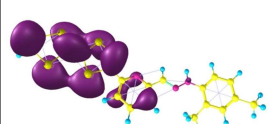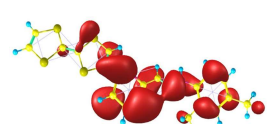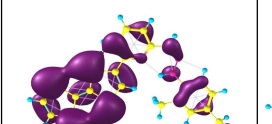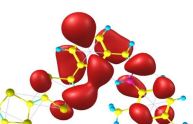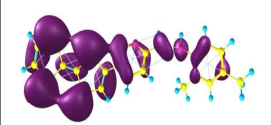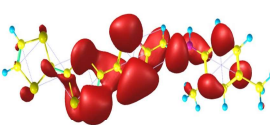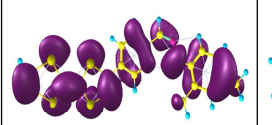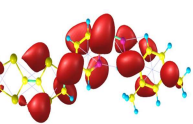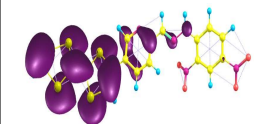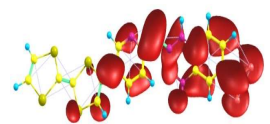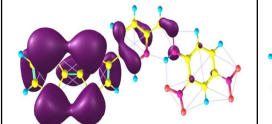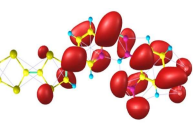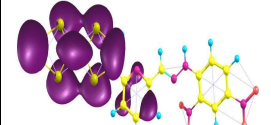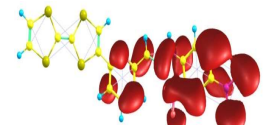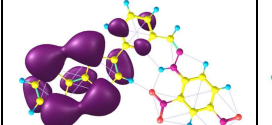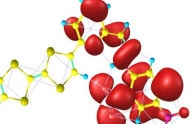
Optimizing geometries of the L1, L2, L3, and L4 molecules, two conformers of each one were found. The conformers are identified as *a* and *b* and their structures are presented in Tab. 7.1. The total energy of the $L3^a$ and $L3^b$ molecules is the same. For the other chromophores, conformer b is more probable than conformer *a*. It is supposed from the fact that the total energy of *b* conformers of molecules L1, L2, and L4 is lower than the energy of conformers *a* but the energy difference is not significant (see Tab. 7.2.). It allows us to conclude that both conformers of the investigated chromophores may exist [10]. The TTF moiety is planar in all chromophores. The TTF group attached to the pyridine in the meta position is most likely to twist the molecule in conformer *b*. The molecules $L2^b$ and $L3^b$ are more elongated than the structures $L1^b$ and $L4^b$. Generally, the molecules depicted as *a* are more elongated than the molecules *b*.

In Tab. 7.1. the frontier molecular orbitals of L1, L2, L3, and L4 molecules in both conformers are collected. The HOMO orbital of all molecules is located in the TTF group. It confirms that the TTF moiety possesses a donor character. The LUMO orbital of all molecules is located at the 2,4-dimethyl phenyl or 2,4-dinitro

phenyl possessing an acceptor nature and additionally, it is spread in the azine group. However, the presence of the 2,4-dimethyl phenyl group in the molecule causes a dispersion of the HOMO orbital on the whole molecule. It is seen in the molecules L1[b], L2[a], and L2[b]. The mentioned effect is less pronounced for the molecule L1[a]. The spread of the HOMO and LUMO orbitals on the molecules will affect their optical properties.

The 2,4-dinitro phenyl moiety decreases the HOMO and LUMO energy level value for both conformers compared to the 2,4-dimethyl phenyl group (see Tab. 7.2.). Conformations *b* of molecules L1 and L4 do not change the energy level of HOMO. It means that the HOMO orbital is localized on the TTF group and conformational changes are not able to affect the geometry of the molecule.

Table 7.1. Structures and frontiers molecular orbitals calculated for L1, L2, L3, and L4 molecules by *ab initio* methodology.

L1[a] HOMO	L1[a] LUMO	L1[b] HOMO	L1[b] LUMO
L2[a] HOMO	L2[a] LUMO	L2[b] HOMO	L2[b] LUMO
L3[a] HOMO	L3[a] LUMO	L3[b] HOMO	L3[b] LUMO
L4[a] HOMO	L4[a] LUMO	L4[b] HOMO	L4[b] LUMO

The molecules L1 and L2 in both conformers possess lower dipole moment than the molecules L3 and L4 (Tab. 7.2). Additionally, molecules L3 and L4 possess lower $\Delta E_{HOMO-LUMO}$ than the L1 and L2 chromophores which allows us to conclude that the 2,4-dinitro phenyl moiety should increases their NLO properties.

The mentioned properties favor the L3 and L4 molecules for the NLO applications. It is not greatly influenced by the conformation of the molecules.

Table 7.2 Total energy and selected electron parameters of the L1, L2, L3, and L4 molecules calculated for both conformers by *ab initio* methodology.

	L1[a]	L1[b]	L2[a]	L2[b]	L3[a]	L3[b]	L4[a]	L4[b]
$E_{tot} \times 10^4$ [kcal/mol]	-158.15	-158.15	-158.15	-158.15	-178.76	-178.76	-178.76	-178.77
HOMO [eV]	-7.36	-7.36	-7.41	-7.27	-7.73	-7.76	-7.52	-7.51
LUMO [eV]	1.01	0.95	1.02	0.97	0.02	0.17	0.00	0.17
$\Delta E_{HOMO-LUMO}$ [eV]	8.37	8.31	8.43	8.24	7.75	7.93	7.52	7.68
λ_{max} [nm]	348.61	347.24	354.08	353.18	350.88	351.27	349.79	349.59
μ [D]	1.02	3.92	1.04	3.93	9.23	11.63	8.58	9.89

The $\Delta E_{HOMO-LUMO}$ values calculated for the L1, L2, L3, and L4 molecules by DFT/LC-BLYP method (see Tab. 7.3.) are similar to the ones calculated by the *ab initio* method presented in Tab. 7.2. The mentioned values have the same tendency. It means that the 2,4-dinitro phenyl moiety decreases the value of the $\Delta E_{HOMO-LUMO}$. The mentioned tendency is also seen in the data obtained by using DFT/B3LYP method but the obtained value are much lower. This situation is in line with the assumptions of the DFT methodology, which gives underestimated values of the $\Delta E_{HOMO-LUMO}$ in comparison with the results of the *ab initio* method.

Table 7.3. Electron and optical properties of the L1, L2, L3, and L4 molecules in conformation *a* and *b* calculated in vacuum and dichloromethane by DFT/B3LYP and DFT/LC-BLYP methods.

	$\Delta E_{HOMO-LUMO}$ [eV]		λ_{max} [nm] (in vacuum)		λ_{max} [nm] (in dichloromethane)		Dipol moment [D]	
	B3LYP	LC-BLYP	B3LYP	LC-BLYP	B3LYP	LC-BLYP	B3LYP	LC-BLYP
L1[a]	3.23	6.90	500.8	409.6	500.1	408.7	1.24	1.00
L1[b]	3.13	7.31	509.0	415.4	500.1	409.1	2.55	2.95
L2[a]	2.94	6.55	520.1	415.2	518.1	414.7	1.56	1.12
L2[b]	2.85	6.89	542.2	423.8	534.2	416.9	2.72	3.3
L3[a]	1.99	6.16	717.5	416.1	718.8	409.3	6.66	6.03
L3[b]	2.13	6.27	680.5	422.9	737.1	415.6	10.56	9.96
L4[a]	1.92	6.15	744.2	416.3	719.6	409.3	6.60	5.92
L4[b]	1.68	5.90	971.7	416.0	891.3	423.9	8.39	8.10

Analyzing the data from Tab. 7.2. and Tab. 7.3. one may see that the electric dipole moments of the L3 and L4 molecules are much higher than the ones of the L1 and L2 molecules. It is seen for the *ab initio* and DFT calculations. This allows us to conclude that the 2,4-dinitro phenyl group in the L3 and L4 structures increases their polarity. The high dipole moment of the molecules L3 and L4 and their relatively low $\Delta E_{HOMO\text{-}LUMO}$ cause the statement that these molecules can potentially be useful for NLO applications.

In Tables 7.2 and 7.3, the positions of the first absorption peak calculated for the L1, L2, L3, and L4 molecules and their conformers by using *ab initio* and DFT/LC-BLYP and DFT/LC-BLYP are presented. The calculations were performed for isolated molecules in a vacuum and molecules in dichloromethane. One can see that the DFT/B3LYP shifts the λ_{max} values into the long-wavelength region and *ab initio* shifts them into the short-wavelength region. According to the methodology reason, the LC-BLYP functional gives the λ_{max} values between these coming from *ab initio* and B3LYP.

The UV-vis absorption spectra were computed for L1, L2, L3, and L4 molecules in both conformational forms using DFT/B3LYP and DFT/LC-BLYP methods and they are presented in Fig. 7.13. The calculations were performed for isolated molecules in a vacuum (Fig. 7.13., left panel) and in dichloromethane (Fig. 7.13., right panel). Comparing the theoretical spectra calculated for the molecules in a vacuum and dichloromethane one may conclude that all molecules exhibit hypsochromic shift. It means that the first absorption peak is created by the n→π* transition. One can also conclude that the investigated molecules are more polar in the ground state than in the excited state [11]. In this case, the non-bonding electrons in the ground state are relatively stabilized by electrostatic interaction with the polar solvent. As a result, the absorption peak is shifted to a shorter wavelength with increasing solvent polarity. The mentioned phenomenon was also checked for THF and 1,1,2-trichloroethane (TCA) solvents but the obtained results are not presented here. The first absorption peak of conformers *a* of molecule L1, L2, and L4 is shifted into red wavelength compared to an absorption of the conformers *b*. It is not valid for molecule L3. It means that the twisting of the molecules L1, L2, and L4 make them more transparent.
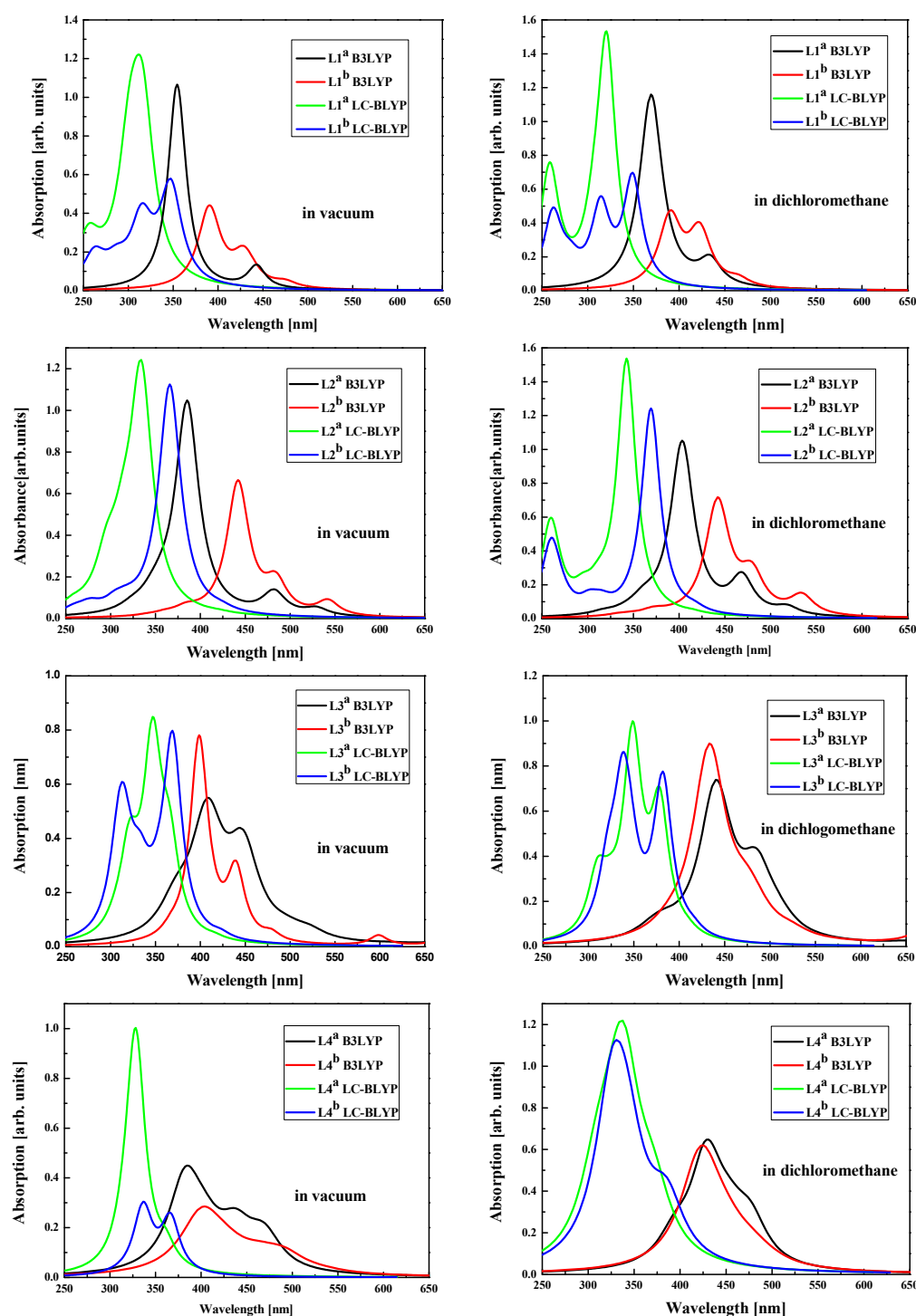
Figure. 7.13. The UV-vis absorption spectra calculated by DFT/B3LYP and DFT/LC-BLYP methodology for L1, L2, L3, and L4 molecules for both isomers a and b in a vacuum (left panel) and dichloromethane (right panel).

The UV-vis spectra calculated in a solvent (see Fig. 7.13, right panel) can be compared to the experimental UV-vis absorption spectra. Molecules L1, L2, L3, and L4 were synthesized according to procedures described in the work [10, 12]. The UV-vis electron absorption spectra of these molecules were recorded in

dichloromethane solution (C-2.6.10^{-5} M) at room temperature in quartz cuvettes using the Perkin Elmer spectrophotometer and they are presented in Fig 7.14. The highest wavelength value of the first absorption peak is noticed for the L3 molecule. Comparing the spectra of L2 and L3 molecules one may conclude that the 2,4-dinitro phenyl group shifts the first absorption band into a higher wavelength creating an additional peak (in the case of the L3) at the red spectrum side. It is also seen comparing spectra of the L1 and L4 molecules. The strong electron absorption band exhibiting for L1, L2, and L4 molecules centered at 350-400 nm is assigned to the n→π* transitions. Molecules L3 absorbs light at the 500 nm assigned to the n→π* transition and at the 375 nm where the π→π* transition is observed. An intramolecular charge transfer (ICT) is noticed in all cases and plays a crucial role in the NLO response. This is reflected in the excitation from the TTF donor moiety to the hydrazine unit located at the opposite part of the molecules, it is also confirmed by accomplished quantum chemical calculations.
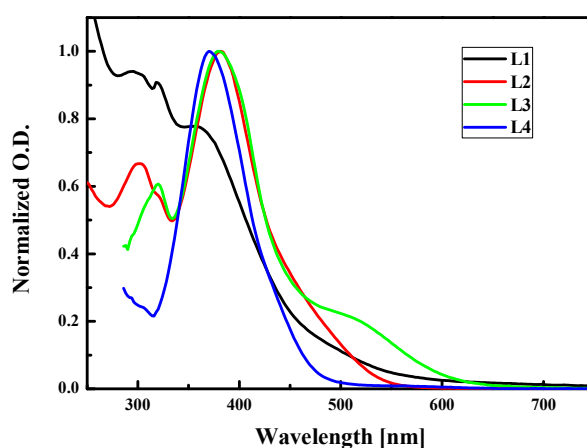
Fig. 7.14. Experimental UV-vis absorption spectra of L1, L2, L3, and L4 chromophores measured in dichloromethane (~C=2.6·10^{-5} M) at room temperature.

Comparing the computationally obtained data to the experimental results one may conclude that the VU-vis spectra calculated with *ab initio* and the DFT/LC-BLYP method suit better experiments than the results obtained by DFT/B3LYP calculations (see Tab. 7.2 and 7.3). For the L1 and L2 molecules, better results are given by the *ab initio* calculations. For the L3 and L4 molecules possessing much higher dipole moment, better results are given by the DFT/LC-BLYP formalism [13]. It is caused by the nature of the method and important charge redistribution in molecules possessing 2,4-dinitro phenyl groups.
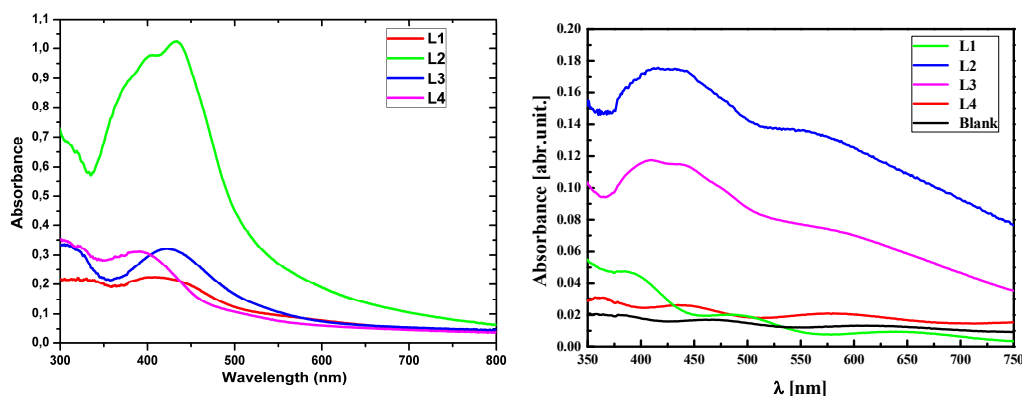
Figure 7.15. UV-vis absorption spectra measured for L1, L2, L3, and L4 based thin films produced by the PLD technique (left panel) and embedded into PMMA thin film matrix (right panel) at room temperature.

The thin films of the L1, L2, L3, and L4 chromophores were also prepared by the pulsed Laser Deposition (PLD) technique. This technique is used to deposit high-quality films of molecules. It uses high-power laser pulses to ionize material from the surface of a target [14,15]. The Lambda 950 UV/Vis/NIR spectrophotometer (PerkinElmer) with the range of 300-1200 nm was used to measure the absorption spectra of the PLD prepared films. These spectra are presented in Fig. 7.15., left panel. The positions of measured absorption peaks of the investigated chromophores are collected in Tab. 7.4. Comparing the UV-vis absorption spectra obtained for the L1, L2, L3, and L4 chromophores in dichloromethane (see Fig. 7.14) with the ones performed for the thin films produced by the PLD techniques one may see that the dichloromethane causes the hypsochromic shift for all components. From the other side, one may conclude that comparing UV-vis spectra calculated for isolated molecules with the ones obtained in dichloromethane and thin films prepared by PLD hypsochromic shift for molecules in a vacuum is observed. The intermolecular interaction occurring in PLD prepared samples shifts UV-vis spectra more significantly into the red side than dichloromethane. It means that the intermolecular interaction occurring between chromophores is higher in PLD prepared thin films than in the solvent – chromophores interactions. It is probably due to the multipolar intermolecular interaction. It should be noted that the studied chromophores (L3 and L4) have large dipole moments, which also appear in their difficult solubility in various solvents. The highest absorption intensity is noticed for the L2 molecule in dichloromethane and PLD prepared samples. The absorption peak observed for L3 at 500 nm in dichloromethane is not present for the thin film deposited by the PLD technique.

For the other molecules, the first absorption peak is shifted to a higher wavelength and they are located abound 400 nm.

Table 7.4. Positions of absorption peaks and the values of absorption coefficients for L1, L2, L3, and L4 thin films produced by the PLD technique.

Compounds	λ_{abs} [nm]	α cm$^{-1}\cdot 10^4$ (at 355nm)
L1	270-321-408	10.80
L2	274-406-434	6.31
L3	299-423	5.23
L4	299-391	7.84

The L1, L2, L3, and L4 molecules were also embedded into PMMA polymeric matrix to measure their UV-vis absorption spectra as well as to evaluate their SHG and THG behavior. The PMMA (Sigma-Aldrich, Mw=350 000 g/mol) was dissolved in 1,1,2-trichloroethane 50g/L to prepare the host system for investigated chromophores. The solvent concentration of the PMMA was equal to 2 wt %. The key technical problem in the preparation of the solutions is component solubility. Prepared solutions were deposited on glass substrates by the spin-coating technique with controlled thickness. The substrate was rotating with an angular speed equal to 1000 rpm. The glass plates were washed in distilled water using an ultrasonic bath, acetone, and ethanol and then they were dried. Obtained *guest-host* polymer films were kept at room temperature for two days to remove any remaining solvent. The thickness of deposited thin films was estimated using the profilometer (Dektak 6M, Veeco) to be about 600 nm. The absorption spectra of the samples were measured by the Lambda 950 UV/Vis/NIR spectrophotometer (PerkinElmer) in the range of 250-1200 nm.

The UV-vis absorption spectra measured for L1, L2, L3, and L4 chromophores embedded into PMMA matrixes deposited as thin films are presented in Fig. 7.15, right panel). The PMMA thin film shows high transmission above ~250 nm which makes it applicable as an optically transparent window material [17]. Analyzing the obtained data one may see that the absorption spectra are more pronounced for L2 and L3 molecules than for L1 and L4. The high absorption intensity is caused by the TTF group attached to the pyridyl group in the para-position and no matter 2,4-dimethyl phenyl nor 2,4-dinitro phenyl group is present in the molecules. The same was seen for the absorption spectra recorded for the PLD films. The absorbance for

all prepared *guest-host* samples is quite low probably due to the small thickness of the material and low concentration of molecules in the thin films. The broadening of the absorption band from the long wavelength side is caused by an amorphous nature of the *guest-host* structure. Comparing the UV-vis absorption spectra measured for the L1, L2, L3, and L4 molecules in dichloromethane and PMMA polymeric matrix one may see that chromophore-polymer interactions cause bathochromic effect for all molecules. Additionally, for the molecules L1, L2, and L4 broad high wavelength peaks appear. It may be caused by the intermolecular charge transfer occurring between chromospheres and polymer.

7.3. Nonlinear optical properties of the TTF-based composite materials

In addition to the linear optical properties of the *guest-host* composites based on PMMA and L1, L2, L3, and L4 molecules also their NLO properties were investigated. The SHG and THG measurements were carried out by the rotational Maker fringe technique [18] for the s- and p- polarized fundamental laser beam. The analyses were performed on *guest-host* thin films using the Nd:YAG/YVO4 laser generating wavelength λ=1064 nm with 30 ps pulse duration and 10 Hz repetition rate. Y-cut crystalline quartz and fused silica plates have been used as reference materials for SHG and THG measurements, respectively. The polarizer and half-wave plate serve to select the incident polarization in front of the focusing lens. Before the lens is mounted the long pass filter RG1000 is installed to cut the visible region of the light. The thin films were mounted on a motorized rotation stage allowing the variation of the incidence angle with a resolution of 0.5-1.0° and were processed by a computer through the controller box. The KG3 filter fix after the rotation stage was used to cut off the infrared laser beam, and the interference filter at 532 nm (or 355 nm) was used to select the desired wavelength of light. The polarization of the second and third harmonic was controlled by a polarizer placed before the photomultiplier. The photomultiplier tube Hamamatsu was connected to a boxcar and processed by a computer. The photodiode was enabled in laser pulse synchronization which was checked by an oscilloscope. The input laser pulses energy was measured by laser power/energy meter (LabMax TOP, COHERENT) to be 116 μJ for SHG and 160 μJ for THG measurements. We got the angular

dependences of SHG/THG or so-called Maker-fringes by rotating the sample towards the axis perpendicular to the direction of beam propagation.

Measurements of the SHG signal were performed by the rotational Maker fringe technique for the p-polarized fundamental laser beam. The *guest-host* thin film samples deposited by spin-coating on a glass plate and used for the NLO investigations were poled using an external electric field to increase the unidirectional orientation of the chromophores in the polymer films. First of all the samples were heated up to 100°C on a hot plate of the poling machine. Then external electric field equal to 5 kV was applied to the tungsten needle fixed at 1 cm above the thin film surface. The heater was switched off with an acting electric field and the samples were cooled down up to room temperature. Finally, the electric field was turned off. The whole poling process has taken about 2.5 hours including up and down temperature changes.

Fig. 7.16. shows the function of incident angle dependences on the SHG signal intensity for all investigated *guest-host* systems. The M-shape angular dependence was obtained for all samples with the maximum signal at about 60° and minimum intensity at normal incidence of the fundamental beam due to the lack of noncentrosymmetry in this direction. In our case, the thin films have thicknesses much less than the coherence length. From Tab. 7.5. one may see that the thickness is similar for all samples. In this case, the obtained signal parameters may be compared. The quadratic NLO susceptibility can be calculated using the following equation [18]:

$$\chi^{(2)} = \chi^{(2)}_{Quartz} \left(\frac{2}{\pi}\right) \left(\frac{l^{coh}_{Quartz}}{d}\right) \left(\frac{I^{2\omega}}{I^{2\omega}_{Quartz}}\right)^{1/2} \tag{7.2}$$

where $\chi^{(2)}_{Quartz}$= 1.0 pm/V, coherent length of quartz $l^{co}_{Quartz} = \frac{\lambda}{4.|n_{2\omega}-n_{\omega}|} = 21$ μm, d is investigated film thickness, $I^{2\omega}$ and $I^{2\omega}_{Quartz}$ are the SHG intensities coming from the investigated samples and quartz, respectively, under the same conditions. The generated signal is p-polarized.

Values of the quadratic NLO susceptibilities calculated applying equation (7.2) for samples L1/PMMA, L2/PMMA, L3/PMMA, and L4/PMMA are presented in Tab. 7.5. The lowest SHG signal is obtained for L3/PMMA composite and the highest value is observed for L2/PMMA *guest-host* composite. It means that the 2,4-dimethyl phenyl group accompanied by the TTF group attached to the pyridine

group in the para-position increases the SHG signal. It may be also caused by the fact that the L2 molecules are more polarised in a polymer film than the other molecules and their back reorientation does not go so fast. It is seen from MD modeling. The L2/PMMA composite in bulk form keeps the aligned chromophores in the back relaxation process at the level of 50 % and at its surface the alignment is equal to 80 %. At the surface of thin film, the L2 chromophores enter into a twisted polymer chain and their back relaxation is prevented by the intermolecular interaction and location in the polymer cages. The lowest value of the SHG signal was measured from L3/PMMA composite. It is caused by very fast back relaxation of the L3 chromophores in the bulk polymer. At the surface of polymer film, the back relaxation of the L3 chromophores is much slower but the chromophores are very difficult to be aligned there. Probably in the experiment, the L3 chromophores in PMMA polymer were not properly aligned.
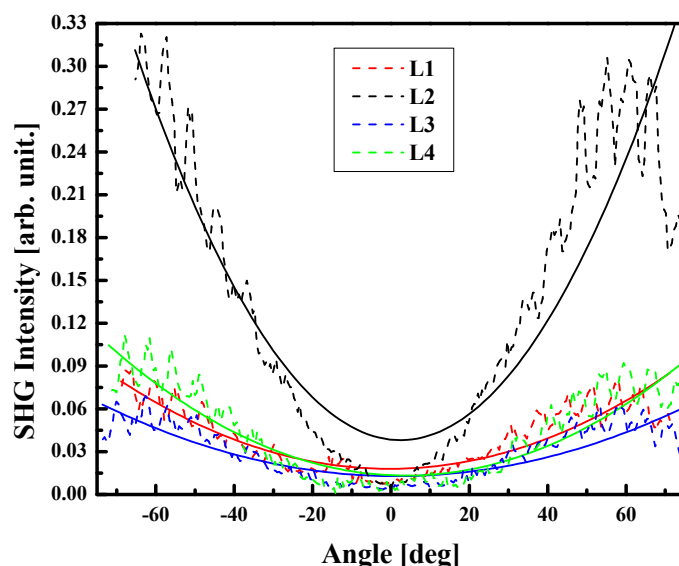
Figure 7.16. SHG signal intensity as a function of the incident angle measured for PMMA thin films with embedded L1, L2, L3, and L4 molecules at the p-polarized fundamental beam.

Table 7.5. Susceptibilities $\chi^{(2)}$ and $\chi^{(3)}$ measured for L1/PMMA, L2/PMMA, L3/PMMA, and L4/PMMA thin films with p-polarization and measured thickens of the samples

Sample	d [μm]	$\chi^{(2)}$ [10^{-12} pmV^{-1}]	$\chi^{(3)}$ [10^{-21} m^{2}V^{-2}]
L1/PMMA	0.6527	1.10	1.70
L2/PMMA	0.6236	2.10	1.80
L3/PMMA	0.7406	0.79	1.60
L4/PMMA	0.6441	1.20	1.70

The measurements of THG signal in *guest-host* thin films based on PMMA polymer and L1, L2, L3, and L4 molecules were performed for s-s incident-generated polarization scheme. The function of incident angle dependences on the THG signal intensity for all investigated *guest-host* systems is presented in Fig. 7.17. To calculate the second-order NLO susceptibilities $\chi^{(3)}$ Kubodera-Kobayashi model [19] was used:

$$\chi^{(3)} = \chi_{Silica}^{(3)} \left(\frac{2}{\pi}\right) \left(\frac{l_{Silica}^{coh}}{d}\right) \left(\frac{\frac{\alpha d}{2}}{1 - e^{-\frac{\alpha d}{2}}}\right) \left(\frac{I^{3\omega}}{I_{Silica}^{3\omega}}\right)^{1/2} \tag{7.3}$$

where $\chi_{Silica}^{(3)} = 2 \times 10^{-22} \text{ m}^2 \text{ V}^{-2}$ [20,21] $l_{Silica}^{coh} = \frac{\lambda}{6|n_{3\omega} - n_{\omega}|} = 6.7 \ \mu m$ is the coherent length of silica, d is the film thickness, l_{Silica}^{coh} and $I_{Silica}^{3\omega}$ are the THG intensities of sample and silica at the same conditions, respectively. The results are collected in Tab. 7.5. Analyzing the presented data one can say that the THG intensity is similar for all systems.
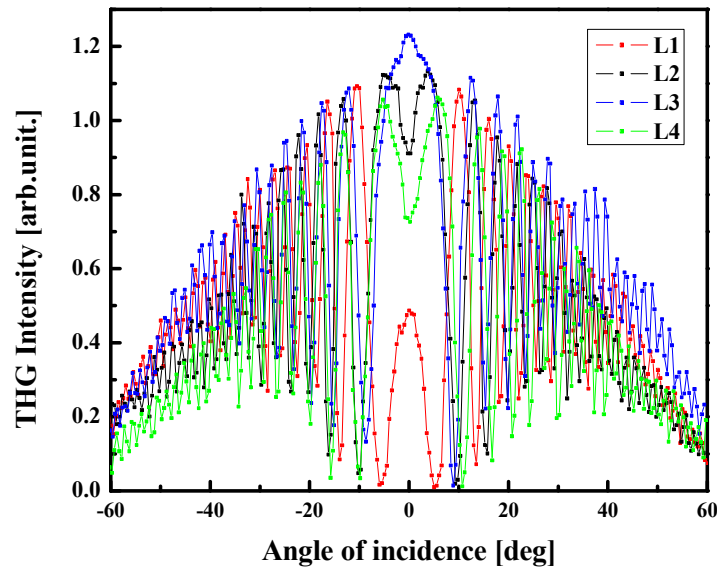
Figure 7.17. The intensity of the THG signal coming from PMMA thin films with embedded L1, L2, L3, and L4 molecules measured at the p-polarized fundamental beam.

The measurements of THG response were also performed for the thin film produced by the PLD technique. The experiment was done for s-s beam-generated polarization and the results are presented in Fig. 7.18. It can be seen that L3 film shows a much higher THG response compared to L1, L2, and L4 films.
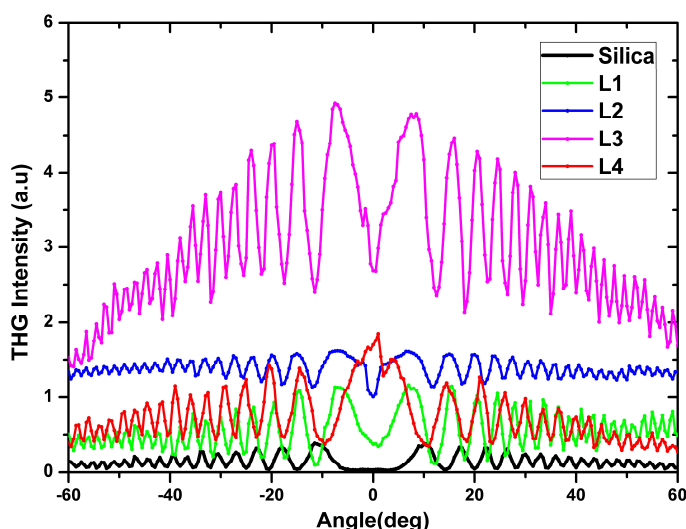
Figure 7.8. THG intensities from L1, L2, L3, and L4 films as a function of incident angle for the s-s polarization of the fundamental beam-generated signal measured for the thin film produced by the PLD technique.

The comparative model described by eq. (7.3) was used to calculate the third-order NLO susceptibility $\chi^{(3)}$ responsible for the THG generation in PLD prepared samples. As the THG originates from the film with the glass substrate, the impact of the substrate was taken into account during data processing and the cubic NLO susceptibility calculations. The values of third-order nonlinear optical susceptibility of the thin films have been estimated at 3.44×10^{-20} m² · V⁻², 0.74×10^{-20} m² · V⁻², 3.41×10^{-20} m² · V⁻², and 2.13×10^{-20} m² · V⁻² for molecules L1, L2, L3, and L4, respectively (Tab. 7.6.). These values are two orders of magnitude larger than $\chi^{(3)}$ of silica, which is the reference material for the THG method and one order of magnitude greater than the values obtained for molecules tested in the PMMA matrix (see Tab. 7.5.). The polymer matrix usually reduces the second-order NLO properties which can be also observed in the research carried out in other works [22]. From Tab. 7.6. one can observe that $\chi^{(3)}$ of L1 and L3 films, is higher than $\chi^{(3)}$ of L2 and L4 films. The L3 and L4 chromophores containing 2,4-dinitro phenyl acceptor differ between the substituting of the TTF donor group (para L3 and meta L4) to the pyridine group, are characterized by a relatively low absorption coefficient and a large figure of merit. Another situation is in the case of the first two compounds L1 and L2 with 2,4-dimethyl phenyl acceptor group, where a better result was obtained for the meta substitution. The values of $\chi^{(3)}$ for L1 is the same as for L3 compounds but the merit factor $\chi^{(3)}/\alpha$ indicates that the best nonlinear properties have compound L3.

Table 7.6. The values of $\chi^{(3)}$ obtained for L1, L2, L3, and L4 thin films produced by the PLD technique.

Compounds	α (cm^{-1})	$\chi^{(3)}$ 10^{-20} (m$^2 \cdot$ V^{-2})	$\chi^{(3)} 10^{-13}$ (esu)	$\frac{\chi^{(3)}}{\alpha}$ (arb.un.)
L1	10.80	3.44	24.63	2.28
L2	6.31	0.74	5.29	0.84
L3	5.23	3.41	24.41	4.67
L4	7.84	2.13	15.24	1.94

The quantum chemical calculations were performed to explain the phenomenon of the NLO properties occurrence and their results were discussed. The polarizabilities, as well as the first and second-order hyperpolarizabilities, were computed applying *ab initio* methodology and the obtained data are presented in Tab. 7.7. – 7.10. The *ab initio* method was chosen after analysis of UV-vis calculated data obtained for the L1, L2, L3, and L4 molecules. First of all the optical parameters were calculated for the L1, L2, L3, and L4 molecules in a vacuum. It is indicated by the column *Fx,Fy,Fz* = 0, 0, 0. When the column is described by the *Fx,Fy,Fz* ≠ 0, 0, 0 it means that the optical parameters were computed, applying a discrete local field model. In this case, the composite structures aligned by an external electric field were taken to calculate the local electric field (*F*) coming from all neighboring atoms acting on the center of mass of the chromophores. The local electric field is calculated for each MD modeled structure and the results are averaged. It is calculated for the first and next neighbors unit cell of the composite up to the moment when the calculated *F* is stable. The chosen difference between F_n-F_{n-1} is taken to be 10^{-4} GV/m The local electric field perturbs Hamiltonian changing the optical parameters of molecules. Because the calculated local electric field comes from the surrounding polymer, the perturbed Hamiltonian models the optical properties of the chromophores affected by the polymer matrix. All chromophores were located in laboratory coordinates in the case to have electric dipole moment in direction of Z-axes.

In Table 7.7 the electron and optical parameters of the **L1** molecule in *a* and *b* conformer calculated by using the *ab initio* method implemented in the Dalton program are presented (Dalton2020.0.beta (2020), http://daltonprogram.org, accessed on 6 March 2022) [23]. The calculations were performed at the RHF level with the standard 6-31++G** basis set in C1 symmetry for all chromophores.

Table 7.7. Electron and optical properties of the L1 molecules calculated in vacuum (F_x,F_y,F_z=0,0,0) and PMMA polymer environment (F_x,F_y,F_z≠0,0,0) in volumetric form by using the *ab initio* method.

Molecule	L1[a]		L1[b]	
Fx,Fy,Fz [GV/m]	0, 0, 0	0.63, -0.26, -0.27	0, 0, 0	0.63, -0.26, -0.27
μ [D]	0.82	1.18	3.75	3.41
$\Delta E_{HOMO-LUMO}$ [eV]	8.24	8.10	8.21	7.94
$\lambda=\infty$ nm				
α_{av}	348.22	348.63	340.75	341.15
$\beta_{(z;z,z)}$	-234.12	-281.44	-993.81	-1192.27
$\beta_{(y;y,y)}$	64.13	44.55	159.44	148.10
$\beta_{(x;x,x)}$	-671.47	-795.03	-299.07	-397.36
$\beta_{(z)}$	513.90	513.06	-1023.06	-1237.10
$\beta_{(y)}$	189.43	153.43	452.1	455.26
$\beta_{(x)}$	-1197.83	-1405.33	-576.88	-756.21
β_{vec}	-1065.28	-1299.30	-1084.00	-1376.59
$\gamma_{(z;z,z,z)}$	316544.26	323376.63	308817.70	323428.03
$\gamma_{(y,y,y,y)}$	38157.89	38147.06	63230.46	63587.61
$\gamma_{(x,x,x,x)}$	139474.14	143342.61	91396.56	94098.83
γ_{vec}	152423.09	156069.64	125806.73	129839.36
$\lambda=1064$ nm				
α_{av}	354.97	355.43	347.15	347.62
$\beta_{(z;z,z)}$	-234.54	-286.65	-1803.34	-2134.06
$\beta_{(y;y,y)}$	74.97	51.56	218.72	207.79
$\beta_{(x;x,x)}$	-945.19	-1110.69	-406.07	-533.23
$\beta_{(z)}$	820.20	842.96	-1876.65	-2211.48
$\beta_{(y)}$	246.43	203.52	679.03	697.06
$\beta_{(x)}$	-1752.64	-2036.67	-892.84	-1137.95
β_{vec}	-1529.15	-1842.83	-1964.15	2387.40
$\gamma_{(z;z,z,z)}$	780156.42	808763.27	1037673.87	1153715.81
$\gamma_{(y,y,y,y)}$	56233.37	56291.49	108037.95	109642.35
$\gamma_{(x,x,x,x)}$	301272.81	316461.11	175243.75	184772.13

Frequency-dependent polarizabilities and hyperpolarizabilities were computed with the random phase approximation (RPA), using the Dalton program package. The local electric field acting on the chromophores L1 is equal to 0.73 GV/m. Analyzing the data presented in Tab. 7.7. one can conclude that the PMMA polymer acting on the chromophore L1[a] increases its dipole moment and decreases its $\Delta E_{HOMO-LUMO}$. These changes are beneficial for the NLO application of the chromophore. The local electric field acting on the L1[b] chromophore oppositely changes its parameters and these changes are unwanted. The PMMA matrix does not affect the static and frequency-dependent polarizability values of the L1 chromophores and it increases insignificantly the second and third-order hyperpolarizabilities. The second-order hyperpolarizability of the L1[b] molecule is

higher than the one of the $L1^a$ molecule. While with the hyperpolarizability γ_{av} the situation is the opposite. The $L1^b$ has a lower γ_{av} value than the $L1^a$.

Table 7.8. Electric and optical properties of the L2 molecules calculated in a vacuum $(F_x,F_y,F_z=0,0,0)$ and PMMA polymer environment $(F_x,F_y,F_z\neq0,0,0)$ in volumetric form by using the *ab initio* method.

Molecule	L2^a		L2^b	
F [GV/m]	0, 0, 0	1.00, 0.08, -0.24	0, 0, 0	1.00, 0.08, -0.24
μ [D]	1.00	1.65	3.76	3.22
$\Delta E_{HOMO\text{-}LUMO}$ [eV]	8.28	7.40	8.14	7.63
$\lambda = \infty$ nm				
α_{av}	350.71	350.10	355.06	355.30
$\beta_{(z;z,z)}$	1044.65	537.31	-2168.85	-2639.76
$\beta_{(y;y,y)}$	41.04	52.70	104.68	109.34
$\beta_{(x;x,x)}$	-248.52	22.73	-100.11	15.51
$\beta_{(z)}$	1523.84	724.76	-2292.25	-2819.59
$\beta_{(y)}$	-136.73	60.13	558.23	491.70
$\beta_{(x)}$	-1006.47	-329.12	-435.71	-159.84
β_{vec}	1135.96	648.52	-2265.53	-2780.98
$\gamma_{(z;z,z,z)}$	343711.47	330617.13	767234.87	791318.81
$\gamma_{(y,y,y,y)}$	48954.49	48539.51	50901.80	50908.98
$\gamma_{(x,x,x,x)}$	115376.98	115549.46	57430.04	57834.65
γ_{vec}	180307.29	176382.50	220527.36	225157.26
$\lambda = 1064$ nm				
α_{av}	357.80	357.12	363.20	363.48
$\beta_{(z;z,z)}$	1572.70	777.96	-4137.86	-4948.54
$\beta_{(y;y,y)}$	46.20	61.85	137.02	143.08
$\beta_{(x;x,x)}$	-324.26	58.71	-133.51	10.03
$\beta_{(z)}$	2217.61	981.05	-4330.76	-5222.10
$\beta_{(y)}$	-184.41	115.23	1013.38	933.95
$\beta_{(x)}$	-1388.61	-391.90	-768.51	-399.55
β_{vec}	1788.29	906.73	4280.09	-5153.42
$\gamma_{(z;z,z,z)}$	993705.63	945275.89	3724893.11	3973896.27
$\gamma_{(y,y,y,y)}$	74163.25	73612.20	79697.59	79753.69
$\gamma_{(x,x,x,x)}$	263106.60	270761.76	92578.30	92535.93

The local electric field calculated for the L2 molecules embedded into the PMMA matrix is equal to the 1.03 GV/m. It is the highest value of the local electric field calculated for the investigated TTF derivatives in PMMA. It is caused by the fact that the L2 molecules are closer to the PMMA structure than the L1. Analyzing data presented in Tab. 7.8. one can see that the PMMA matrix increases the electric dipole moment of the $L2^a$ chromophores decreasing its HOMO-LUMO energy difference. The same situation was noticed for the $L1^a$ molecule. The polymer matrix also decreases $\Delta E_{HOMO\text{-}LUMO}$ of the $L2^b$ molecule simultaneously decreasing

its dipole moment. The changes are not significant. In this case, one can conclude that the molecules L2ᵃ and L2ᵇ can be embedded into the PMMA matrix for NLO applications. The PMMA polymer does not have a significant impact on the polarizability of the L2 chromophores and almost does not affects their third-order NLO parameters. The PMMA drastically increases the second-order hyperpolarizability of the L2ᵇ chromophores. The L2ᵇ possesses the highest β_{av} value of all of the investigated samples. Additionally, these chromophores are not sensitive to the back relaxation process. All these facts give an impact on the highest second-order susceptibility of the L2 chromophores embedded into the PMMA matrix.

Table 7.9. Electric and optical properties of the L3 molecules calculated in vacuum (F_x,F_y,F_z=0,0,0) and PMMA polymer environment ($F_x,F_y,F_z\neq$0,0,0) in volumetric form by using the *ab initio* method.

Molecule	L3ᵃ		L3ᵇ	
F [GV/m]	0, 0, 0	0.02, 0.13, -0.16	0, 0, 0	0.02, 0.13, -0.16
μ [D]	8.87	8.43	11.04	10.69
$\Delta E_{HOMO-LUMO}$ [eV]	7.89	8.03	8.02	8.08
$\lambda=\infty$ nm				
α_{av}	371.32	371.13	371.19	371.06
$\beta_{(z;z,z)}$	1834.58	1533.67	1631.59	1537.15
$\beta_{(y;y,y)}$	272.34	279.97	122.76	124.24
$\beta_{(x;x,x)}$	-37.96	-36.79	-379.67	-366.43
$\beta_{(z)}$	2686.05	2368.38	2458.76	2320.57
$\beta_{(y)}$	852.72	857.34	1527.34	1489.10
$\beta_{(x)}$	-217.8	-207.87	-1400.23	-1348.55
β_{vec}	2809.73	2510.19	2533.30	2404.97
$\gamma_{(z;z,z,z)}$	1059995.74	1038024.70	448094.58	445438.97
$\gamma_{(y,y,y,y)}$	77143.98	76659.42	88791.59	88421.38
$\gamma_{(x,x,x,x)}$	38617.08	38710.17	100760.74	100176.14
γ_{vec}	272530.64	267830.58	179103.70	242816.49
$\lambda=1064$ nm				
α_{av}	380.51	380.28	380.42	380.33
$\beta_{(z;z,z)}$	3403.30	2892.62	2336.48	2178.77
$\beta_{(y;y,y)}$	417.98	425.62	286.57	283.29
$\beta_{(x;x,x)}$	-43.63	-42.20	-627.24	-605.21
$\beta_{(z)}$	4565.24	4030.50	3773.85	3544.41
$\beta_{(y)}$	1189.03	1186.03	2374.46	2299.18
$\beta_{(x)}$	-338.95	-320.26	-2227.31	-2136.91
β_{vec}	4705.35	4189.16	3862.52	3644.54
$\gamma_{(z;z,z,z)}$	4263921.80	4065808.73	1758796.83	1738381.81
$\gamma_{(y,y,y,y)}$	151023.79	149437.26	237004.07	233665.54
$\gamma_{(x,x,x,x)}$	56740.91	56883.22	282141.51	277440.05

The local electric field acting on the L3 molecules embedded into the PMMA matrix is equal to 0.21 GV/m. It is the lowest value obtained for all investigated composites. The optical parameters calculated for the L3 molecules are collected in Table 7.9. One can see that the PMMA matrix is almost neutral for the L3 molecule in both conformers. It does not change the electric dipole moments of the chromophores and their HOMO-LUMO energy difference. Also, the second-order NLO parameters are not affected by the PMMA matrix. The PMMA matrix has an insignificant impact on the third-order NLO parameters of the L3. It confirms the statement that a higher third-order NLO signal obtained for PLD prepared thin films of L3 comes from inter-chromophore interaction and it is the effect of the intrinsic properties of the L3 molecules. PMMA matrix is rather neutral for the L3 chromophores. It is caused by the highest value of the γ_{av} possession by L3[a] chromophores compared to the other investigated molecules.

The local electric field calculated for the L4 molecules embedded into the PMMA matrix is equal to 0.57 GV/m. It increases the electric dipole moment of both conformers by more than 1 D, decreasing the HOMO-LUMO difference of conformer *a* and increases insignificantly this value for *b* conformer (see Fig. 7.10.). The PMMA matrix increases the second-order susceptibility of the L4 molecule in both conformers almost not changing their third-order hyperpolarizabilities values. One should be noted that the L4[b] conformer has a very low β_{av} value. This molecule will not give an important signal of the SHG.

Concluding, the highest polarizabilities calculated in a vacuum are noticed for both conformers of the L3 molecule. The same situation is noticed for static and frequency-dependent data. Also, the second-order and third-order hyperpolarizability of the L3 molecules in both conformers possesses the highest values. Almost the same value of β_{av} was calculated for the L2[b] chromophore. It means that the para-position of the TTF group on the pyridine tends to increase the NLO properties of the investigated chromophores. From experimental investigations, one may see that the highest SHG signal was measured for molecule L2. As it was described above the discrepancies are caused by the intermolecular interactions occurring between molecules L2 and the polymeric matrix. The L2 molecule enters into the cage of polymer interacting with it keeping the alignment during the time.

Table 7.10. Electric and optical properties of the **L4** molecules calculated in vacuum (F_x,F_y,F_z=0,0,0) and PMMA polymer environment (F_x,F_y,F_z≠0,0,0) in volumetric form by using the *ab initio* method.

Molecule	L4[a]		L4[b]	
F [GV/m]	0, 0, 0	0.03, 0.37, 0.43	0, 0, 0	0.03, 0.37, 0.43
μ [D]	8.38	9.60	9.65	10.68
$\Delta E_{HOMO-LUMO}$ [eV]	7.74	7.28	7.83	7.91
$\lambda = \infty$ nm				
α_{av}	362.74	363.61	351.66	351.78
$\beta_{(z;z,z)}$	197.62	576.51	664.40	886.57
$\beta_{(y;y,y)}$	428.23	551.11	-1291.72	-1160.53
$\beta_{(x;x,x)}$	-192.73	-237.06	11.94	11.62
$\beta_{(z)}$	1440.12	2015.46	705.52	978.04
$\beta_{(y)}$	1357.61	1693.42	-540.44	-389.39
$\beta_{(x)}$	-1016.19	-1235.13	-81.82	-69.96
β_{vec}	1698.35	2324.69	446.08	894.45
$\gamma_{(z;z,z,z)}$	355253.54	366340.05	288943.31	296072.59
$\gamma_{(y,y,y,y)}$	93064.68	98642.55	194320.19	186419.31
$\gamma_{(x,x,x,x)}$	54669.37	56463.67	31901.04	31819.16
γ_{vec}	174379.43	182956.26	137652.19	137585.37
$\lambda = 1064$ nm				
α_{xx}	274.67	275.31	167.80	167.75
α_{yy}	353.09	354.33	432.58	431.75
α_{zz}	484.12	485.19	475.93	477.23
α_{av}	370.63	371.61	358.77	358.91
$\beta_{(z;z,z)}$	528.86	1117.53	983.49	1321.85
$\beta_{(y;y,y)}$	643.66	824.10	-1823.62	-1633.18
$\beta_{(x;x,x)}$	-283.40	-350.36	12.05	11.94
$\beta_{(z)}$	2258.99	3146.95	1138.44	1627.22
$\beta_{(y)}$	1944.75	2602.80	-621.31	-707.85
$\beta_{(x)}$	-1454.60	-1796.92	-139.26	-119.70
β_{vec}	2601.77	3667.28	943.73	1460.30
$\gamma_{(z;z,z,z)}$	1018411.52	1093392.47	814810.82	848786.26
$\gamma_{(y,y,y,y)}$	209718.26	235816.59	482526.10	443882.12
$\gamma_{(x,x,x,x)}$	105008.01	113404.92	46965.35	46781.93

The highest dipole moment and second-order hyperpolarizability are observed for molecule L3 but the $\Delta E_{HOMO-LUMO}$ is more or less the same for all the four molecules. In this case, the THG signal should be the highest one for molecule L3 and it is in agreement with the experimental data obtained for the PLD deposited films. For the thin films based on PMMA, the molecules L1, L2, L3, and L4 give a lower signal than for the PLD materials. It is probably due to the aggregation effect which cancels the intensity of dipole moment or the interaction with the polymeric matrix is destructive in this case. It is especially seen for the L4 and L3 molecules with a high dipole moment.

The performed calculations show that a minor modification of the composition and arrangement of the molecule can significantly affect the linear and NLO properties of the composite system. These differences are caused due to different delocalization of π-electrons traveling freely along with the conjugated structure of molecules. These delocalized π-electrons are the key factor to high nonlinearities in organic materials [24 – 26].

7.4. Conclusions

In the present chapter, the *guest-host* composites based on the PMMA polymer and L1, L2, L3, and L4 chromophores in the bulk and thin film form were investigated. The structural properties of modeled systems obtained by MD simulations were discussed. The influence of the external poling electric field on the chromophores arrangement was studied. Also, their optical parameters were measured experimentally and computationally.

Analyzing the MD simulation results one can conclude that the L3 and L4 molecules enter more deeply into the bulk PMMA polymer structure than the L1 and L2 molecules. This behavior is significantly visible for the system in the glassy state (at T=300 K). It can be inferred that the chromophores possessing the 2,4-dinitro phenyl groups tend to be located more between polymer mers than the chromophores with 2,4-dimethyl phenyl groups. Additionally one can add that the para-position of the TTF group on the pyridine tends to the closer location of the chromophores to a polymer chain.

In the case of polymer thin-film, all chromophores are located in the polymer matrix with a distance from PMMA of about 0.4 nm. The chromophores do not enter into the polymer chain (between mers). It means that the surface of the polymer is less dense than it is observed for a bulk *guest-host* composite system. It has a great influence on the chromophore alignment under influence of the external electric field. Is much easier to align the chromophores in the thin film form of the PMMA than in the bulk materials.

The L2 chromophores in the bulk *guest-host* system are the easiest to be aligned compared to the remaining chromophores. The molecules L3 and L4 are significantly more difficult to be aligned than the L1 and L2 chromophores. This is what happens even though the molecules L3 and L4 possess much bigger electric

dipole moment than the L1 and L2 chromophores and their interaction with the external electric field is much higher. The difficult alignment of the molecules L3 and L4 should be caused by their location in the polymer cages where rotation is difficult. However, the structure of composites L3/PMMA and L4/PMMA are more stable concerning the back relaxation of the chromophores.

Electron and optical properties of the L1, L2, L3, and L4 chromophores were investigated computationally by applying quantum chemical methods. These chromophores embedded into the PMMA matrix were also studied experimentally into account of their optical properties. Optimizing the geometry of the L1, L2, L3, and L4 molecules, two conformers of each one were found. Additionally was found that the probability of founding chromophores in both confirmations is almost the same.

The HOMO orbital of all L1, L2, L3, and L4 molecules is located in the TTF group. It confirms that the TTF moiety possesses a donor character. The LUMO orbital of all molecules is located at the 2,4-dimethyl phenyl or 2,4-dinitro phenyl group possessing an acceptor nature. The electric dipole moments of the L3 and L4 molecules are much higher than the ones of the L1 and L2 molecules. This allows us to conclude that the 2,4-dinitro phenyl group in the L3 and L4 structures increases their polarity. According to the high dipole moment of the L3 and L4 molecules was proved that the inter-chromophore interaction is stronger than the interaction between chromophores and polymer. It is due to the multipolar intermolecular interaction.

The UV-vis absorption spectra of the investigated molecules were reproduced by using the *ab initio* and the DFT/LC-BLYP functional. For the L3 and L4 molecules possessing much higher dipole moment, better results are given by the DFT/LC-BLYP formalism. It is caused by the nature of the method and important charge redistribution in molecules possessing 2,4-dinitro phenyl groups.

The nonlinear optical properties of thin films deposited by PLD and spin-coating techniques were investigated by using the SHG and THG techniques. The formation of agglomerates in the polymer matrix makes it difficult to interpret the results and the possibility of comparing them with theoretical data. For this reason, the laser ablation technique gives correct experimental results and good compliance with the obtained theoretical data. Chromophores L1 and L3 exhibit more interesting third-order nonlinear optical properties than L2 and L4. The second-

order NLO signal is given with the highest intensity by the L2/PMMA composite. It can be explained by the fact that the PMMA matrix is acting on the L2 chromophores creating the highest local electric field. The polymer matrix increases the electric dipole moment of the L2^a chromophores decreasing its HOMO-LUMO energy difference. The PMMA drastically increases the second-order hyperpolarizability of the L2^b chromophores. Additionally, the L2^b possesses the highest β_{av} value of all of the investigated samples. The high NLO performance of the L2/PMMA composite is supported by the fact that the L2 chromophores are not sensitive to the back relaxation process. All these facts give an impact on the highest second-order susceptibility of the L2 chromophores embedded into the PMMA matrix.

The results obtained for the L2/PMMA *guest-host* system are encouraging for their different NLO applications like optical communications and optical switching.

References

[1]   Froimowitz M., Biotechniques, 14(6), 1010-3 (1993).

[2]   Abraham M., Hess B., Spoel D. V. D., Lindahl E., Gromacs User Manual, Version 5.0.4. The GROMACS development team at the Royal Institute of Technology and Uppsala University, Sweden. www.gromacs.org

[3]   Hagler A. T., Lifson S., Dauber P., Journal of the American Chemical Society, 5122-5130 (1979).

[4]   Fois E., Gamba A., Tilocca A., Microporous and Mesoporous Materials, 57, 263-272 (2003).

[5]   Kawata M., Nagashima U., Chemical Physics Letters, 340, 165-172 (2001).

[6]   Deserno M., Holm Ch., J. Chem. Phys., 109, 7678-7693 (1998).

[7]   Gordon M.S., Schmidt M.W., Advances in electronic structure theory: GAMESS a Decade Later, C. E. Dykstra, G. Frenking, K.S. Kim, G.E. Scuseria, (eds.), in: Theory and Applications of Computational Chemistry: the first forty years. Elsevier, Amsterdam, Netherlands, 1167-1189 (2005).

[8]   Mennucci B., WIREs Comput Mol Sci, 2, 386-404 (2012).

[9]   Davidson E. R., Methods in computational molecular physics, Reidel, Boston 95-113 (1983).

[10]   Ayadi A., Mydlova L., Zouari N., Makowska-Janusik M., Sahraoui B., El-Ghayoury A., Opt. Mat. 56, 27-35 (2016).

[11]   Patil S. K., Wari M. N., Yohannan Panicker C., Inamdar, S. R., Int. J. Adv. Res. 1, 616-626 (2013).

[12]   Ayadi A., Alamy, A. E., Alévêque, O., Allain, M., Zouari, N., Bouachrine, M., El-Ghayoury, A., Beilstein J. Org. Chem. 11, 1379-1391 (2015).

[13]   B. M. Wong, Mater. Res. Soc. Symp. Proc. 1120, 01-03 (2009).

[14]   Zawadzka A., Płóciennik P., Strzelecki J., Korcala A., Arof A. K., Sahraoui B., Dyes and Pigments, 101, 212-220 (2014).

[15]   Zawadzka A., Waszkowska K., Karakas A., Plociennik P., Korcala A., Wisniewski Z., Karakaya M., Sahraoui B., Dyes And Pigments, 157, 151-162 (2018).

[16]   Svorcık V., Lyutakov O., Huttel I., J Mater Sci: Mater. Electron., 19, 363–367 (2008).

[17]   Maker P.D., Terhune R.W.,Nisenhoff M., Savage C. M., Phys. Rev. Lett., 8, 21-22 (1962).

[18]   Lee G. J., Cha S. W., Jeon S. J., Jin J.-I., Yoon J. S., J.-Korean Phys. Soc., 39, 912-915 (2001).

[19]   Kubodera K., Kobayashi H., Mol. Cryst. Liq. Cryst. Inc. Nonlinear Opt. 182, 103-113 (1992).

[20]   Kurtz S. K., Jerphagnon J., Choy M. M., Landolt-Boernstein New Series, 11, 671 (1979).

[21]   Kajzar F., Okada-Shudo Y., Meritt C., Kafafi Z., Synth. Met., 117, 189 (2001).

[22]   Cho M. J., Choi D. H., Sullivan P. A., Akelaitis A. J. P., Dalton L. R., Progress in Polymeric Science, 33, 1013-1058 (2008).

[23]   Aidas K., Angeli C., Bak K. L., Bakken V., Bast R., Boman L., Christiansen O., Cimiraglia R., Coriani S., Dahle P., Dalskov E. K., Ekström U., Enevoldsen T., Eriksen J. J., Ettenhuber P., Fernández B., Ferrighi L., Fliegl H., Frediani L., Hald K., Halkier A., Hättig C., Heiberg H., Helgaker T., Hennum A. C., Hettema H., Hjertenæs E., Høst S., Høyvik I.-M., Iozzi M. F., Jansik B., Jensen H. J. Aa., Jonsson D., Jørgensen P., Kauczor J., Kirpekar S., Kjærgaard T., Klopper W., Knecht S., Kobayashi R., Koch H., Kongsted J., Krapp A., Kristensen K., Ligabue A., Lutnæs O. B., Melo J. I., Mikkelsen K. V., Myhre R. H., Neiss C., Nielsen C. B., Norman P., Olsen J., Olsen J. M. H., Osted A., Packer M. J., Pawlowski F., Pedersen T. B., Provasi P. F., Reine S., Rinkevicius Z., Ruden T. A., Ruud K., Rybkin V., Salek P., Samson C. C. M., Sánchez de Merás A., Saue T., Sauer S. P. A., Schimmelpfennig B., Sneskov K., Steindal A. H., Sylvester-Hvid K. O., Taylor P. R., Teale A. M., Tellgren E. I., Tew D. P., Thorvaldsen A. J., Thøgersen L., Vahtras O., Watson M. A., Wilson D. J D., Ziolkowski M., and Ågren H., WIREs Comput. Mol. Sci. 4, 269–284 (2014).

[24]   Sahraoui B., Sylla M., Bourdin J. P., Rivoire G., Zaremba J., Nguyen T. T., Sallé M., Journal Of Modern Optics, 42, 10 , 2095-2107 (1995).

[25]   Terkia-Derdra N., Andreu R., Sallé M., Levillain E., Orduna J., Garin J., Orti E., Viruela R., Pou-Amérigo R., Sahraoui B., Gorgues A., Favard J.-F., Riou A., Chemistry-A European Journal, 6, 7, 1199-1213 (2000).

[26]   Fuks-Janczarek I., Luc J., Sahraoui B., Dumur F., Hudhomme P., Berdowski J., Kityk I. V., Journal Of Physical Chemistry B, 109, 20, 10179-10183 (2005).

Chapter 7

Chapter 8

Physical properties of benzonitrile-based composite materials

Despite all efforts, the handling of L1, L2, L3, and L4 molecules presented in Chapter 7 has been very time-consuming and difficult. Additionally, the agglomeration of the L1, L2, L3, and L4 molecules embedded in the PMMA polymer matrix decreases the NLO signal coming from synthesized composites. Because of this, it was decided to continue the investigation with new three molecules based on benzonitrile derivatives.

This chapter is devoted to describing the structural, electronic, and optical properties of A, B, and C chromophores (see Fig. 8.1) embedded in the polymer matrix. Two different environments were considered as a host, namely poly(1-vinylcarbazole) (PVK) and poly (methyl methacrylate) (PMMA) polymers. The chosen polymers have different electric dipole moments and can react on the

chromophores with different intensities. The structural properties of the composite materials were modeled by using the molecular dynamic (MD) method. The optical properties of the composites were calculated by applying the discrete local field model. The obtained results were compared with the experimentally measured data. In addition, structural, electron, and optical properties of isolated chromophores based on benzonitrile derivatives were investigated computationally by applying quantum chemical methods. The obtained parameters were discussed in the context of the polymer matrix's influence on the physical properties of chromophores.
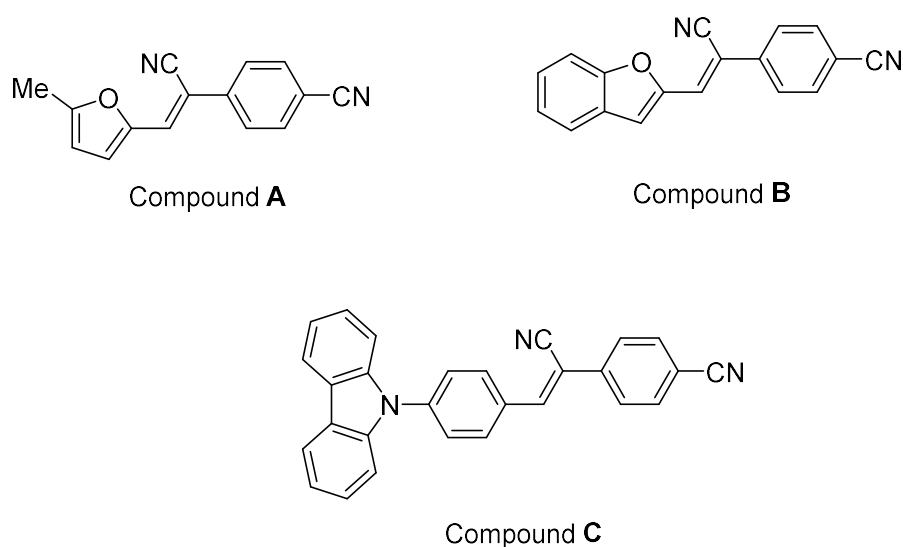
Figure 8.1. Structures of investigated chromophores A, B, and C

8.1. Molecular dynamic simulation of *guest-host* materials based on PMMA and PVK polymer matrixes and benzonitrile derivatives

8.1.1. Methodology of MD simulations

The *guest-host* structures based on A, B, and C molecules embedded into PMMA and PVK polymer were built using the MD simulations technique implemented in GROMACS 5.0.4 software [1]. Three initial complexes based on two chromophore molecules and one polymer chain closed in one unit cell were created for each A, B, and C chromophores and each polymer matrix. The polymer was built as one isotactic 90-mer PMMA or 90-mer PVK chain with a molecular weight of 9012.58 amu and 9501.03 amu for PMMA and PVK, respectively. Every

investigated unit cells were cubic with an edge length equal to 26.12 Å for A, B, and C molecules with PMMA and 25.40 Å for systems based on PVK polymer matrix. The corresponding density was equal to 1.0 g/cm^3 for A/PMMA (5.5 wt % of the A molecules in the system), 1.0 g/cm^3 for B/PMMA (5.8 wt %), and C/PMMA (6.3 wt %). For the PVK-based composites, these densities were equal to 0.96 g/cm^3 for A/PVK (4.7 wt % of the A molecules in the system), 1.0 g/cm^3 for B/PVK (5.2 wt %), and 1.0 g/cm^3 C/PVK (5.9 wt %). The obtained densities correspond to the liquid state of the investigated complexes. An example of the composite system is presented in Fig. 8.2.
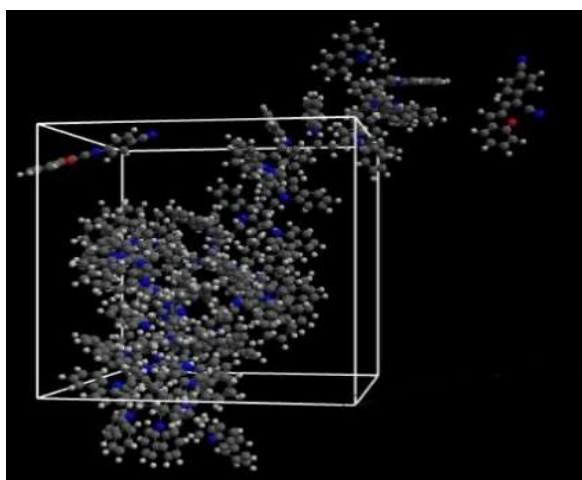
Figure 8.2. An example of the A/PMMA composite system in a liquid state (at T=500 K) modeled by the MD method.

Each initial composite structure has been optimized by two methods. Firstly, the steepest descent algorithm was used with a convergence criterion equal to 200 kcal mol^{-1} Å^{-1}. Then the optimization procedure was continued by the conjugate gradient method with a convergence criterion equal to 50 kcal mol^{-1} Å^{-1}. The MD simulations were performed in the x, y, and z periodic boundary conditions.

The classic MD simulations were performed for all modeled composite systems solving the classical equations of motion for the time-dependent positions (and velocities) of atoms as it was described in Chapter 7. The non-bonded interactions were calculated with the Lennard-Jones 12-6 potential. The Coulombic potential was calculated using fixed partial charges of atoms. Bonded interactions were computed due to a fixed list of atoms. Bond stretching and bond bending were described by harmonic potentials, whereas dihedral angle distortions were modeled

by a simple cosine function. The all-atom consistent valence force field (CVFF) [2,3] was selected for the presented MD study.

All MD simulations described in this chapter were performed with the following parameters: the simulation time step was 1 fs, and the short-range neighbor list was created employing the grid search method with a cut-off distance of 1.00 nm. Lennard-Jones and Coulomb interactions were computed within the neighbor list applying periodic boundary conditions. The long-range interactions were calculated using the three-dimensional particle-mesh Ewald method (PME) [4,5] with the cut-off distance equal to 1.1 nm for all complexes. The energies, coordinates, and velocities were recorded every 1 ps. The major part of the simulations was performed in the NVT canonical ensemble employing the Nose-Hoover extended algorithm. Also, simulations in an NPT ensemble were performed applying the Rahman-Parrinello method to control the pressure during simulations.

First of all the geometry optimized composite structures were relaxed for 2.0 ns at 500 K to obtain their equilibrium state. The stable total energy was reached after 1.5 ns of the MD simulations for all structures. The next step of the MD simulations was devoted to aligning the chromophores in a polymeric matrix above the T_g temperature. In this case, the poling external electric field in the Z-direction to all systems was applied and the structures were modeled during 1.5 ns. The intensity of the applied electric field for bulk complexes was equal to 1, 3, 5, 10, or 15 kV/μm. One should notice that the experimentally commonly-used electric field in the corona poling process is equal to 5 kV. However, we want to achieve the steady states of the composite system within the time scale of the simulations, so electric field intensity should be correspondingly higher. The simulation conditions of bulk materials and thin films were the same for all composite systems to maintain the consistency and uniformity of the results so that the results could be compared.

Studies described in the work [6] have proved that using the CVFF force field the T_g of the PMMA with embedded chromophores is lower than 500 K. Experimentally was shown that the T_g of the PMMA is 378-438 K [7]. Experimentally measured T_g of the PVK is equal to 435 K [8]. In this case, was decided that the PVK and PMMA polymer with small chromophores in its matrix can be modeled at 500 K in a liquid state and at 300 K in a glassy solid state. Based on these results we assumed that the simulated structures at 500 K are a little bit above the glass transition temperature with the chromophores able to be rotated

according to the application of the external electric field. To model solid-state structures representing the experimentally used *guest-host* materials, the simulated annealing (SA) process was implemented for all investigated systems. In this case, the simulations were performed in NPT condition during 1.5 ns cooling of the systems from 500 K up to 300 K. During the simulation the external electric field was acting. The cooling rate in all cases was 1.3×10^{11} K/s. After annealing, the simulated systems were relaxed during 1.5 ns in the NVT assemble without an external electric field.

Three different thin-film structures were created from each of the bulk A/PMMA, B/PMMA, C/PMMA, A/PVK, B/PVK, and C/PVK composite systems. All of them consist of one isotactic 90-mer polymer chain and two chromophores as was in the case of bulk composites. The simulation boxes of the investigated thin-film composites were equal to 26.12 Å × 26.12 Å × 78.36 Å for PMMA based systems, and 26.88 Å × 26.88 Å × 80.64 Å for PVK composite systems. The three equivalent structures were simulated by MD for each thin-film system. The change of cubic cell of bulk materials to thin-film unit cell as well as all molecular simulations were performed using the GROMACS 5.0.4 software package. The geometry of each thin-film composite system was optimized according to the total energy minimization by the steepest descent method applying a convergence criterion equal to 100 kcal mol^{-1} Å^{-1} and then by conjugate gradient method with a convergence criterion of 20 kcal mol^{-1} Å^{-1}, followed by an NVT and NPT MD simulation. The composite systems were relaxed using the MD simulation with the time of 1.5 ns at 500 K using a step size of 1 fs. The trajectories were recorded every 1 ps. The CVFF was implemented for the MD study.

Investigated thin-film composites were simulated by MD at temperature *T*=500K using two-dimensional (3D) periodic boundary conditions but the long-range non-bonded interactions were calculated using the 2D Ewald method. Infinite extensions of the composite systems have been applied along the X and Y axes and finite-length in Z-direction was defined. The constant temperature during simulations was achieved by the NVT canonical ensemble using the Nose-Hoover method as well as the constant pressure was maintained by the Parrinello-Rahman method (NPT ensemble). The obtained structures in a liquid state were exposed to a poling external electric field applied along the Z-axes and simulated for a further

1.5 ns. The values of the external poling field were equal to 0.5, 1, 3, or 5 kV/μm. Then the thin-film structures were annealed from 500 K up to 300 K, from liquid to glassy state. It was done with the presence of the poling electric field during 1.5 ns with a cooling rate of 1.3×10^{11} K/s.

8.1.2. Structure of PMMA based composite systems

The spatial distribution of the chromophores in the polymer matrix was examined using the intermolecular radial distribution function (RDF) defined between the center of mass (COM) of selected groups of chromophores and the selected groups of the PMMA mers. These groups are presented in Fig. 8.3. The COM of the cyanovinyl (CN) moiety in both positions of the A, B, and C molecules were selected and named as 1.CN (CN at the side of the molecule) and 2.CN (CN at the back of the molecule). Also, the third active group of each chromophore was chosen. Namely, the COM of the methyl group (Me) in molecule A, the benzofuran of the B molecule, and the carbazole of the C molecule were chosen. The COMs of PMMA as the CH_2, bCH_3 (methyl group bonded to the back-bone α-carbon atom), sCH_3 (methyl group bonded to COO), and COO were defined to compute the RDFs. The COMs of the PMMA polymer were defined in the same way as it was done in Chapter 7.
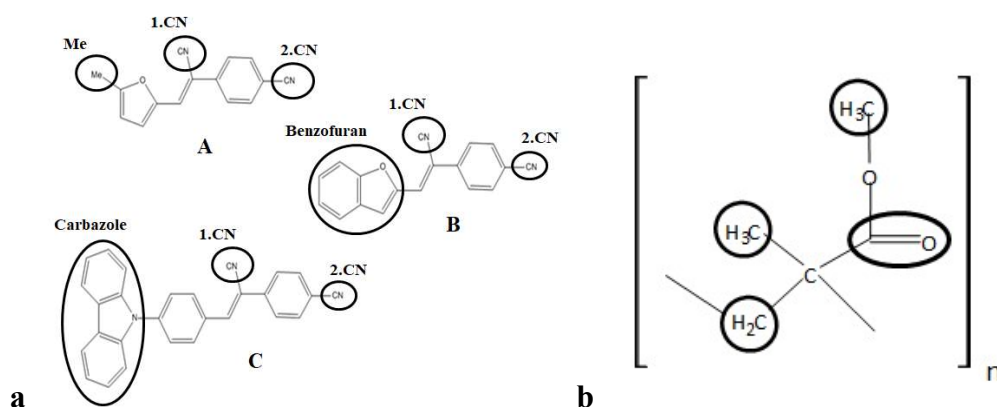
Figure 8.3. The COM groups defined for the RDFs calculations in structures of investigated chromophores A, B, C (a), and mer of the PMMA polymer (b).

The RDFs calculated at T=500 K and T=300 K for the bulk structures are presented in Figures: 8.4, 8.5, 8.6, and for the thin-film systems in Figures: 8.7, 8.8, 8.9. The methyl group of the A chromophore embedded into the bulk PMMA matrix

in the liquid state is located close to the side group sCH$_3$ and back bCH$_3$ group of the polymer chain and a distance is equal to 0.4 nm (see Fig. 8.4 (a)). The observed behavior is the same for other chosen groups of the A chromophores (see Fig. 8.4 (c) and Fig. 8.4 (e)). After solidification more pronounced is peak dependent on the distance between all selected groups of the A chromophore and the sCH$_3$ group of the polymer. It means that the structure is more ordered. The A chromophores in the glassy polymer do not enter between mers of the PMMA.

Figure 8.4. Partial RDFs calculated for distances between the center of mass of different moieties of the A molecule and different subunits of PMMA at T = 500K (a,c,e) and T=300K (b,d,f) for the bulk system. The RDFs are presented for methyl group (Me) of A molecule and different subunits of PMMA mer (a, b); for cyanovinyl CN1 at the side of the molecule A and different subunits of PMMA mer (c,d) and cyanovinyl CN2 at the back of the molecule A and different subunits of PMMA mer (e,f).

Figure 8.5. Partial RDFs calculated for distances between the center of mass of different moieties of the B molecule and different subunits of PMMA at T = 500K (a,c,e) and T=300K (b,d,f) for the bulk system. The RDFs are presented for the benzofuran group of B molecule and different subunits of PMMA mer (a, b); for cyanovinyl CN1 at the side of the molecule B and different subunits of PMMA mer (c,d) and cyanovinyl CN2 at the back of the molecule B and different subunits of PMMA mer (e,f).

The RDFs obtained for the B/PMMA composite in a liquid state (see Fig. 8.5) show the shortest distance equal to the 0.4 nm between benzofuran and sCH$_3$, as well as between the 2.CN and sCH$_3$ (see Fig. 8.5 (a) and Fig. 8.5 (e). The distance calculated for the 1.CN and all groups of the PMMA is equal to 0.4 nm for the system in a liquid state (see Fig. 8.5 (c)). The same behavior is seen after the solidification of the composites (see Fig. 8.5 (d)). One can see that in the

B/PMMA glassy system distances between benzofuran and 2.CN of the B chromophore and the bCH3 groups of the PMMA appeared to be equal to 0.4 nm. It means that chromophores B enter into the structure of the PMMA polymer.

Figure 8.6. Partial RDFs calculated for distances between the center of mass of different moieties of the C molecule and different subunits of PMMA at T = 500K (a,c,e) and T=300K (b,d,f) for the bulk system. The RDFs are presented for the carbazole group of the C molecule and different subunits of PMMA mer (a, b); for cyanovinyl CN1 at the side of the molecule C and different subunits of PMMA mer (c,d) and cyanovinyl CN2 at the back of the molecule C and different subunits of PMMA mer (e,f).

The RDFs obtained for the C/PMMA system in a liquid state (see Fig. 8.6 (a, c, e)) show similar behavior to the one presented for the A/PMMA material (see Fig. 8.4 (a, c, e)). The closest distance between selected groups of C chromophores and polymer is equal to 0.4 nm and chromophores enter into the PMMA structure.

In the glassy state, the carbazole group of the C is located at a distance of 0.3 nm from the polymer in the C/PMMA composite. It is noticed mostly for the carbazole-sCH$_3$ distances. The remaining groups of C molecules are located at a distance of 0.4 nm from the sCH$_3$ group of PMMA. It means that the C chromophore does not enter into the structure of the polymer in a glassy state but is located very close to it.

The RDFs calculated for thin films of the A/PMMA, B/PMMA, and C/PMMA composite materials are presented in Fig. 8.7, 8.8, and 8.9. The RDFs calculated for thin films of the liquid A/PMMA (see Fig. 7.7 (a, c, e)) are similar to the ones calculated for bulk systems (see Fig. 8.4 (a, c, e)). The distance between chromophores A and polymer is equal to 0.4 nm and it stays the same after solidification. The solidified A/PMMA structure has more evident peaks representing the distances between all selected groups of chromophores and the sCH$_3$ and bCH$_3$ of polymer (see Fig. 8.7 (b, d, f)). It means that contrary to the bulk system, the chromophores enter into polymer structure when the A/PMMA composite is in thin-film form.

The B chromophores of the liquid B/PMMA thin-film system (see Fig. 8.8 (a, c, e)) do not enter into the polymer chain as was observed for the bulk structure (see Fig. 8.5 (a, c, e)). There the peak corresponding to the 1.CN – bCH$_3$ and 1.CN – sCH$_3$ distances equal to 0.4 nm can be observed. The other groups of the B molecules are located the closest to sCH$_3$ of the PMMA. In the glassy state of B/PMMA thin film the 1.CN and 2.CN groups are located at 0.4 nm from bCH$_3$ and sCH$_3$ groups of the PMMA (see Fig. 8.8 (b, d, f)). It allows us to conclude that in glassy thin-film B/PMMA the chromophores enter the polymer structure.

The C molecules composing the C/PMMA thin-film are not located so close to the polymer as is observed for the bulk material (see Fig. 8.9). There, the C molecules are located at 0.4 nm from sCH$_3$ and bCH$_3$ groups of the polymer. It allows us to conclude that the system is not so dense and the chromophores enter into polymer chain (see Fig. 8.9 (a, c, e)). When the system is solidified the chromophores are located close to the sCH$_3$ groups of the PMMA and they do not enter between mer units.
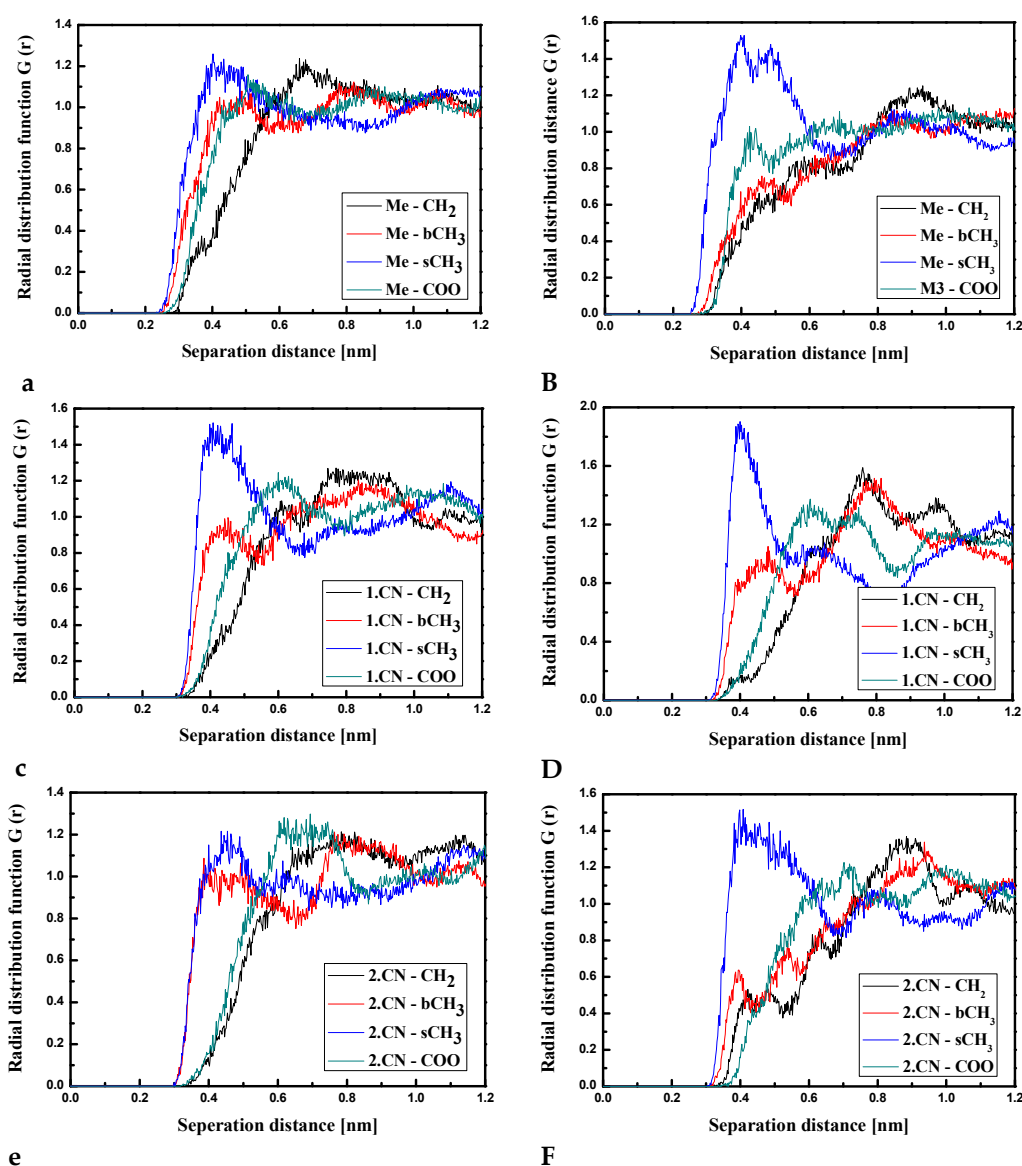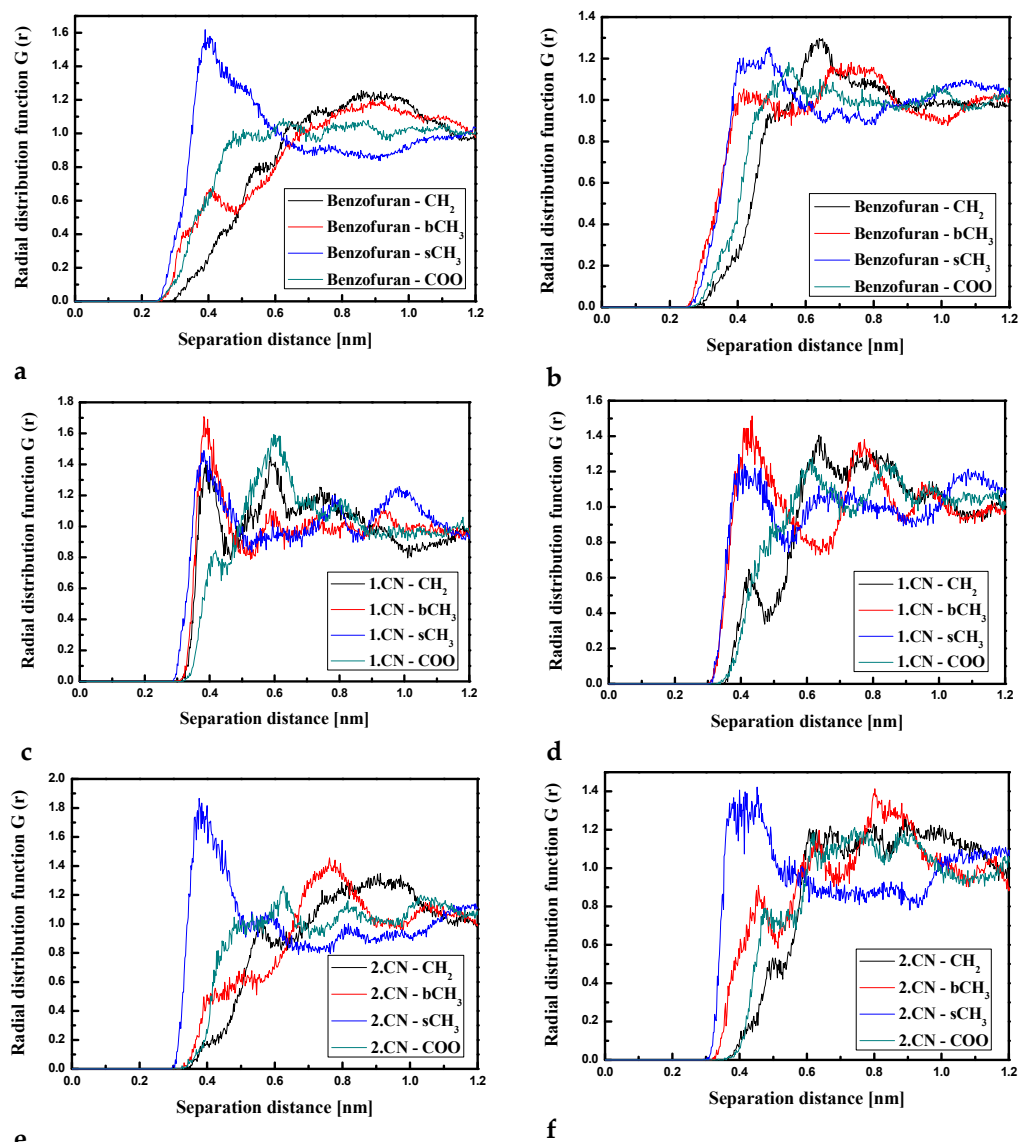
Figure 8.7. Partial RDFs calculated for distances between the center of mass of different moieties of the A molecule and different subunits of PMMA at T = 500K (a,c,e) and T=300K (b,d,f) for the thin film composite system. The RDFs are presented for methyl group (Me) of A molecule and different subunits of PMMA mer (a, b); for cyanovinyl CN1 at the side of the molecule A and different subunits of PMMA mer (c,d) and cyanovinyl CN2 at the back of the molecule A and different subunits of PMMA mer (e,f).

Figure 8.8. Partial RDFs calculated for distances between the center of mass of different moieties of the B molecule and different subunits of PVK at T = 500K (a,c,e) and T=300K (b,d,f) for the thin-film system. The RDFs are presented for the benzofuran group of B molecule and different subunits of PVK mer (a, b); for cyanovinyl CN1 at the side of the molecule B and different subunits of PVK mer (c,d) and cyanovinyl CN2 at the back of the molecule B and different subunits of PVK mer (e,f).
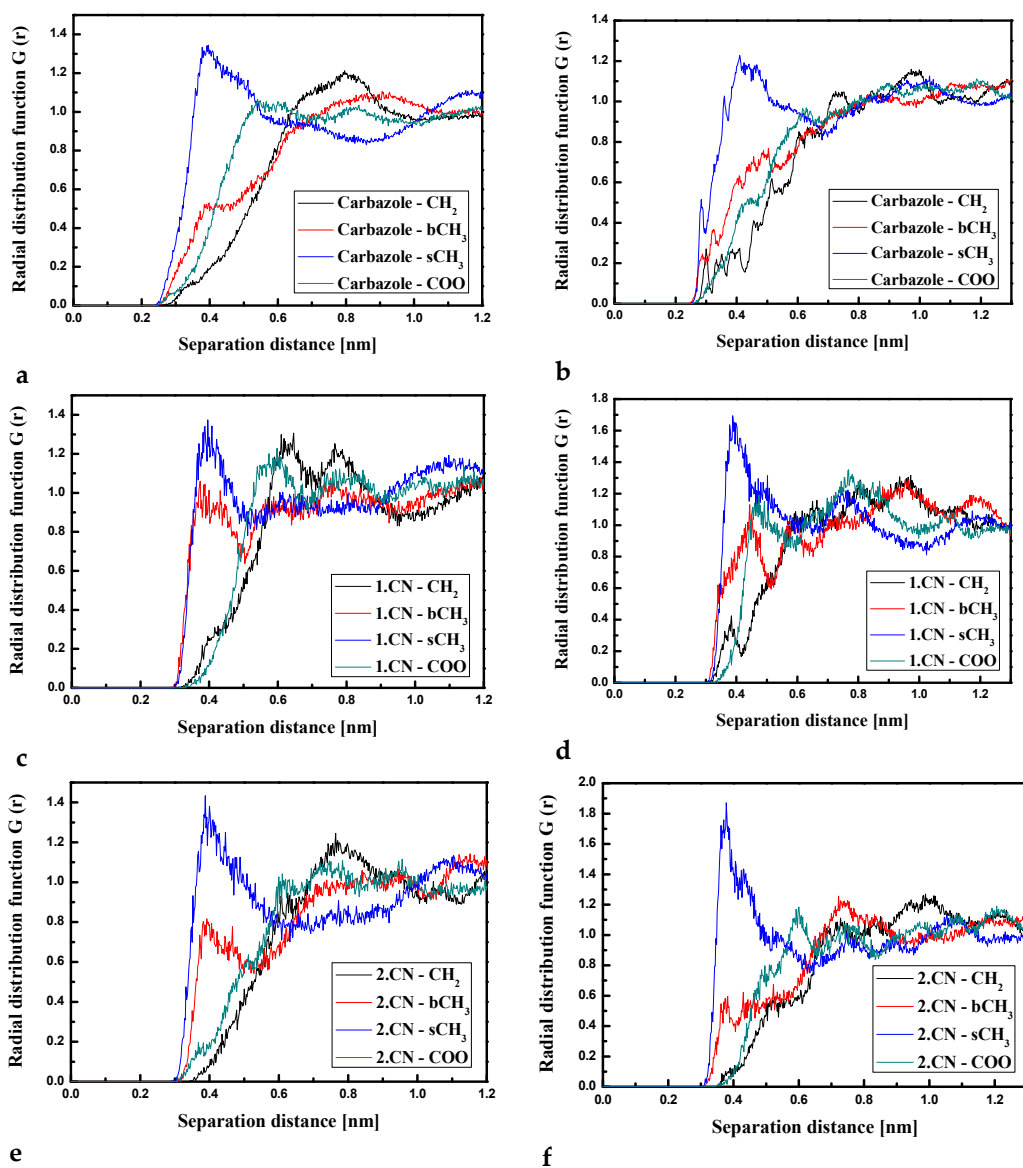
Figure 8.9. Partial RDFs calculated for distances between the center of mass of different moieties of the C molecule and different subunits of PVK at T = 500K (a,c,e) and T=300K (b,d,f) for the thin-film system. The RDFs are presented for the carbazole group of the C molecule and different subunits of PVK mer (a, b); for cyanovinyl CN1 at the side of the molecule C and different subunits of PVK mer (c,d) and cyanovinyl CN2 at the back of the molecule C and different subunits of PVK mer (e,f).

The A/PMMA, B/PMMA, and C/PMMA systems in bulk and thin-film forms were polled by an external electric field to obtain a noncentrosymmetric composite material useful for the generation of the second-order NLO signal. The system A/PMMA in the liquid state shows an almost complete alignment performed by an external electric field equal to 15, 10, and 5 kV/μm. At the end of the simulation process also the A/PMMA liquid system ordered by 3 kV/μm is aligned at 80 % (see Fig. 8.10 (a)). Solidification decreases the alignment of these systems up to 70-80 % giving relatively higher order. One can notice that molecules C shows a similar degree of alignment and it is even better than molecule A. In the case of

liquid bulk C/PMMA system, all used external electric fields align chromophores in 60 – 90 %. It is worthy to notice that the solidification does not decrease the chromophores' alignment. The B/PMMA system is the worst to be ordered. Here the even highest used external electric field aligns chromophores only in 70 % (see Fig. 8.10 (c)). The used electric fields equal to 1 and 3 kV/μm are too small to rotate chromophores located in the polymer cage. It is probably to the fact that the chromophores B enter into the polymer structure. The solidification does not decrease the order of the system (see Fig. 8.10 (d)).
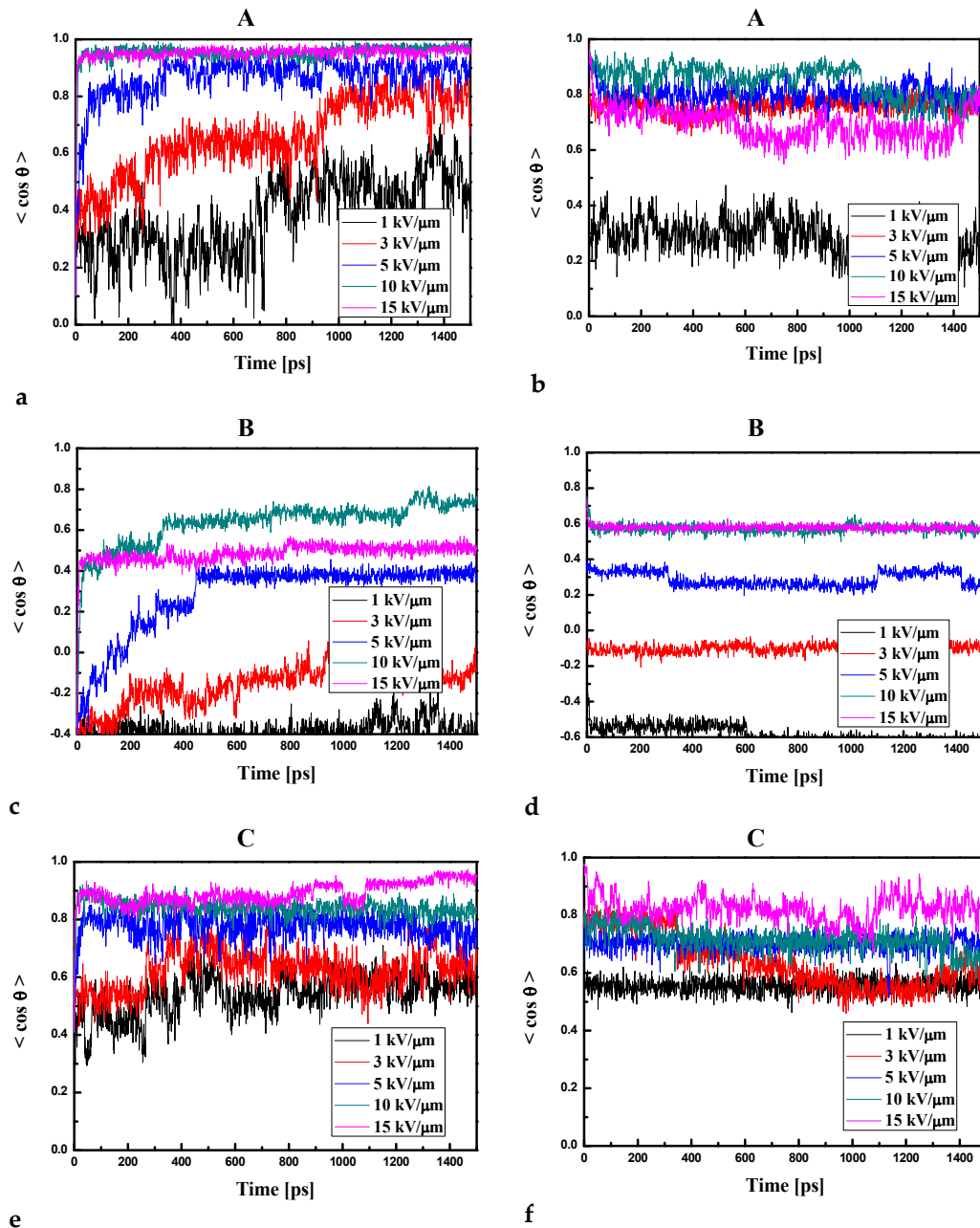
Figure 8.10. Changes in the value of the order parameter *<cosθ(t)>* versus the time of simulation and applied external electric field calculated by MD technique for the A/PMMA (a,b), B/PMMA (c,d), and C/PMMA (e,f) composites in the volumetric form at the temperature of 500 K (a,c,e) and glassy state (300 K) after the simulated annealing (b,d,f).
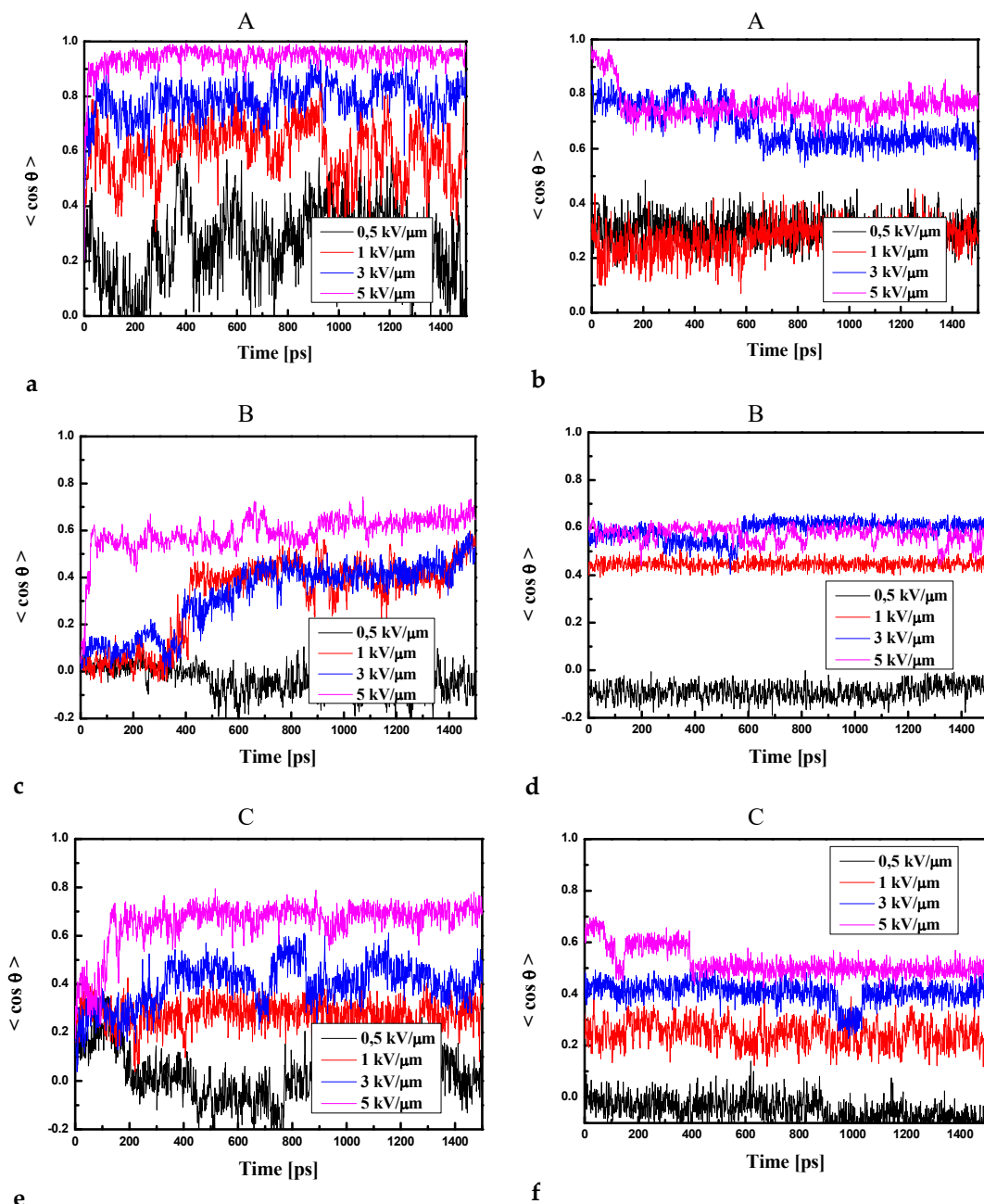
Figure 8.11. Changes in the value of the order parameter *<cosθ(t)>* versus the time of simulation and applied external electric field calculated by MD technique for the A/PMMA (a,b), B/PMMA (c,d), and C/PMMA (e,f) composites in the thin film form at the temperature of 500 K (a,c,e) and glassy state (300 K) after the simulated annealing (b,d,f).

The simulation of the alignment of chromophores was also performed for the thin-film systems of A/PMMA, B/PMMA, and C/PMMA (see Fig. 8.11). The applied external electric field is lower (0.5, 1, 3, and 5 kV/μm) than the one used for bulk material. During the initial setup of the external electric field, the order of A chromophores increased up to 90 % (see Fig. 8.11 (a)). The order degree slowly decreased as the values of the external local field decreased. During controlled

cooling, the order parameter slightly dropped to 80% and 60% for an external electric field equal to 5 kV/μm and 3kV/μm, respectively (see Fig. 8.11 (b)). The order parameters of the system aligned by 0.5 and 1 kV/μm decrease up to 30 %. As it was observed for the bulk composites also the B/PMMA system in thin-film form is the worst to be aligned. However, it should be noticed that the alignment difference between B/PMMA and C/PMMA in thin-film form is not so drastic as it was noticed for bulk composites. In both cases, of the B/PMMA and C/PMMA in thin-film form, the solidification does not decrease the order degree.

8.1.3. Structures of PVK based composite systems

The spatial distribution of the A, B, and C chromophores in the PVK polymer matrix was examined using the intermolecular radial distribution function (RDF) defined between the center of mass (COM) of selected groups of chromophores and the selected groups of the PVK mers (see Fig. 8.12). The COM groups of the chromophores were defined exactly as it was done in the case of the PMMA-based systems (see Fig. 8.3). Four COM groups for the PVK mer were defined. They were namely nitrogen (N) in the middle of the carbazole group, the CH_2 in the main chain of the PVK, and two benzenes, the first on the left labeled as $1.C_6H_6$ and the second one on the right labeled as $2. C_6H_6$ were chosen. The COMs of the different groups were computed for each snapshot.
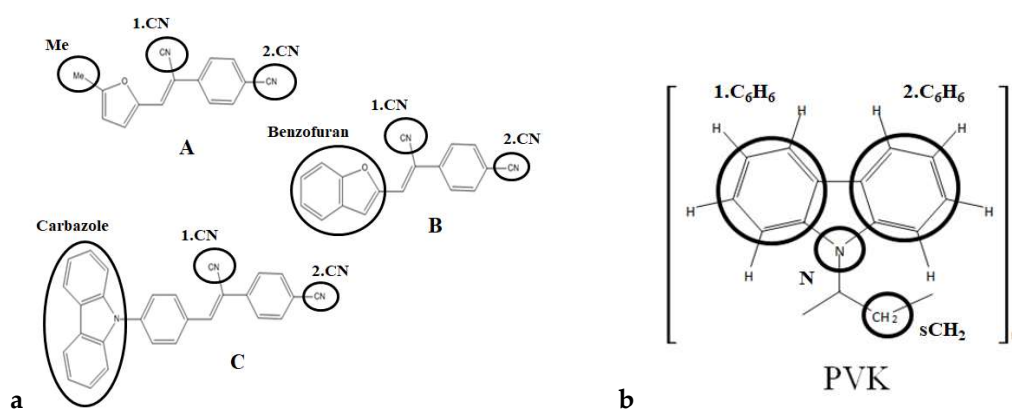
Figure 8.12. Structures of investigated chromophores A, B, C (a), mer of the PVK polymer (b) with marked their atomic groups chosen for the RDFs calculations.

The RDFs calculated for the A/PVK, B/PVK, and C/PVK structures investigated at T=500 K and T=300 K are presented in Figures 8.13-8.15 for bulk composite systems and Figures 8.16-8.18 for thin films.
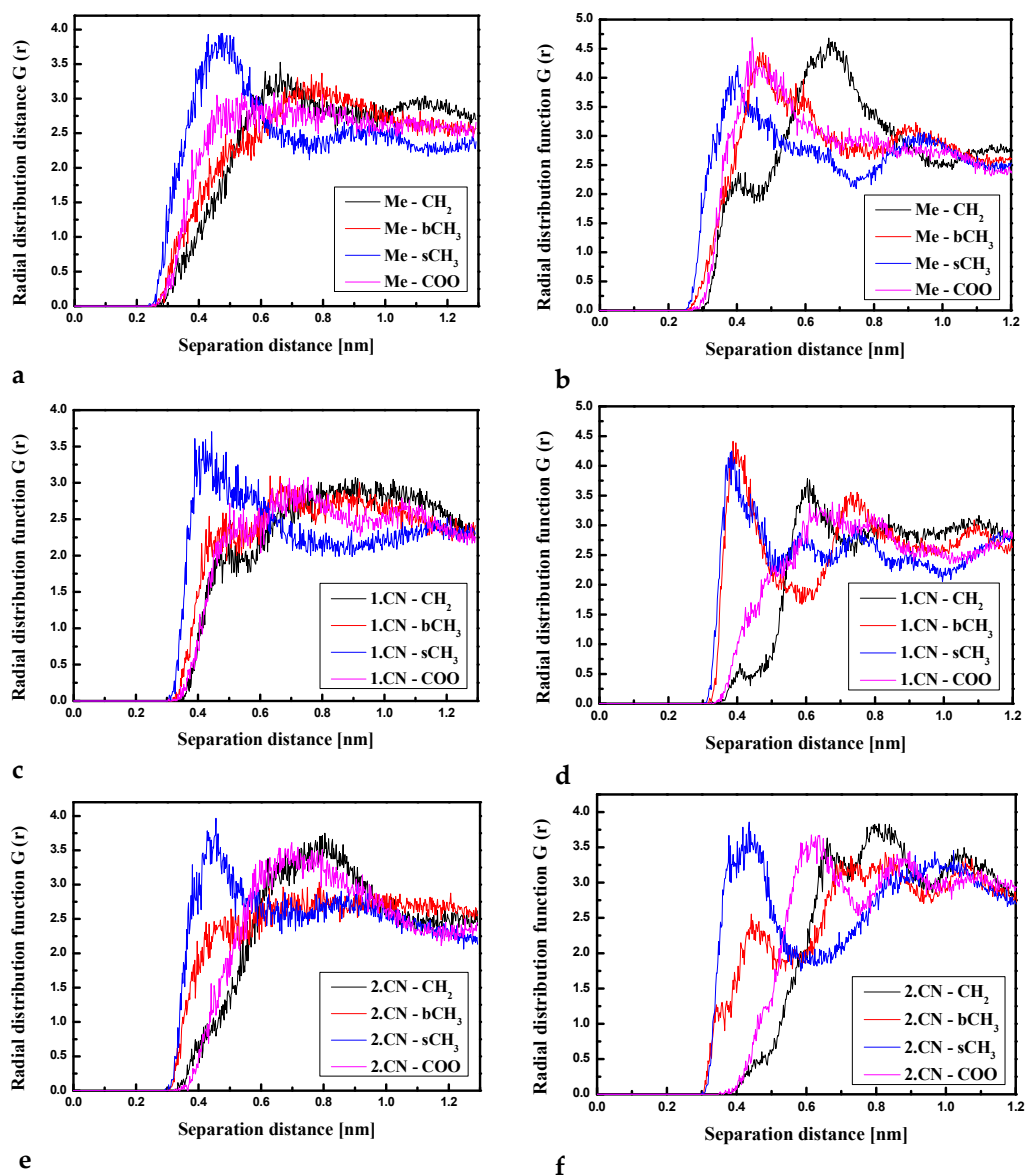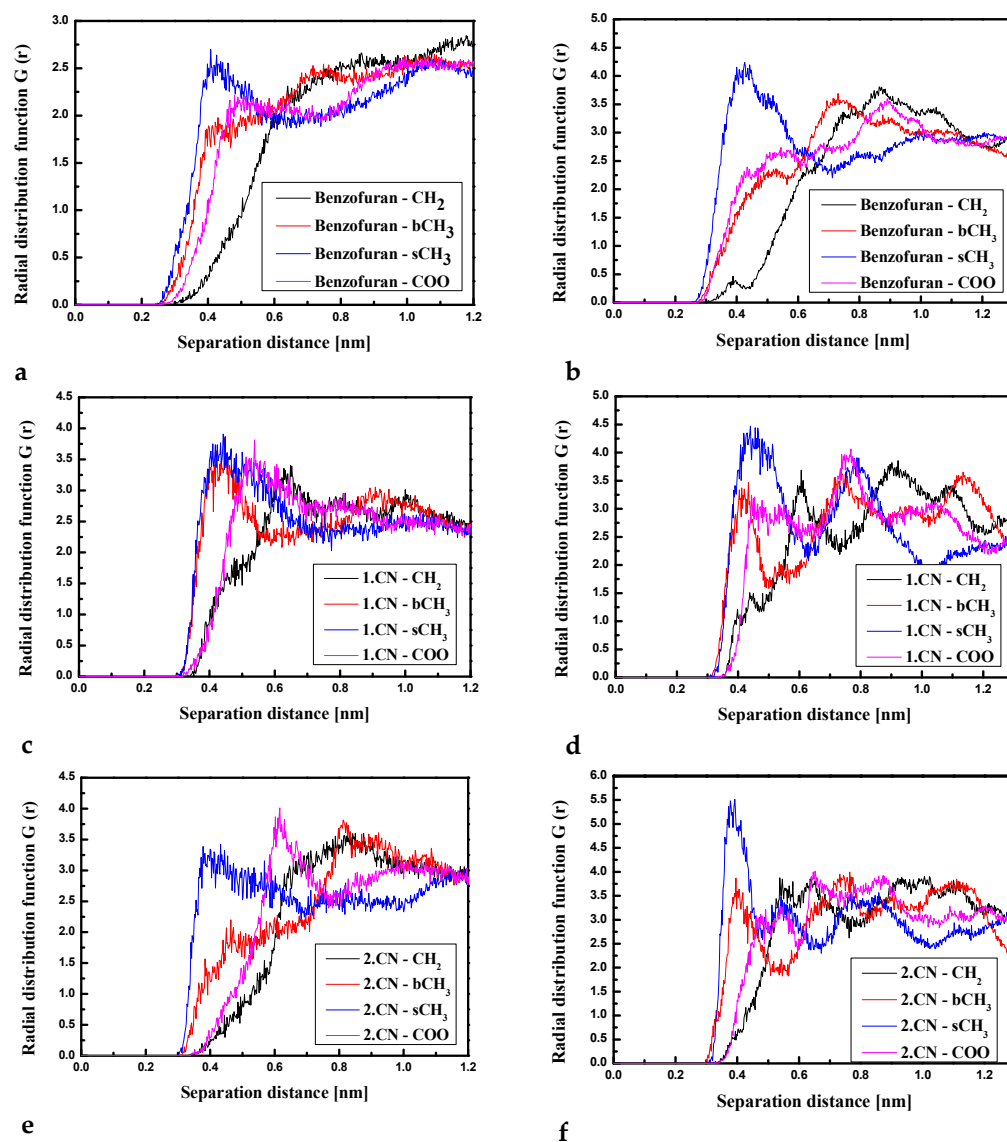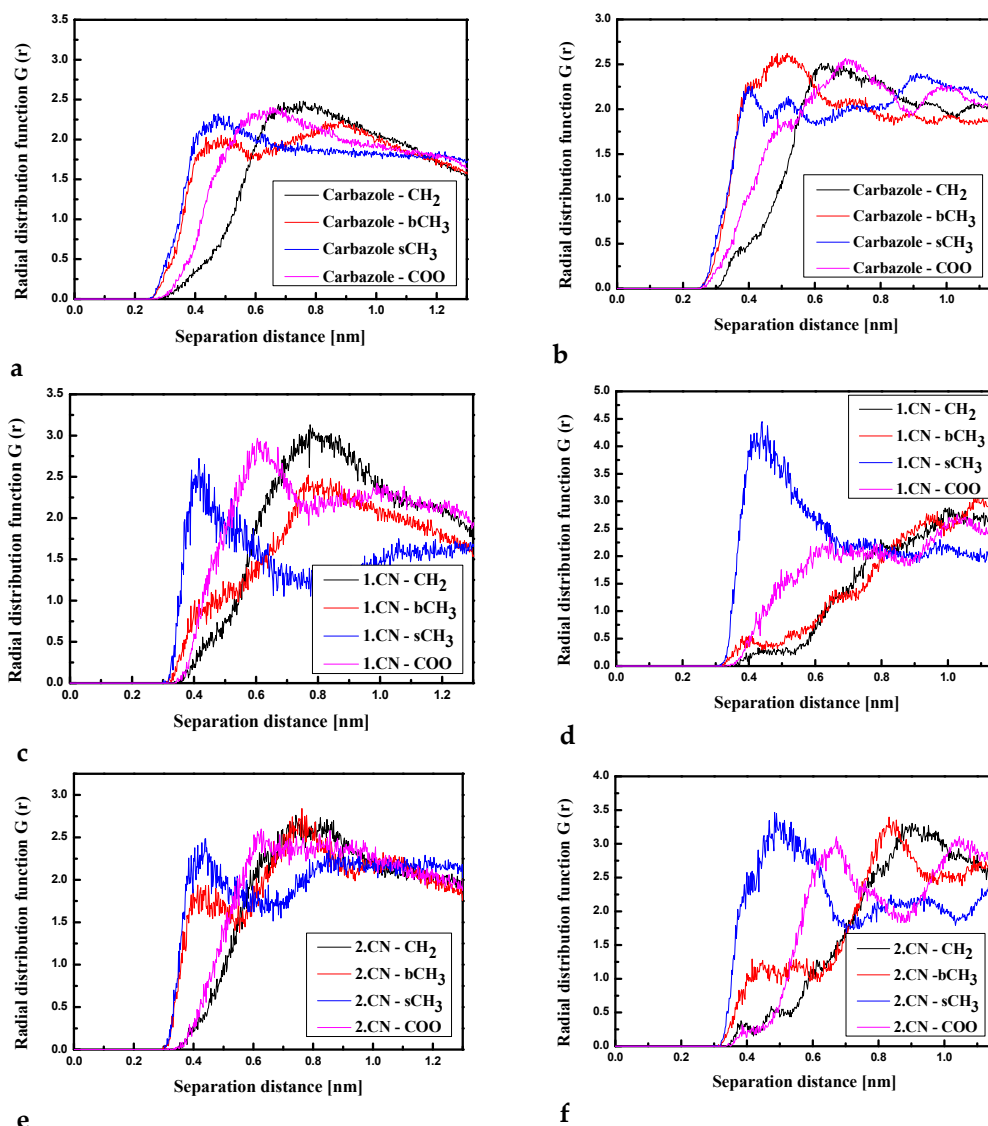

Figure 8.13. Partial RDFs calculated for distances between the center of mass of different moieties of the A molecule and different subunits of PVK at T = 500K (a,c,e) and T=300K (b,d,f) for the bulk system. The RDFs are presented for methyl group (Me) of A molecule and different subunits of PVK mer (a, b); for cyanovinyl 1.CN at the side of the molecule A and different subunits of PVK mer (c,d) and cyanovinyl 2.CN at the back of the molecule A and different subunits of PVK mer (e,f).

Analyzing data presented in Fig. 8.13 one can see that the A molecule is located close to the carbazole group of the PVK polymer chain. The closest distance between all defined groups of molecule A (both CN groups and Me group) is equal

to 0.4 nm for the system in the liquid phase (at 500 K) (see Fig. 8.13 (a, c, e)). The distance between Me groups of the A molecule and both C_6H_6 groups of the PVK is going to be shorter (0.3 nm) when the A/PVK system is in a glassy state (at 300 K) (see Fig. 8.13 (b)). It allows us to conclude that in the A/PVK composite the polymer is rolled up such that its carbazole groups remain outside.

Figure 8.14. Partial RDFs calculated for distances between the center of mass of different moieties of the B molecule and different subunits of PVK at T = 500K (a,c,e) and T=300K (b,d,f) for the bulk system. The RDFs are presented for benzofuran group of B molecule and different subunits of PVK mer (a, b); for cyanovinyl CN1 at the side of the molecule B and different subunits of PVK mer (c,d) and cyanovinyl CN2 at the back of the molecule B and different subunits of PVK mer (e,f).

The same situation is observed for the B/PVK system (see Fig. 8.14). One can see that molecule B even in a liquid state (see Fig. 8.14 (a, c, e)) is closer to the polymer chain than molecule A. Distance between the benzofuran group of molecule B and both C_6H_6 groups of PVK is equal to 0.3 nm (Fig. 8.14 (a)). It means that these two flat groups assume a parallel arrangement to one another. In the glassy state, the distance between the 2.CN group of the B molecule and the C_6H_6 groups of PVK is equal to 0.3 nm (see Fig. 8.14 (f)). In addition, the distance between the 2.CN group and sCH_2 becomes shorter (0.35 nm) compared with the liquid state (see Fig. 8.14 (e). It means that in the glassy state molecule B goes deeper into the structure of the twisted polymer.

Molecule C is located at a distance of 0.4 nm from the side groups of the polymer chain (see Fig. 8.15). In addition, also here the polymer is twisted keeping the carbazole group outside the twisted chain. In the liquid state (see Fig. 8.15 (a)), the carbazole group of molecule C is located at the closest distance to the polymer. The RDF peak corresponding to the carbazole-1.C_6H_6 or carbazole-2.C_6H_6 distance is more spread than is observed for the other RDF functions (Fig. 8.15 (a)). Molecule C enters deeper into the polymer in the glassy state (Fig. 8.15 (b, d, f)). It is seen from emerging peaks characterizing Carbazole-N distance (see Fig. 8.15 (f)).

The RDFs calculated for the thin films of the A/PVK, B/PVK, and C/PVK composites are presented in Fig. 8.16 -8.18. One may see that also here the distance between A, B, and C molecule and PVK is equal to 0.4 nm in the liquid state (see Fig. 8.16 - 8.18 labeled as a, c and d). Chromophores are located close to the carbazole moiety of the PVK polymer. One can conclude that the character of the RDFs of the thin films in a liquid state is similar to the one of the bulk system (see Fig. 8.13 - 8.15 labeled as a, c and d). The first RDFs peaks observed for the A/PVK composite are wider than was observed for the bulk system (see Fig. 8.16). It proves that the surface of the system is less dense than the interior of composites. As it was observed for the bulk form of the B/PVK system also in a glassy state of the B/PVK thin film the B molecule is going to be deeper inside the polymer chain.
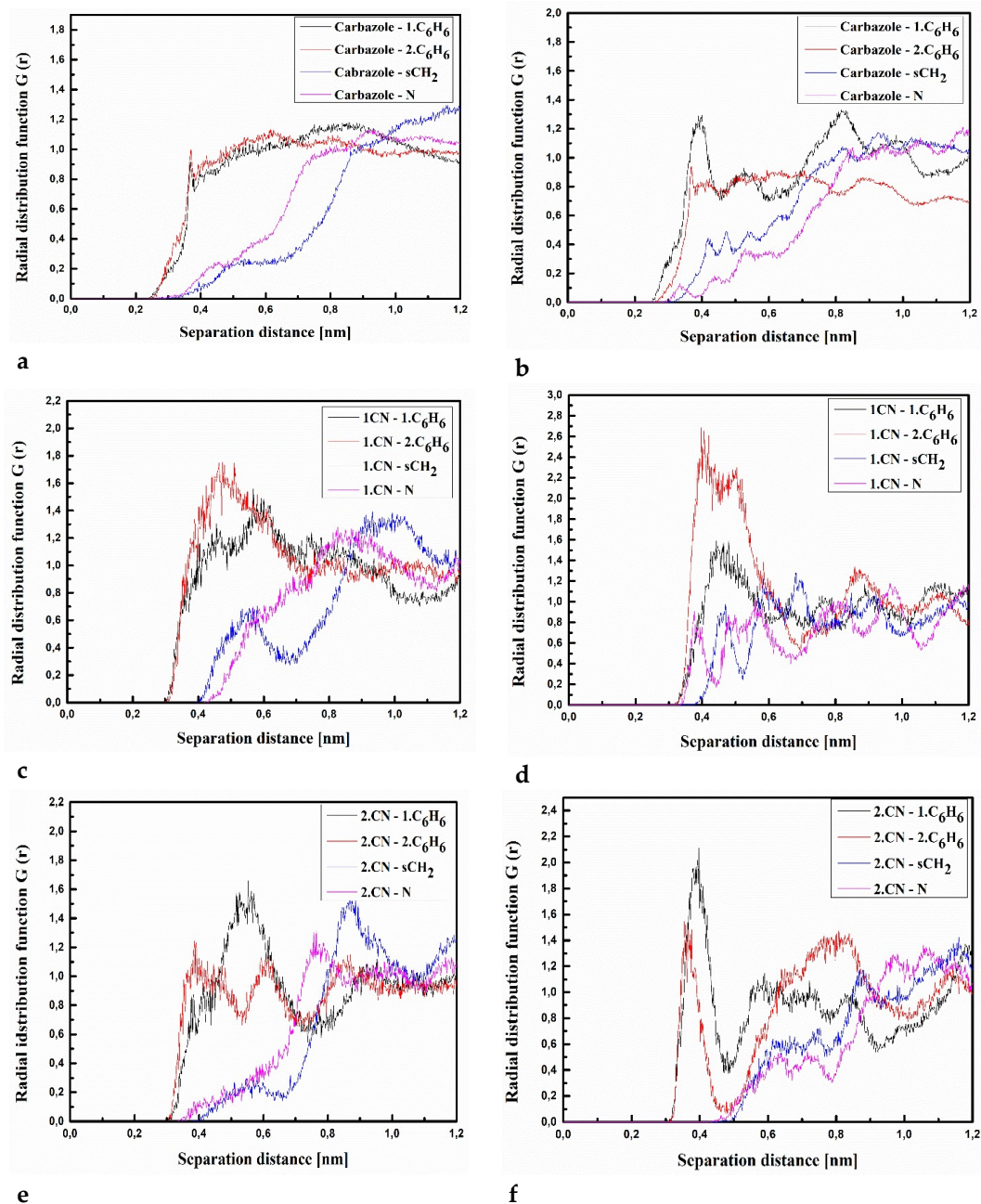
Figure 8.15. Partial RDFs calculated for distances between the center of mass of different moieties of the C molecule and different subunits of PVK at T = 500K (a,c,e) and T=300K (b,d,f) for the bulk system. The RDFs are presented for the carbazole group of the C molecule and different subunits of PVK mer (a, b); for cyanovinyl CN1 at the side of the molecule C and different subunits of PVK mer (c,d) and cyanovinyl CN2 at the back of the molecule C and different subunits of PVK mer (e,f).
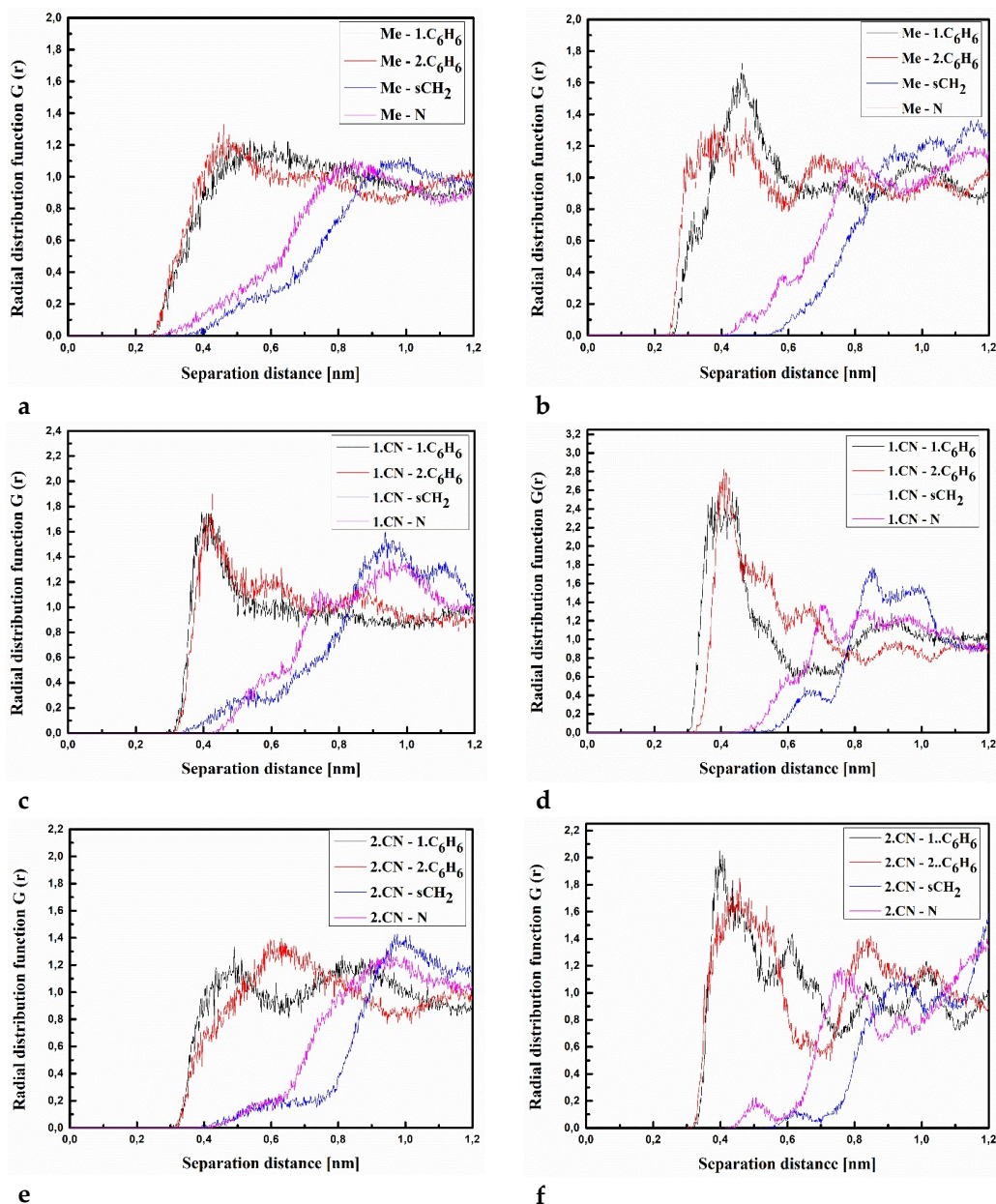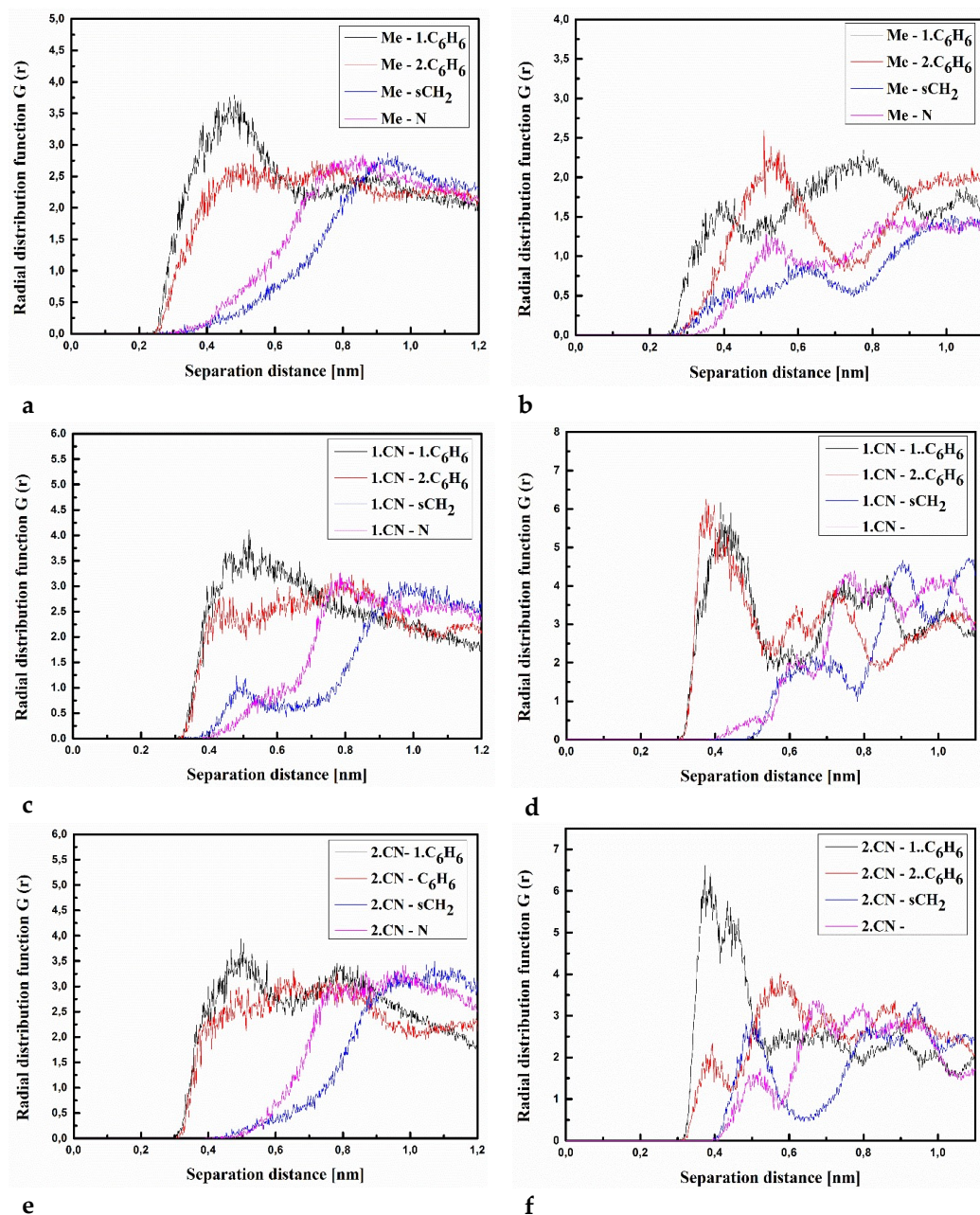
Figure 8.16. Partial RDFs calculated for distances between the center of mass of different moieties of the A molecule and different subunits of PVK at T = 500K (a,c,e) and T=300K (b,d,f) for the thin film composite system. The RDFs are presented for methyl group (Me) of A molecule and different subunits of PVK mer (a, b); for cyanovinyl CN1 at the side of the molecule A and different subunits of PVK mer (c,d) and cyanovinyl CN2 at the back of the molecule A and different subunits of PVK mer (e,f).
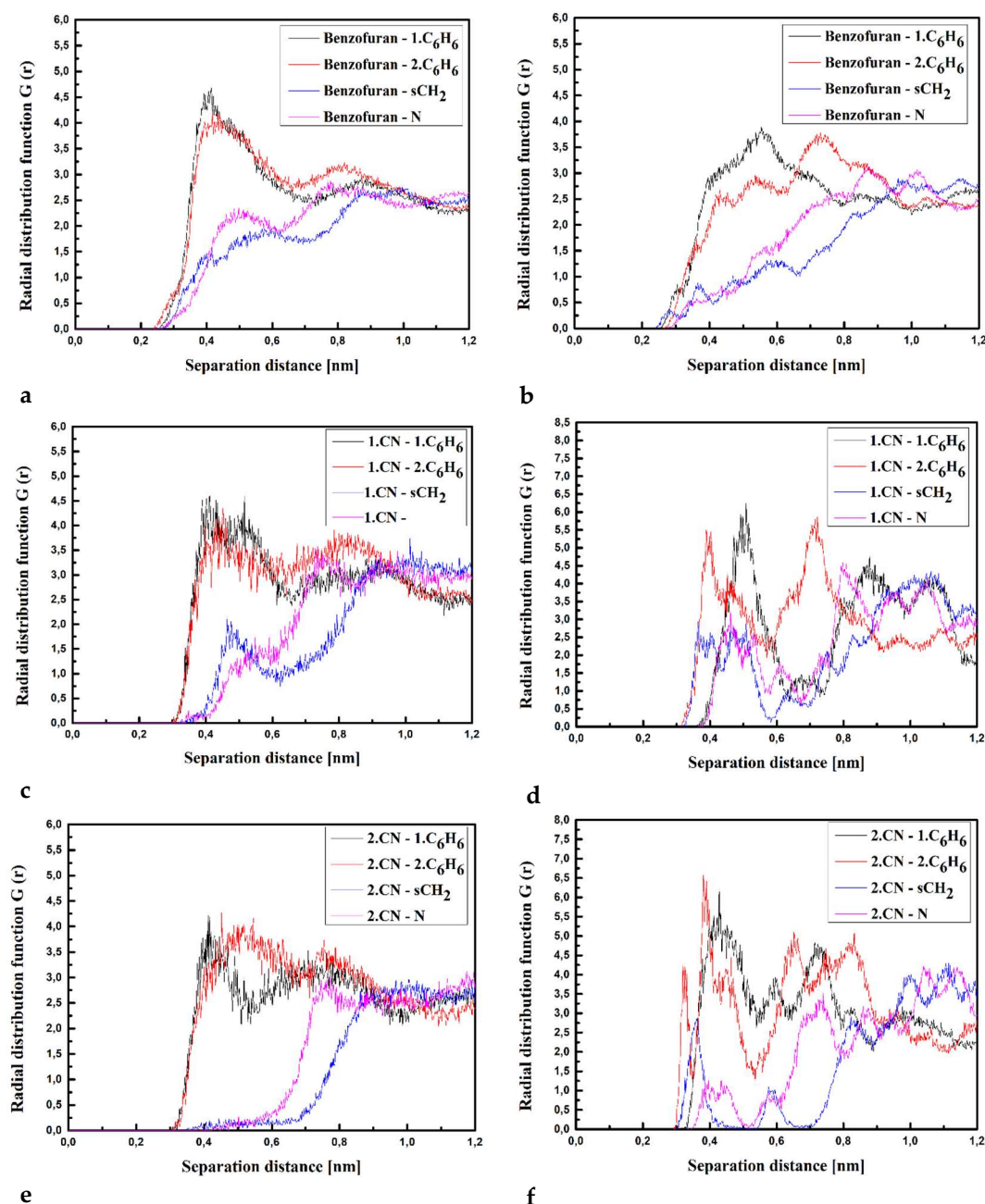
Figure 8.17. Partial RDFs calculated for distances between the center of mass of different moieties of the B molecule and different subunits of PVK at T = 500K (a,c,e) and T=300K (b,d,f) for the thin-film system. The RDFs are presented for the benzofuran group of B molecule and different subunits of PVK mer (a, b); for cyanovinyl CN1 at the side of the molecule B and different subunits of PVK mer (c,d) and cyanovinyl CN2 at the back of the molecule B and different subunits of PVK mer (e,f).

The significant peak characterizing the 2.CN-sCH$_2$ distance poofs this statement (see Fig. 8.17 (e)). Presented data allow us to conclude that the PVK has exposed sCH$_2$ groups when twisting the polymer chain. The C molecule of the C/PVK thin film in the liquid state is located close to the carbazole group of the polymer (see Fig. 8.18 (a)). In the glassy state of the C/PVK thin film, the carbazole group of the

C is going to be close to the sCH$_2$ and N groups of the PVK (see Fig. 8.18 (b)). Concluding, one can say that the close distance between PVK and chromophores appearing in B/PVK and C/PVK systems can affect the optical properties of the composites.
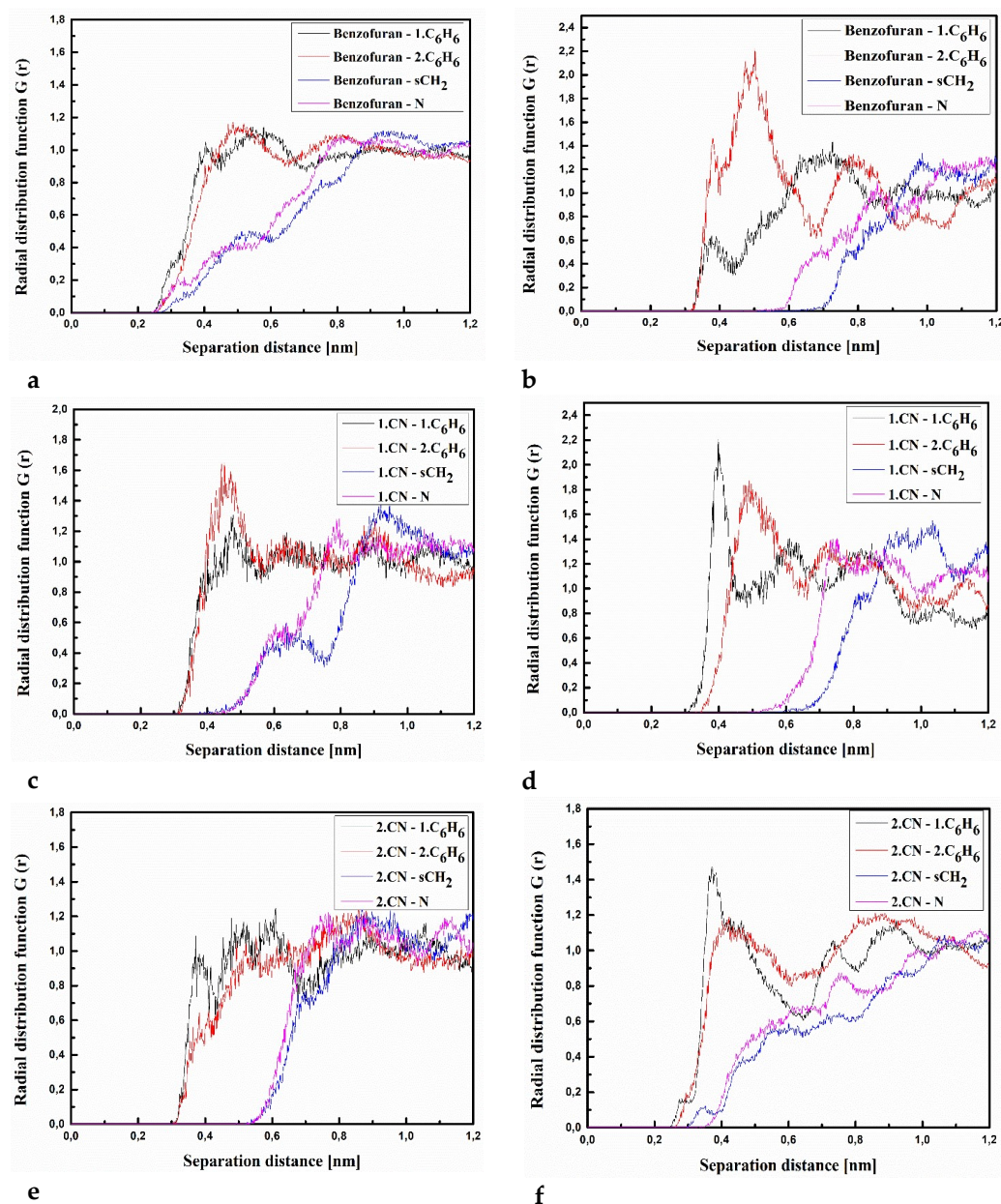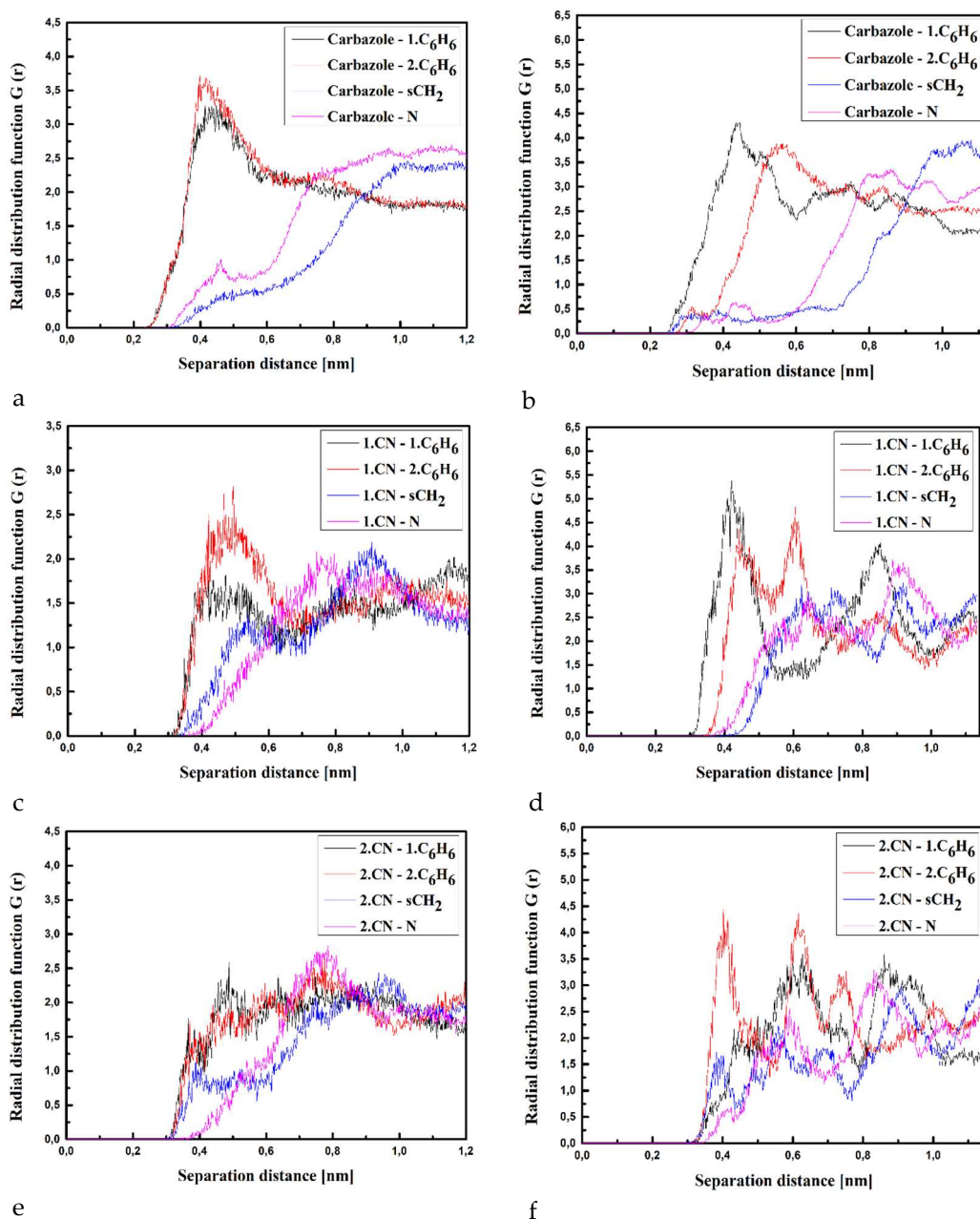

Figure 8.18. Partial RDFs calculated for distances between the center of mass of different moieties of the C molecule and different subunits of PVK at T = 500K (a,c,e) and T=300K (b,d,f) for the thin-film system. The RDFs are presented for the carbazole group of the C molecule and different subunits of PVK mer (a, b); for cyanovinyl CN1 at the side of the molecule C and different subunits of PVK mer (c,d) and cyanovinyl CN2 at the back of the molecule C and different subunits of PVK mer (e,f).

The external electric field-induced reorientation of the chromophores was investigated by computing the $<cos\theta(t)>$ based on the time-dependent angle

139

between the electric dipole moment of the chromophore and the direction of an external electric field. The degree of alignment depends on the electric field strength and the spatial extension of the dipolar molecules. The values of $<cos\theta(t)>$ versus time of simulation and external electric field intensity are presented in Fig. 8.19 and Fig. 8.20 for volumetric (bulk) and thin-film forms, respectively. Presented data have been computed by averaging over modeled equivalent structures of each of the three composites A/PVK, B/PVK, and C/PVK. The external electric field was applied for the A/PVK, B/PVK, and C/PVK composites in bulk form when they were in the liquid state at 500 K. Then the investigated composites were modeled by SA to be in a glassy state (at 300 K). The SA was performed in the presence of an external electric field.

The A/PVK composite in bulk form poled by the external electric field equal to 15, 10, and 5 kV/μm has almost completely aligned chromophores (see Fig. 8.19 (a)). The flexibility of the A/PVK composite is significant and an electric field equal to 1 or 3 kV/μm aligns the A molecules at 40 %. The SA stabilizes an alignment of the chromophores from 60 % up to 80 % (see Fig. 8.19 (b)). It is important to notice that chromophores aligned at 500 K by the field 1 and 3 kV/μm were further tidied up during the SA.

The B/PVK composite exhibits a very satisfactory alignment of the system by applying an external electric field equal to 15, 10, and 5 kV/μm (Fig. 8.19 (c)). These electric fields align chromophores B in 80 – 95 %. Lower electric fields as 1 and 3 kV/μm align chromophores B in 40 % and 60 %, respectively. The SA keeps the alignment of the chromophores treated by 15, 10, and 5 kV/μm electric field at the level of 80-90 % but the lower electric field is too small to keep the alignment of the B chromophores at the appropriate level (see Fig. 8.19 (d)). The alignment of B chromophores decreases up to 30% in the liquid state (at 300 K).

One may see that composite material C/PVK achieved a slightly lower degree of alignment in comparison to A/PVK and B/PVK systems. The order parameter $<cos\theta(t)>$ calculated for C/PVK in the glassy state oscillates around the value of 70 % for the system aligned by an electric field equal to 5, 10, or 15 kV/μm (see Fig. 8.19 (e)). The C/PVK composites with applied electric fields equal to 3 or 1 kV/μm achieved the order parameter below 40 %. The SA solidification of the C/PVK does not change significantly the poling alignment of the C molecules compared to the system in a glassy state (see Fig. 8.19 (f)). One may conclude that the C molecules

are inferior to order them but also they do not reorient during SA. This is due to the size of molecules C, which is larger than molecules A or B.
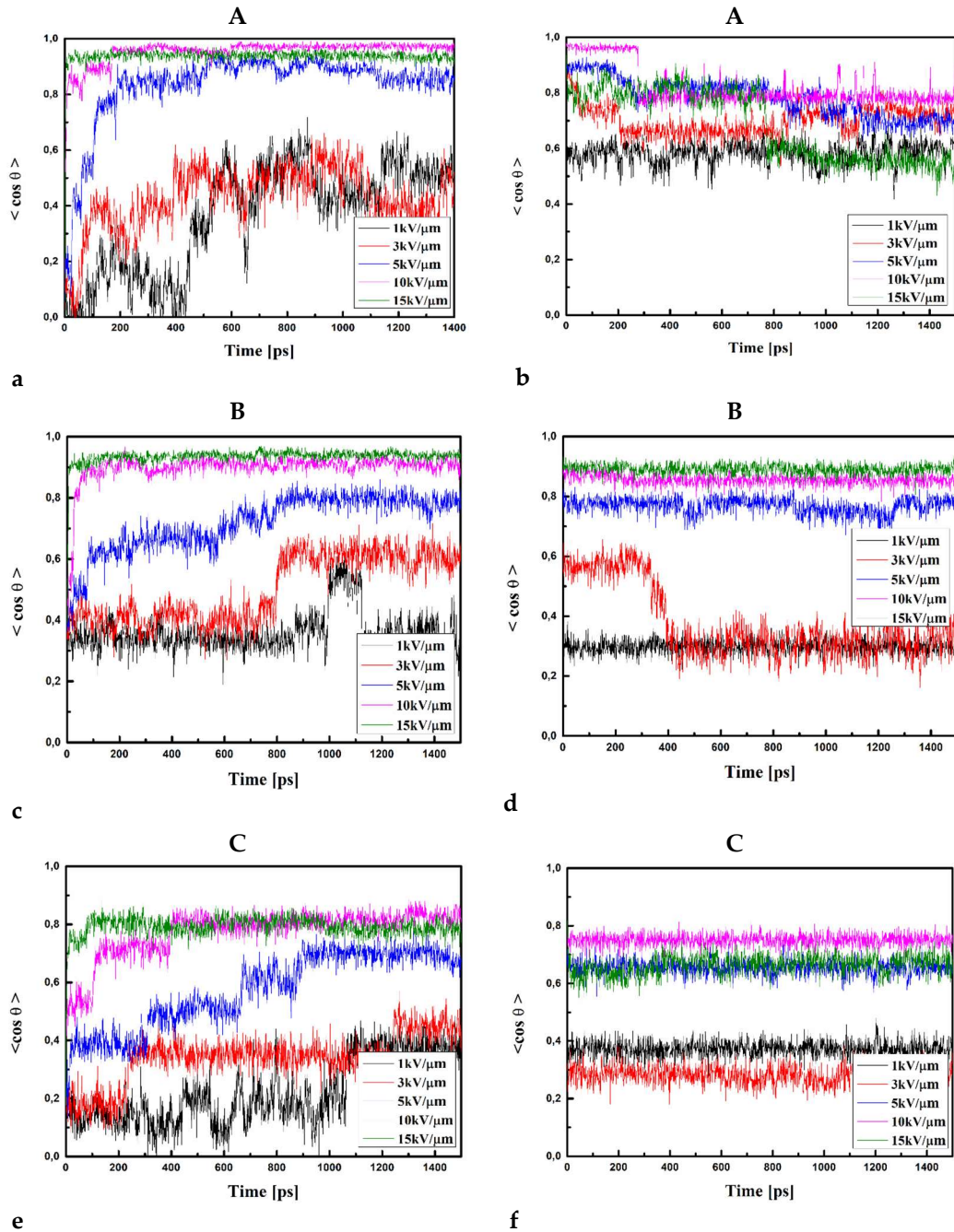
Figure 8.19. Changes in the value of the order parameter $<cos\theta(t)>$ versus the time of simulation and applied external electric field calculated by MD technique for the A/PVK (a,b), B/PVK (c,d), and C/PVK (e,f) composites in the volumetric form at the temperature of 500 K (a,c,e) and glassy state (300 K) after the simulated annealing (b,d,f).

The same procedures of pooling simulations were implemented for thin films of the A/PVK, B/PVK, and C/PVK composites, and the results are presented in Fig. 8.20. The used external electric field equal to 0.5, 1, 3, or 5 kV/μm, is lower than

the one used for bulk materials. The A/PVK thin film shows that using an external electric field of 5 kV/μm the degree of chromophore arrangement is set at 95 % (see Fig. 8.20 (a)) and for an electric field equal to 3 kV/μm is around 80 %. During controlled cooling, their order parameters dropped slightly to 93 % for an external electric field equal to 5 kV/μm and the value of 75 % for 3 kV/μm (see Fig. 8.20 (b)). The order parameter achieved for a thin film of A/PVK with an external electric field equal to 0.5 and 1 kV/μm is fixed on the level of 15 % and 20 %, respectively.
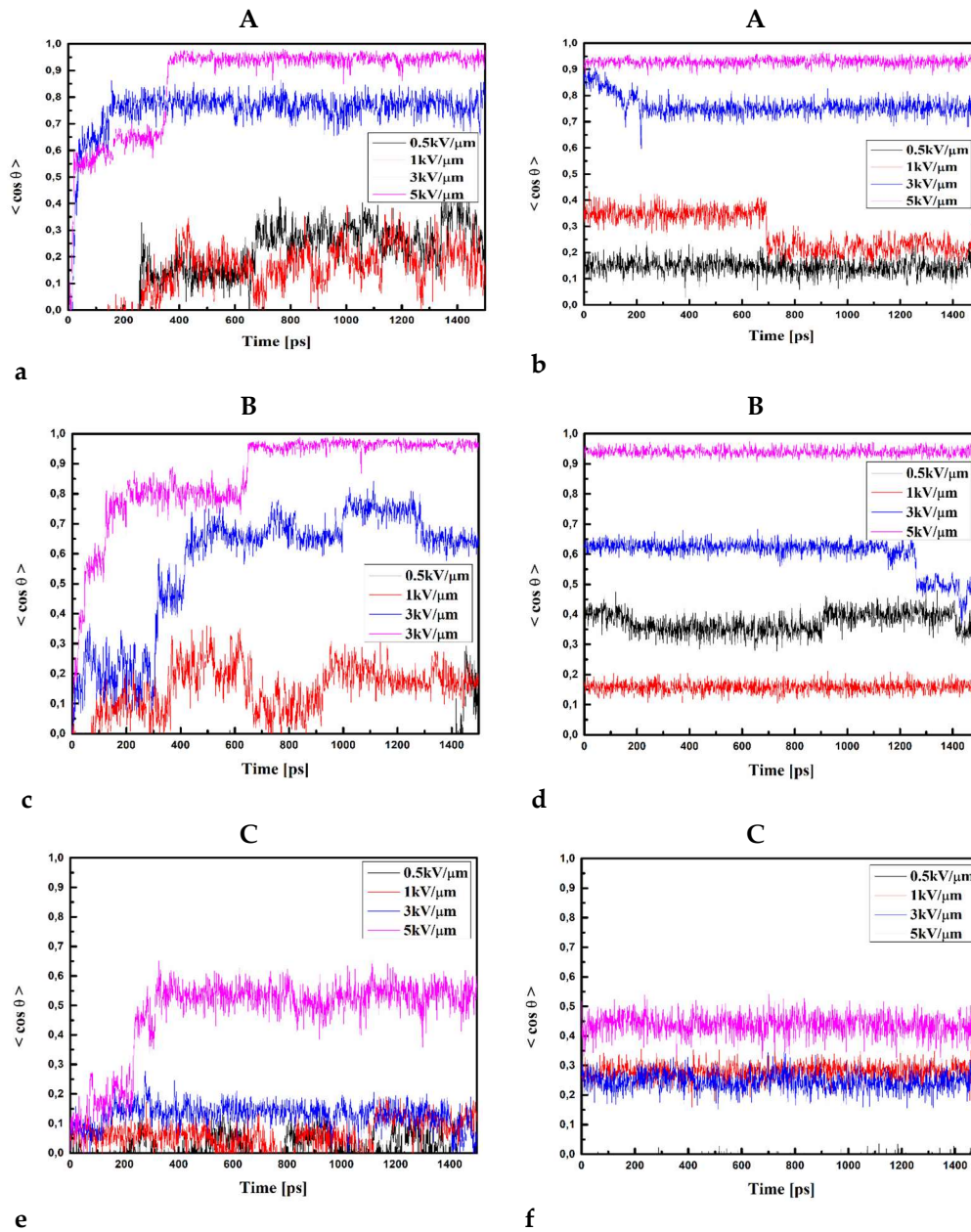
Figure 8.20. Changes in the value of the order parameter $<cos\theta(t)>$ versus the time of simulation and applied external electric field calculated by MD technique for the A/PVK (a,b), B/PVK (c,d), and C/PVK (e,f) composites in the thin film form at the temperature of 500 K (a,c,e) and glassy state (300 K) after the simulated annealing (b,d,f).

Regarding the B/PVK thin film, one may see that using an external electric field of 5 kV/μm, the orientation of the chromophores is achieved at the level of 95 % (see Fig. 8.20 (c)). Additionally, this order parameter is maintained also after the SA procedure (Fig. 8.20 (d)). The B molecules aligned by an electric field equal to 3 kV/μm obtain an order parameter of 60 % but the alignment is not stable during the time and decreases after the SA process (see Fig. 8.20 (c) and 8.20 (d), respectively). Using an electric field equal to 1 or 0.5 kV/μm an insufficient structure arrangement was achieved.

The order parameters of C/PVK thin films poled by an external electric field with intensity 1, 3, or 5 kV/μm is achieved at level 10, 15, and 50 %, respectively (see Fig. 8.20 (e)). Simulated cooling does not decrease the achieved order parameters (see Fig. 8.20 (f)). The thin film of the C/PVK is difficult to be poled but instead it is also stable during the cooling and solidification procedure. One may see that the C/PVK thin film is the most difficult system to achieve a high degree of chromophores arrangement. It is as difficult to be aligned as it was noticed for the bulk C/PVK composite. It could be due to the appearance of the intermolecular interactions between polymer and chromophores lying close one to the other as well as due to the size of the C chromophore.

8.2. Structural, electron, and optical properties of the A, B, and C chromophores

Structural, electron, and optical properties of the A, B, and C chromophores were performed computationally using quantum chemical methods. Theoretical calculations of the electron and optical properties of the A, B, and C molecules (see Fig. 8.1) start with the procedure of their structural optimization. Their geometries were optimized by applying the *ab initio* Hartree-Fock (HF) formalism implemented in the Gamess program package [9,10]. The procedure has been performed for isolated structures in a vacuum. The minimum of the potential energy surface was computed at the restricted HF (RHF) [11] level with the 6-311G basis set in C1 symmetry. The gradient convergence criterion was equal to 10^{-6} Hartree/Bohr. Geometries of the investigated molecules were found by applying the quadratic approximation (QA) optimization algorithm [12] based on augmented

Hessian techniques. The RHF SCF energy convergence criterion was chosen to be 10^{-10} Hartree.

Electron properties of the investigated chromophores were computed at the SCF RHF [11] level by applying the 6-311++G** basis set [13 – 15] within the *ab initio* and the density functional theory (DFT) methodology. The DFT calculations were carried out implementing different exchange-correlation (XC) functionals, namely the B3LYP [16–18] CAM-B3LYP [19], and LC-BLYP [20] with separation parameter μ equal to 0.33. The UV–vis absorption spectra were calculated using the iterative Davidson method [21] with an accuracy equal to 10^{-12} Hartree. The calculations were performed using the GAMESS program for isolated molecules placed in a vacuum.

To investigate the solvent effect of the chloroform on the optical properties of the A, B, and C molecules the conductor-like Polarizable Continuum Model (C-PCM) was used [22]. The UV–vis absorption spectra of the studied molecules in chloroform solution were calculated applying the DFT/B3LYP methodology with the parameters mentioned above. The calculations were performed in the GAMESS program.

The polarizabilities and hyperpolarizabilities of the molecules were calculated using *ab initio* methodology. To compare the theoretically obtained parameters between molecules, they were rotated to have an electric dipole moment along the Z-axis. The nonlinear optical properties were computed within the Dalton program, applying the parameters mentioned above.

Theoretical and experimental structural data (bond lengths and dihedral angles) of the A, B, and C molecules are collected in Table 8.1. Numbering is given according to Figure 8.21. Linear regression analysis for the calculated and experimental bond lengths was performed. The linear correlation Pearson coefficients R2 equal to 0.992 and 0.996 for A and C molecules, respectively has been obtained. One may say, that theoretical and experimental parameters are in a good convergence (see Fig. 8.22). It should be emphasized, that the calculations were carried out in the gas phase while the experimental results belong to the solid phase structure. One can be noticed, that by analyzing the presented data, the studied structural parameters calculated within the *ab initio* HF method are very close to the experimental results.

Table 8.1. Experimental and optimized by ab initio methodology using 6-311G basis set bond lengths and dihedral angles selected in A, B, and C molecules – experimental (exp), theoretical (th).

Dihedral angle [°]	Molecule				
	A^th	A^exp	B^th	C^th	C^exp
C4-C5-C8-C10	146	179	145	145	158
C12-C11-C10-C8	178	177	178	156	162
C17-N3-C14-C15	-	-	–	109	134
Bond lengths Å					
C1-C2	1.434	1.474		1.434	1.440
C1-N1	1.143	1.142		1.143	1.147
C2-C3	1.391	1.386		1.391	1.396
C3-C4	1.382	1.383		1.382	1.380
C4-C5	1.395	1.394		1.394	1.398
C5-C6	1.395	1.403		1.394	1.402
C6-C7	1.382	1.382		1.382	1.380
C7-C2	1.391	1.395		1.391	1.396
C5-C8	1.489	1.484		1.491	1.485
C8-C9	1.436	1.441		1.437	1.442
C9-N2	1.142	1.148		1.143	1.145
C10-C8	1.340	1.351		1.338	1.349
C10-C11	1.436	1.424		1.471	1.460
C11-O1	1.374	1.376		-	-
C14-O1	1.368	1.369		-	-
C13-C14	1.349	1.354		1.388	1.398
C12-C13	1.435	1.413		1.382	1.380
C11-C12	1.352	1.361		1.397	1.403
C14-C15	1.481	1.479		1.388	1.397
C15-C16	-	-		1.384	1.380
C11-C16	-	-		1.395	1.403
C15-N3	-	-		1.418	1.414
C17-N3	-	-		1.397	1.403
C17-C18	-	-		1.388	1.395
C18-C19	-	-		1.384	1.391
C19-C20	-	-		1.396	1.396
C20-C21	-	-		1.383	1.382
C21-C22	-	-		1.389	1.399
C22-C23	-	-		1.453	1.440
C22-C17	-	-		1.401	1.408
C23-C28	-	-		1.401	1.410
C28-N3	-	-		1.397	1.400

Analyzing data presented in Table 8.1 one can see that the benzonitrile group remains planar (see Fig. 8.21) for all molecules. The furan moiety in molecule A and the benzofuran in molecule B and the carbazole group in molecule C are also planar. Based on the theoretical calculation one can see that the benzofuran compared with the furan moiety does not twist the molecules anymore. Even adding the carbazole moiety the dihedral C4-C5-C8-C10 selected in molecule C has the same value as it is observed for the molecules A and B. The dihedral C12-C11-C10-C8 is significantly twisted in molecule C compared with the A and B molecules and it also affects the dihedral angle C17-N3-C14-C15. In summarising,

one can say that the molecules C is more twisted than the molecules A and B. Twisting the plane of the molecules should affect the electron absorption spectrum shifting it into the red wavelength side [23]. The most significant differences between the calculated and experimental geometries are seen for the dihedral angle C4-C5-C8-C10 of the A (Ath equal to 146° but A^{exp} equal to 179°, see Table 8.1). The observed difference can be explained by the fact that experimental studies were carried out for the crystal structure while theoretical calculations are made for the molecule in a vacuum. One can conclude that the theoretical and calculated bond lengths and dihedral angles show acceptable convergence.
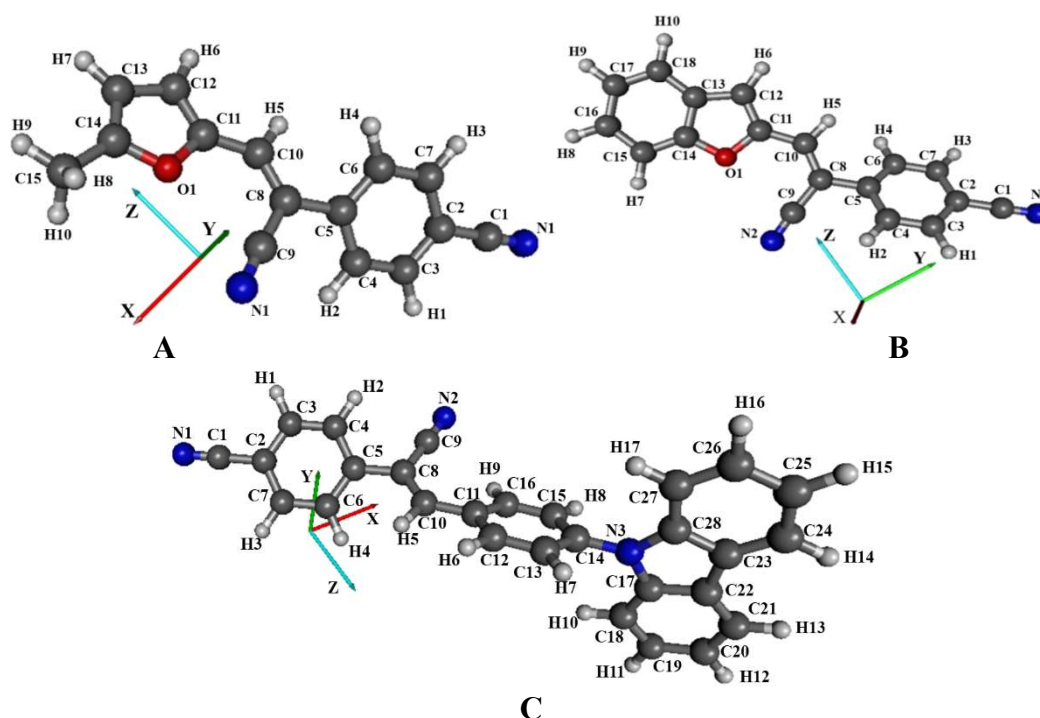
Figure 8.21. Schemes of the A, B, and C molecules after geometry optimization procedure performed by ab initio methodology using 6-311G basis set.

The optimized structures were used to calculate UV–vis absorption spectra and compare them to the experimentally predicted ones. The A, B, and C molecules were synthesized at Institute MOLTECH-Anjou at Université d'Angers in France. The procedure of synthesis was described in supplementary materials of our work [24]. The benzonitrile group present in all investigated molecules (see Fig. 8.1) works as the acceptor moiety attached to the donor part of chromophores through the cyano-vinyl chain. In the case of two molecules (A and B) the donor is

represented by the methylfuran and benzo-furan moiety, respectively, and the C molecule is composed of the carbazole group. These different donor moieties of the investigated molecules influence their structural and electronic properties.
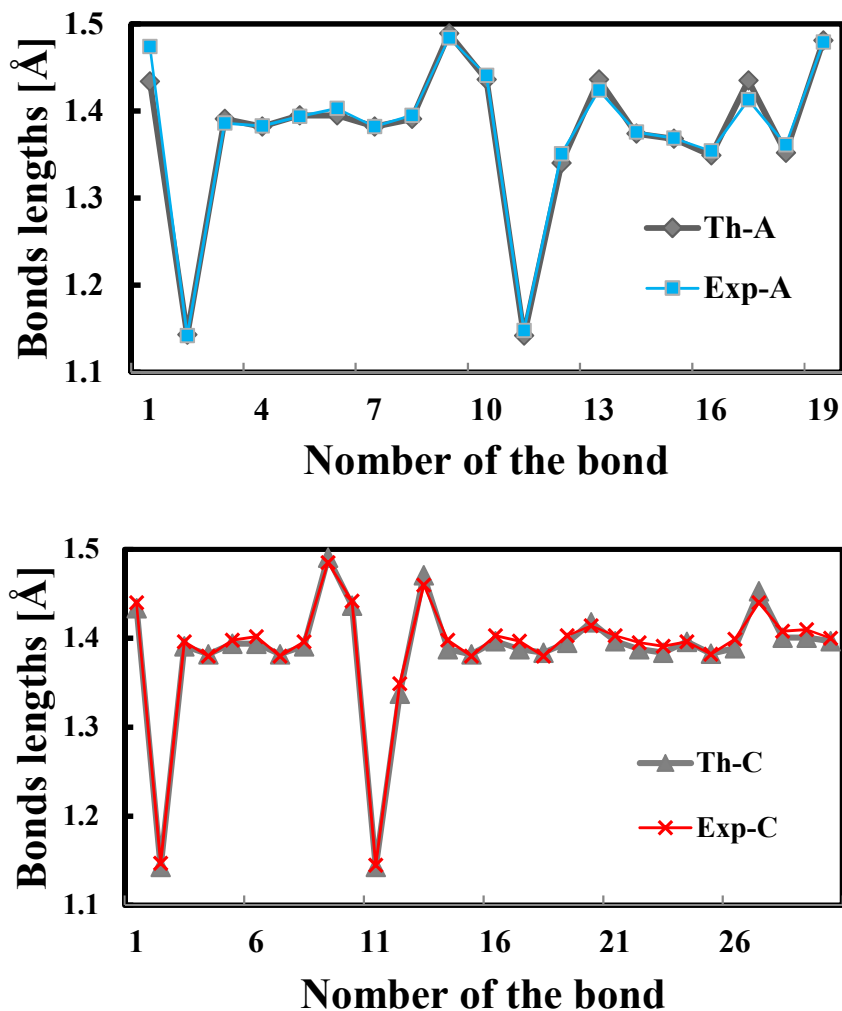
Figure 8.22. Comparison between calculated and experimental values of bond lengths for compounds A (a) and C (b).

The experimental UV–vis absorption spectra were measured in chloroform and they are presented in Fig. 8.23 (a). One can see that the first absorption peak measured for the A and B molecules occurs at the same position of spectra. The first absorption peak measured for the C molecule is shifted into red wavelength compared with measured spectra for the A and B molecules. It means that the carbazole group decreases the optical energy gap of molecule C.
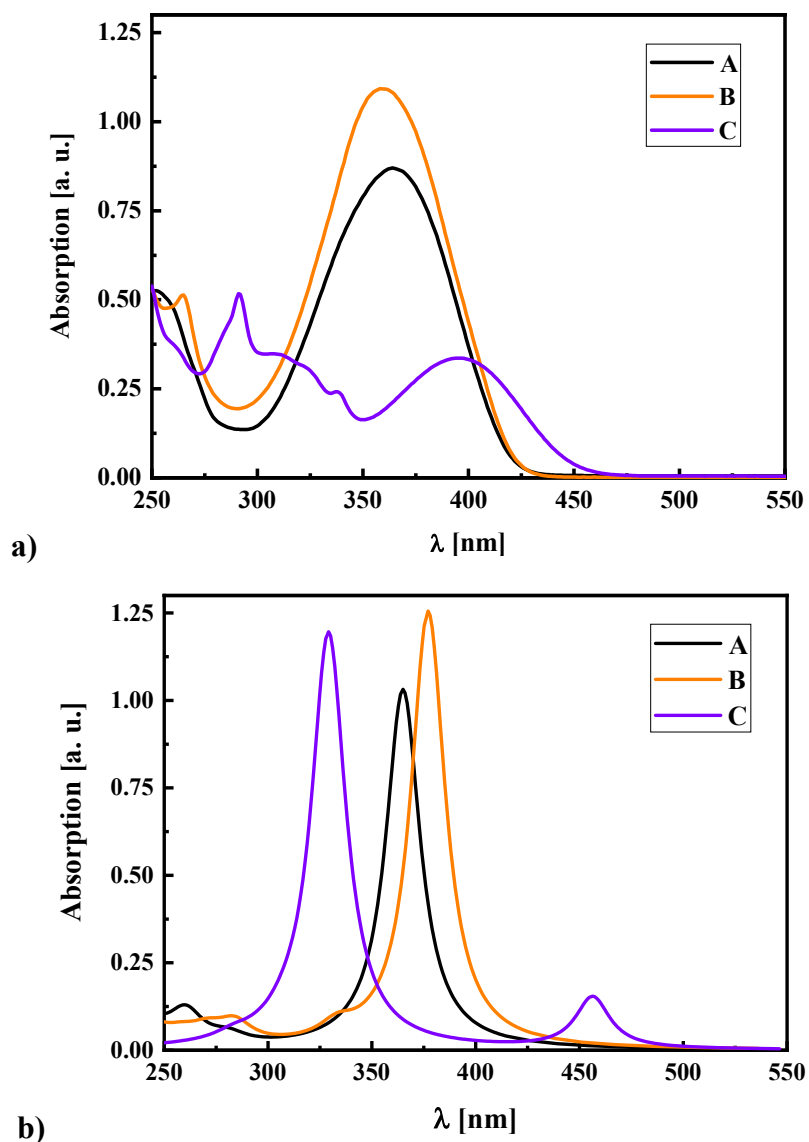
Figure 8.23. UV-vis absorption spectra measured experimentally for the A, B, and C molecules in chloroform as a solvent (a), and these spectra calculated in chloroform by using the DFT/B3LYP method (b)

Table 8.2. The first UV-vis absorption peak measured for the **A**, **B**, and **C** molecules dissolved in chloroform as well as calculated by using HF and the DFT methodology with different functionals.

Molecule	Experimental λ_{max} [nm]	Calculated λ_{max} [nm]				
		In vacuum				In chloroform
		HF	DFT/B3LYP	DFT/CAM-B3LYP	DFT/LC-BLYP	DFT/B3LYP
A	364	276	344	317	306	364
B	361	282	359	324	311	377
C	396	262	485	334	299	458

The positions of first absorption peaks measured experimentally and corresponding data obtained by quantum chemical calculations are collected in Table 8.2. The computed data come from the HF and DFT calculations applying

a)

b)

c)
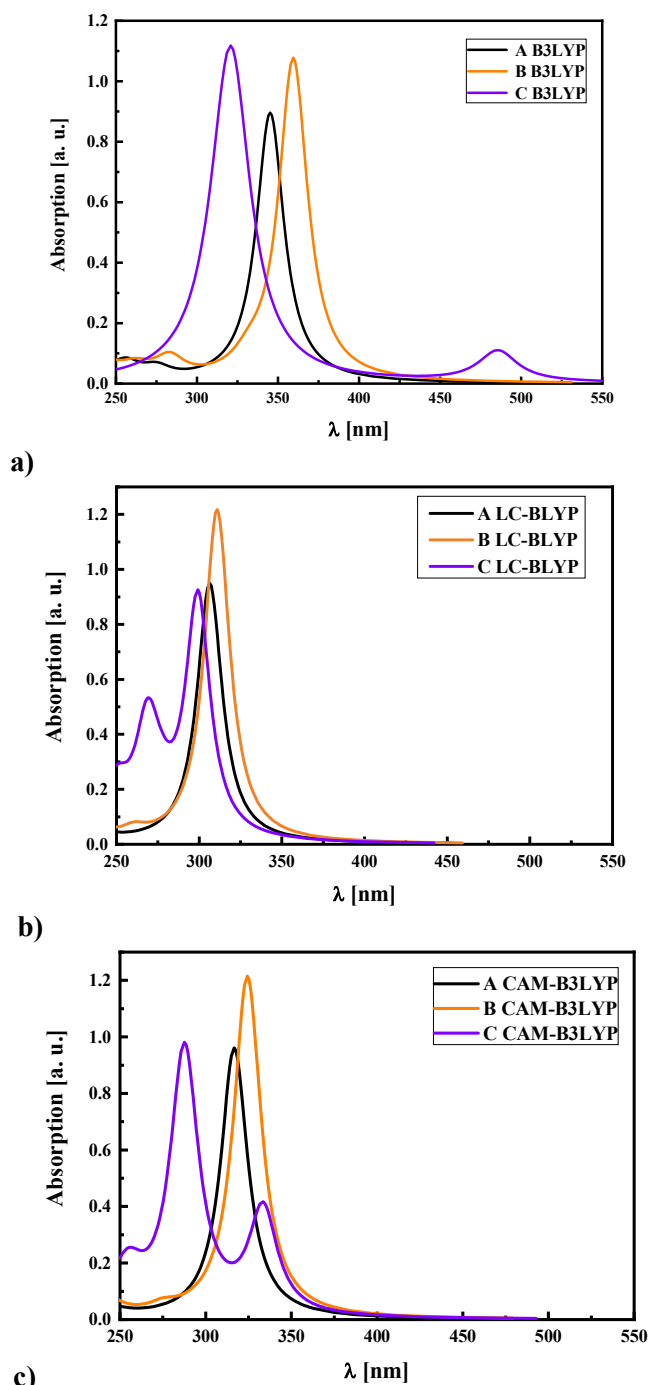
Figure 8.24. UV-vis absorption spectra calculated in vacuum for A, B, and C molecules by using the DFT methodology with B3LYP (a), LC-BLYP (b), and CAM-B3LYP functionals.

the B3LYP, CAM-BLYP, and LC-BLYP functionals. One can see that the HF method overestimates the difference ($\Delta E_{HOMO\text{-}LUMO}$) between the highest occupied molecular orbital (HOMO) and the lowest unoccupied molecular orbital (LUMO). It is seen that the first absorption peaks obtained by the HF method are significantly shifted into lower wavelengths for all molecules. Therefore, the UV–vis absorption spectra were also calculated by using DFT/B3LYP, DFT/LC-BLYP, and
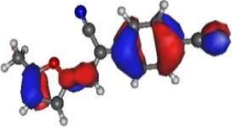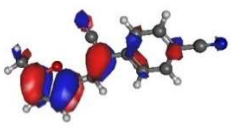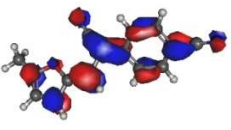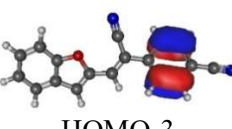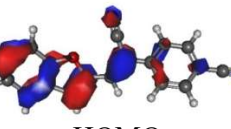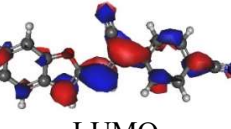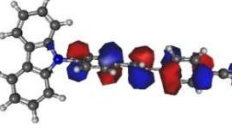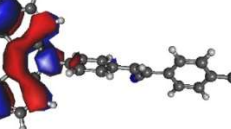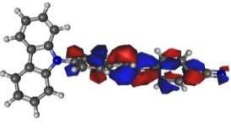
DFT/CAM-B3LYP methods, and they are presented in Fig. 8.24. These spectra are more in line with the experimental results. However, following the presented statement and analyzing data collected in Table 8.2 and Fig. 8.24, one can see that the spectral maximum wavelengths calculated for A and B molecules are shifted to the blue side compared with experimental spectra (see Fig. 8.23 (a)). Spectra calculated for molecule C by using the DFT/LC-BLYP and DFT/CAM-B3LYP functionals are shifted into the blue side but the ones calculated by DFT/B3LYP method are shifted into the red side. It means that the long correlated functionals overestimate the optical energy gap of the A, B, and C molecules as is observed for the *ab initio* HF method. One can conclude that the results calculated by the DFT/B3LYP method most correlate with experimental data.

To prove the proposed statement the UV–vis absorption spectra of the A, B, and C molecules were also calculated by using DFT/B3LYP method in chloroform and they are presented in Fig. 8.23 (b). In this case, one can see that the applying the DFT/B3LYP method one can well reproduce the UV–vis absorption spectrum of the A molecule. The discrepancy between experimental and calculated results is also not significant for B and C molecules (see Table 8.2). The chloroform effect gives better results for the C molecule than it was in the case of vacuum calculations. It confirms that the DFT/B3LYP method can be used to calculate the electronic and optical properties of the investigated compounds.

Analyzing the calculated UV–vis absorption spectra (see Fig. 8.23 (b)) one can say that the first UV–vis absorption peak is assigned to intramolecular charge transfer (ICT) occurring between donor and acceptor part of molecules and it is related to the π–π* transitions. The mentioned electron excitation is associated with the electron transfer from HOMO to LUMO orbital. The frontier orbitals of the A, B, and C molecules calculated by the DFT/B3LYP method are presented in Table 8.3. The second absorption peak is associated with the electron transfer from HOMO-1, HOMO-3, and HOMO-2 to LUMO orbital for A, B, and C molecules, respectively. The mentioned orbitals are presented in Table 8.3. The HOMO and LUMO orbitals of the A and B molecules are distributed almost over the entire atomic structure in contrast to the C molecule where the frontier orbitals are more separated one from the other. Separation of the frontier orbitals generally increases the NLO properties of molecules. In all cases, the donating character of the furan, benzofuran, and carbazole moiety in A, B, and C molecules, respectively is seen.

The benzonitrile moiety has an acceptor nature and mostly there the LUMO orbital is located.

Table 8.3. Frontier orbitals and orbitals involved in the creation of the second absorption peak seen in UV-vis absorption spectra calculated for the A, B, and C molecules by the DFT/B3LYP method in chloroform (see Fig. 23b)

Molecule A		
HOMO-1	HOMO	LUMO
Molecule B		
HOMO-3	HOMO	LUMO
Molecule C		
HOMO-2	HOMO	LUMO

In conclusion, it can be said that the UV-vis absorption spectra measured experimentally and the calculated ones correlate with each other (Fig. 8.23). However, the first UV-vis absorption peak calculated for the C molecule is significantly shifted into long-wavelength compared to the experimental data. Probably it is caused by the electron correlation interaction that is not taken into account in the B3LYP functional. The carbazole moiety increases an electron-donating strength that causes the absorption maximum shift from 360 nm in A and B molecules to 390 nm in the C molecule.

The electron properties of the isolated A, B, and C molecules were calculated applying the DFT/B3LYP method and the obtained results are presented in Table 8.4. One may see that the A and B molecules possess similar $\Delta E_{HOMO-LUMO}$. The carbazole moiety twisting the molecular structure significantly decreases the $\Delta E_{HOMO-LUMO}$ of molecule C compared with the A and B compounds but at the same time, it reduces its dipole moment. The carbazole group also decreases the electronegativity χ of molecule C. Molecule A possesses the highest electronegativity value (χ=1.87 eV) of all compounds so, it is the best electron acceptor. This behavior is not appropriate for the NLO applications. Analyzing results presented in Tab. 8.4 one can see that the most polar are the molecules A

and then B. Molecule C is the longest one but its dipole moment is not so significant. The NLO properties of the molecules are proportional to the dipole moment and inversely proportional to the HOMO-LUMO energy gap difference. In this case, the molecules A and B should be favorable for the NLO applications but in the next part of the work, we will show that this is not a sufficient condition to achieve high NLO hyperpolarizabilities.

Table 8.4. Electron properties of the A, B, and C molecules calculated by the DFT/B3LYP method

Molecule	HOMO [eV]	LUMO [eV]	χ [eV]	$\Delta E_{HOMO-LUMO}$ [eV]	Dipole moment μ [D]
A	-6.20	-2.45	1.87	3.75	7.48
B	-6.33	-2.71	1.81	3.62	6.88
C	-5.71	-2.72	1.50	2.99	4.00

8.3. Optical properties of the A,B, and C molecules embedded into PMMA matrix

The A, B, and C molecules were embedded into PMMA polymeric matrix to investigate the electron and optical properties of the synthesized composite materials. The samples were prepared in the form of thin films using the spin-coating deposition technique. The solution of 1,1,2-trichloroethane containing PMMA 25 g/L and 5 or 10 wt.% of the chromophores was prepared. The thin films were coated on glass slides. The angular speed of spin-coating deposition was chosen to be 2000 rpm for the duration of 60 s. Immediately after deposition, the thin films were dried in a vacuum at 60 °C for 2 h to remove the residual solvent. The thickness of deposited films was measured by the profilometer (Dektak6M, Veeco) and was found to be 400 nm for samples with 5 wt.% of chromophores and 200 nm with 10 wt.% of chromophores. The UV–vis spectroscopy measurements were performed in the 230–1000 nm spectral region at room temperature for thin films deposited on glass substrates using a Shimadzu UV-1800 spectrometer.

Spectra measured for the samples with the 5 wt% of dopants are presented in Fig 8.25. One can see that these spectra possess the first absorption peak above 300 nm. It means that the prepared samples contain the A, B, and C chromophores

because the PMMA polymer does not absorb visible light. The first absorption peak measured for the PMMA is located below 300 nm [25]. Comparing the spectra presented in Fig. 8.23 (a) and Fig. 8.25 one can see that the ones measured in the polymer are insignificantly shifted into the red spectral range. Deconvoluted first absorption peak measured for A/PMMA, B/PMMA, and C/PMMA sample gives maximum at 374 nm, 362 nm, and 407 nm, respectively. Comparing these data with the ones presented in Table 8.2 one can see a small bathochromic shift for the spectra measured in PMMA.
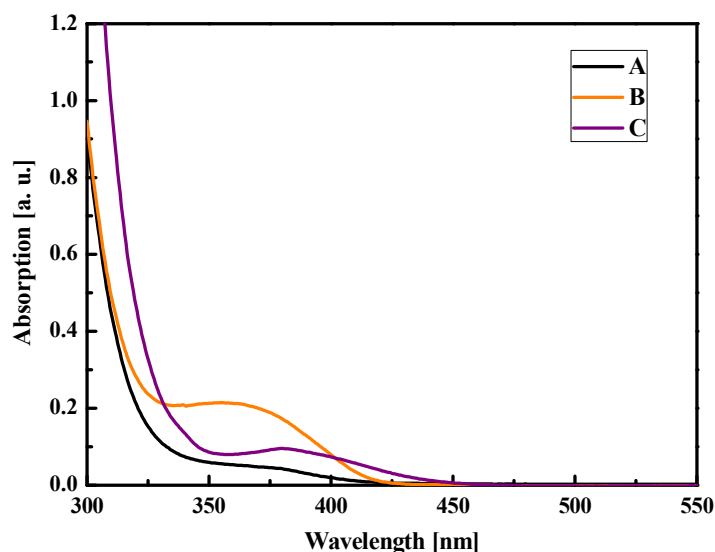
Figure 8.25. Measured UV-vis absorption spectra obtained for the 5 wt% of the A, B, and C chromophores embedded into PMMA polymeric thin film

The UV-vis absorption spectra measured for the A/PMMA, B/PMMA, and C/PMMA samples with a concentration of chromophores equal to 10 wt% are similar to the ones presented in Fig. 8.25. Concluding the performed measurements one can say that interaction between chromophores and PMMA is higher than it is observed in chloroform. This can be inferred from the shift of the UV-vis absorption spectra (see Fig. 8.25) into red wavelength compared with the spectra measured in solvent (Fig. 8.23 (a)). Additionally, it should be noted that the dielectric constant of the chloroform is higher ($\varepsilon=4.81$) than the dielectric constant of the PMMA ($\varepsilon=3.00$) and despite this electrostatic and multipolar interaction between PMMA and chromophores is more significant.

The samples with deposited thin films of PMMA with embedded A, B, and C chromophores were polled in an external electric field. They were placed on a hot

plate and heated at poling temperature equal to 95 °C. The external electric field was provided by applying a voltage equal to 5 kV to a tungsten needle fixed 1 cm above at guest-host composite material. The heater was switched out within the remaining electric field, and the sample was cooled down to room temperature. The electric field was acting along the Z-axis of the studied system to align the chromophores in one direction. In the end, the corona field was turned off. The entire process took about 2.5 h. The second-harmonic generation (SHG) and third-harmonic generation (THG) measurements were carried out employing the rotational Maker fringe technique [26] in the transmission scheme for the s- and p-polarized fundamental laser beam. A y-cut crystalline quartz plate was used as reference material for SHG measurements and a fused silica plate for THG measurements. The samples were irradiated by the mode-locked Nd:YAG/YVO laser (EKSPLA) beam with wavelength $\lambda = 1064$ nm, 30 ps pulse duration, and 10 Hz repetition rate.

Fig. 8.26 presents the dependences of the SHG intensity generated in the A, B, and C-based *guest-host* thin films with two concentrations of chromophores embedded into PMMA polymeric matrix as the function of incident angle. The maximum of the signal was reached at 60° for all samples and minimal intensity was measured at normal incidence of the fundamental beam due to the lack of noncentrosymmetry in this direction. The signal recorded for the composite C confirms their highest $\chi^{(2)}$ susceptibility.

The quadratic NLO susceptibility can be calculated using the following equation [27]:

$$\chi^{(2)} = \chi^{(2)}_{Quartz} \left(\frac{2}{\pi}\right) \left(\frac{l^{co}_{Quartz}}{d}\right) \left(\frac{I^{2\omega}}{I^{2\omega}_{Quartz}}\right)^{1/2} \tag{8.1}$$

where $\chi^{(2)}_{Quartz} = 1.0$ pm/V [28], coherent length of quartz $l^{coh}_{Quartz} = \frac{\lambda}{4.|n_{2\omega} - n_\omega|} = 21$ μm, d is investigated film thickness, $I^{2\omega}$ and $I^{2\omega}_{Quartz}$ are the SHG intensities coming from the investigated samples and quartz, respectively, under the same conditions. The calculated susceptibilities are collected in Table 8.5.

a)

b)

Figure 8.26. The SHG intensity as a function of the incident angle measured for A, B, and C molecules based films with 5 wt% (a) and 10 wt% (b) of chromophores embedded into the PMMA matrix

Table 8.5. Second $\chi^{(2)}$ and third-order susceptibility $\chi^{(3)}$ measured for polarization p-p for the sample with 5 wt% and 10 wt% of chromophores in the PMMA matrix and the thickness of the prepared chromophore/PMMA thin films

	Chromophores concentration	A	B	C
$\chi^{(2)}$ [10^{-12} pmV^{-1}]	5 wt%	0.25	0.37	0.79
	10 wt%	0.28	0.29	0.36
$\chi^{(3)}$ [10^{-22} m^{2}V^{-2}]	5 wt%	5.96	4.28	12.26
	10 wt%	20.60	11.36	20.84
d [μm]	5 wt%	0.57	0.40	0.38
	10 wt%	0.17	0.18	0.17

The thickness of the tested samples is also shown in Table 8.5. Generally, the samples with chromophores concentration equal to 10 wt% are thinner than the ones with chromophores concentration equal to 5 wt%. One may see that for both groups of samples (5 wt% and 10 wt%) the increase of susceptibility $\chi^{(2)}$ has the same tendency. Compound C exhibit the highest SHG parameters and the lowest ones exhibit compound A. A more extended conjugated character of molecule C relating

to its strong push-pull character and narrow band gap causes a high SHG signal even if the dipole moment of the molecule is not so high. The obtained results allow concluding that the corona polling used to order the chromophores in the polymeric matrix is the most efficient for the C molecules. These molecules are long and their back relaxation to a disordered state is not so easy. In consequence, a signal of the SHG is intense for thin-film with chromophore C.

The measured second-order susceptibilities of corona-poled A/PMMA, B/PMMA, and C/PMMA composites possess the values in the range 0.25-0.79 $\times 10^{-12}$ pm/V. These values are comparable with the second-order susceptibility of the urea ($\chi^{(2)}$=1.0 $\times 10^{-12}$ pm/V) [29]. The urea molecule is the most used reference material when assessing the second-order NLO properties of molecular systems. The other molecular systems with similar size to the investigated compounds eg. conjugated organic push-pull ligands poses susceptibility $\chi^{(2)}$=0.79-2.1 $\times 10^{-12}$ pm/V [30] or benzodifuran derivatives have susceptibilities even lower than the investigated molecules ($\chi^{(2)}$=0.12-0.37 $\times 10^{-12}$ pm/V) [31]. Therefore, one can conclude that the second-order susceptibilities of the A, B, and C molecules are comparable with the second-order susceptibilities of other similar systems.

Measurements of the THG signal occurring for A/PMMA, B/PMMA, and C/PMMA composites were performed for both s-s and p-p polarization. Here, only the Maker fringes measured for p-polarization are presented because s-s dependence exhibits similar behavior (Fig. 8.27). To calculate the third-order NLO susceptibilities Kubodera-Kobayashi model [32] was used:

$$\chi^{(3)} = \chi^{(3)}_{Silica} \left(\frac{2}{\pi}\right) \left(\frac{l^{coh}_{Silica}}{d}\right) \left(\frac{\frac{\alpha d}{2}}{1-e^{-\frac{\alpha d}{2}}}\right) \left(\frac{I^{3\omega}}{I^{3\omega}_{Silica}}\right)^{1/2} \tag{8.2}$$

where $\chi^{(3)}_{Silica} = 2 \times 10^{-22}$ m^2 V^{-2} [32,27], $l^{coh}_{Silica} = \frac{\lambda}{6|n_{3\omega}-n_\omega|} = 6.7 \ \mu m$ is the coherent length of silica, d is the film thickness, l^{coh}_{Silica} and $I^{3\omega}_{Silica}$ are the THG intensities of sample and silica at the same conditions, respectively. The obtained values of $\chi^{(3)}$ for p-polarization are presented in Table 8.5. Compound C exhibit the highest THG parameter as it was noticed for the SHG signal. However, the lowest $\chi^{(3)}$ value was obtained for the B compound. The measured $\chi^{(3)}$ for investigated materials is in the range 11.36 - 20.84 $\times 10^{-22}$ m^{2}V^{-2} and it is much higher than the respective value of the reference material. The obtained $\chi^{(3)}$ value for the C molecule is roughly ten times larger than vales measured by the same technique for

the reference glass plate and much higher than the $\chi^{(3)}$ susceptibility values for a similar system [30].

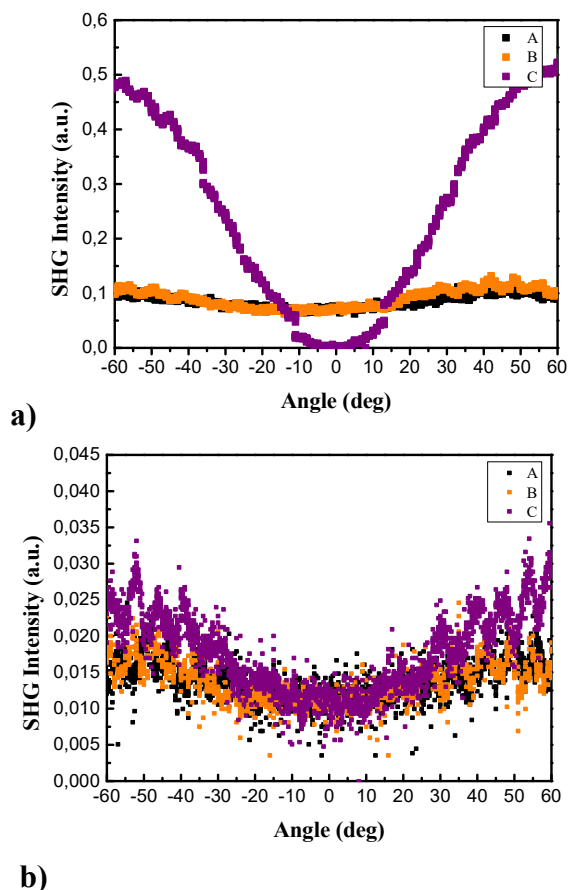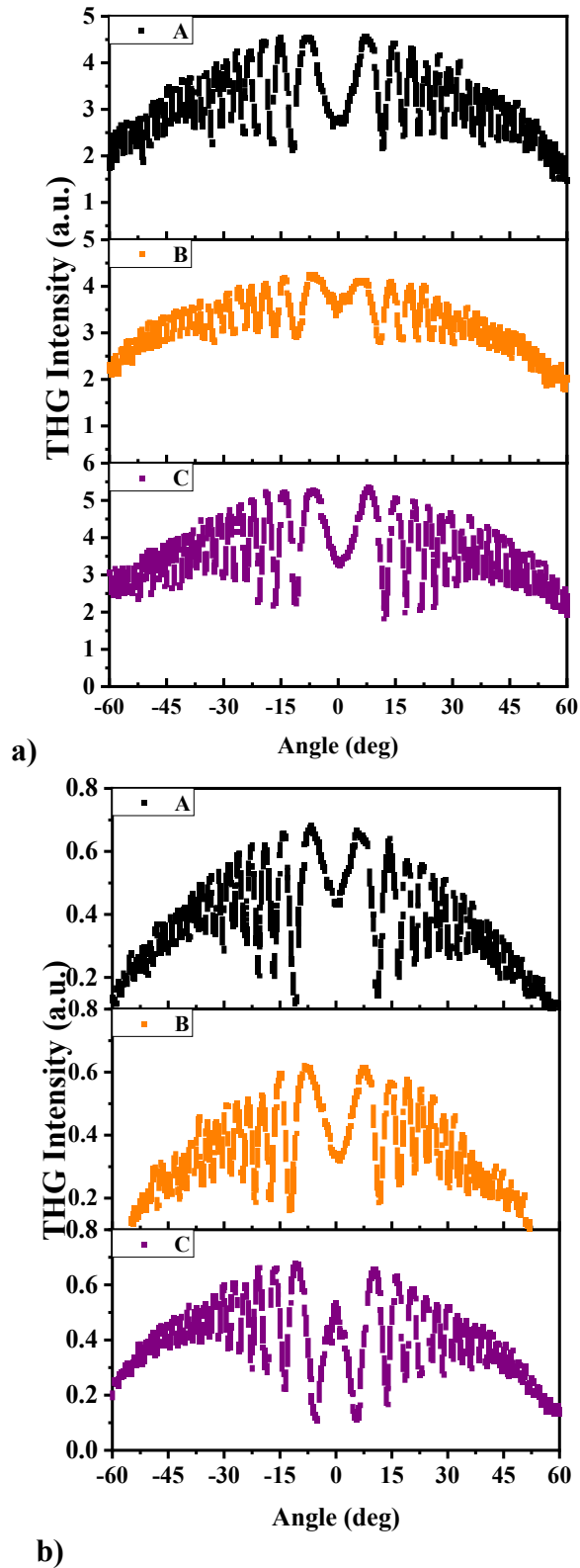**Figure 8.27.** The THG intensity as a function of the incident angle measured for A, B, and C films with 5 wt% (a) and 10 wt% (b) of chromophores embedded into the PMMA matrix

The susceptibilities $\chi^{(2)}$ and $\chi^{(3)}$ collected in Table 8.5 are proportional to the second-order and third-order hyperpolarizabilities, respectively. Therefore, the static polarizability α and static hyperpolarizabilities β and γ, and also their frequency dependence values were calculated using the *ab initio* method and they are presented in Table 8.6. The *ab initio* method was chosen because it gives the $\Delta E_{HOMO\text{-}LUMO}$ enough big to not be in resonance with the THG generation. The value described by the $(F_x,F_y,F_z=0,0,0)$ were calculated for the isolated molecules in a vacuum. The value of electric dipole moment and $\Delta E_{HOMO\text{-}LUMO}$ obtained by *ab initio* calculations correlate with the data predicted by the DFT/B3LYP calculations. In this case, the tendency of the polarizabilities and hyperpolarizabilities changes calculated for the A, B, and C molecules can be compared.

One may see that molecule C has the highest static and frequency-dependent polarizability α_{av} compared with the molecules A and B. The same tendency is observed for the static γ_{av} values. Static β_{av} values obtained for the A and B molecules are twice higher than the corresponding value obtained for the C molecule. It is because of the significant difference between the dipole moment of A, B and C molecules (see Table 8.6). The same dependence is seen for the frequency-dependent β_{av} but the difference between A and B molecules in the hyperpolarizability is much more significant. The frequency-dependent β_{av} has the highest value for molecule B even if the dipole moment has the highest value for molecule A. In addition, the highest value of the frequency-dependent γ_{av} was calculated for the B molecule.

Determination of theoretically obtained average second and third-order hyperpolarizability of a molecule is often used to understand the affinity between the molecular structure and NLO properties. One can observe that the value of first hyperpolarizability $\beta_{av}(-2\omega;\omega,\omega)= 2267.26$ a.u. $(\lambda = \infty$ nm) (see Table 8.6.) obtained for chromophore B is two orders higher than the one for urea (static first hyperpolarizability for urea molecule $\beta(-2\omega;\omega,\omega) = 35.735$ a.u. [31]. Leupacher et al. [33] reported the third-order hyperpolarizability of methylene blue equal to $\gamma(-3\omega;\omega,\omega,\omega)=63500$ a.u. employing THG measurements and the value of compound B $\gamma(-3\omega;\omega,\omega,\omega)=163926.96$ a.u. is much higher (see Table 8.6).

Generally, one may conclude that calculated hyperpolarizabilities β and γ indicate significantly higher values compare to reference material. The observed discrepancy may be due to the intramolecular multipolar interaction, which is not taken here into account. The other factor not included here is the alignment of the molecules and their intermolecular interaction which is also not taken into account. To explain the nature of NLO properties of the chromophore/PMMA composites molecular dynamic modeling should be performed.

Data presented in Table 8.6 in columns depicted as Fx,Fy,Fz≠0,0,0 for PMMA are calculated applying the local field model as it was described in Chapter 7. These data reproduce the NLO parameters of the molecules affected by the polymer environment. The structures taken into account are these modeled at 300 K with removed poling external electric field. It means that the chromophores located in the polymer matrix were firstly aligned in the liquid state, then the systems were cooled up to a glassy state keeping the external electric field acting and then the electric field was switched off and the system was relaxed during a time equal to 1.5 ns. The last structure obtained from the described simulation was taken to calculate the intensity of the local electric field (F) acting on the chromophore according to the theory of local field approximation [34]. In the framework of local field theory, linear and nonlinear macroscopic susceptibilities are related to molecular properties changed by local field factors, which describe the effect of the electric field on a molecular site induced by the intermolecular interaction. In discrete local field theory, the F is computed by considering the molecular environment rigorously, without resorting to a continuum or mean-field approximations.

Analyzing data presented in Table 8.6 one may see that the highest F is acting on the B molecule embedded into the PMMA matrix. It is probably caused by the fact that the B chromophore enters between mers of PMMA. The PMMA decreases $\Delta E_{HOMO\text{-}LUMO}$ of all chromophores increasing the electric dipole moment of the B and C molecules. In consequence of these changes, the B and C molecules should potentially be better chromophores for NLO applications than the A.

.

Table 8.6 Electron and optical properties of the A, B, and C molecules calculated in vacuum ($F_x,F_y,F_z=0,0,0$), in PMMA, and PVK polymer ($F_x,F_y,F_z\neq0,0,0$) in volumetric form by using *ab initio* HF method

Molecule	A			B			C		
Environment	vacuum	PVK	PMMA	vacuum	PVK	PMMA	vacuum	PVK	PMMA
Electric field F_x,F_y,F_z [GV/m]	0, 0, 0	1.62, 1.86, 0.69	1.13, -2.31, 0.42	0, 0, 0	0.91, -1.31, -0.93	2.32, 2.62, 2.39	0, 0, 0	-1.03, -0.16, 3.82	1.32, 1.59, 1.32
F_{av} [GV/m]	0.00	2.56	2.61	0.00	1.85	4.24	0.00	3.82	2.45
μ [D]	7.48	8.26	7.23	6.88	6.20	9.99	5.02	12.39	9.73
HOMO [eV]	-8.26	-7.14	-9.62	-8.29	-8.80	-5.93	-7.90	-5.30	-5.30
LUMO [eV]	0.72	1.68	-1.19	0.44	-0.38	2.67	0.55	0.35	1.21
$\Delta E_{HOMO\text{-}LUMO}$ [eV]	8.98	8.82	8.44	8.73	8.42	8.59	8.45	5.65	6.52
$\lambda=\infty$ nm									
α_{xx}	202.37	202.54	202.44	125.65	125.76	125.77	324.57	330.38	328.59
α_{yy}	103.10	103.19	103.35	249.38	249.60	251.27	302.48	301.64	301.62
α_{zz}	284.75	283.97	285.41	338.22	338.88	340.71	422.19	430.97	429.41
α_{av}	196.74	196.57	197.07	237.75	238.08	239.25	349.75	354.33	353.21
$\beta_{(z;z,z)}$	1241.12	1140.79	1303.96	1204.01	1325.92	1595.40	577.38	2634.78	2087.61
$\beta_{(y;y,y)}$	11.75	84.43	-78.38	-456.22	-552.36	-524.48	-122.93	-184.25	166.75
$\beta_{(x;x,x)}$	258.13	191.98	298.16	-27.93	18.48	86.77	228.04	886.73	910.48
$\beta_{(z)}$	839.62	1614.11	1769.44	1792.10	1953.61	2516.88	761.32	4080.97	3150.99
$\beta_{(y)}$	161.67	272.13	11.21	-1358.69	-1616.80	-1628.46	153.15	506.09	905.5
$\beta_{(x)}$	1201.90	1032.03	1311.27	287.80	392.50	618.85	691.34	2610.98	2520.86

β_{vec}	1475.01	1935.07	5731.53	2267.26	1164.73	25141.80	1039.72	4871.10	4135.63
$\gamma_{(z;z,z,z)}$	208040.85	200317.58	214206.75	263309.47	273839.92	269001.10	273389.68	457070.81	404299.81
$\gamma_{(y;y,y,y)}$	19477.92	20032.40	20032.01	117496.68	119559.23	128795.41	100163.57	102105.10	101443.00
$\gamma_{(x;x,x,x)}$	49115.54	50269.74	49248.72	25541.68	25684.65	25844.01	113038.68	167368.97	151114.62
γ_{vec}	100789.57	98809.38	68254.41	163926.96	168691.04	106486.16	173638.70	120339.68	158200.98
$\lambda = 1064$ nm									
α_{xx}	205.67	205.85	205.73	126.81	126.76	126.94	330.32	336.85	334.85
α_{yy}	103.86	103.95	104.12	254.61	249.60	256.71	307.44	306.58	306.55
α_{zz}	295.62	294.75	296.36	351.91	338.88	354.93	433.84	444.11	442.19
α_{av}	201.72	201.52	202.07	244.44	238.41	246.19	357.20	362.51	361.20
$\beta_{(z;z,z)}$	2064.29	1888.23	2175.27	2186.69	2420.72	2875.84	961.18	4502.21	3538.76
$\beta_{(y;y,y)}$	13.76	96.30	-88.58	-695.71	-827.07	-851.80	-150.87	-230.18	215.13
$\beta_{(x;x,x)}$	368.09	290.41	413.11	-34.04	19.55	98.01	340.76	1465.61	1389.80
$\beta_{(z)}$	2766.83	2581.94	2874.58	3153.36	3473.87	4342.51	1279.00	6836.45	5268.59
$\beta_{(y)}$	235.78	359.37	62.54	-2210.82	-2596.59	-2735.23	240.71	886.64	1330.79
$\beta_{(x)}$	1789.19	1560.42	1934.33	473.16	611.72	922.04	1056.34	4419.36	4004.46
β_{vec}	3303.35	3038.17	3465.36	3880.11	2387.40	3496.58	1676.20	8188.65	6750.17
$\gamma_{(z;z,z,z)}$	822873.92	779529.69	856993.07	1220822.88	1295989.98	1373564.33	836301.70	2839445.09	1954510.60
$\gamma_{(y;y,y,y)}$	25252.81	26348.88	26358.52	359805.25	373794.63	424162.40	170852.50	177345.01	174306.85
$\gamma_{(x;x,x,x)}$	116815.30	118530.66	117537.11	34558.06	34849.19	35616.46	255860.36	695963.78	511434.78

The PMMA environment increases the β_{vec} values of the A and C molecules not changing the mentioned value for the B. The β_{vec} induced by the local electric field is the highest one for the C/PMMA composite. It allows us to suppose that the experimentally measured second-order NLO signal will be the highest for the C/PMMA.

Unfortunately, the third-order parameters calculated for the A, B, and C chromophores embedded into the PMMA matrix decrease compared to the values obtained for the isolated molecules. It means that the PMMA matrix cancels the third-order NLO parameters of investigated chromophores and should not be used for these applications.

8.4. Optical properties of the A, B, and C molecules embedded into PVK matrix

To investigate the influence of polymer matrix with different polarity than PMMA the A, B, and C chromophores were embedded into the PVK matrix. The PVK polymer is more polar than the PMMA. The electron and optical properties of A/PVK, B/PVK, and C/PVK composites were investigated computationally and experimentally by measuring UV-vis absorption spectra as well as SHG and THG generated signals.

Electron and optical properties of the A, B, and C molecules were calculated in a vacuum and PVK polymer environment using the *ab initio* method. All obtained results are collected in Table 8.6. The properties of the molecules for which calculations were carried out in a vacuum correspond to the values described as $F_x, F_y, F_z = 0,0,0$. Data obtained for A, B and C molecules in PVK polymer are denoted as $F_x, F_y, F_z \neq 0,0,0$. Electron properties of the A, B, and C molecules in PVK were calculated based on the structures of composites in the volumetric form obtained from MD simulations as it was described in the previous chapter for the PMMA-based composites.

Analyzing data collected in Table 8.6 one can see that the highest local electric field ($F=3.82$ GV/m) is acting on the C molecules in direction of Z of the laboratory coordinate system. It is also the direction of the electric dipole moment of the chromophore C. The local electric field acting on A and B molecules is equal

to 2.56 and 1.85 GV/m, respectively. One may see that the high intensity of the local electric field acting on molecule C changes significantly its electric properties. The important changes are seen in the increase of electric dipole moment from 5.02 D up to 12.39 D as well as in the decrease of the $\Delta E_{HOMO\text{-}LUMO}$ from 8.45 eV up to 5.65 eV. The NLO properties of the molecules are proportional to the dipole moment and inversely proportional to the *HOMO-LUMO* energy gap difference. In this case, molecule C embedded into the PVK matrix should be favorable for the NLO applications.

In Table 8.6 static and frequency-dependent polarizabilities ($\lambda = \frac{2\pi c}{\omega} = 1064\ nm$) calculated for A, B, and C molecules in a vacuum, and PVK in the volumetric form are presented. Here also the selected components of the second and third-order hyperpolarizabilities are collected. Should be mentioned that all molecules were rotated to have a static electric dipole moment along the Z-axis of the laboratory coordinate system.

The average value of polarizability (α_{av}) has the highest value for the C molecule. It is true for the static and frequency-dependent parameters. The acting local electric field does not change the values of the calculated polarizabilities for A and B molecules but it increases static and frequency-dependent polarizabilities of C molecules. The local electric field drastically increases the β_{vec} for the C molecule, decreasing the mentioned parameter for the B molecule in the static and frequency-dependent regime. The local electric field almost does not change the β_{vec} for A molecule. The third-order hyperpolarizabilities of the investigated chromophores are also affected by the local electric field. The static γ_{vec} decreases with the local electric field for the A and C molecules and slightly increases for the B molecule. However, the frequency-dependent γ_{vec} of the C molecule increases significantly in the PVK environment. The changes observed for the A and B molecules in the PVK environment are not so spectacular.

The A, B, and C molecules were dissolved in 1 ml of the 1,1,2-trichloroethane (1,1,2-TCA) with 30 mg of PVK forming 5 wt % and 10 wt % solutions. Thin films were prepared by spin coating method on appropriately cleaned glass substrates. The thickness of prepared thin films was measured by using a profilometer (Dektak 6M). UV–Vis spectra were measured for all prepared films by using the Shimadzu

UV-1800 spectrometer (Shimadzu USA Manufacturing, INC. 1900 SE 4th Ave. Canby. Oregon 97013, USA) in the range of 250–1100 nm. The second-harmonic generation SHG and third-harmonic generation THG measurements were carried out by using the Maker fringe setup. Samples were rotated from −60° to +60° and the intensity of the generated harmonics as a function of incident angle was measured in S- and P-polarization. No restriction of polarization has been noted for THG measurements. The fundamental wavelength of the laser beam was 1064 nm, frequency 10 Hz, pulse duration 30 ps, and energy 90 μJ.

The absorption spectra of the A, B, and C-based samples were measured in a range of UV-vis wavelengths (Fig. 8.28). It was noted that at a wavelength corresponding to generated second harmonic (532 nm), the absorbance is insignificant, However, at 355 nm which corresponds to generated third harmonic, absorbance is not negligible. It means that UV-Vis absorption influences the response results. It determines that the generated response is at the same time absorbed. It is necessary to take into count the absorption coefficient in NLO calculations. Calculated values of absorption coefficients for 355 nm (THG) are given in Table 8.7. The peaks at 331 and 344 nm come from polymer matrix PVK. Spectra presented in Fig. 8.28 correspond with computationally predicted $\Delta E_{HOMO\text{-}LUMO}$ collected in Table 8.6.
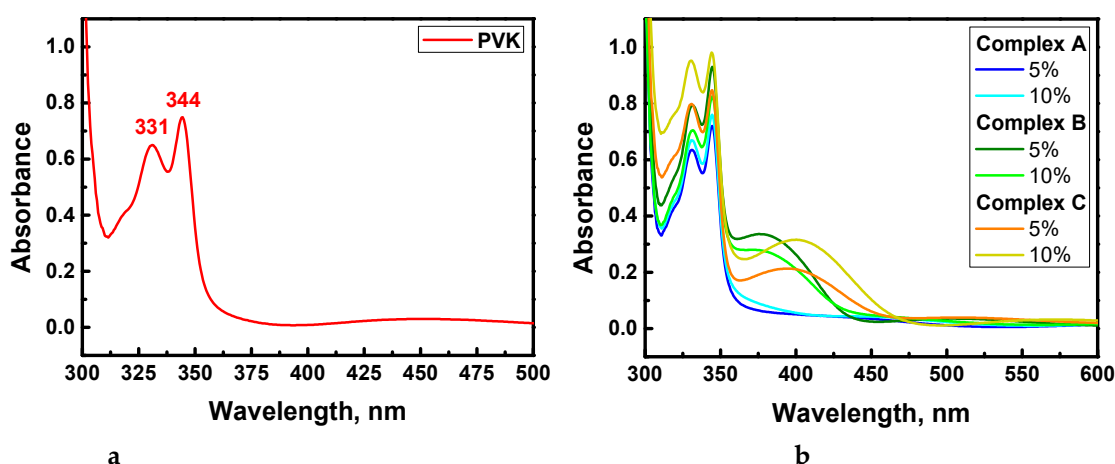
Figure 8.28. Absorption spectra measured for PVK (a) and studied A/PVK, B/PVK, and C/PVK composites (b) in form of thin films.

Second and third-order NLO susceptibilities were calculated using theoretical comparative models and then analyzed. The measurements of SHG response of polymer films with embedded A, B, and C molecules have been performed after

their poling. The dipole moments of chromophores are oriented perpendicularly to the substrate surface, the maximum interaction between the electric field of the fundamental beam with the dipole moments will be obtained at an angle of $\theta = \pm 45°$. This targeting will go to zero for the angle of $\theta = 0°$. The measurements in two polarization configurations of fundamental and harmonic waves (*s-p* and *p-p*) were performed. It was observed that in the case of SHG the polarization influences obtained results. A typical SHG signal exhibits two characteristic bands on either side of the origin for both configurations of polarizations (*s-p* and *p-p*) (see Fig. 8.29).
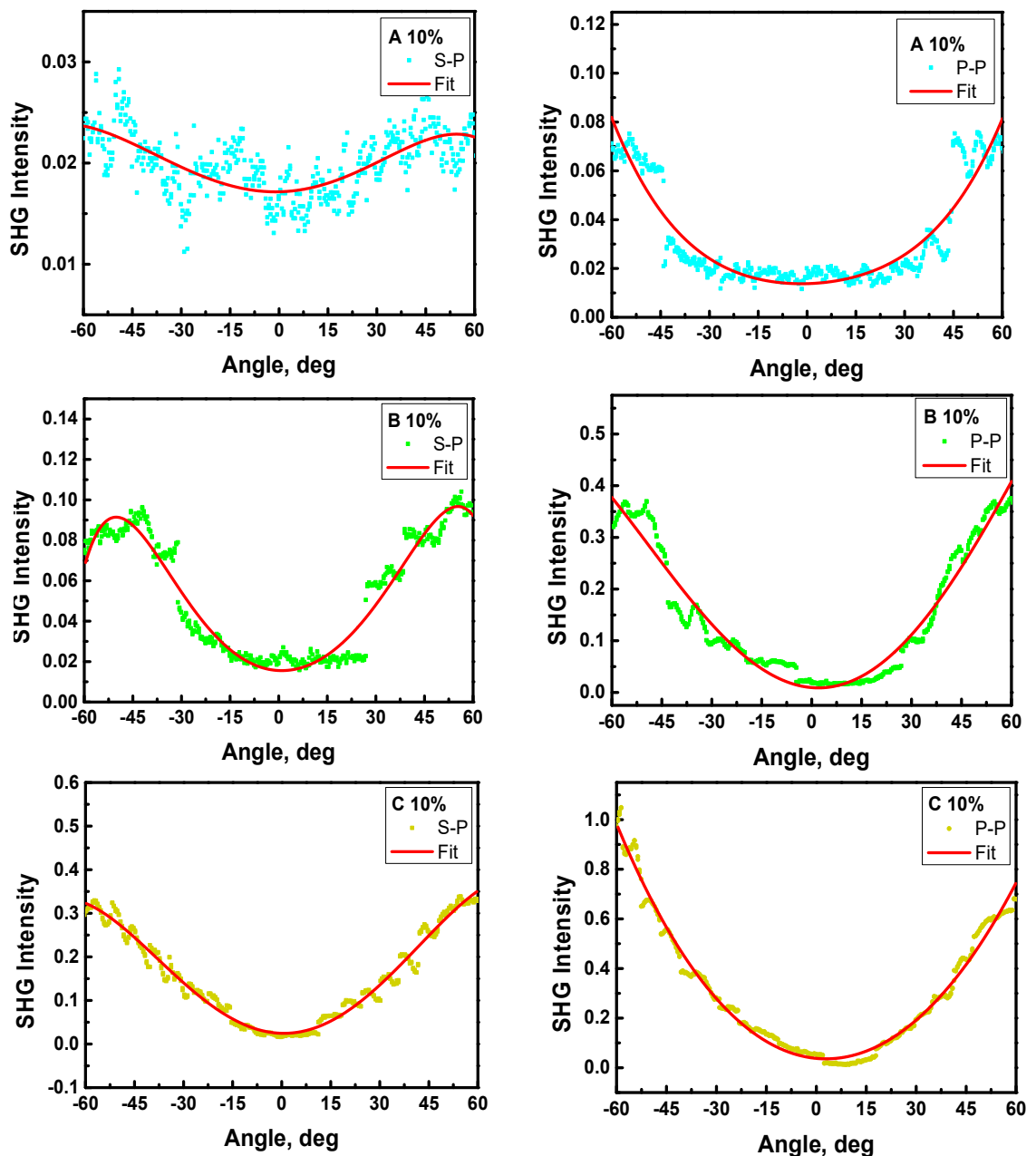
Figure 8.29. SHG intensity as a function of the incident angle measured for complexes A/PVK, B/PVK, and C/PVK with 10 wt% of A, B, C chromophores in s-p (left) and p-p (right) polarization.

Second-order nonlinear optical susceptibility was calculated by using data presented in Fig. 8.29 and applying the Lee model and, third-order nonlinear optical susceptibility was calculated by using the Kubodera-Kobayashi model. The used equations are presented in subchapter 8.3 by equations 8.1 and 8.2. Obtained data are collected in Table 8.7. They're also the measured thicknesses of the samples are presented.

Table 8.7. The thickness of the layers of the tested samples, the absorption coefficients assigned to them, and effective $\chi^{(2)}$ and $\chi^{(3)}$ values obtained for A, B, and C films in the PVK matrix, taking into account experimentally measure data.

Sample	Thickness [nm]	α_{355nm} [10^3 cm^{-1}]	$\chi^{(2)}$ [pmV^{-1}]		$\chi^{(3)}$ [10^{-22} m^{2}V^{-2}]
			s-p	p-p	p-p
Quartz	1000	-	1.00		-
Silica			-		2.00
A 5 wt%	360	10.72	0.085 ± 0.028	0.114 ± 0.030	24.75 ± 0.75
A 10 wt%	320	14.09	0.111 ± 0.028	0.214 ± 0.022	**27.61 ± 0.93**
B 5 wt%	570	16.03	0.124 ± 0.008	0.319 ± 0.008	14.45 ± 0.32
B 10 wt%	410	18.26	0.162 ± 0.012	0.373 ± 0.013	19.38 ± 0.55
C 5 wt%	510	10.25	0.187 ± 0.008	0.396 ± 0.009	19.72 ± 0.45
C 10 wt%	460	16.27	**0.269 ± 0.009**	**0.446 ± 0.012**	**25.71 ± 0.62**

The experimental SHG response from A/PVK, B/PVK, and C/PVK films for the *p-p* input-output configuration of polarization was found to be much higher than that for the *s-p* polarization. It means that the studied compounds polarize the beam in the vertical direction, which may be noticed in Table 8.7 and Fig. 8.30. It is also the direction of the electric dipole moment of the chromophores. The obtained SHG results came from the difference in values of $\chi^{(2)}$ tensor elements responsible for the corresponding scheme of the experiment ($\chi^{(2)}_{zzz}$ and $\chi^{(2)}_{zxx}$). The $\chi^{(2)}_{zzz}$ and $\chi^{(2)}_{zxx}$ values obtained for investigated molecular systems remain in the ratio $\chi^{(2)}_{zzz}/\chi^{(2)}_{zxx}=3$ [35]. A lower SHG response has been obtained for the A compound, where a substituent is a methyl-furan group. It is going well with performed calculations. From Table 8.6 one can see that the lowest value of the β_{zzz} is obtained for the A molecule. The β_{vec} calculated for molecules in PVK is a little bit lower for the B than for the A molecule but the obtained discrepancies may be caused by the too high alignment of the chromophores inside the polymer matrix.

Computationally obtained alignment is equal to 90% which is much higher than in the experimentally observed systems.

Higher second-order NLO susceptibility of 10 wt% C/PVK compared to 10 wt% A/PVK is caused by the presence of donor carbazole group contributing to better charge transfer occurring in this molecule.
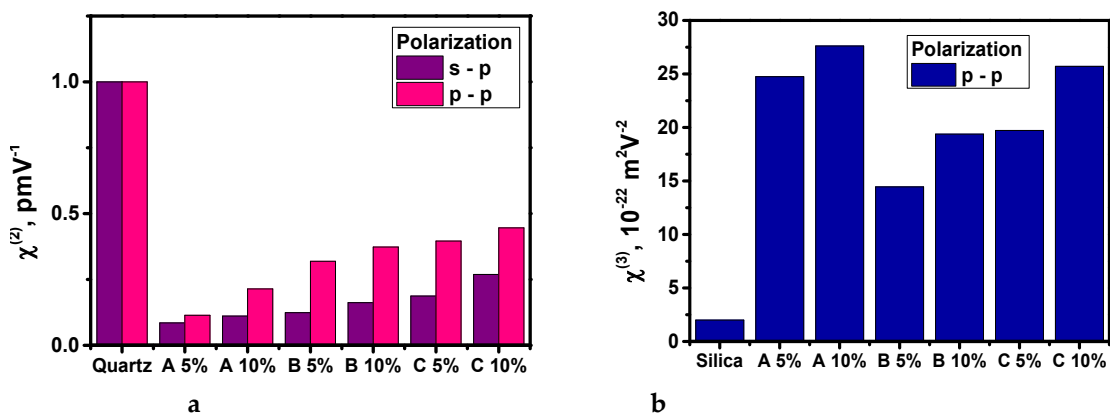
Figure 8.30. Second (a) and third-order (b) NLO susceptibilities calculated for studied A/PVK, B/PVK, and C/PVK thin films with different content of chromophores taking into account experimentally obtained data.

The third-order NLO properties of A/PVK, B/PVK, and C/PVK thin films were investigated experimentally using the third-harmonic generation technique (THG). In Fig. 8.31 the dependences of THG signal on fundamental laser beam incident angle are presented. In the case of THG is observed that response did not depend on the polarization of the laser beam. As it can be seen, the C/PVK film is characterized by a much higher THG response than the other systems. It is going well with performed quantum chemical calculations taking into account the influence of polymer matrix on properties of the chromophores applying the local field approach. The frequency-dependent γ_{vec} of the C molecule grows significantly in the PVK environment (Table 8.6).

In Table 8.7 and Figure 8.30 the obtained values of third-order NLO susceptibility are given. These values were calculated with consideration of the optical absorption coefficient α_{355nm} at the wavelength of the third harmonic. From the THG theory, it is known that only electronic contribution is included in obtained values of $\chi^{(3)}$. A higher THG response after taking into account the absorption coefficient has been observed for complexes A/PVK and C/PVK in 10 wt% of solutions.
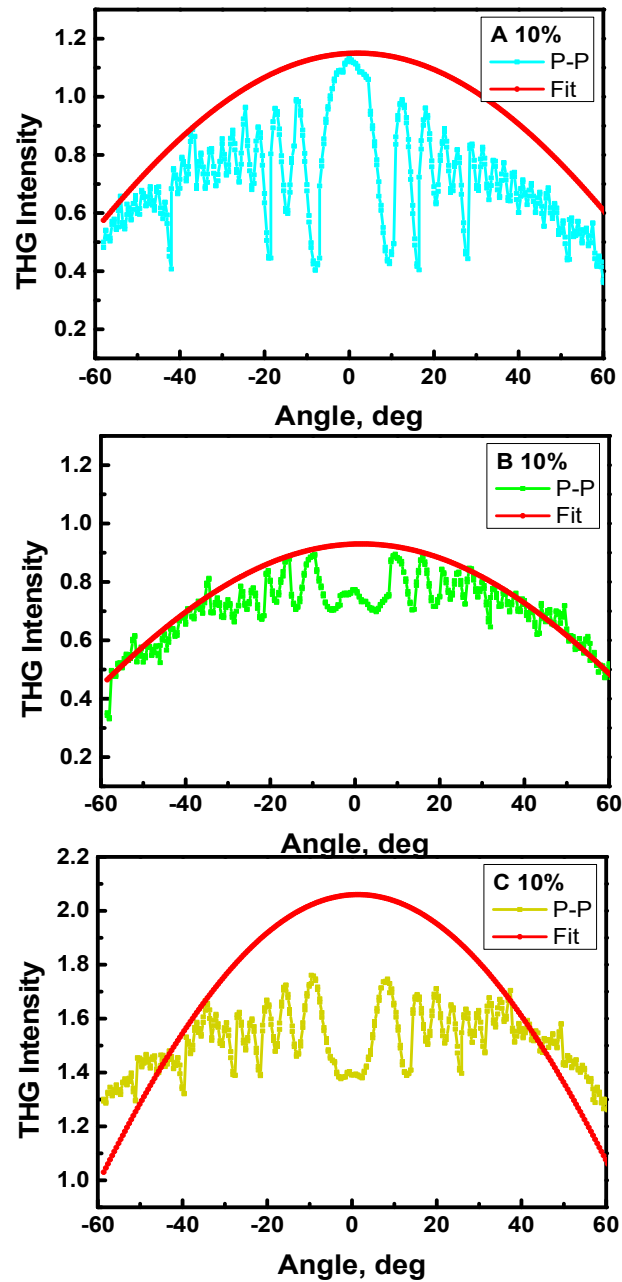
Figure 8.31. THG intensity as a function of incident angle

The obtained values of the second-order nonlinear coefficients for the samples A/PVK, B/PVK, and C/PVK ordered by the external electric field are within the range: $0.21 - 0.45 \times 10^{-12}$ pm/V for 10 wt% (p-p polarization). They are comparable with the second-order susceptibilities of the urea ($\chi^{(2)}=1.0 \times 10^{-12}$ pm/V [29]), and other similar systems [30,31]. These values are slightly higher compared to the second-order susceptibility of the A/PMMA, B/PMMA, and C/PMMA films with

the same concentration ($\chi^{(2)}$=0.28 - 0.36 $\times 10^{-12}$ pm/V) [24]. The measured $\chi^{(3)}$ for investigated materials are in the range of: 19.38 - 27.61 $\times 10^{-22}$ m²V⁻² for 10 wt% systems and are much higher than the respective value of the reference material as silica (see Tab. 8.7). One can also note that the obtained $\chi^{(3)}$ values for A, B, and C molecules integrated into PVK matrices are higher than the $\chi^{(3)}$ susceptibility values for A, B, and C in PMMA films with 10 wt% (11.36 - 20.84 $\times 10^{-22}$ m²V⁻²) [24].

It can be concluded that higher values of NLO factors, especially of the third-order response, were obtained for the tested A, B, and C compounds incorporated into the PVK matrix compared to the PMMA matrix. These observations agree with theoretical studies showing that the environment of a PVK polymer matrix enhances the hyperpolarizability values. This is especially observed for C molecule-based systems.

8.5. Conclusions

Computational and experimental investigations of the structural, electron, and optical properties of A, B, and C molecules, as well as composites composed of these chromophores and PMMA or PVK matrixes, are presented in this Chapter. The studied molecules A, B, and C exhibit quadratic and cubic optical nonlinearities related to the different substitution of donor groups.

Was noticed that the benzofuran moiety (chromophore B) causes the highest value of β_{vec} and the carbazole group causes the lowest value of the β_{vec} (chromophore C) when the molecules are in a vacuum. The mentioned properties are completely changed when the molecules are in the polymer matrix. The PMMA polymer increases the static β_{vec} value for the A and C molecules. However, it does not change the static β_{vec} of the B molecule. Also, the PVK matrix increases the static β_{vec} for A and C molecules decreasing the β_{vec} of the B molecules. In this case, the destructive influence of the host material on the NLO properties of the chromophore is seen.

Was observed that the frequency-dependent β_{vec} increases only for the C molecules in both matrixes. The C molecule is compatible with the PMMA and PVK matrix enhancing the NLO properties of the chromophores. The influence of

the polymer on the electron and optical properties of the chromophores was modeled by applying the discrete local electric field model and its correctness was proved experimentally. Was shown that the obtained NLO parameters are in agreement with experimental data.

The SHG signal recorded for the C/PMMA and C/PVK composites confirms their high $\chi^{(2)}$ susceptibility. A more extended conjugated character of molecule **C** relating to its strong push-pull character and narrow bandgap causes a high SHG signal even if the dipole moment of the molecule is not so important. The obtained results allow also concluding that the corona polling used to align the chromophores in the polymeric matrix is more efficient for the C molecules than for the chromophores A and B. The C molecules are long and their back relaxation to a disordered state is prevented. It was also proven computationally by performing MD simulations.

Analyzing the structures of modeled composites was found that chromophores C are located very close to the PMMA but they are not caught by the polymer cages. In this case, the alignment of C molecules in PMMA is easier than that of the other chromophores. The surface of the PMMA does not help in the alignment of the chromophores. The surface of PMMA thin-film is less dense and the chromophores enter into the polymer structure where their rotation is limited. The C molecules are also located close to the PVK polymer chain entering into its structure. It is the reason why the high local electric field is acting on the chromophore C and the significant increase of the second-order NLO output of the C/PVK system is observed.

Unfortunately, even though a high local electric field is acting on the molecules C in PVK polymer their second-order NLO signal is not so spectacular because the alignment of these chromophores in PVK is difficult. However, the C/PVK composite is the most stable structure during time with its chromophore alignment and can be used as potential materials for NLO devices applications. The C/PMMA and C/PVK have also vary high $\chi^{(3)}$ values which are in agreement with computational data. The C/PMMA and C/PVK give almost the same $\chi^{(2)}$ susceptibility value for 10 % of chromophores concentration but for 5 % the mentioned parameter is much higher for the PMMA matrix. It forces necessitates considering additional effects of matrices on the NLO properties of the composites, such as agglomeration of chromophores in the matrix.

Was found that the high dipole moment and low energy gap are not the only parameters determining the NLO properties of chromophores. An important role is played by the charge transfer occurring in the molecules under influence of the electric field and laser beam irradiation. The obtained results indicate that the NLO properties of the material are influenced by both the value of the appropriate hyperpolarizability and the tendency to organize chromophores in a polymer matrix under the influence of an external electric field

References

[1]   Abraham M., Hess B., Spoel D. V. D., Lindahl E., Gromacs User Manual, Version 5.0.4. *The GROMACS development team at the Royal Institute of Technology and Uppsala University, Sweden,* 2014.

[2]   Hagler A. T., Lifson S., Dauber P., Journal of the American Chemical Society, 101, 18, 5122-5130 (1979).

[3]   Fois E., Gamba A., Tilocca A., Microporous and Mesoporous Materials, 57, 3, 263-272 (2993).

[4]   Kawata M., Nagashima U., Chemical Physics Letters, 340, 1-2, 165-172 (2001).

[5]   Deserno M., Holm Ch., The Journal of Chemical Physics, 109, 18, 7678-7693 (1998).

[6]   Makowska-Janusik M., Reis H., Papadopoulos M. G., Economou I. G., Zacharopoulos N., *The Journal of Physical Chemistry B*, 108, 2, 588-596 (2004).

[7]   Teng H., Koike K., Zhou D., Satoh Z., Koike Y., Okamoto Y.,
Journal of Polymer Science Part A: Polymer Chemistry, 47, 1, 315-317 (2008).

[8]   Reyna-González J. M., Roquero P., Rivera E., Designed Monomers and Polymers, 12, 3, 233–245 (2009).

[9]   Schmidt M. W., Baldridge K. K., Boatz J. A., Elbert S. T., Gordon M. S., Jensen J. H., Koseki S., Matsunaga N., Nguyen K. A., Su S. J., Windus T. L., Dupuis M., Montgomery J. A., Journal of Computational Chemistry, 14, 1347-1363 (1993).

[10]   Gordon M.S., Schmidt M.W., Advances in electronic structure theory: GAMESS a Decade Later, C. E. Dykstra, G. Frenking, K.S. Kim, G.E. Scuseria, (eds.), in: Theory and Applications of Computational Chemistry: the first forty years. Elsevier, Amsterdam, Netherlands, 1167-1189 (2005).

[11]   Roothaan C. C. J., Reviews of Modern Physics, 23, 69-89 (1951).

[12]   Jensen F., The Journal of Chemical Physics, 102, 6706-6718 (1995).

[13]   Haharan P. C., Pople J. A., Theoret. Chim. Acta. 28, 213-222 (1973).

[14]   Frisch M. J., Pople J. A., Binkley J. S., J. Chem. Phys. 80, 3265-3269 (1984).

[15]   Clark T., Chandrasekhar J., Spitznagel G. W., Schleyer P., J. Comput. Chem. 4, 294-301 (1983).

[16]   Becke A. D., Phys. Rev. A 38, 3098-3100 (1988).

[17]   Becke A. D., J. Chem. Phys. 98, 5648-5652 (1993).

[18]   Lee C., Yang W., Parr R. G., Phys. Rev. B 37, 785-789 (1988).

[19]   Yanai T., Tew D. P., Handy N. C., Chem. Phys. Lett. 393, 51-57 (2004).

[20]   Iikura H., Tsuneda T., Yanai T., Hirao K., J. Chem. Phys. 115, 3540-3544 (2001).

[21]   Davidson E. R., Methods in computational molecular physics, Reidel, Boston 95-113 (1983).

[22]   Cossi M., Rega N., Scalmani G., Barone V., J.Comput. Chem., 24(6), 669-681 (2003).

[23]   Boni L. D., Toro C., Zilio S. C., Mendonca C. R., Hernandez F. E., Chem. Phys. Lett. 487, 226–231 (2010).

[24]   Mydlova L., Taboukhat S., Waszkowska K., Ibrahim N., Migalska-Zalas A., Sahraoui B., Frere P., Makowska-Janusik M.,Journal of Molecular Liquids 314, 113622 (2020).

[25]   Havermeyer F., Pruner C., Rupp R. A., Schubert D. W., Krätzig E., Appl. Phys. B 72, 201–205 (2001).

[26]   P.D.Maker, R.W. Terhune, M. Nisenhoff, C.M. Savage, Phys. Rev. Lett. 8, 21–22 (1962).

[27]   Lee G. J., Cha S. W., Jeon S. J., Jin J.-I., Yoon J. S., J.-Korean Phys. Soc., 39, 912-915 (2001).

[28]   Kajzar F., Okada-Shudo Y., Merrit C., Kafafi C., *Synthetic Metals, 117*, 189–193 (2001).

[29]   Ferrero M., Civalleri B., Rérat M., Orlando R., Dovesi R., J. Chem. Phys. 131, 214704 (2009).

[30]   Mydlova L.,Taboukhat S., Ayadi A., Migalska-Zalas A., El-Ghayoury A., Zawadzka A., Makowska-Janusik M., Sahraoui B., Opt. Materials 86, 304–310 (2018).

[31]   Migalska-Zalas A., Korchi K. E., Chtouki T., Optical and Quantum Electronics 50, 389-10 (2018).

[32]   Kubodera K., Kobayashi H., Mol. Cryst. Liq. Cryst. Inc. Nonlinear Opt. 182, 103-113 (1992).

[33]   Leupacher W., Penzkofer A., Appl. Phys. B Lasers Opt. 36, 25–31 (1985).

[34]   Reis H., Makowska-Janusik M., Papadopoulos M. G., The Journal of Physical Chemistry B, 108, 26, 8931-8940 (2004).

[35]   Prasad P.N., Williams D.J., *Introduction to Nonlinear Optical Effects in Molecules and Polymers.*; Wiley, New York, United States of America, (1991).

Chapter 9

Conclusions

Organic nonlinear optical (NLO) materials provide strong potential advantages for the generation of higher harmonics of light. They are considered as most promising candidates for application in electro-optics and photonic devices. They are generally synthesized in the form of composite *guest-host* materials by mixing NLO chromophores possessing large molecular hyperpolarizabilities and amorphous polymer. A variety of *guest-host* systems can be prepared simply by mixing two components. To generate second-order NLO activity, the *guest-host* system is poled under an external electric field at an elevated temperature, which induces a degree of orientation order.

To achieve good device functionality, the NLO chromophore has to possess high microscopic molecular nonlinearity ($\mu\beta$), and particularly weak molecular electrostatic interaction in the polymer matrix simultaneously. There are cases when the polymer matrix modifies or even eliminates the NLO properties of chromophores through intermolecular interactions. The mentioned problem was formulated as the thesis of the presented dissertation.

To prove this statement, two different polymer matrixes as PMMA and PVK were chosen to be host materials keeping two different groups of chromophores: TTF and benzonitrile derivatives. These composites were investigated experimentally by measuring their SHG and THG output signals and linear optical properties. The obtained results were compared with the computationally obtained data predicting the optical properties of composites and their components. In consequence, a universal model to predict the macroscopic optical properties of composite materials in thin-film forms was developed.

Using MD simulations four composite materials with TTF-derivatives and PMMA host as L1/PMMA, L2/PMMA, L3/PMMA, and L4/PMMA were modeled. Also, six *guest-host* materials based on PMMA and PVK matrixes with benzonitrile derivatives were studied, namely A/PMMA, B/PMMA, C/PMMA, A/PVK, B/PVK, and C/PVK. Computer simulations were performed for bulk and thin-film materials.

Was shown that benzonitrile derivatives (A, B, C) exhibit different $\chi^{(2)}$ and $\chi^{(3)}$ values in PMMA and PVK polymers. The $\chi^{(2)}$ value is higher for PVK than for PMMA-based composites comparing systems with 10 % of chromophores. Also, $\chi^{(3)}$ is higher for the PVK than for PMMA-based systems. It shows that the polymer matrix changes the NLO properties of the components. To explain obtained results location of the chromophores in the polymer matrix as well as their reorientation ability was investigated using molecular dynamic simulations.

One can conclude that the location of the chromophores in the polymer matrix depends on the structure of the chromophore and the polymer. Based on the intermolecular interactions chromophores enter into polymer structure locating themselves in free volume cages. This situation was observed for the PMMA polymer with embedded B, L3, and L4 chromophores into it. The chromophores located in polymer cages are more difficult to be polled by an external electric field. As consequence, they give a low second-order NLO signal. In the presented work was proved that the advantageous situation is that the chromophores are close to the polymer chain but not in their cages. Was observed that the A, B, and C molecules are located closer to the PVK polymer chain than to the PMMA polymer which is the reason for the polymer shape. Even the observed difference is insignificant it gives visible changes in SHG and THG signals coming from C/PMMA and C/PVK

composites. It is the consequence of the fact that the polymer surrounding chromophores acts on them by multipolar intermolecular interaction changing their electron properties.

Composites used for second-order NLO applications should be aligned in the polymer matrix. The alignment of the chromophores is easier where the composite is less dense which a feature of the surface is. Was found that in the alignment process more important is the location of the chromophores than their electric dipole moments.

This statement permits to development discrete local field model allowing computing optical properties of chromophores embedded into a polymer environment. The hierarchical approach applied for the studied systems showed the correctness of the proposed methodology of calculations by comparing the obtained computational data with the experimental results of the SHG and THG measurements. The calculated local electric field mostly depends on polymer characteristics such as the presence of the polar groups, and the location of the chromophores in the polymer matrix.

The local electric field model gives the possibility to calculate the NLO properties of investigated composites. Was shown that the C molecule is compatible with the PMMA and PVK matrix. Both matrixes increase the second-order hyperpolarizability of the chromophores increasing the second-order NLO properties of composite materials. The chromophore C has the highest value of electron dipole moment of all benzonitrile derivatives. One can conclude that the polymer matrix changes the properties of polar chromophores more than it is done for molecules with an insignificant electric dipole moment. The local electric field changes the electric dipole moment of the chromophores as well as over the location of the frontiers orbitals affecting by it their NLO properties.

In the presented work was shown that the discrete local field model can be used to describe the linear and NLO properties of composite materials in the form of bulk and thin films. Obtained consistency of the theoretical and experimental results is appropriate. However, probably better results can be obtained computationally by dividing chromophores into subfragments to calculate electric local field intensity. These investigations can be a good idea for future research work.

OŚWIADCZENIE

Ja, niżej podpisana Lucia Nechalova

Imię i Nazwisko

~~doktorant~~* / doktorantka* Wydziału Nauk Ścisłych, Przyrodniczych i Technicznych, Uniwersytetu Humanistyczno-Przyrodniczego im. Jana Długosza w Częstochowie oświadczam, że przedkładaną pracę doktorską pt.

The influence of environment on the electronic and optical properties of thin-film composite materials

napisałam samodzielnie. Oznacza to, że przy pisaniu pracy, poza niezbędnymi konsultacjami, nie korzystałam z pomocy innych osób, a w szczególności nie zlecałam opracowania rozprawy lub jej części innym osobom, ani nie odpisywałam tej rozprawy lub jej części od innych osób.

Oświadczam również, że drukowana wersja pracy jest identyczna z załączoną wersją elektroniczną.

Jednocześnie przyjmuję do wiadomości, że gdyby powyższe oświadczenie okazało się nieprawdziwe, decyzja o wydaniu mi dyplomu zostanie cofnięta.

Ponieważ niniejsza praca jest moją własnością intelektualną, chronioną prawem autorskim, w związku z zamysłem wydania jej drukiem wyrażam zgodę* / ~~nie wyrażam zgody~~* na udostępnianie mojej rozprawy doktorskiej do celów naukowych i badawczych w internecie.

Częstochowa, dnia 28. 04. 2022

Lucia Nechalova

podpis

* - niepotrzebne skreślić